Biologically Inspired Sensors for Attitude Determination and Color Processing

Łukasz Farian

May 24, 2019

Thesis submitted for the degree of Philosophiæ Doctor

Abstract

"The imagination of nature is far, far greater than the imagination of the man"

(Richard Feynman)

More than two centuries ago a French inventor, Nicéphore Niépce, successfully took a first photographic image by a camera prototype built by himself. The first images captured by his devices faded away very fast when exposed to light used for viewing. In the next years, the photolithography process became better understood and first commercial analog cameras appeared. Analog cameras gradually became more affordable and ergonomic by miniaturizing mechanical parts and thanks to inventing photographic films. Besides still photography cameras, also video cameras able to capture motion pictures were invented.

Due to advancements in electronics and computerization, the first digital (video) cameras appeared in the late 1980s. Digital cameras use photoactive properties of silicon to transform incoming light into electron charges and then convert them into digital form. Further progress in electronic integration helped to encapsulate a whole digital sensor with all the critical electronic components within one chip, measuring only a few square-millimeters in dimension. Thanks to a small form factor, nowadays digital cameras can be found in any smartphone, laptop, and many other consumer electronics devices. Today, cameras find applications in many areas not only related to photography and cinematography - for instance they have become key components of machine vision systems. There is a great demand for high performance vision sensors for robotic and automotive applications. For example, fully autonomous driving sensory systems set very high-performance requirements for future vision sensors to operate within very wide range of scene illumination levels, to adapt to the environment outside the vehicle, and deliver a clear image even with direct sunlight within the scene. Also, their Signal to Noise Ratio (SNR) should be remarkably low to provide clear im-

ages at low light conditions, they should be highly sensitive to each photon hitting the sensor photosensitive array, and operate with very high speed to provide meaningful images while driving.

Currently, almost all commercially available video cameras are based on capturing a sequence of image-frames. Frame-based sensors have inherent limitations of bandwidth as they continuously sample the entire scene with a fixed rate. Likewise, their dynamic range is reduced because Automatic Gain Control (AGC) and exposure time is globally set equally for the entire pixel matrix. Frame-based video cameras generate redundant data because they always periodically transmit information from all the pixels regardless if the scene has changed or not.

The recently emerged new type of biologically inspired frame-less sensors can overcome limitations of their frame-based counterparts. Biologically inspired sensors are massively parallel, and data driven devices. Since they consist of many inter-connected specialized sub-blocks performing parallel tasks, these systems can process information very efficiently.

Bio-inspired sensors are a result of the Neuromorphic engineering development. Neuromorphic engineering is a concept describing the use integrated analog electronic circuits to mimic neuro-biological principles of operation present in the nervous system. Mimicking nature is motivated by the fact that biological systems easily outperform conventional artificial ones in terms of processing and power efficiency. For vision sensors, a specialized light-sensitive tissue located under eye, called retina, serves as an inspiration. The retina is greatly optimized to perform complex parallel pre-processing of the visual scene and to efficiently extract relevant information from it.

In this thesis, two topics related to bio-inspired sensors were studied. First, a spiking vision sensor detecting transients between three primary colors was designed to address a challenge of trichromatic transient color detection inspired by color processing found in mammalian retinas. The second part of the PhD research focused on the design of an event-driven sun sensor on the framework of a collaborative project for space application scenarios. Two different approaches of using spiking luminance sensors to implement a sun sensor were explored. Advantages of the developed systems are studied over the state-of-the-art solutions.

Acknowledgments

This work is submitted to Department of Informatics (IFI), Faculty of Mathematics and Natural Sciences at University of Oslo (UiO) as a part of the requirements for the degree of Doctor of Philosophy (Ph.D). The thesis is written as a compendium of eight academic papers. The main body of the thesis provides the summary of the main methods, findings and conclusions. For main details the reader should refer to the attached academic papers.

This research was undertaken at the Nanoelectronics group, Department of Informatics, University of Oslo, with Professor Philipp Häfliger as a main supervisor, Associate Professor Juan A. Leñero-Bardallo and Associate Professor Ketil Røed as co-supervisors.

I would like to thank Professor Philipp Häfliger for putting trust in my abilities for conducting this research, and then competently directing my research. I appreciate his enthusiasm, indulgence and inspirational suggestions, but also a given freedom to pursue my research, while silently ensuring that I stay on course.

I want to express my deepest appreciation to Associate Professor Juan A. Leñero-Bardallo for his great support and guidance. Thank you for taking active role in supervision of this PhD research at every stage, for your great involvement in progress of this thesis and for motivating me to complete the work.

Furthermore, I would like to thank Associate Professor Ketil Røed for his technical assistance, especially for sharing his expertise in radiation effects in electronic components.

I would like to thank Associate Professor Wojciech Miloch for creating this research opportunity within 4DSpace project, and also, for inspiring 4Dspace lunch seminars.

Moreover, I acknowledge Senior Engineer Olav Stanly Kyrvestad for assistance with chip fabrication, setting up measurements and general guidance. I thank Senior Engineer Espen Trondsen for his assistance with instrumentation and help with conducting measurements.

Part of this research work was conducted in a collaboration with Institute of Microelectronics, University of Sevilla. I would like to acknowledge Associate Professor Ricardo Carmona-Galán, Professor José Maria Guerrero Rodríguez and Professor Ángel Rodríguez-Vázquez.

I would like to thank Werner Luzi from Nordic Semiconductor for support in proof-reading my publication, especially in terms of English wording and Hung Bui from Nordic Semiconductor for his help in programming development boards for a live demonstration, Professor Tobi Delbrück for the jAER software, and the anonymous reviewers that have contributed to improve the quality of the publications.

I thank my parents for bringing me to this world and raising me to who I am today.

Finally, I thank my wife, Malihe Zarre Dooghabadi, for supporting me at every stage of this PhD. I truly appreciate your endless patience and understanding for bringing my work home and staying late nights and weekends working. I dedicate this work to our newborn son, Armin, who is a new inspiration in my life.

Contents

Chapter 1

Introduction

The first model approximating behavior of the human retina was built with discrete components by Fukushima in the 1970s [1]. Eighteen years later Mahowald proposed the first integrated biologically inspired vision sensor capable of detecting spatial contrast within the visual scene by modeling operation of biological cells found in the retina [2]. Since then, various types of vision sensors taking inspiration from biology were proposed [3].

The structure of the retina is very complex, it consists of many specialized cells interconnected in three-dimensional structures. Many of the retinal internal processes are already well understood [4]. Probably the most prominent and best understood property of the retina is a spatio-temporal processing capable of extracting edges and shapes from the scene. Top layer of the retina consists of photoreceptors (cons and rods) transforming incoming light into an electrical signal, which is then converted into synaptic spike trains [5]. The output from the photoreceptors drives horizontal cells and bipolar cells in the layer beneath. Horizontal cells are laterally connected to each other to create a spatio-temporal low-pass filtering network able to average signals from neighboring photoreceptors. Bipolar cells flag bright and dark spatio-temporal contrast by comparing the local photoreceptor's signals to averaged illumination from the horizontal mesh. Before being converted into spike trains, spatio-temporal information extracted by this process is further processed to extract most relevant properties out of the scene [3], such as:

- automatic change of local gain of the photoreceptor to adapt to absolute lighting conditions and extend retina's dynamic range,
- low-pass filtering of spatio-temporal outputs to reject noise and reduce data

bandwidth,

- rejection of opposed responses of bright and dark bipolar cells flags to reduce spike-firing,

- amplification of temporal variations to magnify temporal changes in the scene.

Biologically inspired vision sensors can be categorized into three groups depending on which retinal property they mimic: spatio-temporal contrast sensors, Dynamic Vision Sensors (DVS), and spiking luminance sensors (also known as octopus retinas).

The first silicon retina proposed by Mahowald [2] was a faithful copy of spatial processing observed in the retina. The original topology is shown in Fig. 1.1.

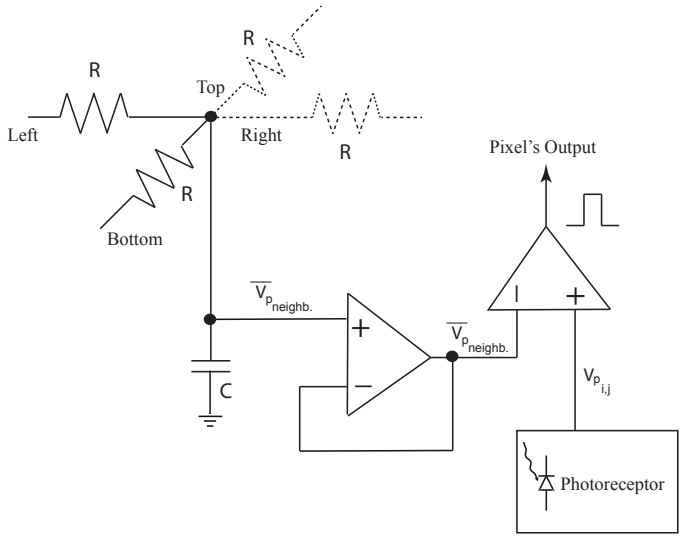

Figure 1.1: Original retina contrast detection pixel [2]. Spatial averaging of the neighboring pixels was achieved by a network of resistors. The averaged illumination value $V_{p_{neighb.}}$ is compared to the local pixel illumination $V_{p_{i,j}}$. The differential amplifier amplifies the difference between the output from the photoreceptor and the local average and outputs flag to indicate difference between these values.

Pixels detect light with a photodiode that transduces the photo-current into a voltage (equivalent to a photoreceptor in the retina). This voltage is then averaged

within a neighborhood by a diffusive resistive network interconnecting neighboring pixels. If the average illumination value in the neighborhood, $V_{p_{neighb.}}$, differs from the pixel's local illumination value, $V_{p_{i,j}}$, the pixel will spike, indicating the detection of spatial contrast.

Dynamic Vision Sensors (DVS) are sensitive to temporal contrast - i.e. they respond to the scene dynamics such that they directly respond to changes in the scene. A first functional DVS sensor was proposed by Lichsteiner [6] in 2008. Pixel's topology is depicted in Fig. 1.2. Input light is amplified in a logarithmic fashion in order to improve the photoreceptor's dynamic range. After amplification, an output voltage v_i is fed into a differencing circuit that computes temporal derivative v_{diff}. At the output, two comparators flag whenever transient variations exceed either positive or negative predefined thresholds.

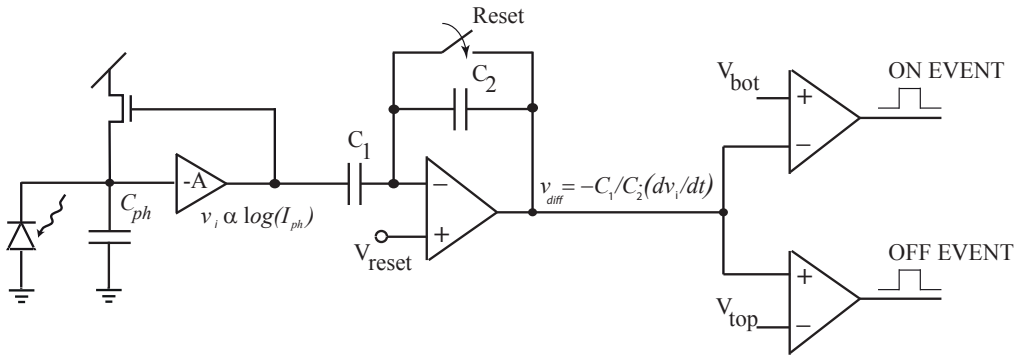

Figure 1.2: Pixel's topology of a first functional DVS sensor proposed by Lichsteiner [6].

DVS sensors can detect fast changes of illumination, with low power and low data bandwidth consumption. Data bandwidth is preserved by transmitting information only about changes in the scene rather than information about usually redundant static foreground. Dynamic Vision Sensors are able to track precisely and almost in real time changes within the scene containing both, very bright and dark regions. Temporal resolution and intra-scene dynamic range are dramatically better than in standard commercial image sensors by taking inspiration from a biological fully parallel approach, where pixels operate independently from each other and can adapt locally to absolute light conditions. Additionally, logarithmic compression helps to encapsulate a wide range of input light intensities into the smaller output range. Such high temporal resolution is not achievable by stan-

dard image sensors because they operate in synchronous, frame-based fashion. State-of-the-art image sensors extract visual information by capturing a series of 'snapshots' of the visual scene, called frames. Each frame of the scene is recorded at discrete time point, with a time resolution defined by a fixed frame rate.

The last category of sensors are spiking luminance sensors, which perform light-to-frequency conversion - i.e. they spike with a frequency directly proportional to luminance levels of the visual scene [7]. Simplified diagram and principle of operation are shown in Fig. 1.3.

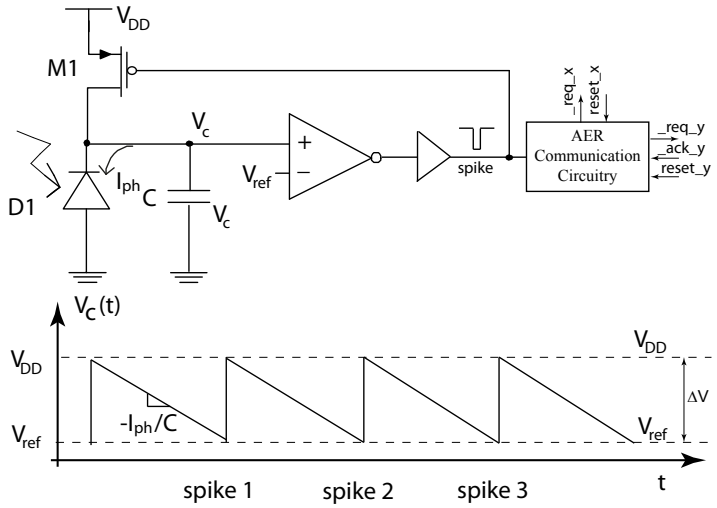

Figure 1.3: Simplified block diagram of an Integrate-and-Fire (I&F) pixel. Pixels spike with a frequency proportional to light intensity. Every time that this occurs, pixel addresses are transmitted asynchronously off-chip. Asynchronous digital signals involved in the data transmission are displayed on the right.

The pixel operation is analogous to integrate-and-fire neuron. Initially the pre-charged capacitance C is discharged with the rate proportional to the photodiode's $D1$ photocurrent. When the voltage V_C reaches a programmable threshold V_{ref}, the comparator initiates pixel reset and charge integration starts again. Similarly, as DVS sensors, pixels in this sensor operate independently from each other. Only pixels which are illuminated elicit spikes, and dark pixels stay silent. In some applications where dark pixels are redundant, this approach helps to save data bandwidth. Also, for this group of sensors, pixels integration time is not limited by a frame rate, and hence they can operate for wide range of illumination levels of dynamic range higher than 100dB [7].

Due to their spiking nature, biologically inspired sensors are called event-based or spiking vision sensors. Sensors from all three groups described above share the same event-driven operation - i.e. information about some properties of the visual scene is encoded by asynchronous pixels and conveyed by their spiking activity. Spiking sensors readout is complex because each pixel in the array can spike at any time and at any location. The readout must preserve precise timing and location of the origin of each spike. In order to provide such point-to-point communication to each pixel, an Address Event Representation (AER) protocol was proposed originally by Caltech research lab [8]. The AER principles adapted

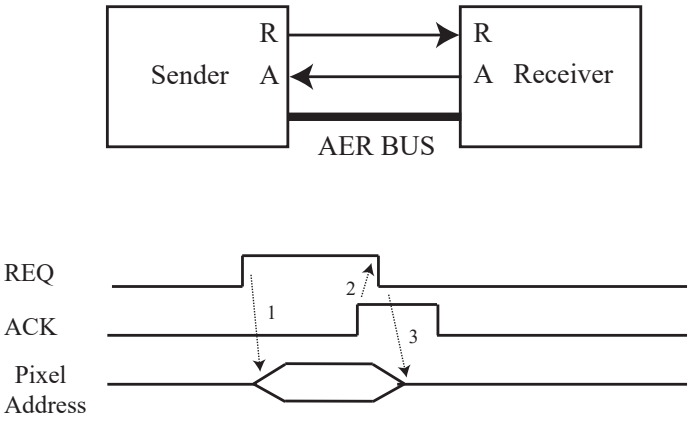

Figure 1.4: AER communication protocol 4-phase handshake cycle. A sender sends a request (REQ) and puts a valid pixel address at the AER bus at time "1". A receiver confirms successful readout of the address by eliciting acknowledge pulse (ACK) at time "2". Then, the sender withdraws its request signals and address from the AER bus, at time "3".

in our implementation is to assign a unique address to each neuron (or pixel), arbitrate spikes from the array of neurons, and provide convenient handshake readout interface of these events. Fig. 1.4 illustrates a principle of operation of AER communication protocol. In case of event (spike), pixel's coordinates transmission through an asynchronous AER bus is preceded by a "request - acknowledge" handshake. As a result, the sensor output data is a stream of address events representing (x,y) coordinates in time. Temporal information of timing of the events is explicitly added to the address of the pixel in the form of a timestamp by the receiver side.

Fig. 1.5 shows a block level view of an exemplary 4x4 pixel array combined

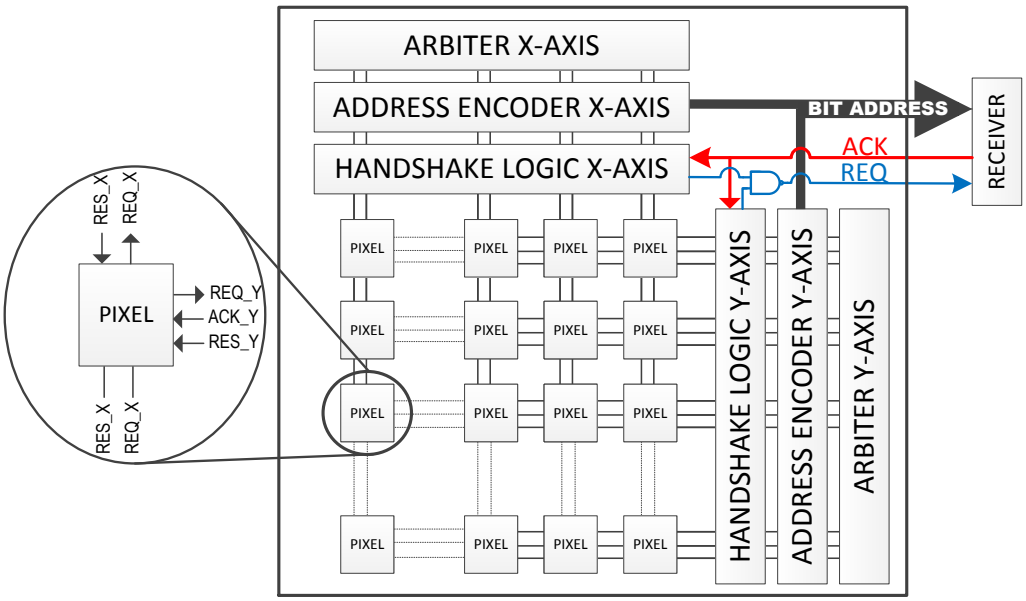

Figure 1.5: Block level view of the pixel array and the AER communication periphery. The number of pixels is decreased for clarity. The USBAERmini board serves as a receiver (which further interfaces with a PC).

with the AER peripherial circuitry: handshake logic, address encoders and arbiters [9]. Handshake logic handles communication and addressing active pixels in asynchronous fashion by acknowledging pixel's requests in x- and y-coordinates. Address encoders generate address of currently active pixel at the output bus. Since the output bus is shared between all pixels, glitches may happen if two or more pixels spike at the same time. To ensure that only one pixel can access the address bus at the time, arbiters restrict access to the bus, such that in case of high pixels activity, pixels' pending requests are queued. Arbiters are organized in a binary tree structure in order to provide arbitration to entire array. Receiver communicates asynchronously with the array (REQ, ACK) and conveys pixels addresses via output address bus.

Other variants of the AER communication protocol such as handshake-less [10] and unarbitrated [11] types are less commonly used.

1.1 4Dspace Research Initiative

This PhD Research Fellowship was a part of the 4DSpace project [12]. The 4DSpace project is an initiative at the Faculty of Mathematics and Natural Sciences at the University of Oslo, combining Departments of Physics, Informatics, and Mathematics. The main goal of the 4DSpace project is to study the role of the turbulence and instabilities in the polar ionosphere in the energy transfer and transport mechanisms at different scales in the near-Earth space. The ionospheric electron density irregularities affect the trans ionospheric radio waves. Radio waves that pass through such regions cause signal degradation, which is known as ionospheric scintillations [13]. Positioning accuracy of for instance Global Navigation Satellite System (GNSS), in the presence of scintillation, can severely degrade.

In order to understand ionospheric turbulence and instabilities, they should be sensed in-situ with the multi-scale 4D (space and time) experimental approach by rocket and satellite-based instruments, payloads and daughter payloads. Hence, the ultimate goal for 4DSpace is to develop a fully integrated System-on-Chip (SoC) using an Application Specific Integrated Circuits (ASICs) with the aim of fully integrating necessary electronic sub-blocks, such as front-ends to control sub-probes of sounding rockets, analog-to-digital (A/D) converters and sensors determining orientation of the instrument with respect to the sun as a part of Sounding Rocket Attitude Determination System (SRAD). A sounding rocket will carry and eject a small swarm of hockey-puck-sized daughter micro-probes which will gather data in a volume around the rocket and will revisit the same region, such that both temporal and spatial information can be retrieved. Integration of all electronics into a single SoC is important especially for the miniaturized daughter payloads as their carrying capacity is limited. The sounding rockets and micro-probes will intentionally have high spinning rates to stabilize their attitude during their flight. This has set requirement for the sun sensor to be able to track sun position with high temporal resolution and very low readout latency.

1.2 Research Objectives

This PhD research fellowship focused on two distinctive topics: on exploring trichromatic vision for DVS sensors, and on designing an event-driven sun sensor for 4DSpace project.

As a first part of this research, an event-driven vision sensor was designed to address a challenge of trichromatic transient color detection inspired by color

processing found in mammalian retinas. Biological retinas process visual images by means of color opponencies, and are capable of detecting transients between three primary colors. This research investigated feasibility and advantages of such system implemented in silicon. It was based on a DVS sensor and served as a starting point to gain expertise on the implementation of event-based sensors. The chip was a proof-of-concept with low resolution not aimed for a particular research project.

The second part of this PhD research was more comprehensive and focused on the design of an event-driven sun sensor on the framework of a collaborative project. Here a functional and competitive device was on demand, and performance requirements were predefined by the project. For this case, the proposed solution was based on an octopus spiking image sensor. Two different approaches of implementing sun sensor were explored: a pinhole-based design and full-custom design.

1.3 Thesis Outline

This thesis is organized as follows: the current chapter gives an overview of objectives for this PhD research fellowship and briefly sketches research activities. Also, background of event-based vision sensors and their main types are explained for reader's better understanding. Chapter 2 introduces state-of-the-art Color Dynamic Vision Sensor and describes first Tri-color Temporal Contrast Vision Sensor developed during this research. Chapter 3 focuses on bio-inspired sun sensors and gives detailed description of two event-driven sun sensors implemented on the framework of a collaborative project. Finally, Chapters 4 and 5 discuss outlook and future work, and draw conclusions.

This thesis is written as a compendium of academic papers. The thesis main body provides a summary of the methods, findings and conclusions. For main details the reader should refer to the attached academic papers.

Chapter 2

Color Dynamic Vision Sensors

At this moment spiking vision sensors cannot compete with commercial sensors in terms of quality and resolution of the image because they suffer from high noise and resolution limitation [3]. Due to high pixels complexity, their fill factor is low, and hence resolution of the image is much lower than for commercial sensors. Frame-based techniques have matured over years and have been greatly improved. As a result, today cameras used for consumer electronics, photography or cinematography achieve high image resolution, dynamic range, and color saturation to faithfully copy the visual-scene [14]. However, for many applications, response time, operation in high intra-scene dynamic range, low data bandwidth or low power consumption are more important than faithful constitution of a scene.

For some applications, information about motion (change of a state) and spectral color of the tracked object is more important than information about a static foreground. For instance, robotic and automotive vision systems are required to detect and track colored objects of interest and obstacles in real time. Also, in production lines it is essential to detect defective samples or match items of the same colors with high speed to increase production efficiency. In that sense, the good temporal resolution of DVS sensors, their low latency and their low redundancy makes them good candidates for such applications.

The first DVS sensor [6] was operating in a greyscale mode - i.e. it detected temporal contrast of incoming light regardless of color. Color filters require to have different pixels dedicated to detect each color. Extending DVS sensor with color discrimination was neglected because its pixel topology was already complex, and adding extra color processing and filters would further decrease already low fill factor and consequently the array resolution.

In 2011 Berner et al. [15] proposed a design of a DVS pixel with reasonable fill

factor by using an alternative method of vertical stacking photodiodes at different depths in silicon. The pixel was capable of detecting transitions between two colors.

The concept of stacked photo-diodes was originally introduced and patented in 1980 [16] and then twenty years later refined and commercialized by the company Foveon [17, 18]. It is worth mentioning that there are also color spiking luminance sensors which use stacked photodiodes. These sensors are able to extract color information of a static scene. Olsson et al. [19] implemented a sensor distinguishing static light sources of two different colors. Leñero-Bardallo et al. [20] further extended the spiking luminance sensor and achieved spectral selectivity within three colors.

2.1 Tri-color Temporal Contrast Vision Sensor

During this research a first DVS sensor detecting shifts between three primary colors was proposed [21, 22, 23]. Due to use of temporal contrast event-based processing scheme this novel sensor is capable of extracting transient emissions shifts within the visual spectrum with a very high speed and high dynamic range. The pixel design is inspired by the one proposed by Berner et al. [15] to detect color transitions. That one was based on the original one with switched capacitors proposed by Lichsteiner et al. [6]. The new pixel proposed in this work has been extended to operate with three stacked photodiodes, the AER readout circuitry was implemented to handle the AER communication of a pixel matrix and post-processing algorithm to display color information was developed.

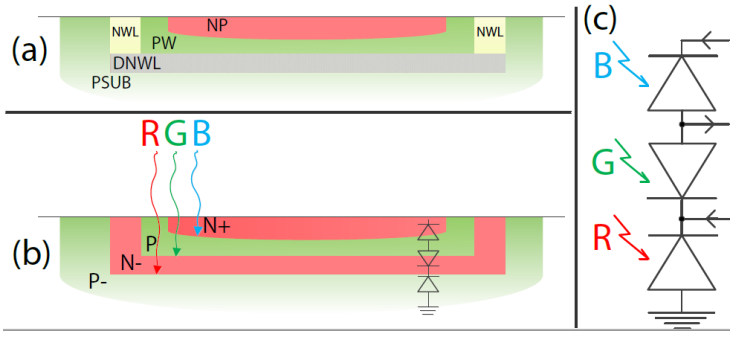

Figure 2.1: Stacked photodiodes cross section diagram. (a) Design layers used in fabrication process, (b) n-p junctions, (c) stacked photodiodes equivalent diagram.

The sensor operation is based on color processing found in the retina. The solution incorporates pixels processing visual spectra in so called color opponent fashion, such that certain pairs of colors (opponents) are mutually exclusive. Certain hues are never perceived to occur simultaneously. In the human retina, there is a red/green opponency and a blue/yellow opponency. Ganglion cells receive inhibition or excitation from these different opponents that are always antagonistic [4].

In order to improve a sensor fill factor, instead of using multiple color filters on top of pixels, a stack of three photodiodes is implemented by means of n-well and deep n-well diffusion diodes, shown in Fig. 2.1. Modern fabrication technologies allow to stack photodiodes at different depths to obtain different color absorption spectra [24, 16]. The principle operation of stacked photodiodes is based on the fact that light penetration depth depends on the photons' wavelength [25]. Photons with higher energy (shorter wavelengths) travel statistically less time though the crystal before generating electron-hole pairs. Hence, the top photodiode is more sensitive to blue light, and the bottom ones more sensitive to longer wavelengths.

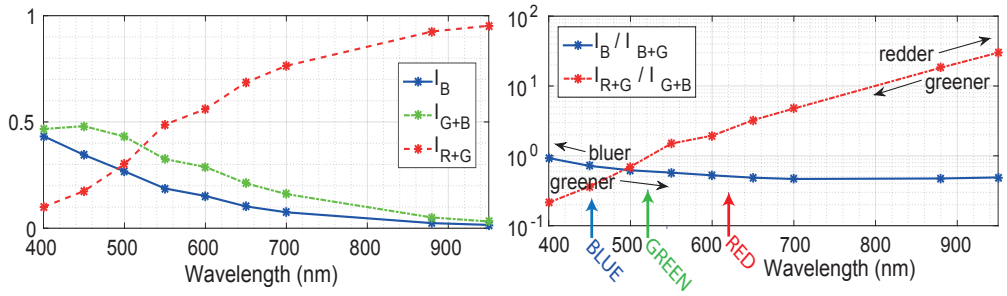

(a) Measured photocurrents relative values. (b) Computed Photocurrents ratios.

Figure 2.2: Spectral response of three stacked photo diodes in TSMC 90nm technology. The values are corrected by the Halogen Light Source irradiance factor and color filters transmission efficiency.

Since the photodiodes depths are not disclosed by the foundry, the exact spectral sensitivity of each photodiode cannot be estimated. Due to this fact, photodiodes are characterized in terms of spectral sensitivity. Fig. 2.2a shows the measured spectral response of the three photodiodes normalized with the sum of the three photocurrents. The top photodiode is the least sensitive to light, and the bottom one is the most sensitive. The bottom one has higher quantum efficiency because the size of its depletion region is bigger than the others'.

Fig. 2.2b displays the computed values of the two current ratios and illustrates

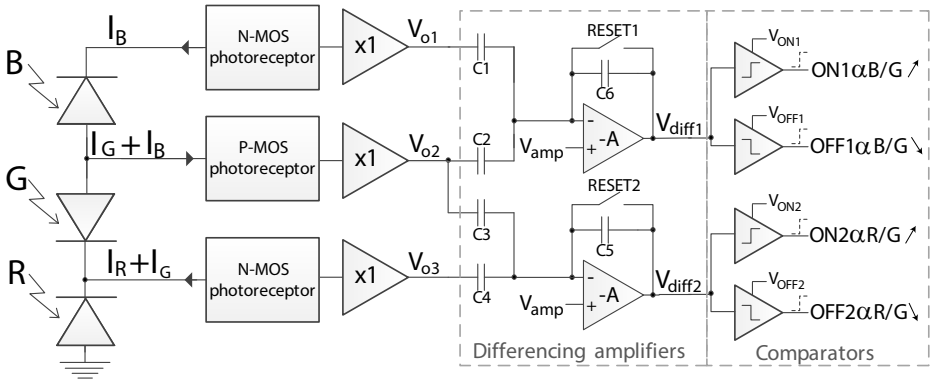

Figure 2.3: Pixel core main blocks.

how these ratios can be used to discriminate between colors. Photocurrents ratios are proportional to spectral ratios. The R/G ratio increases when the color spectrum shifts towards red, and B/G ratio decreases when the color spectrum shifts towards blue. The ratio B/G exhibits weaker dependence on color spectra, it has steepest slope up to 650nm and after that is flat, while the R/G ratio has almost constant slope over the entire tested spectrum. The ratio B/G exhibits weak dependence on longer spectrum wavelengths because both the top and the middle photodiode are least sensitive in this region. Possibly the top and the middle photodiodes are located much shallower than the third one, so only very energetic photons can be caught by these photodiodes.

Fig. 2.3 shows the main pixel core constitutive blocks. It contains circuitry to detect temporal color changes. Different combinations of the photocurrents from the three stacked photodiodes are fed through the logarithmic photoreceptors. The next stage amplifies transient variations of the first stage and then the outputs, followed by several comparators, send out spikes. As a result, incident radiations shifts within the visual spectra cause transient photocurrent variations that are detected by the pixels processing circuitry. Each pixel can generate four different kinds of events ON_*, OFF_* that indicate four different color transitions between adjacent color spectra: red-green, and blue-green. Table 2.1 depicts how different ON_* and OFF_* events are translated into spectral ratio variations and color changes.

It is important to note that, as illustrated in 2.2b, relative ratios between corresponding photocurrents rather than absolute values of each photocurrent provoke events that indicate color transitions. This is an important difference compared to

Table 2.1: Translation of ON_*, OFF_* events into color changes.

Event	Spectra ratio	Color change
ON_1	$\propto \frac{B}{G} \nearrow$	bluer
OFF_1	$\propto \frac{B}{G} \searrow$	greener
ON_2	$\propto \frac{R}{G} \nearrow$	redder
OFF_2	$\propto \frac{R}{G} \searrow$	greener

conventional monochromatic DVS sensors, as our sensor responds only to spectrum shifts, but it is not sensitive to total light conditions changes.

The pixels core circuitry is designed to mimic color opponencies among two color pairs: red-green and blue-green. In order to further enhance the color processing of the proposed sensor, a new off-chip processing approach of analyzing the resulting events is proposed to provide direct discrimination between blue and red spectra. In order to discriminate between red and blue spectra, all events are always interpreted as transitions between adjacent spectra. In other words, based on how many events had been accumulated, events are decoded as a color transitions from red through green and finally to blue, and inversely, events are decoded as a color transitions from blue through green to red. An interface displaying in real-time recorded color changes by means of colored pixels was implemented. Fig. 2.4a shows a sensor response to a rotating green dot over red background as a space-time plot (left) and a live image snapshot from the interface. Fig. 2.4b demonstrates sensor ability to track color transitions of a rotating painted disk.

This vision sensor has good potential for an automotive robotics applications where high-speed temporal color contrast recognition, especially of fast-moving objects in different lighting conditions, is demanded [23].

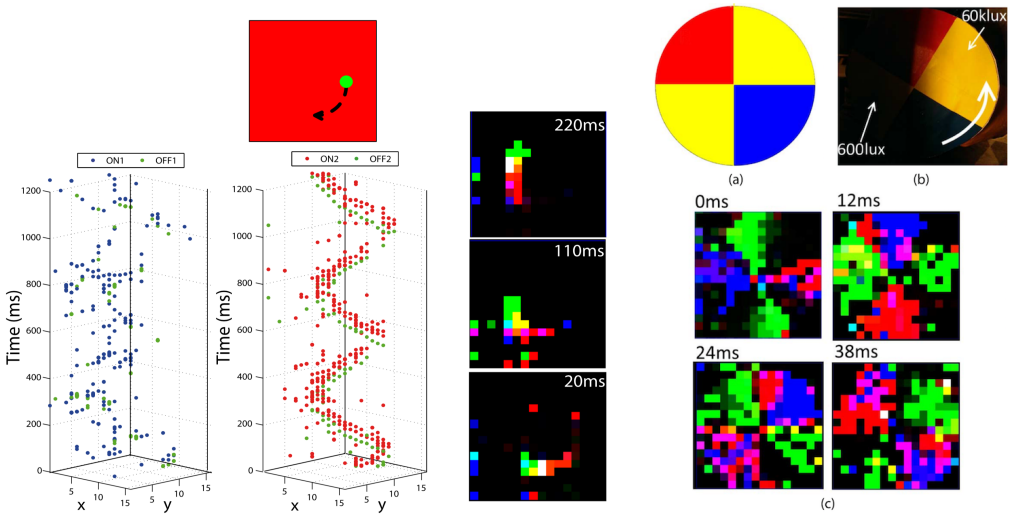

(a) (b)

Figure 2.4: Performance of tri-color DVS sensor. (a) Response to a rotating green dot over red background shown as space-time plot and actual image, (b) demonstration of sensor high intra-scene dynamic range and high-speed temporal color contrast recognition. Disk rotation frequency was 20 rps. Reconstructed pictures for four different accumulation periods are shown on the right.

Chapter 3

Bio-inspired sun sensors for micro probes

Sun sensors provide a measurement of the sun vector typically in two axes in the instrument's coordinates. They are widely used as a reference by many systems from space sector such as satellites and launch rockets [26, 27], and also, they have great potential for terrestrial applications involving renewable energies for tracking the sun to improve the photovoltaic plants efficiency [28]. In space applications sun sensors are part of the Attitude Determination and Control System (ADCS) to determine the orientation of space instruments.

The sounding rockets and micro-probes used for 4DSpace project achieve high angular velocity of 300 rpm. High spinning rate is desirable as it stabilizes attitude of the devices during their flight. In order to provide a reasonable angular resolution of at least 3^o for this application, the sensor frame rate is expected to be equal to at least $600\ Hz$, which is approximately equivalent to $1.7ms$ time delay. This has set demand for the sun sensor capable of tracking sun with a high temporal resolution and low readout latency. As mentioned before, the 4DSpace ultimate goal is to integrate all necessary electronic sub-blocks, such as front-ends to control sub-probes of sounding rockets, A/D converters, and the new sun sensor inside one SoC. For this reason, the sensor small form-factor was of great significance. Other sensor parameters such as low mass, and low power consumption are always of interest, as carrying capacity of the rockets and available power are severely restricted.

The state-of-the-art sun sensors typically use frame-based imagers as sensing elements [29, 30]. As described in previous chapters, principle operation of frame-based sensors is to readout frames of entire image at discrete predefined

time stamps. These sensors divide the visual scene into small pieces (pixels), digitize each piece, and then send out a digital information representing spectral composition of each pixel to reconstruct entire frame of the image. Due to continuous readout of entire frame, the frame rate of these sensors is typically limited down to $10 - 30\ Hz$, which is significantly less than requirement set by the 4DSpace project.

For a typical sun sensor, location of a centroid (also called region of interest - ROI) of the sun spot or an intersection point from the array is required to determine attitude with respect to the Sun. A reduced number of most intensively illuminated pixels from ROI is sufficient to locate a sun spot, and determine azimuth and elevation angles of the sun's direction from the reference axis. Hence, spiking luminance sensors seem to be much more applicable to sense ROI region, as pixels which are illuminated will spike and generate output data, and dark pixels will remain silent. Due to their independent operation scheme, spiking luminance sensors help to reduce readout time of small selected regions of pixels from the focal plane, and hence significantly increase temporal resolution and improve readout efficiency of the sun sensor.

Two novel spiking sun sensors were developed during this PhD Research Fellowship: a pinhole based and a slit-based sensor. A presentation given in WASC 2017 [31] provides an overview of designed sun sensors with event-based operation and compare them against traditional sun sensors. In the first work, potential of combining an existing event-based sensor array with a pinhole optics mounted on top was explored [32, 33]. The second sensor was a custom-designed event-based pixels vector combined with an L-shape optical slit [34, 35]. The next section describes both approaches in more detail.

3.1 Pinhole Based Sensor

In this article [35, 34], we proposed a novel sun sensor based on the AER luminance sensor. The proposed sun sensor that takes advantage of the highly reduced output data flow and high readout speed of event-based sensor, and also, a simplicity of pinhole optics. The sensing array consists of spiking luminance sensors, which perform light-to-frequency conversion [7, 36]. The pixel array of spiking pixels are covered by an opaque lid with a pinhole. Principle of extracting sun vector is illustrated in Fig. 3.1. Fig. 3.2a shows a sensor front view and Fig. 3.2b shows a lid with a pinhole manufactured to implement the sun sensor. Only a

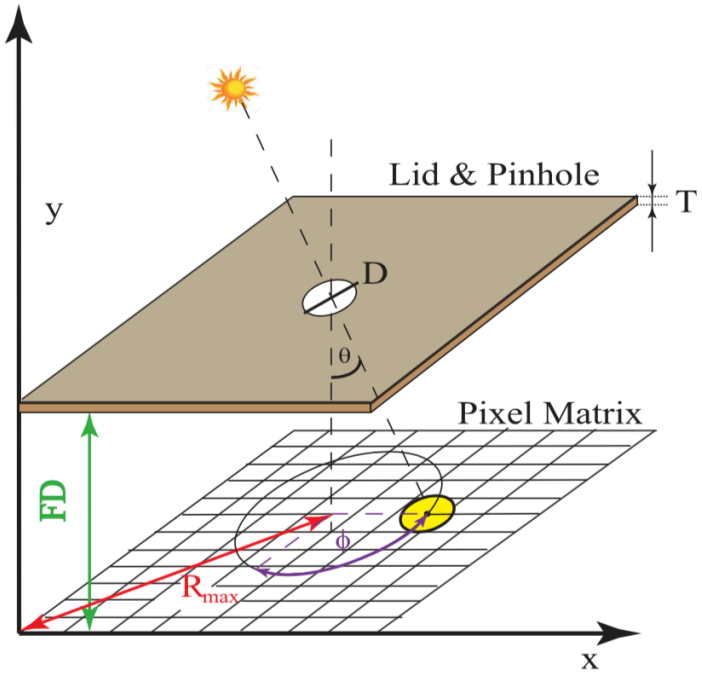

Figure 3.1: Pinhole sensor operation principle [33], [32].

small number of pixels is illuminated by the sunlight projection. The rest of pixels is relatively dark and sends no data.

A great advantage of this sensor over the other solutions is its simplicity of implementation. Many sensors use patterned masks, such as slits, multi-aperture arrays, or multiple pinhole structures to project the pattern on the photosensitive sensors located underneath. Such masks are complicated (expensive) to manufacture, and challenging in terms of alignment with the photo-sensing array. On the other hand, pinhole optics used in this work [33, 32], are compact and easy to manufacture, as they require only a PCB laser machine to laser burn a single hole. The lid does not need a perfect alignment to operate. Any offset in the measurements is systematic and can be calibrated at software level. Hence, this is an advantage over the systems with more complex optics that require precise alignment before operating.

Each of the pixels in the array converts light into frequency. Pixel operation is initiated with a global reset. After that, pixel internal capacitors are discharged with a speed proportional to the local illumination. The algorithm implemented off-chip uses the centroid of the illuminated pixels to compute the sun position

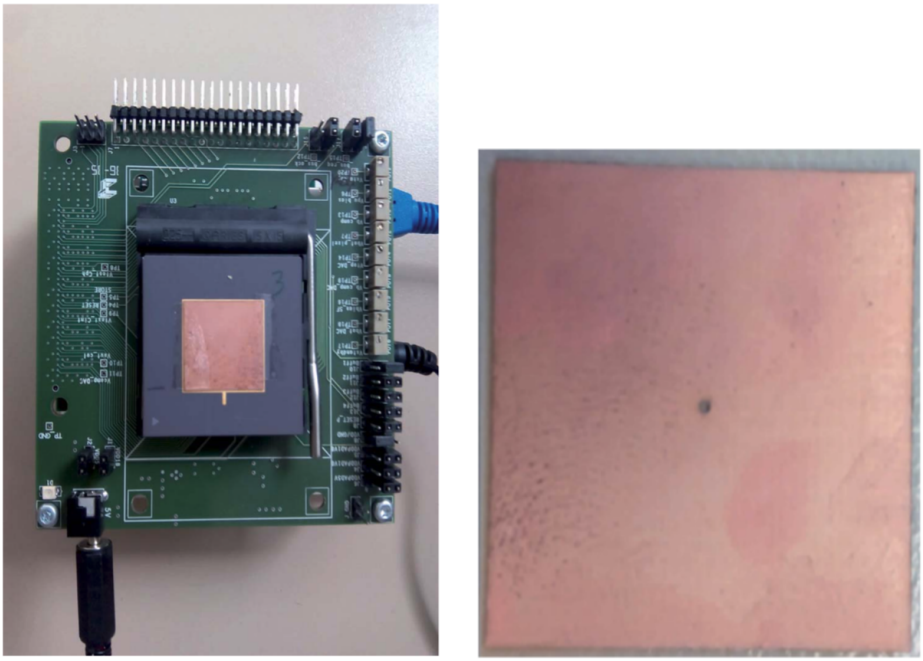

(a) (b)

Figure 3.2: Sensor front view photograph (a), and the lid with a pinhole manufactured to implement the sun sensor (b). The side that faces the sun is metallic to reflect the sun radiation. The side that is directly located above the chip is anti-reflective. Lid thickness: T=100um, width=length=20mm, pinhole radius=50um.

that is determined by the sun latitude and the azimuth. The proposed algorithm can be implemented on an FPGA or a microcontroller. The sun position is not determined until a certain number of events is received. Hence, the amount of data used to determine the sun position is always the same. If no data is received, the sun position will not be computed. Pixel array reset initiating the pixels readout can be used as a timer to reset the entire array after a certain time interval if the number of events received is lower than given threshold needed for algorithm to determine the sun position. All in all, the new sun sensor operates in a simpler and faster way than the previous reported digital sensors, that require elaborate design and readout procedures to avoid reading redundant black pixels. The new sun vector determination is efficient in terms of speed and output data flow as only illuminated pixels are readout, and their positions in array are used for further processing. Since pixels operate asynchronously, a dynamic range of the entire array is not limited by array fixed shutter (as it is for frame-based sensors).

Therefore, the developed sun sensor offers high dynamic range of $> 100dB$, high readout speed of $< 5ms$ at $1klux$ light conditions, and low power consumption of $52mW$.

3.2 Slit-based Sun Sensor

The sensor described in the previous section consists of an entire array and a pinhole optics. The illuminated pixels in the array are continuously operating (spiking), which is not efficient in terms of power consumption. External global reset controlled by a dedicated off-chip digital state machine could be implemented to address this problem. However, this would add an additional complexity and further increase power consumption of the system. Also, additional off-chip post-processing algorithm is required to accumulate pixels spikes and estimate the sun vector. The algorithm efficiency depends on the number of events available to compute the pixel spiking frequencies.

In the next work the sun sensor with much lower power consumption, lower readout latency and more efficient and robust sun vector extraction method is proposed. In this case, events accumulation and the asynchronous resetting is implemented on-chip with two programmable counters. The new concept of the sun sensor is based on a custom-designed event-based pixels vector with an on-chip processing algorithm and an L-shape optical slit [35]. A novel idea of organizing pixel lines in an L-shape and reading out the sensor array in Winner-Take-All (WTA) fashion improves a readout speed, and temporal resolution compared to existing solutions. The chip comprises two one-dimensional pixel lines organized in an L-shape, and the glass lid located above with L-shape slit rotated 180^o with respect to the pixels lines. The principal operation of the sun sensor is to detect two intersection points of an illuminated sunlight pattern and a photosensitive pixels lines, as illustrated in Fig. 3.3. The intersection points are sensed by spiking pixels, which are the base components of the activity-driven event-based vision sensors. Addresses of the intersection points are used to resolve an orthonormal vector towards sun in two axes. The proposed vision sensor conveys a compressed image information in the form of time-encoded events instead of conventional frames. Therefore, the sensor output bus state can be directly converted into the azimuthal and elevation angles without need of reading out the entire array as for frame-based sensors.

The event-based pixels arrays operate in an asynchronous fashion. Two ded-

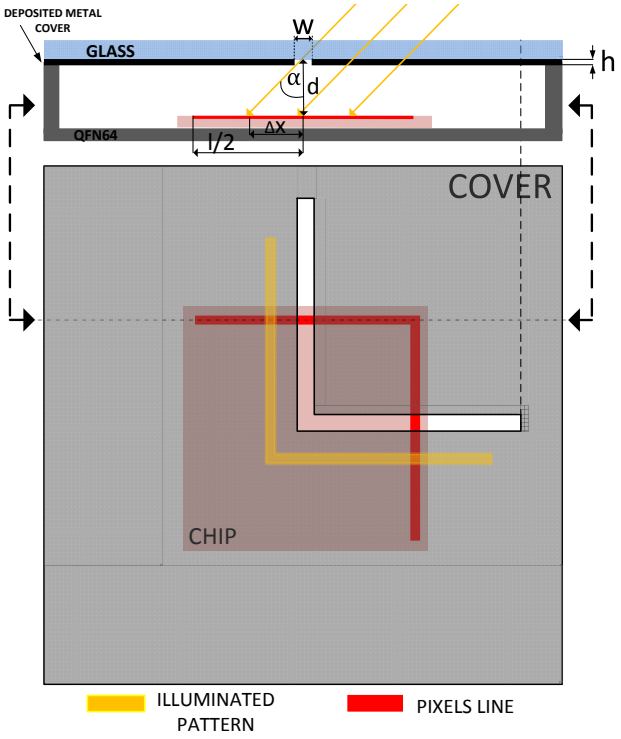

Figure 3.3: Vertical cross-section and horizontal view of the sun sensor structure, d=356μm, h=100nm, W=50μm, l=2256μm.

icated arbitrating Address Event Representation (AER) peripherals read-out the spiking pixels in form of time-stamped events from bort 1D pixels arrays. The previous version of the sun sensor requires external FPGA to control readout time-out to extract addresses of only the most illuminated pixels.

In this work we proposed a hardware implemented Time-to-First-n-Spikes (TFnS) with time-out readout arbitration protocol [37], called a *timed TFnS*. Since only a small portion of the pixels line is illuminated during sun sensor operation, a proposed TFnS with time-out readout mode ensures instantaneous conveying of address of only a few most illuminated pixels carrying most vital information about the sun vector, and suppresses the rest of the array. In neural systems, TFnS operation can be considered as a Winner-take-all (WTA) mechanism. WTA is a computational principle inspired by neural networks activities by which neurons compete with each other for transmitting their electrical activities (action potentials). WTA ensures that only neurons which are most active (strongest) are allowed to spike, whereas the weaker ones are inhibited from transmitting their

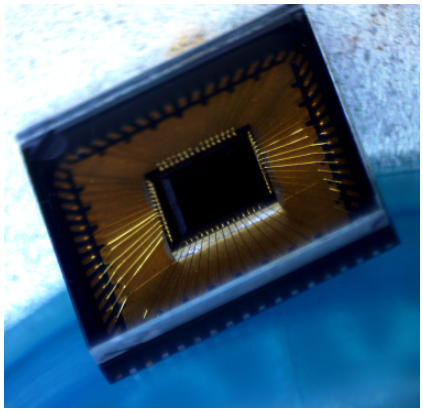

(a) QFN64 package with wire-bonded chip inside.

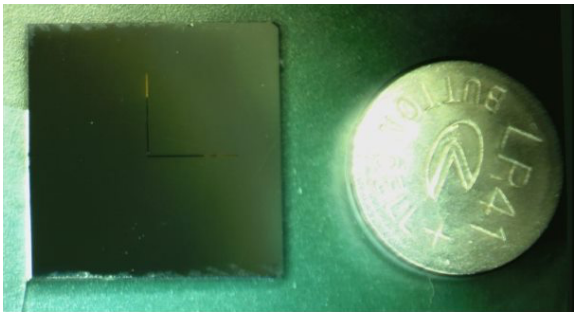

(b) Complete sun sensor with L-shape mask attached, next to standard LR41 watch battery.

Figure 3.4: Sun sensor before and after mask placement.

action potentials. In neural network studies, a variant of the WTA which allows multiple winners instead of only one is called a soft WTA [38]. Thanks to implementing two 1-D pixel vectors instead of a 2D array in a standard CMOS process, the sun sensor occupies only 8% of the chip area, and the remaining area can be used for other sensor interfaces required for 4DSpace project. This is a great improvement compared to the pinhole-based sun sensor prototype [33], [32].

3.2.1 System Design

Different solutions for the slit optics were considered at the early stage of the design. Geometrical properties of the optical slit are determined by the pixel size and the distance between the array and the slits. In order to ensure good resolution and wide viewing angles, the optical slit was required to be 10μm - 200μm wide, as thin as possible, and manufactured with a resolution higher than the slit width. A simple approach of using a 3D printer to print a cavity with optical slit was discarded due to not sufficient resolution, and not acceptable slit thickness. Another solution of building an LTCC cavity over a wire-bonded chip was discarded due to complexity of the manufacturing process. Most suitable solution for manufacturing the optics, turned out to be a photolithography method of depositing a thin metal mask on a thin microscope glass. The mask was manufactured by depositing a 100nm-thick light reflecting nickel chromium metal film on a 600μm thick microscope glass. A complete sun sensor was encapsulated inside a QFN64 package. The glass with the deposited pattern was diced into a 9 x 9 mm square

which fits the package shape. Fig. 3.4a shows a microphotograph of the QFN64 package with wire-bonded chip inside and Fig. 3.4b shows a final version of a sun sensor with L-shape mask attached on the top of the QFN64 package.

3.3 Sensor Testing and Performance

Characterization of the sun sensor made up a considerable part of this research. A final version of the sun sensor with calibration procedure and comprehensive experimental results were presented in [34].

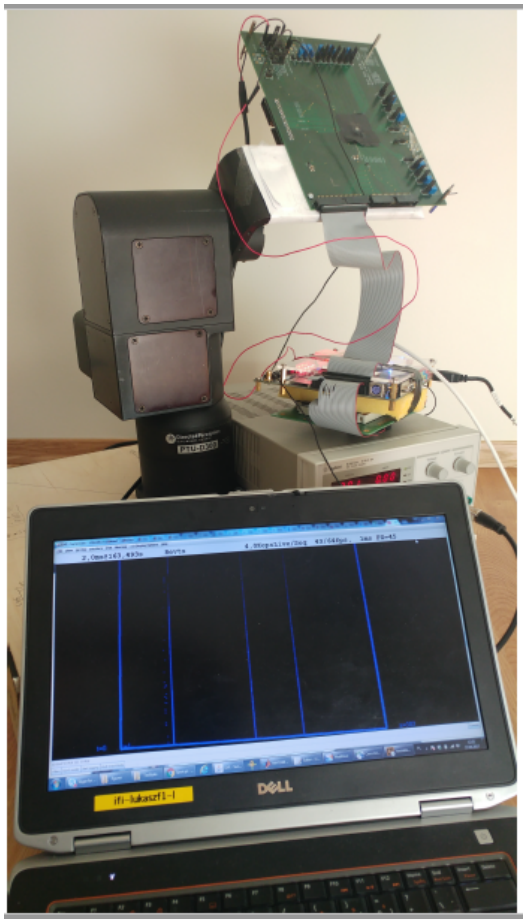

Figure 3.5: A setup using PTU for characterizing sun sensor FOV and accuracy. Sun sensor PCB (on top) is connected through a bus to a data logger located on a DC source.

For the measurements, a USBAERmini2 [39] board was used as a receiver to extract asynchronous time-encoded events from the sun sensor. The USBAER-mini2 board communicates asynchronously with the array (REQ, ACK) and conveys pixels addresses via an output address bus. It also adds temporal information of timing of the incoming events (timestamp) to the conveyed addresses of the active pixels to preserve timing information.

The PCB with the sun sensor was attached to the pan-tilt unit PTU-D300 to rotate the sensor in pitch and yaw with respect to a light source. Fig. 3.5 shows a setup with PTU for characterizing sun sensor FOV and accuracy. An example video illustrating pan and tilt rotation of the sun sensor by use of the PTU is provided in [40]. A model with rotation matrices was developed to transform pan and tilt coordinates of the PTU into pitch and yaw of the sun sensor coordinates, with respect to a halogen lamp source that modeled the Sun. A setup configuration with PTU was used to characterize sensor accuracy and Field-of-View (FOV). Besides, the following sensor parameters were characterized: readout latency, precision and power consumption.

The sensor readout latency was characterized for a direct sunlight in Norway in winter season. Due to high latitude the solar radiation receipt was a fraction of the total solar irradiance conditions during rocket flight. However, even when exposed only to a fraction of solar irradiance, the sun sensor measured readout latency was sufficient for the 4DSpace project application. Latency between two consecutive sensor readouts was equal to $88\mu s$, which was equivalent to a speed of 11.3 Kframes/s in a conventional sensor. Even better readout latency was expected for total solar irradiance exposure.

A proposed TFnS with time-out framework adds on-chip processing of the pixels spike-events at array readout stage. This helps to shorten the sensor readout time and to lower the output data bandwidth by extracting only the most relevant information about the sun vector. TFNs with single winner either limited in time or not gives only a single pixel winner at the time of each readout which can directly be converted into azimuthal or elevation angle. As a result, only two pixels addresses are readout to obtain sun vector. Additionally, time-out readout threshold helps to discard spurious readouts due to Earth or Moon albedo [34].

Multiple winners TFnS mode can be enabled for a moment to sample the wider field of view, and assess if the sun is within the sensor FOV. TFnS mode with multiple winners extracts profile of the incident light in the form of time stamped events. The beam that passes through the slit and hits the photoactive array of pixels becomes collimated, but also contains diverging rays. These diverging rays

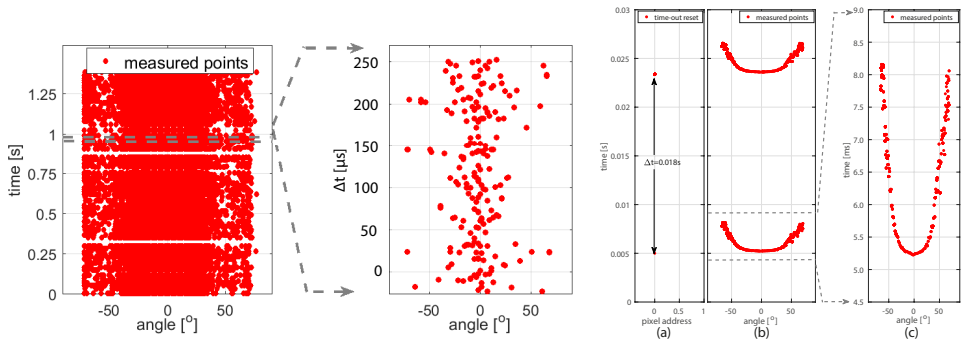

(a) Free-running mode. (b) Time-out readout mode.

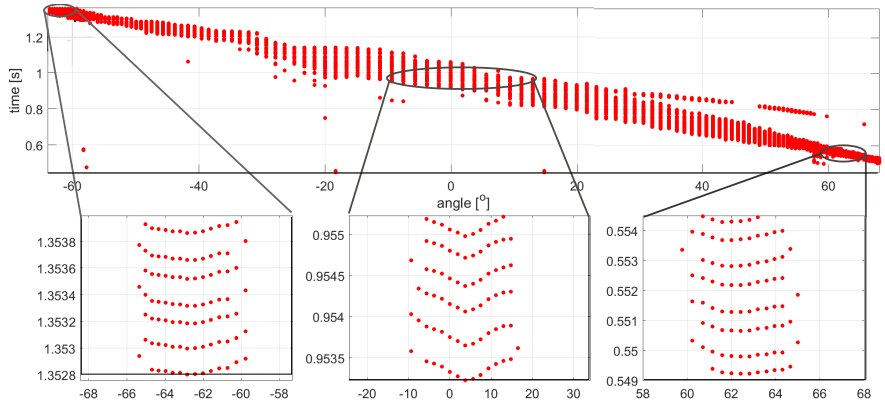

(c) TFnS with time-out mode with 15 winners.

Figure 3.6: Sun sensor readout modes.

spread as the ray propagates, and cause the light beam to disperse with distance. As a result, a sharp cusp characterizes a profile of a strong light source, such as Sun, while profiles of reflections are flatter. Hence, the extracted incident light profile can help distinguish between the sun and other distractors, and also, to further analyze the incident sun light properties. Three different readout modes were illustrated in Fig. 3.6. Fig. 3.6a shows readout without the TFnS enhancement - i.e. all pixels were self-resetting as in standard octopus retina. Fig. 3.6b shows readout for sun sensor configured in time-out readout mode with common reset, and Fig. 3.6c illustrates recorded light profile by sun sensor operating in TFnS timeout-out mode with a limit of 15 winners. Thanks to use of only two pixels vectors, and an on-chip arbitration interface, the sensor power consumption is reduced down to $6.3\mu W$.

Table 3.1 compares the features and performance of the proposed work with other sun sensors: an analog sun sensor [41], and two frame-based sensors [30,

	Ortega et al.[41]	Xie et al.[30]	Liebe et al.[42]	**This work [34]**
Type	Analog Sun Sensor	APS Digital Sensor	APS Digital Sensor	**Event Based Sensor**
Operation Principle	Photodiodes Ratio	Frame-based	Frame-based	**TFnS**
Technology	ND	$0.18\,\mu$m 1P4M	$0.5\,\mu$m CMOS	**AMS 0.35 μm opto (C350)**
Power Supply	ND	$3.3/1.8\,$V	ND	**3 V**
Packaged sensor size	$(3 \times 3 \times 1.2)\ cm^3$ (including auxiliary electronics)	ND	$4.2\,\text{cm}^3$ (including complete APS chip)	$\mathbf{(9.5 \times 9.5 \times 1)\ mm^2}$ **(including auxiliary electronics in silicon)**
Sensor Weight	24 grams (including auxiliary electronics)	ND	11 grams (including complete APS chip)	**0.3 grams (including auxiliary electronics in silicon)**
Pixel array	4 photodiodes	368×368 pixels	512×512 pixels	$\mathbf{2 \times 192}$ **pixels**
Pixel size	$0.75\,\text{mm} \times 2\,\text{mm}$	$6.5\,\mu\text{m} \times 6.5\,\mu\text{m}$	$12\,\mu\text{m} \times 12\,\mu\text{m}$	$\mathbf{11.75\ \mu m \times 72\ \mu m}$
Silicon die size	$(7.5 \times 8.5)\ mm^2$	$(5 \times 5)\ mm^2$	$(6.1 \times 6.1)\ mm^2$	$\mathbf{(2.5 \times 2.5)\ mm^2}$ **(8% of area used)**
FOV	120^o	$\pm 47^o$	160^o	$\mathbf{144^o}$
Resolution	ND	0.004^o	ND	$\mathbf{0.22^o - 1.88^o}$
Accuracy	0.15^o	ND	$\approx 0.04^o$	$\mathbf{0.98^o}(\theta)$ and $\mathbf{0.42^o}(\phi)$.
Precision	ND	0.01^o	ND	$\mathbf{0.104^o}(\theta)$, $\mathbf{0.061^o}(\phi)$
Latency	ND	10 fps	30 fps	**88 μs (equivalent to** $\mathbf{11.3\ kfps}$)
Power consumption	ND	42.73 mW	30 mW	$\mathbf{6.3\ \mu W}$
Dynamic Range	ND	52dB	ND	**>80dB**
Amount of data	4 analog voltages	368 pixels (acquisition mode) + 25 × 25 pixels (tracking mode) = 945 pixels	512 × 512 pixels = 262 kpixels	**1-2 events**

Table 3.1: State-of-the-art comparison [34].

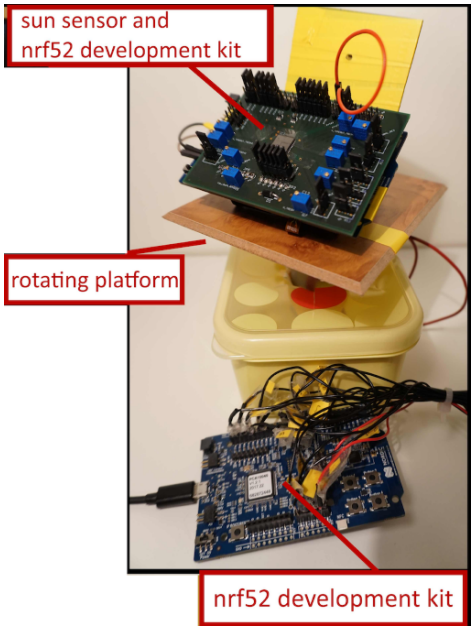

Figure 3.7: A demonstration of a wireless version of the sun sensor attached to a rotating platform.

42]. To the best of our knowledge, there have been no other event-based sun sensors reported before. The proposed sun sensor is smaller and lighter than any other reported sun sensor. Thanks to implementing auxiliary electronics in silicon and using a QFN64 package, our sensor volume is 120 times smaller and much lighter than [41]. Also, in terms of used silicon area, our sun sensor is much smaller. Digital sun sensors [30, 42] use entire imager matrices, and require high performance analog-to-digital converters, and extra digital processing circuits for complex centroid algorithms.

Sun sensors [30, 42] require processor intensive algorithms to extract angles. To obtain the sun angle, these sensors require many steps: readout all pixels' analog values, compare all pixels' values with thresholds, detect the brightest point, and calculate the centroid position. Due to implementation of TFnS and time-out readout framework, most of the processing in our sensor is performed on-chip and the sun sensor generates compressed information about the angle in the form of time-encoded events.

Since the proposed sensor is event-based, it is not limited by a fixed frame rate, and its speed exceeds 11keps. On the other hand, the speed of digital frame-based sun sensors in Table 3.1 is limited to 10 fps and 30 fps respectively. Analog sun

sensors speed is limited by the conversion time of analog-to-digital converters, which is not reported in [41].
Thanks to a new readout framework, and low circuit simplicity, the sun sensor power consumption is kept very low, and is over three decades lower than reported power consumption of other works. Reported power consumption in [30, 42] is much higher due to use of APS sensor, and in [41] due to use of discrete components to implement auxiliary electronics.
The accuracy of a proposed sun sensor is worse than [41, 42]. It could be improved if a more elaborated run calibration approach and more complex model were used to calculate angles. For example, the calibration procedure in [41] consisted of a high-accuracy Angular Positioning System instrument to achieve high precision calibration curves and to compensate any misalignment suffered by the sensor in their manufacturing steps.
There are three main error contributors to the sensor overall accuracy: the quantization error, the misalignment between the mask and the pixel vectors, and an accuracy of the sensor model. The quantization error related to the sensor resolution contributes between $0.22^o - 1.88^o$. The misalignment between the L-shape mask and the pixel vectors contributes maximum 2.83^o. The quantization error can be improved by decreasing the pixel pitch, by increasing the sensor resolution, or by increasing the distance between the chip and the lid. More precise calibration scheme using multiple pixels readout to extract the incident light profile could be used to improve the alignment between the mask and the pixels vectors.

A live demonstration presenting the sensor capabilities was presented at ISCAS 2018 and described in [43]. During the live demonstration the sun sensor response speed, and all available sensor readout modes were presented. Advantages of other solutions were explained to the conference visitors. A wireless solution of the sun sensor sending output data through Bluetooth Low Energy was also presented, shown in Fig. 3.7. The battery powered wireless version of the sun sensor was installed on a rotating table to mimic a real conditions of a sounding rocket flight. An example video demonstrating the demo experience was provided in [44].

Chapter 4

Conclusion

In this thesis, two topics in the area of bio-inspired sensors were studied. First, implementation of a spiking vision sensor detecting transients between three primary colors was explored. A low-resolution proof-of-concept sensor was designed for this purpose. The second part of the PhD research focused on practical usage of spiking sensors to build a very high-performance and low power sun sensor on the framework of a collaborative project related to the space application.

Advantages of the developed event-driven systems were reported over the frame-based systems. As a result of abandoning frame paradigm, and letting pixels operate independently, systems based on spiking sensors can reach much better temporal resolution, lower readout latency, and low data redundancy compared to the state-of-the-art frame-based solutions.

4.1 Tri-Color Dynamic Vision Sensor

The developed Tri-Color Dynamic Vision Sensor proves that modeling color processing found in the biological retina can help to extract image transient features in color in more efficient way than frame-based systems do today. Machine vision and other systems use conventional cameras to capture frames of the scene and then perform intensive post-processing to extract features out of the set of recorded images. This approach is very power hungry and challenging, as all frames, including redundant ones, are continuously post-processed. Also, speed of such systems is severely limited by camera inherent frame rate.
Image features extraction preserving color information for machine vision can be done in much more efficient and faster way by using the proposed trichromatic

transient color detection. The designed Tri-Color Dynamic Vision Sensor proved that systems can profit from such approach in terms of temporal resolution, response time, and power consumption.

4.2 Spiking Sun Sensors for Space Applications

The second part of the PhD research explored how to use spiking luminance sensors to implement high performance and low power sun sensor for space application. Two different approaches of using spiking luminance sensors to implement a sun sensor were explored.

The two developed prototypes of sun sensors prove that spiking luminance sensors are applicable to efficiently sense small regions of interest (ROIs) from the pixel array, and help to improve performance of the sun sensors. Due to an independent operation scheme, only pixels which are illuminated, spike and generate output data, and dark pixels remain silent, which helps to reduce readout time of ROI regions, and significantly improves temporal resolution and readout latency of the device.

Thanks to implementing two 1-D pixel vectors instead of a 2D array in a standard CMOS process, the slit-based sun sensor occupies only 8% of the chip area. Only the outer bottom and outer left areas of the chip are occupied by the sensor and the remaining chip area will be used for other sensor interfaces required for 4DSpace project.

The small form factor and less than 1 gram weight of the slit-based sensor is a great advantage over the other solutions [26]. Thanks to an internal angle extraction the sun sensors proposed in this thesis can be implemented into many applications at low cost. Hence, they are suitable for applications not only related to space, but also for terrestrial cases involving renewable energies to track the sun to improve the photovoltaic plants and solar collectors efficiency.

Chapter 5

Discussion

The progress reported in this thesis shows that biological systems can be used as an inspiration to build better devices. Event-driven sensors are great example how natural processes can be utilized by electronic circuits to overcome limitations of conventional frame-based approach. It must be stressed however, that spiking sensors should not be considered as a direct competition for frame-based vision sensors. Due to their entirely different principle of operation, these sensors can complement each other, such that great quality and high-resolution images from frame-based sensors can be supported by computationally efficient and low latency spiking sensors able to extract some features from the same scene.

5.1 Tri-color DVS

5.1.1 Sensor Scalability

This section discusses challenges which have to be addressed to increase the Tri-color DVS sensor resolution up to a megapixel (MP) range.

The first challenge is related to the AER communication protocol scalability. Typical delays for transmitting address-events by the AER protocol from the sensor to receiver range from $30ns$ to $1\mu s$ [3]. In case of high activity in the MP array (many pixels spiking multiple times at the same time), these delays become limiting factor of the AER protocol efficacy to handle stream of asynchronous events. In case of high activity, pixels requests may be lost due to overrun of the AER circuitry or the receiver buffer. In addition, numbers of arbiters in AER protocol scales with the number of pixels according to formula: $2 \cdot \sqrt{N_{pix}} - 2$, where N_{pix} is a number of pixels. Hence, for a 1MP event-based sensor (1024 x 1024

pixels) more than 2000 arbiter cells organized in 10-layer binary tree structure are required to handle asynchronous requests. For high frequency operation, timing of incoming address-events may become inaccurate due to arbiters inherent mismatch or their greediness.
The pixel design of the proposed tri-color DVS sensor was conservative in terms of area because the photodiodes' spectral sensitivity was unknown beforehand. Hence, only a small array of 16 x 16 large pixels was developed in this research. Photodiode size was $41.5\mu m$ x $43.4\mu m$, pixel size was $82\mu m$ x $82\mu m$ and fill factor was 27%. Pixel size can be reduced considerably by decreasing size of the stacked photodiodes. Even with minimum allowable size determined by the CMOS process, stacked photodiodes consume more area than traditional single PN junction photodiodes. This is because stacked photodiodes require depositing deep n-well structures under an isolated p-well, and deep n-well spacing rules are usually conservative in CMOS process. Size reduction of the stacked photodiodes does not affect their ability to discriminate between different spectra because their operation is based on photocurrent ratios rather than their absolute values. However, size reduction is done at the expense of sensor noise performance, accuracy, and cross-talk. The photodiode located deepest in the substrate is formed by a PN junction between deep nwell and the p-substrate. The p-substrate is not isolated but shared between other photodiodes. As a result, noise from adjacent pixels' circuitry couples through the substrate into a very sensitive photodiode, which leads to cross-talk between pixels.
Pixel complexity is another challenge which has to be addressed to increase sensor resolution - a pixel contains 58 transistors and 6 metal-insulator-metal (MIM) capacitors (MIM capacitors occupy 39% of the pixel total area). MIM capacitors sizes can be reduced by careful design decisions considering trade-offs between capacitors size, mismatch and noise performance.

5.1.2 Frame-based vs. Event-based

Traditional frame-based vision sensors are optimized to achieve high image resolution, dynamic range, and color saturation to faithfully copy the visual-scene. Pixels in standard CMOS image sensor (CIS) typically measure couple micrometers and their internal circuitry is limited to few n-type transistors to obtain high resolution and fill factor. Small microlenses are placed on top of the pixels to further maximize light delivered to the pixel surface. To extract color information from the visual scene, traditional vision sensors use color filters (for instance

Bayer filters), such that each pixel is dedicated to extract one color.
Due to large number of additional devices inside pixels, the proposed tri-color DVS sensor has lower fill factor compared to industry standard frame-based sensors. Also, as reported in [23], due to high temporal noise figure (caused by subthreshold operation), pixels generate many spurious events at low illumination levels. Uniformity of response test showed relatively high standard deviation of the events per color transition due to comparators mismatch.
The main advantage of a proposed tri-color DVS sensor over a CIS sensor is pixel bandwidth and power consumption. Pixels inside DVS sensor can track changes with frequency up to 2.7 kHz independently. To obtain similar temporal color information with a comparable bandwidth, frame-based vision sensor should perform frame scanning and digital conversion of the image at rate at least twice higher than 2.7 kHz and then further post-processing information from the entire frame. To obtain reliable spectral information at frame rates above 5 kHz, expensive high-speed peripheral circuitry (parallel A/D conversion circuits), advanced synchronization of the array, and noise reduction techniques are necessary. On the other hand, due to its inherent parallel operation, DVS sensors do not require synchronizing of the array at high speed, specialized A/D conversion techniques, nor complex parallel signal processing. Stacked photo-diodes helped to improve sensor fill factor by extracting information about all three colors from each pixel. It should be noted however, that cross-talk between RGB channels is inherent in the stacked photodiode because stacked photodiodes are essentially connected in series, and hence, each photodiode shares at least one of its P or N junction with another diode.
Considering significant architectural differences between the two discussed types of vision sensors, event-based color change detectors could coexist with other frame-based vision sensors in the same chip to model part of the visual processing of the human retina.

5.2 Spiking Sun Sensors for Space Applications

5.2.1 From Prototype to Product

For this prototype, a mature AMS $0.35\mu m$ CMOS process was used and 192 pixels were implemented inside each 1D array. In order to increase sun sensor resolution, a more advanced CMOS process can be used. Higher resolution would reduce quantization error which contributes between $0.22^o - 1.88^o$. Photodiode

size can be reduced without affecting the sensor performance. This is because TFnS with time-out readout mode ensures instantaneous conveying of addresses of only a few most illuminated pixels, not the entire array. Hence, only a local mismatch between adjacent pixels contributes to the sensor accuracy, and larger global mismatch within the entire array is discarded by a TFnS readout technique. Due to geometrical relation between pixel pitch and location of the illuminated sunlight pattern, the sensor quantization error varies across its field-of-view between $0.22^o - 1.88^o$. The quantization error can be unified by using pixels with different size across the array.

A simple geometry model for transforming pixel address into angle was sufficient to prove a principle of this new concept. The model can be further improved to include a refractive coefficient of the glass, and include more than one winner to interpolate the peak of the incident light pattern to calculate the angle. This would improve the accuracy and spatial resolution of the sun sensor. Moreover, more precise calibration scheme using multiple pixels readout to extract the incident light profile could be used to improve the alignment between the mask and the pixels vectors.

The AER protocol was used to stream out the sun sensor output data in form of address events representing coordinates in time. It is not necessary to use the dedicated AER board for normal operation of the sun sensor. Instead, a simple state machine with few logic cells can be used to acknowledge incoming requests and readout the sensor output (for instance a fixed frequency clock could be used to periodically acknowledge the incoming requests from the array).

The proposed sun sensor has not been radiation hardened because the sounding rockets used for 4DSpace project fly up to the altitude of ionosphere where cosmic radiation is not harmful for the electronics. However, if the sensor is intended to be used on satellites, radiation hardening is necessary.

The developed slit-based spiking sun sensor has been taken further with the aim of product development by a postdoctoral researcher and the company EIDEL (Eidsvoll Electronics AS). In the continued work by a postdoctoral researcher of the same group, the available area is used for a core processor to handle redundancy of reading-out multiple L-shaped patterns, and other relevant circuitry for 4DSpace project.

5.3 Event-based Sensors: General Outlook and Future Work

The commercial success of asynchronous vision sensors is still far away from frame-based sensors. However, there are several private companies which have seen potential in biologically inspired devices, and are attempting to commercialize the fabrication of event-based cameras. A start-up company Prophesee[1] is currently developing a system combining event-based vision sensor and AI algorithms for visual sensing and processing in autonomous vehicles, connected devices, security and surveillance systems. Another start-up company Insightness AG[2] is building an event-based vision system for computer vision to give mobile devices spatial awareness (Silicon Eye Technology[45]). IniVation[3] invents and produces neuromorphic technologies with a special focus on event-based Dynamic Vision Sensors (DVS). Also, IBM has notices potential of this area, and has initiated Research Synapse project[4] together with Samsung and IniLabs to combine a brain-inspired machine (TrueNorth chip) with a retinal camera [46].

This trend will continue, and more practical applications will make use of neuromorphic systems [47]. The demand of vision sensors with low power and bandwidth consumption, and the capability of processing the visual scene makes spiking sensors attractive in many applications, especially in situations where image quality is not of highest priority.

There are many challenges in front of academic research and industry to solve in order to facilitate these and future biologically inspired devices. The first challenge is a limited knowledge about entire processes occurring inside a human body, especially inside the brain. That is important, if once the ultimate goal of neuromorphic engineering to build artificial intelligence should be achieved.

Another topic is related to the sensors asynchronous readout and lack of a standard synchronous interface. Today AER protocol is used to stream out sensor output data in form of address events representing coordinates in time. The output data is generated in an asynchronous fashion, which puts a challenge to a typically synchronous (clocked) system on the receiver side. A simple solution to convert event-based data into more intuitive frame-based representation is to convert accumulated events into fixed event-number frames, and then synchronize

[1] http://www.prophesee.ai/
[2] http://www.insightness.com/
[3] https://inivation.com/
[4] http://www.research.ibm.com/artificial-intelligence/

such frames with clock. Potential solutions must be studied to develop a complete standard communication interface.

An interesting research topic is to develop new vision algorithms which can exploit high temporal resolution and preserve system asynchronous nature. Recently, new solutions using convolutional neural networks have been proposed [48]. The convolutional networks are artificial neural networks able to efficiently analyze visual imagery from acquired and accumulated events coming from the DVS sensor.

There are many open possibilities to be explored in this research field. Trends in self-driving cars, visual odometry and upcoming 3D technologies will /probably boost interest in the alternative event-based vision sensors sector. Such topics as a real time motion and optical flow estimation, or image depth extraction will probably drive interest in sensors studied in this thesis.

Bibliography

[1] K. Fukushima, Y. Yamaguchi, M. Yasuda, and S. Nagata, "An electronic model of the retina," *Proceedings of the IEEE*, vol. 58, no. 12, pp. 1950–1951, Dec 1970.

[2] M. Mahowald, *An Analog VLSI System for Stereoscopic Vision*. Kluwer, 1994.

[3] C. Posch, T. Serrano-Gotarredona, B. Linares-Barranco, and T. Delbruck, "Retinomorphic event-based vision sensors: Bioinspired cameras with spiking output," *Proceedings of the IEEE*, vol. 102, no. 10, pp. 1470–1484, Oct 2014.

[4] J. E. Dowling, *The Retina: An Approachable Part of the Brain*, 2nd ed. The Belknap Press of Harvard University Press, 2012.

[5] R. W. Rodieck, "The first steps in seeing," in *Trends in Neurosciences*, 1999.

[6] P. Lichtsteiner, C. Posch, and T. Delbruck, "A 128×128 120dB $15\mu s$ latency asynchronous temporal contrast vision sensor," *IEEE Journal of Solid-State Circuits*, vol. 43, no. 2, pp. 566–576, February 2008.

[7] E. Culurciello, R. Etienne-Cummings, and K. Boahen, "A biomorphic digital image sensor," *Solid-State Circuits, IEEE Journal of*, vol. 38, no. 2, pp. 281–294, Feb 2003.

[8] M. Silvilotti, "Wiring considerations in analog vlsi systems with application to field-programmable networks," Ph.D. dissertation, Cal. Inst. of Tech., Pasadena, California, 1991.

[9] K. A. Boahen, "Point-to-point connectivity between neuromorphic chips using address events," *IEEE Trans. Circuits Syst. II*, vol. 47, no. 5, pp. 416–434, 2000.

[10] T. Iakymchuk, A. Rosado, T. Serrano-Gotarredona, B. Linares-Barranco, A. Jiménez-Fernández, A. Linares-Barranco, and G. Jiménez-Moreno, "An aer handshake-less modular infrastructure pcb with x8 2.5gbps lvds serial links," in *2014 IEEE International Symposium on Circuits and Systems (ISCAS)*, June 2014, pp. 1556–1559.

[11] A. Mortara, E. A. Vittoz, and P. Venier, "A communication scheme for analog vlsi perceptive systems," *IEEE Journal of Solid-State Circuits*, vol. 30, no. 6, pp. 660–669, June 1995.

[12] UiO, 4DSpace - strategic research initiative. [Online]. Available: http://www.mn.uio.no/fysikk/english/research/projects/4dspace/

[13] K. C. Yeh and C.-H. Liu, "Radio wave scintillations in the ionosphere," *Proceedings of the IEEE*, vol. 70, no. 4, pp. 324–360, 1982.

[14] Blackmagic URSA Mini Pro Technical Specifications. Blackmagic Design. [Online]. Available: https://www.blackmagicdesign.com/products/blackmagicursaminipro/techspecs/W-URSA-20

[15] R. Berner and T. Delbruck, "Event-based pixel sensitive to changes of color and brightness," *IEEE Transactions On Circuits and Systems I*, vol. 58, no. 7, pp. 1581–1590, 2011.

[16] W. N. Carr, "United states patent 4,238,760," Patent, 1980.

[17] R. F. Lyon and P. M. Hubel, "Eyeing the camera: Into the next century," in *10th Color Imaging Conf.*, 2002, pp. 349–355.

[18] R. B. Merrill, "United states patent 6,632,701," Patent, 2003.

[19] J. M. A. Olsson and P. Hafliger, "Two color asynchronous event phot pixel," in *ISCAS*, 2008, pp. 169–172.

[20] J. A. Leñero-Bardallo, D. Bryn, and P. Häfliger, "Bio-inspired asynchronous pixel event tricolor vision sensor," *Biomedical Circuits and Systems, IEEE Transactions on*, vol. 8, no. 3, pp. 345–357, June 2014.

[21] Ł. Farian, J. A. Leñero-Bardallo, and P. Häfliger, "A bio-inspired aer temporal tri-color differentiator," *IEEE Biomedical Circuits and Systems Conference (BioCAS), Lausanne, Switzerland*, pp. 524–527, October 2014.

[22] ——, "Live demonstration: A bio-inspired aer temporal tri-color differentiator," *IEEE Biomedical Circuits and Systems Conference (BioCAS), Lausanne, Switzerland*, p. 171, October 2014.

[23] ——, "A bio-inspired aer temporal tri-color differentiator pixel array," *IEEE Transactions on Biomedical Circuits and Systems*, vol. 9, no. 5, pp. 686–698, Oct 2015.

[24] M. B. Choulkha, G. N. Lu, M. Sedjill, G. Sou, and G. Atquie, "Buried triple p-n junction structure in a bicmos technology for color detection," in *Proceedings of the 1997 Bipolar/BiCMOS Circuits and Technology Meeting*, Sept 1997, pp. 108–111.

[25] R. Feynman, R. Leighton, M. Sands, and E. Hafner, *The Feynman Lectures on Physics; Vol. I.* AAPT, 1965, vol. 33.

[26] United States, "Spacecraft sun sensors, nasa space vehicle design criteria, guidance and control," *NASA*, no. NASA-SP-8047, 1970.

[27] N. M. Hatcher, "A survey of attitude sensors for spacecraft," *United States*, no. NASA-SP-145, 1967.

[28] L. A. Lopez and A. M. Viacheslav, "Concentrator photovoltaics," in *Springer*, 2007.

[29] C. Liebe and S. Mobasser, "Mems based sun sensor," in *Aerospace Conference, IEEE Proceedings.*, vol. 3, 2001, pp. 3/1565–3/1572.

[30] N. Xie and A. Theuwissen, "A miniaturized micro-digital sun sensor by means of low-power low-noise cmos imager," *Sensors Journal, IEEE*, vol. 14, no. 1, pp. 96–103, Jan 2014.

[31] J. A. Leñero-Bardallo, L. Farian, J. Guerrero-Rodríguez, R. Carmona-Galán, and A. Rodríguez-Vázquez, "On the design of sun sensors with event-based operation," 2017, workshop on Architecture of Smart Cameras, WASC 2017. [Online]. Available: http://eunevis.org/wasc2017/wp-content/uploads/2017/05/WASC_SunSensors_2017.pdf

[32] J. A. Leñero-Bardallo, J. Guerrero-Rodríguez, L. Farian, R. Carmona-Galán, and A. Rodríguez-Vázquez, "A sun sensor implemented with an asynchronous luminance vision sensor," in *ESSCIRC 2017 - 43rd IEEE European Solid State Circuits Conference*, Sept 2017, pp. 67–70.

[33] J. A. Leñero-Bardallo, L. Farian, J. Guerrero-Rodríguez, R. Carmona-Galán, and A. Rodríguez-Vázquez, "Sun sensor based on a luminance spiking pixel array," *IEEE Sensors Journal*, vol. 17, no. 20, pp. 6578–6588, Oct 2017.

[34] Ł. Farian, P. Häfliger, and J. A. Leñero-Bardallo, "A miniaturized two-axis ultra low latency and low-power sun sensor for attitude determination of micro space probes," *IEEE Transactions on Circuits and Systems I: Regular Papers*, vol. 65, no. 5, pp. 1543–1554, May 2018.

[35] ——, "Miniaturized sun sensor with in-pixel processing for attitude determination of micro space probes," in *Event-based Control, Communication, and Signal Processing (EBCCSP), 2015 International Conference on*, June 2015, pp. 1–6.

[36] J. A. Leñero-Bardallo, R. Carmona-Galán, and A. Rodríguez-Vázquez., "A bio-inspired vision sensor with dual operation and readout modes," *Sensors Journal, IEEE*, vol. PP, no. 99, pp. 1–1, 2015.

[37] Ł. Farian, J. A. Leñero-Bardallo, and P. Häfliger, "A time-to-first-n-spikes and time-out read-out extension to the aer arbitration system," in *Event-based Control, Communication, and Signal Processing (EBCCSP), 2016 International Conference on*, June 2016.

[38] Y. Chen, "Mechanisms for stable bump activity, winner-take-all and group selection in neuronal spiking networks," *bioRxiv*, 2016. [Online]. Available: https://www.biorxiv.org/content/early/2016/09/26/077396

[39] "jAER open source project," http://sourceforge.net/projects/jaer/.

[40] Ł. Farian. Sun sensor measurement setup p.1. Youtube. [Online]. Available: https://www.youtube.com/watch?v=zf9UUiSX1tM

[41] P. Ortega, G. Lopez-Rodriguez, J. Ricart, M. Dominguez, L. Castaner, J. Quero, C. Tarrida, J. Garcia, M. Reina, A. Gras, and M. Angulo, "A miniaturized two axis sun sensor for attitude control of nano-satellites," *Sensors Journal, IEEE*, vol. 10, no. 10, pp. 1623–1632, Oct 2010.

[42] C. C. Liebe, S. Mobasser, Y. Bae, C. J. Wrigley, J. R. Schroeder, and A. M. Howard, "Micro sun sensor," in *Proceedings, IEEE Aerospace Conference*, vol. 5, 2002, pp. 5–2263–5–2273 vol.5.

[43] Ł. Farian, J. A. Leñero-Bardallo, and P. Häfliger, "Live demonstration: A miniaturized two-axis low latency and low-power sun sensor for attitude determination of sounding rockets," in *IEEE International Symposium on Circuits and Systems*, May 2018, p. 1.

[44] Ł. Farian. Live demonstration proposal: A miniaturized two-axis low latency and low-power sun sensor. Youtube. [Online]. Available: https://youtu.be/wdfOjKqEiS4

[45] Brandli. Keeping our Skies Safe: Insightness Solves Collision Avoidance for Drones. Insightness. [Online]. Available: http://www.insightness.com/?p=361

[46] S. Shankland. Samsung turns IBM's brain-like chip into a digital eye. CNET.com. [Online]. Available: https://www.cnet.com/news/samsung-turns-ibms-brain-like-chip-into-a-digital-eye/

[47] M. A. C. Maher, S. P. Deweerth, M. A. Mahowald, and C. A. Mead, "Implementing neural architectures using analog vlsi circuits," *IEEE Transactions on Circuits and Systems*, vol. 36, no. 5, pp. 643–652, May 1989.

[48] I. A. Lungu, F. Corradi, and T. Delbrück, "Live demonstration: Convolutional neural network driven by dynamic vision sensor playing roshambo," in *2017 IEEE International Symposium on Circuits and Systems (ISCAS)*, May 2017, pp. 1–1.

List of Publications

PAPER I:
A Bio-Inspired AER Temporal Tri-Color Differentiator Pixel Array
IEEE Transactions on Biomedical Circuits and Systems, 2014
PAPER II:
Miniaturized Sun Sensor with In-Pixel Processing for Attitude Determination of Micro Space Probes
International Conference on Event-based Control, Communication, and Signal Processing, 2015
PAPER III:
A Time-to-First-n-Spikes and Time-out Read-out Extension to the AER Arbitration System
Second International Conference on Event-based Control, Communication, and Signal Processing, 2016
PAPER IV:
A sun sensor implemented with an asynchronous luminance vision sensor
IEEE European Solid State Circuits Conference, 2017
PAPER V:
Sun Sensor Based on a Luminance Spiking Pixel Array
IEEE Sensors Journal, 2017
PAPER VI:
A Miniaturized Two-Axis Ultra Low Latency and Low-Power Sun Sensor for Attitude Determination of Micro Space Probes
IEEE Transactions on Circuits and Systems I: Regular Papers, 2017
PAPER VII:
Live Demonstration: A Miniaturized Two-Axis Low Latency and Low-Power Sun Sensor for Attitude Determination of Sounding Rockets
IEEE International Symposium on Circuits and Systems, 2018

Workshop Presentation I:
On the Design of Sun Sensors with Event-Based Operation.
Workshop on Architecture of Smart Cameras, 2017

Paper I:

Ł. Farian, J.A. Leñero-Bardallo, P. Häfliger
A Bio-Inspired AER Temporal Tri-Color Differentiator Pixel Array
IEEE Transactions on Biomedical Circuits and Systems, 2014

A Bio-Inspired AER Temporal Tri-Color Differentiator Pixel Array

Łukasz Farian, *Member, IEEE*, Juan Antonio Leñero-Bardallo, and Philipp Häfliger, *Senior Member, IEEE*

***Abstract*—This article investigates the potential of a bio-inspired vision sensor with pixels that detect transients between three primary colors. The in-pixel color processing is inspired by the retinal color opponency that are found in mammalian retinas. Color transitions in a pixel are represented by voltage spikes, which are akin to a neuron's action potential. These spikes are conveyed off-chip by the Address Event Representation (AER) protocol. To achieve sensitivity to three different color spectra within the visual spectrum, each pixel has three stacked photodiodes at different depths in the silicon substrate. The sensor has been fabricated in the standard TSMC 90 nm CMOS technology. A post-processing method to decode events into color transitions has been proposed and implemented as a custom interface to display real-time color changes in the visual scene. Experimental results are provided. Color transitions can be detected at high speed (up to 2.7 kHz). The sensor has a dynamic range of 58 dB and a power consumption of 22.5 mW. This type of sensor can be of use in industrial, robotics, automotive and other applications where essential information is contained in transient emissions shifts within the visual spectrum.**

***Index Terms*—Address Event Representation (AER), asynchronous vision sensor, CMOS pixel, color processing, dynamic vision sensor, high-speed vision sensor, image sensors, temporal contrast.**

I. Introduction

COLOR enriches our visual world remarkably. The first steps in sensing color occurs in the retina. Thomas Young in the 19th century was the first to suggest that human color vision is trichromatic [1]. The trichromatic theory simply assumed that three images of the world were formed by these three sets of receptors and then transmitted to the brain where the ratios of the signals in each of the images were compared in order to sort out color appearances. That is roughly the operation that frame-based cameras with color filters perform to render color images. However, the idea of three images being transmitted to the brain is both inefficient and fails to explain several visually observed phenomena [2]. In fact, there is a complex retinal processing of the color information that is essential for our color perception.

Several authors have designed various artificial sensors trying to implement part of the retinal processing. The first bio-inspired vision sensor was presented by Fukushima [3] in the 1970s. Twenty years later Mahowald proposed the first integrated bio-inspired retina [4]. These sensors have been mainly focused on implementing the spatio-temporal processing performed in the human retina. More recently, several authors have started to pay attention to the color detection using bio-inspired vision sensors. However, to the best of our knowledge, the color processing made by retina has not been completely modeled with electronic circuits yet.

Conventional frame-based cameras usually place color filters over different pixels to render color images. Typically, a Bayer mask with filters centered at blue, green, and red is arranged over groups of four pixels. Then their outputs are combined to reconstruct color images. However, as previously stated, the retinal color processing is quite different. There are certain pairs of colors (opponents) that are mutually exclusive. Hering noted that certain hues were never perceived to occur simultaneously and he proposed an opponent-colors theory of color vision. These opponents are located in separated photoreceptors. In the human retina, there is a red/green opponency and a blue/yellow opponency. Ganglion cells receive inhibition or excitation from these different opponents that are always antagonistic [2].

Color detection has been traditionally neglected in bio-inspired vision sensors. The main reason is that adding extra pixel processing decreases the fill factor and consequently the array resolution. Color filters require to have different pixels dedicated to detect each color. This is not something affordable when the array resolution is low. Recently, several authors have started to conceive the possibility of incorporating color processing with bio-inspired vision sensors [5]–[7]. This has been mainly motivated by the fact that modern fabrication technologies allow to stack photodiodes at different depths with different spectral sensitivity [7]–[9].

Color processing is quite important for some industrial processes, navigation systems, and robotics. For instance, it is essential to match samples of various colored materials or to operate mobile equipment for which the operating signals are colored lights [10]. In that sense, the good temporal resolution of bio-inspired cameras, their low latency and their low redundancy makes them good candidates for such applications.

In this article we present a bio-inspired vision sensor that can detect transient changes between primary colors at high speed.

Manuscript received January 15, 2015; revised May 30, 2015 and September 01, 2015; accepted October 09, 2015. Date of publication October 30, 2015; date of current version November 24, 2015. J. A. Leñero-Bardallo was supported in part by ONR project N00014-14-1-0355, project MONDEGO (TEC2012-38921-C02-02) MINECO, project SMART CIS-3D (P12-TIC-2338), and project MINECO IPT-2011-1625-430000. This paper was recommended by Associate Editor P. Georgiou.

Ł. Farian and P. Häfliger are with the Nanoelectronics Group, Department of Informatics, University of Oslo, Blindern 1072, Norway (e-mail: lukaszf@ifi.uio.no; hafliger@ifi.uio.no).

J. A. Leñero-Bardallo is with the Institute of Microelectronics of Seville, CSIC-Universidad de Sevilla, Sevilla 41004, Spain (e-mail: juanle@imse-cnm.csic.es).

Color versions of one or more of the figures in this paper are available online at http://ieeexplore.ieee.org.

Digital Object Identifier 10.1109/TBCAS.2015.2492460

Changes between colors are detected by processing the photocurrent transient variations of three different stacked photodiodes with different spectral sensitivity. Temporal changes between three different colors are detected and opponencies between different colors in the retina are modeled. This work starts from our prior experience in processing color information with event-based color vision sensors [7]. In that work we demonstrated that it was possible to render trichromatic images with event-based vision sensors and we proposed methods to sense and process the information coming from three stacked photodiodes. An octopus retina capable of generating RGB images was presented. With this work we aim to implement specific color processing conveyed in the retina, i.e., color temporal contrast detection. Moreover, some of our new work is inspired by the results previously published by Berner *et al.* [6]. Berner *et al.* designed a pixel that can detect transitions between two colors. With this new system, all transitions between the three primary colors can be detected. Furthermore, we have implemented a pixel array, and arbitration system, and programmed a dedicated interface to render real time images displaying the color transitions detected in the focal plane by the pixels that made up the pixel array. To the best of our knowledge, this is the first pixel array that can detect temporal color changes with an event-based bio-inspired vision sensor. Some preliminary results of this work were reported and displayed in BioCAS 2014 [11], [12]. In this invited paper, we provide a more detailed system description, a deeper insight into the system performance, more detailed and elaborated experimental results. Moreover, detailed descriptions of the experimental setup and the experiments conducted to characterize the sensor are provided.

This article is organized as follows: Section II explains the pixel design and the system description, including the AER arbiters. Section III describes the system experimental setup. Detailed experimental results of a single test pixel and the entire pixel array are provided. Finally, Section IV draws some conclusions and further system improvements.

II. System Description

Fig. 1 displays the main system blocks. The color change temporal differentiator is made up of a 16 × 16 pixel matrix. Each pixel has three stacked photodiodes and some circuitry to detect temporal color changes. Pixels send out events when detecting transient color changes. Each pixel can generate four different kinds of events that indicate four different color transitions. For this reason, two extra bits are needed to encode the event type sent by each pixel. One bit of the event type bits is attached to the 4-bit column address, and one to the 4-bit row address, these are multiplexed. Therefore five bits are needed to encode the column addresses and five bits are needed to encode the row addresses. We used the arbitration scheme proposed by Häfliger in his PhD dissertation [13]. Such arbitration scheme is based on the one proposed by Boahen [14], with some modifications to add pipeline operation at the row operation. The circuitry has been previously implemented in other designs [7], [15] and can handle events rates up to 10Meps that is enough to arbitrate event rates from medium size pixel arrays. It is made up of some logic to handle the AER communication, multiplexers, and arbiters. In addition, a test pixel was included in the chip. The test pixel has several scan buffers connected to its internal nodes to measure their voltages as it will be depicted in the Experimental Results section.

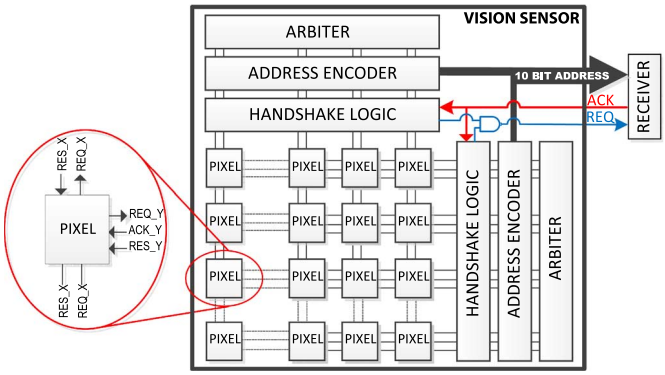

Fig. 1. Block level view of the pixel array and the AER communication periphery.

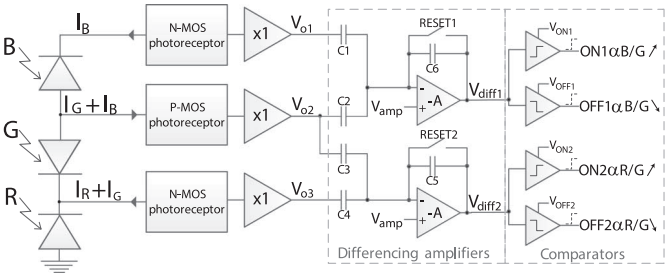

Fig. 2. Pixel core main blocks.

A. Pixel Design

Fig. 2 shows the main pixel core constitutive blocks. The pixel design is inspired by the one proposed by Berner *et al.* [6] to detect color transitions. That one was based on the original one with switched capacitors proposed by Lichsteiner *et al.* [16]. The new pixel has been extended to operate with three stacked photodiodes and to handle the AER communication of a pixel matrix. Each pixel has three stacked photodiodes at different depths. Light penetration depth depends on photons wavelength [7]. Photons with higher energy (shorter wavelengths) travel less time though the crystal before generating electron-hole pairs. Hence, the top photodiode is more sensitive to blue light, and the bottom one more sensitive to longer wavelengths. For simplicity, let us denote I_B, I_G, and I_R the photocurrents through the top, the middle, and the bottom photodiodes. Combination of these currents go to logarithmic photoreceptors whose outputs are voltages that depend on their input photocurrents. The next stage consists of two different amplifiers that amplify transient variations of their input voltages. Inputs to the amplifiers are buffered by source followers. Amplifiers are followed by several comparators that send out spikes. Finally there is some logic to handle the AER communication that is also included in the pixel and will be explained afterwards.

Fig. 3 depicts the logarithmic photoreceptors circuitry and how the two kind of photoreceptors are connected to the stacked

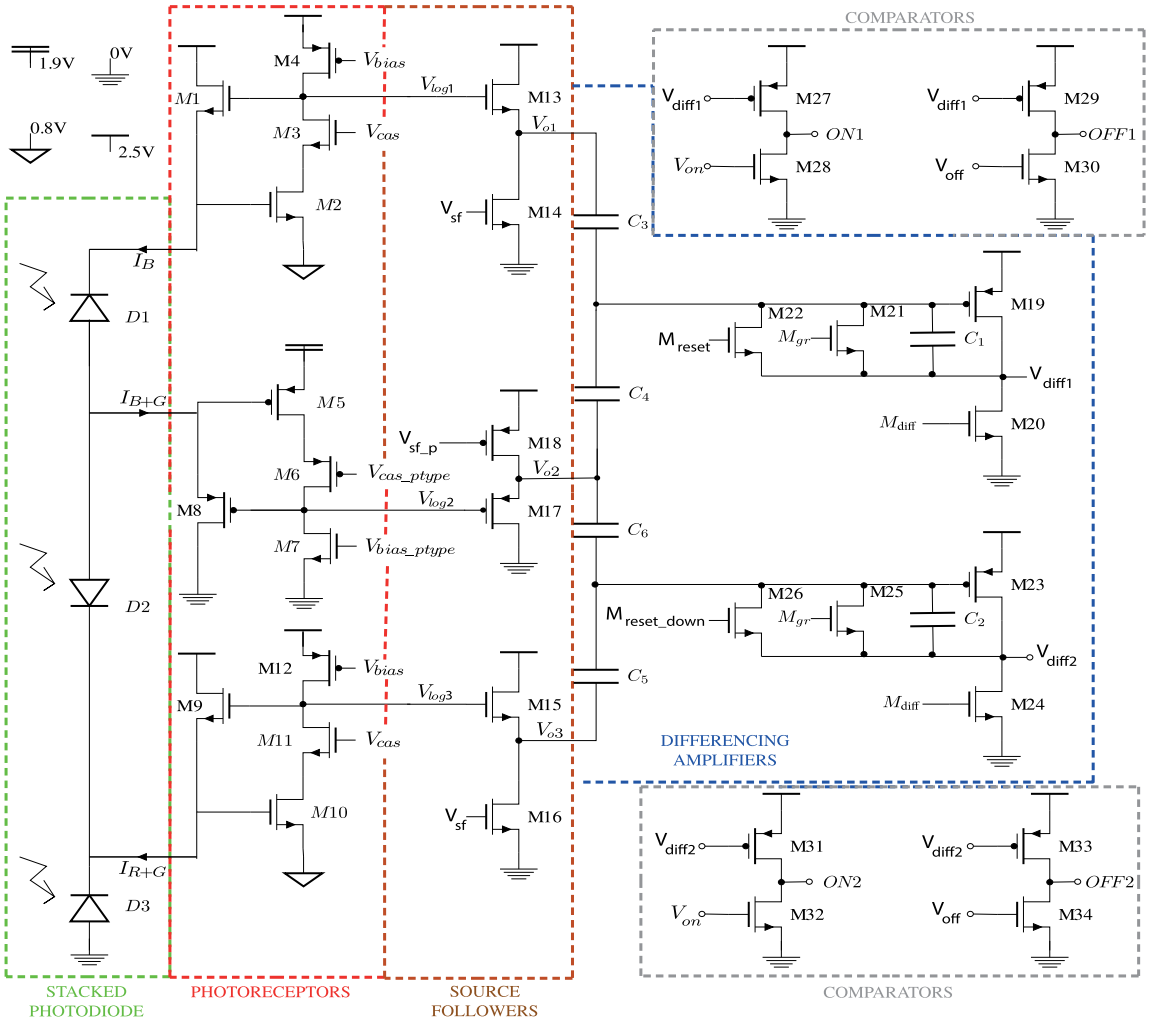

Fig. 3. Detailed pixel core schematics. It includes logarithmic photoreceptors, source followers, differencing amplifiers, and comparators. Transistor sizes are: (W/L) μm/μm $M_1 = M_9 = 0.4/0.5$, $M_8 = 0.4/2$, $M_2 = M_5 = M_{10} = 1/0.5$, $M_3 = M_6 = M_{11} = 2/0.4$, $M_4 = M_7 = M_{12} = 0.5/5$, $M_{13} = M_{14} = M_{15} = M_{16} = 0.6/0.3$, $M_{17} = 0.5/1.6$, $M_{18} = 1.2/0.4$, $M_{19} = M_{23} = M_{27} = M_{29} = M_{31} = M_{33} = 1.1/0.6$, $M_{20} = M_{24} = M_{28} = M_{30} = M_{32} = M_{34} = 1/2.3$. Nominal bias voltages: $V_{bias} = 1.7$ V, $V_{bias\_ptype} = 0.7$ V, $V_{cas} = 1.6$ V, $V_{cas\_ptype} = 1$ V, $V_{sf} = 0.7$ V, $V_{sf\_p} = 1.9$ V, $M_{diff} = 1.1$ V, $V_{on} = 1$ V, $V_{off} = 1.2$ V.

photodiodes. Since the photocurrents flowing through the photodiodes have different directions, an N-MOS version and P-MOS version of the photoreceptor have to be used depending if the photocurrents sink or go out of the photoreceptors. The outputs of three logarithmic photoreceptors are

$$V_{log_1} = U_T \frac{1}{\kappa_1} ln\left(\frac{I_B}{I_{s_1}}\right) + V_T \tag{1}$$

$$V_{log_2} = -U_T \frac{1}{\kappa_8} ln\left(\frac{I_B + I_G}{I_{s_8}}\right) + V_T \tag{2}$$

$$V_{log_3} = U_T \frac{1}{\kappa_9} ln\left(\frac{I_G + I_R}{I_{s_9}}\right) + V_T. \tag{3}$$

Please note that the P-MOS version of the photoreceptor has negative gain. The voltage variations at the source followers outputs will be

$$\Delta V_{o1} = U_T \frac{\kappa_{13}}{\kappa_1} \Delta ln\left(\frac{I_B}{I_{s_1}}\right) \tag{4}$$

$$\Delta V_{o2} = -U_T \frac{\kappa_{17}}{\kappa_8} \Delta ln\left(\frac{I_B + I_G}{I_{s_8}}\right) \tag{5}$$

$$\Delta V_{o3} = U_T \frac{\kappa_{15}}{\kappa_9} \Delta ln\left(\frac{I_G + I_R}{I_{s_9}}\right). \tag{6}$$

Source followers are necessary to drive the output voltages to the differencing amplifiers that have a high input capacitive load. The output voltage variations at the differencing amplifiers outputs can be approximated as:

$$\Delta V_{diff} \approx -\frac{C_{in}}{C_{out}} \Delta V_{in} = -A \Delta V_{in} \tag{7}$$

The input voltages $V_{o1} - V_{o2}$ and $V_{o3} - V_{o2}$ of (4)–(6) will be amplified by the differencing amplifiers

$$\Delta V_{diff_1} = -A_1 U_T \frac{\kappa_{13}}{\kappa_1} \Delta ln\left(\frac{I_B}{I_{s_1}}\right) + A_2 U_T \frac{\kappa_{17}}{\kappa_8} \Delta ln\left(\frac{I_B + I_G}{I_{s_8}}\right) \tag{8}$$

$$\Delta V_{diff_2} = -A_3 U_T \frac{\kappa_{15}}{\kappa_9} \Delta ln\left(\frac{I_B + I_G}{I_{s_9}}\right) + A_4 U_T \frac{\kappa_{17}}{\kappa_8} \Delta ln\left(\frac{I_G + I_R}{I_{s_9}}\right). \quad (9)$$

For simplicity, we can assume that all the κ_* coefficients values are the same. The capacitors values have been chosen the same to obtain identical gain values, i.e., $A_1 = A_2 = A_3 = A_4 = C_3/C_1 = C_4/C_1 = C_5/C_2 = C_6/C_2$. Hence, the previous equations can be simplified

$$\Delta V_{diff_1} = -AU_T \Delta ln\left(\frac{I_B}{I_B + I_G}\right) \quad (10)$$

$$\Delta V_{diff_2} = -AU_T \Delta ln\left(\frac{I_G + I_R}{I_B + I_G}\right). \quad (11)$$

Examining (10) and (11), we can deduce that a negative increment of V_{diff_1} can be interpreted as a shift to the blue and positive increment means a shift to the green in the spectrum. A negative increment of V_{diff_2} can be interpreted as a shift to the red/near infrared and positive increment means a shift to the green in the spectrum. Amplifiers outputs are connected to comparators with adjustable thresholds monitoring whether V_{diff*} has increased or decreased. Hence, four different event types can be sent out by the pixel: ON_1, OFF_1, ON_2, OFF_2, as it is displayed in Fig. 3.

In Fig. 3 the area of the gate of the PMOS transistor M8 is smaller compared to NMOS transistors M1 and M9 in order to compensate the difference between κ_8 and $\kappa_{1/9}$. The slope factor for the transistors operating in subthreshold region is determined by $n = 1/\kappa = 1 + C_{j0}/C_{ox}$, where C_{ox} is a gate capacitance and C_{j0} is a junction capacitance. Due to the higher doping level in n-well compared to PSUB, the depletion capacitance C_{j0} for the PMOS transistor is higher. Based on $C_{j0} = WL\sqrt{q\epsilon_0 N_{sub}/(4\Phi_F)}$, by reducing the area of PMOS transistor M8 the junction capacitance decreases, which results in similar values of κ_8 and $\kappa_{1/9}$.[1]

B. Pixel AER Logic

Pixels use Address Event Representation (AER) protocol to send out spikes when detecting color changes [13]. To handle the AER communication, some logic circuitry have to be added to the pixel as it is displayed in Fig. 4. Pixels can generate four different event types $(ON_1, OFF_1, ON_2, OFF_2)$. For arbitration purposes, each pixel can be considered as an array of four pixels arranged in a 2×2 pixel matrix as it is depicted on the top-right corner of Fig. 4. Two bits are used to encode the different four event types. The X—and Y-addresses have five bits. Four of them are dedicated to encode the pixel column/row number and the other one contains event type information. Therefore, logic to handle the AER communication has to be replicated twice. Every time that the input signals RES_X_* and RES_Y_* are active simultaneously, the corresponding differencing amplifier that has elicited one spike is reset. Note that one differencing amplifier cannot generate ON_* and OFF_* events simultaneously. The voltage V_{refr} is a tunable pull up voltage that controls the rise time of the reset pulses. This rise time is called a refractory time. As it is in real neurons, a refractory time is a silent time between consecutive spikes of the same pixel. It is useful to limit pixels activity.

[1]q is electrical charge of the electron, ϵ_0 is absolute permittivity, N_{sub} is channel doping and Φ_F is Fermi potential.

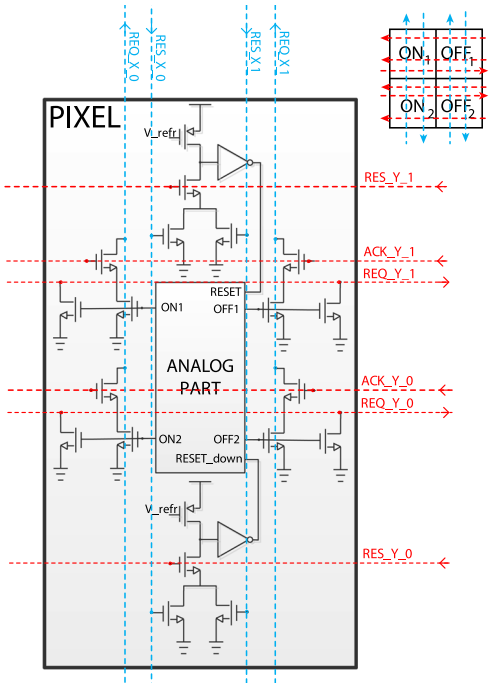

Fig. 4. Complete pixel block diagram including AER logic. Analog part is described in Fig. 3.

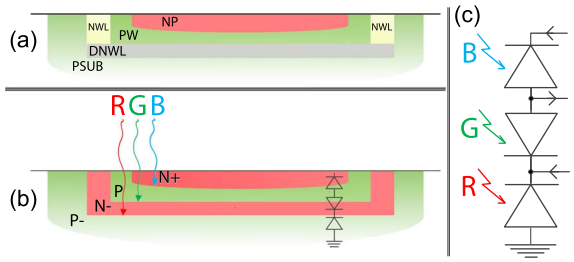

Fig. 5. Stacked photodiodes cross section diagram. (a) Design layers. (b) n-p junctions. (c) Stacked photodiodes diagram.

C. Stacked Photodiodes

Some modern CMOS fabrication technologies offer the possibility of fabricating a deep n-well to isolate the substrate of p—or n-MOS transistors. This n-well diffusion can be also used to create two buried photodiodes that can also sense photons. If we combine a n-well diffusion with a deep n-well diffusion as is shown in Fig. 5, it is possible to stack three different photodiodes in silicon. Each one will have different spectral sensitivity. The top one will have a peak of sensitivity closer to the blue, the middle one will have more sensitivity close to the green, and the bottom one will be more sensitive to light in the red/NIR band. Unfortunately, the depth of the different p+/n+ junctions is not disclosed by the foundry and cannot be chosen by the designer. We will refer in the paper to the photodiodes spectra as B, G,

TABLE I
TRANSLATION OF ON_*, OFF_* EVENTS INTO COLOR CHANGES

Event	Spectra ratio	Color change
ON_1	$\propto \frac{B}{G} \nearrow$	bluer
OFF_1	$\propto \frac{B}{G} \searrow$	greener
ON_2	$\propto \frac{R}{G} \nearrow$	redder
OFF_2	$\propto \frac{R}{G} \searrow$	greener

TABLE II
CHIP SPECIFICATIONS

Fabrication process	TSMC 90nm CMOS
Power Supply	2.5V
Type	Temporal color contrast detection
Color transitions detected	R↔G↔B
Interface	AER
Pixel size	82μm x 82μm
Photodiode size	41.5μm x 43.4μm
Fill factor	27%
Pixel complexity	58 transistors, 6 MIM capacitors
Array size	16x16
Die size	1.3mm x 1.3mm
Power consumption	9 – 19mA @ 2.5V
Dynamic Range	58dB
Intra-Scene Dynamic Range	40dB
Pixel bandwidth	2.7kHz

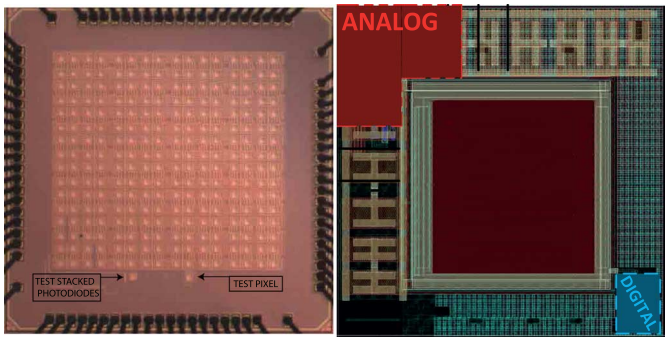

(a) (b)

Fig. 6. (a) Chip microphotograph. (b) Pixel layout. Chip dimensions are 1.3 mm × 1.3 mm. Pixel dimensions are 82 μm × 82 μm.

and R. Incident radiations shifts within the visual spectra will cause transient photocurrent variations that will be detected by the pixels processing circuitry. We assume that spectral ratios are equivalent to measured photodiodes current ratios. Table I depicts how different ON_* and OFF_* events are translated into spectral ratio variations and color changes.

III. EXPERIMENTAL RESULTS

A 16 × 16 pixel array was fabricated in the standard TSMC 90 nm CMOS process. A custom PCB with an attached 4 mm $F/1.2$ C-mount lens was designed to test the system. The AER data from the vision sensor was logged by the USBAERmini2 board [17] and then this data was sent through a USB port to a PC. A custom Java interface was adapted to show real time color transitions [18]. Main system specifications are summarized in Table II. Chip dimensions are 1.3 mm × 1.3 mm. Fig. 6(a) and (b) show a chip microphotograph and the pixel layout of a single

TABLE III
TEST LED SPECIFICATIONS

	Min. Wavelength	Typ. Wavelength	Max. Wavelength
Red	618nm	625nm	630nm
Green	520nm	525nm	535nm
Blue	455nm	460nm	465nm

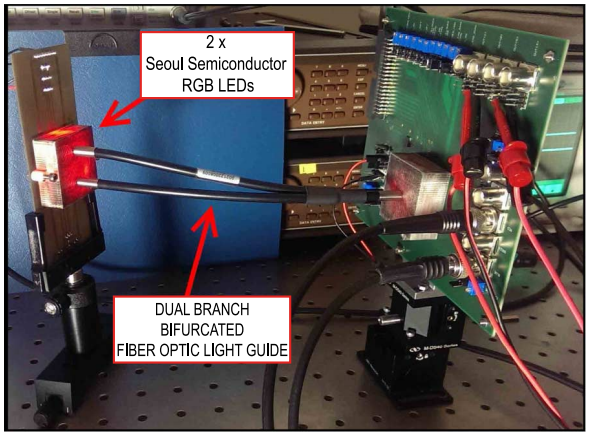

Fig. 7. Experimental setup to test a single pixel response to different color changes. Light from a RGB LEDs is transmitted with a fiber cable.

pixel, respectively. In addiction to the 16 × 16 pixel matrix, the pixel and its arbitration system, two test structures were included in the chip: a set of three stacked photodiodes and a test pixel with several analog scan buffers as it is shown in Fig. 6(a).

A. Experimental Setup

We describe here the different experimental setups for the different measurements that will be explained in the next subsections.

To characterize the photodiodes spectral sensitivity (see Section III-B), the chip was illuminated with the BPS101 Tungsten Halogen Light Source with different color filters, centered at different wavelengths ranging between 400 nm and 950 nm. The sensitivity measurements, light source irradiance for different wavelengths, filters attenuation factors and bandwidths (50 nm or 80 nm, depending on the filter) were taken into account. In order to characterize DC responses of logarithmic photoreceptors, the BPS101 Tungsten Halogen Light Source with different attached neutral density filters was used (see Section III-C-1). To measure the color change sensitivity of the test pixel (see Section III-C-2) and the pixel bandwidth (see Section III-C-4), a test bench to dynamically change input colors was built. Three high-power full color LEDs F50360 from Seoul Semiconductor emitting light at different wavelengths were available for the experiments (see diodes specifications on Table III). In the test bench shown in Fig. 7, two LEDs were used simultaneously to introduce controlled transient color changes. Light from two separate RGB diodes was mixed and transmitted by a dual branch light guide (Dolan-Jenner E809). Two input branches of the light guide were attached to the PCB with individual RGB diodes. The output branch was attached to the PCB with the sensor. The light intensity of the diodes was controlled by a waveform generator. Such solution enabled to vary different colors ratios

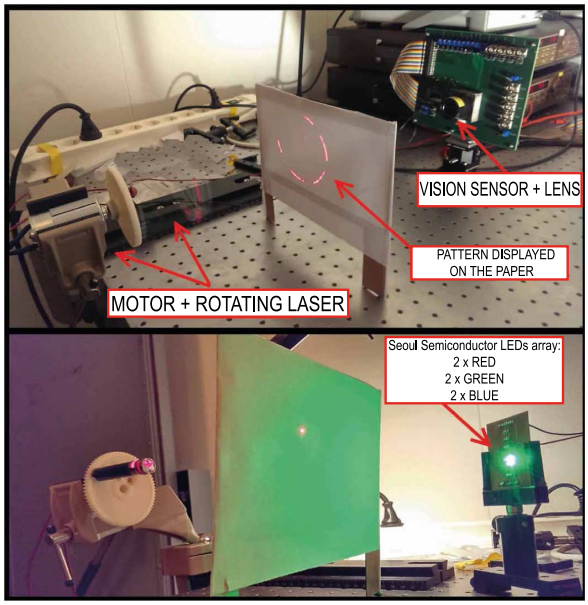

Fig. 8. Experimental setup to test the pixel array with different color stimuli moving over different color backgrounds.

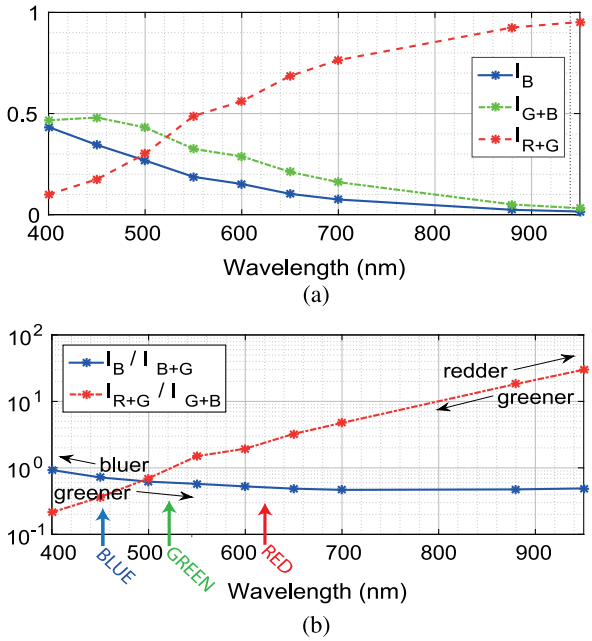

Fig. 9. Spectral response of three stacked photo diodes in TSMC 90 nm technology. The values were corrected by the Halogen Light Source irradiance factor and color filters transmission efficiency. (a) Measured photocurrents relative values. (b) Computed Photocurrents ratios.

of emitted light in order to measure the pixel sensitivity to changes in colors ratios.

To determine the sensor matrix array response to moving color stimuli (see Sections III-D-1 and III-D-3), the experimental setup of Fig. 8 was set. The vision sensor was stimulated by a beam of a collimated light (strong light dot) over different color backgrounds. The background color was projected by another PCB equipped with six single color LEDs (two red, two green, and two blue SZB05A0A diodes). Such solution provided scattered light suitable to project a background illumination.

B. Photodiodes Spectral Response

As we explained previously, the photodiodes depths are not disclosed by the foundry. For this reason, the photodiodes design was conservative ($41.5\ \mu\text{m} \times 43.4\ \mu\text{m}$) and not optimized in terms of area consumption. Fig. 9(a) shows the measured spectral response of the three photodiodes normalized with the sum of the three photocurrents that we measured. Photodiodes have different quantum efficiencies and different junction capacitances that are not known accurately. As we were expecting, the top one is the least sensitive to light, and the bottom one is the most sensitive. The bottom one has higher quantum efficiency and the size of its depletion region is bigger than others. Note that we are not interested in photocurrent absolute values to detect color transitions. The current ratio variations is what is processed to detect color changes. Fig. 9(b) displays the computed values of the two current ratios [see (10) and (11)], whose variations provoke events that indicate color transitions and illustrates how these ratios can be used to discriminate between colors. As we discussed previously, photocurrent ratios are proportional to spectral ratios. The R/G ratio increases when the color spectrum shifts towards red, and B/G ratio decreases when the color spectrum shifts towards blue. The ratio B/G exhibits weaker dependence on color spectra, it has steepest slope up

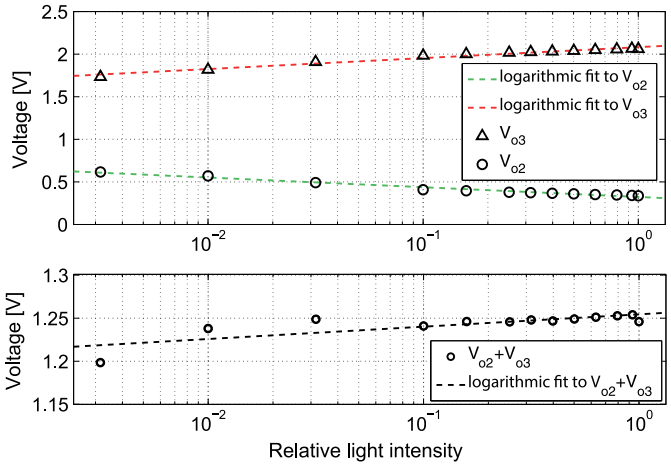

Fig. 10. Experimental measurement of DC responses of logarithmic photoreceptors. Different combinations of the Newport metallic neutral density filters were used: (0.03, 0.1, 0.3, 1, 2, 3)OD. Top: outputs V_{o2} and V_{o3}. Bottom: sum $V_{o2} + V_{o3}$.

to 650 nm and after that is flat, while the R/G ratio has almost constant slope over the entire tested spectrum. The ratio B/G exhibits weak dependence on longer spectrum wavelengths because both the top and the middle photodiode are least sensitive in this region. Possibly the top and the middle photodiodes are located much shallower than the third one, so only very energetic photons can be caught by these photodiodes. Thus, if a narrow band light source moves from 600 nm to 400 nm wavelength it would clearly lead to positive B/G events and negative R/G events as it is summarized in Table I. Inversely, if a narrow band light source moves from 600 nm to 900 nm wavelengths, it would lead to positive R/G events. Eventually, it would also lead to a few negative G/B events.

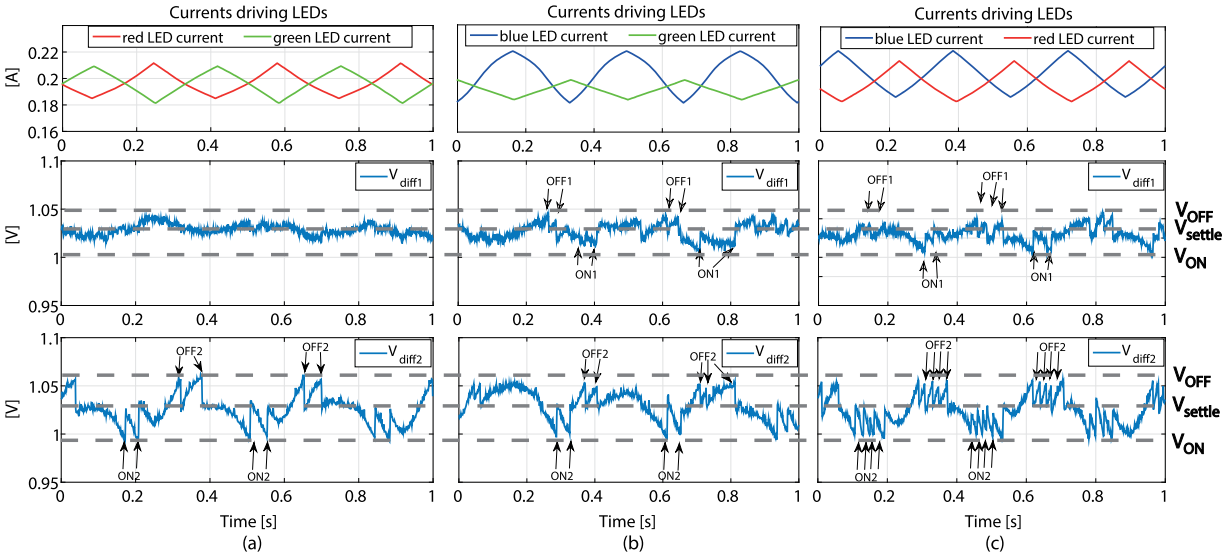

Fig. 11. Pixel response to the continuous. (a) Red-green color change. (b) Blue-red color change. (c) Blue-green color change. The intensity of red and green LEDs light was swept approximately one decade from 800lux to 8klux, whereas the blue LED light was swept 1.5 decade in order to compensate the lower sensitivity of the top photodiode.

C. Pixel Performance

1) Logarithmic Response: The sensor was illuminated by the coherent flat spectrum light beam. Different combinations of the Newport metallic neutral density filters of different transmittance were placed between the light source and the camera. The outputs of logarithmic photoreceptors from Fig. 3 were measured with scan buffers included on chip. The resulting responses are shown in Fig. 10 (top). Voltage V_{o2} is the output of the P-MOS version of the logarithmic photoreceptor and voltage V_{o3} is the output of the N-MOS photoreceptor. Tested photoreceptors perform logarithmic amplification over the entire measurement range. They have opposite gains because P-MOS photoreceptor sinks and N-MOS photoreceptor drives the photocurrents.

Both logarithmic photoreceptors responded oppositely to a light transient intensity change. Ideally, if both signal pathways had the same gains, the sum $V_{o2} + V_{o3}$ would give a flat line. In bottom plot in Fig. 10 we observed a change of the sum approximately 50 mV over 3 decades light intensity change. In section *System Description*, we discussed how to size the PMOS transistor M_8 and NMOS transistors M_1/M_9 so the difference between their slope factors was minimized as the simulation results suggested. However, the bottom plot in Fig. 10 suggests that slope factor in subthreshold region in TSMC90 nm CMOS process is not accurately modeled, as it was also reported for another process by Berner *et al.* [6].

2) Color Changes Detection: We characterized the pixel response to different color intensity changes and compared these responses with the assumed translations from Table I.

First, we measured the pixel response to a continuous red-green intensity change by illuminating its surface with 3 Hz triangular out-of-phase red and green light beams. The V_{ON_x} voltage thresholds were set to $V_{ON_x} = 0.99$ V and $V_{OFF_x} = 1.06$ V. Top plots in Fig. 11 show the currents through the LEDs and remaining plots show the V_{diff_*} voltages responses of a single test pixel to such stimuli. V_{settle} is the differencing amplifiers output voltage when reseting them. As shown in Fig. 11(a), transient shifts between the R to the G spectra provoke events when variations of the output voltage V_{diff2}, representing the R/G spectra ratios, exceeds the voltage thresholds V_{ON_2} and V_{OFF_2}. We observed roughly four ON_2/OFF_2 events. We did not observe ON_1/OFF_1 events from the variations of the second photocurrent ratio I_B/I_{B+G}. Ideally, with no blue light change stimulus we would expect strong variations of V_{diff1}. However, as shown in Fig. 9(a), since the photodiodes have not narrowband spectra, the top photodiode also responds to green light, resulting in the same proportional change of the nominator and the denominator of the photocurrents ratio I_B/I_{B+G}. The transient shifts between the B to the G spectra [Fig. 11(b)] provoked four types of events. Events ON_1 occur for the positive increment of blue light (B/G increases) and conversely, OFF_1 events occur for the positive increment of green light (B/G ratio decreases). Besides that, we received a similar number of OFF_2 and blueON_2 events. blue The current driving the blue LED in the most upper plot of Fig. 11(b) had higher range compared to other currents because the top photodiode has lower quantum efficiency than the rest of the photodiodes. The shape of the current driving the blue LED did not follow the triangular shape because the circuit controlling the brightness of the LED was providing almost its maximum output current for this experiment. Finally, for the continuous blue-red contrast changes [Fig. 11(c)], we observed the same response scheme as for the spectra shifting between B and G, but with higher variations of the output voltage V_{diff2}, and the moderate activity of the output voltage V_{diff1}. The output voltage V_{diff2} exhibits high activity for spectra shifting between B and R because the change coefficient $\Delta(I_R/I_G)$ is higher for this case as shown in Fig. 9(b)

The comparator thresholds ON_* and OFF_* were set identical because they are set and determined by identical comparators. However, the plots in Fig. 11 suggest that the events generated by V_{diff1} are triggered for lower thresholds than for

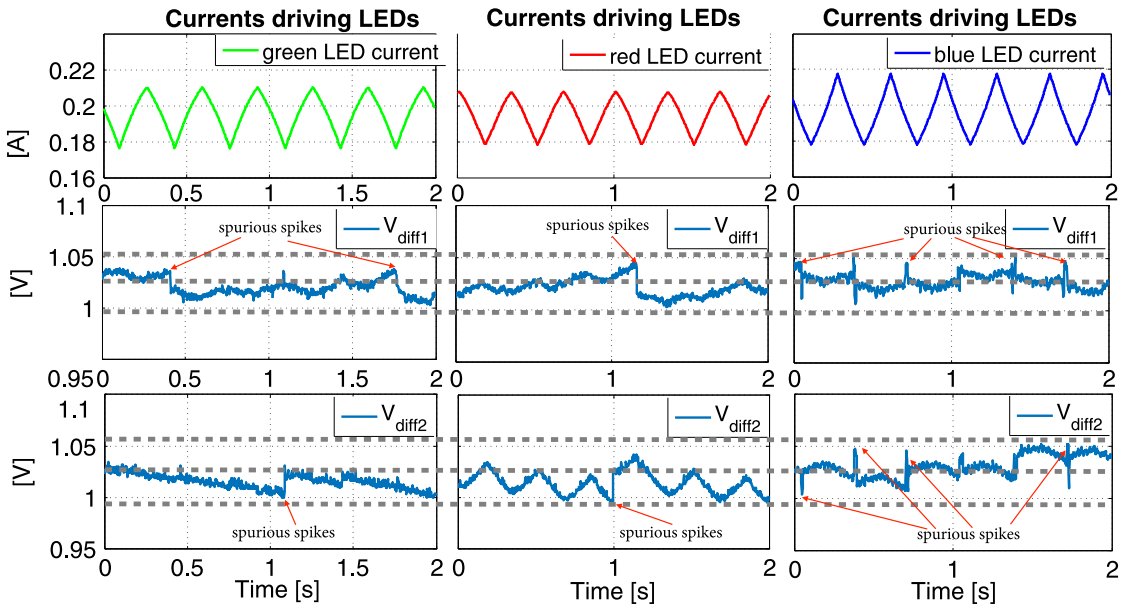

Fig. 12. Pixel response to light intensity change, without changing the spectral color. The LEDs intensity was swept within similar range as in Fig. 11.

V_{diff2}. The reason for this is the mismatch between two analog buffers which bring voltage outputs V_{diff1} and V_{diff2} to the output pads.

The final observations conclude that pixels are more sensitive to R/G variations rather than B/G, because, as it was shown in Fig. 9(b), the R/G ratio has much steeper slope than B/G ratio for color changes. For the color transitions between R and G spectra, only R/G events are elicited [Fig. 11(a)]. On the other hand, if the color transitions between spectra involve shorter wavelengths [Fig. 11(b) and (c)] we obtain both R/G and B/G types of events out of phase, e.g., positive R/G events always follow negative B/G events and vice versa.

3) Light Intensity Change: Fig. 12 shows the pixel response to an intensity change. We modulated the intensity of only one LED and the other one was turned off, so only the light intensity was modulated, without changing the spectral color. The LEDs intensity was swept within similar range as in Fig. 11. We kept the same V_{ON_x} and V_{OFF_x} voltage thresholds as in the previous test. The fluctuations of the output voltages V_{diff1} and V_{diff2} for the red and green light intensity changes are due to the non-identical gains in signal pathways V_{o1}, V_{o2} and V_{o3}. Recording events during 2 seconds, we observed 1-2 spurious spikes when stimulating with the red and green LEDs. We received 4-5 spurious spikes for the blue color intensity variations, what is more than for the two other colors intensity variations. This behavior can be explained by the low sensitivity of the stacked photodiodes to short wavelengths. The blue color does not penetrate through the substrate sufficiently and does not generate a sufficient amount of photocurrent in all three photodiodes. As a result, the assumptions of the logarithmic gains in (10) and (11) are not always valid and the pixel does not operate properly.

4) Pixel Bandwidth: The test pixel was stimulated by a sinusoidal red LED light of 1klux brightness with a green LED generating a constant background. The bias values were set to optimize speed of the differencing amplifiers and the refractory period was set much smaller than the all stimuli period values

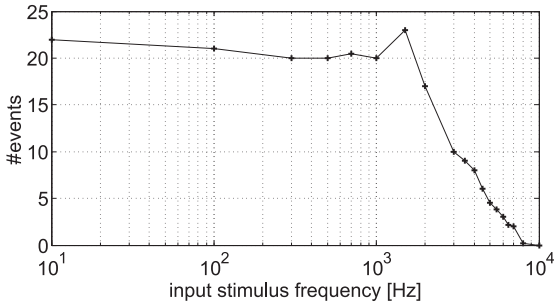

Fig. 13. Pixel frequency response. A test pixel was illuminated simultaneously with a uniform green background light and with a red LED light modulated with a sinusoidal signal. The number of counted events divided by number of sine wave cycles is plotted for different sinusoidal frequency values.

in the experiment to ensure it did not affect the bandwidth measurements. Events ON_2/OFF_2 were counted for 20 cycles for the stimulus frequency ranging from 10 Hz to 10 kHz and results were divided by the number of stimulus cycles. The pixel has a second order response as is shown in Fig. 13 with a resonance peak about 1.5 kHz before the response rolls off. For the frequency value of 2.7 kHz the measured pixel sensitivity is reduced to the half, what is equivalent to the pixel bandwidth.

D. Matrix Array Performance

1) Focal Plane Color Changes Detection: The remaining tests were performed on the entire pixel matrix with a rotating intensive light dot (beam of a collimated light) over different color backgrounds. For different stimuli the sensor generated asynchronous pixel events that were conveyed off-chip by the Address Event Representation (AER) protocol and recorded. Then we used this recorded data to reconstruct space-temporal images, as shown in Fig. 14. Fig. 14(a) shows the response to a rotating green dot over a red background, Fig. 14(b) shows the response to a rotating green dot over a blue background, and Fig. 14(c) shows a rotating red dot over a blue background.

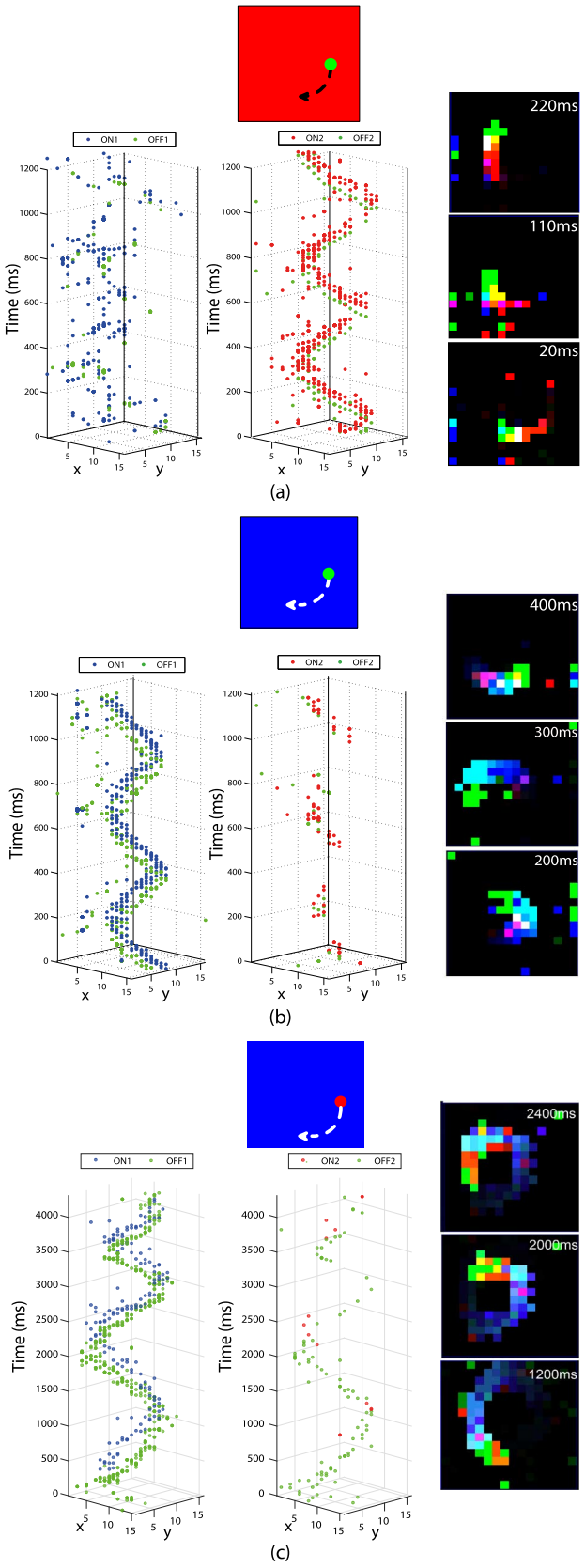

Fig. 14. Space-time plots (left) and snapshots from a live image (right) show the response to (a) a rotating green dot over red background ($\#ON_1 = 951$, $\#OFF_1 = 811$, $\#ON_2 = 3048$, $\#OFF_2 = 1819$ events in 1.2 s), (b) a rotating green dot over blue background ($\#ON_1 = 649$, $\#OFF_1 = 1241$, $\#ON_2 = 127$, $\#OFF_2 = 85$ events in 1.2 s), and (c) a rotating red dot over blue background ($\#ON_1 = 332$, $\#OFF_1 = 1531$, $\#ON_2 = 14$, $\#OFF_2 = 104$ events in 4.0 s).

Rotating dots and the background illumination were generated by the narrow band photodiodes described in Section III-A. Comparing Fig. 14(a) with Fig. 14(b), (c), we observed that for the first case (green dot over on a red background) much more events representing changes of the R/G ratio are registered. We can identify the green-red transitions: *green* events precede while *red* events follow the stimulus. The pattern in Fig. 14(a) is similar to the one from Fig. 11, where we obtained much more ON2/OFF2 events. Spurious events ON1/OFF1 are most probably elicited by the crosstalk between ON2/OFF2 and ON1/OFF1 events types. The tests in Fig. 14(b) and (c) which involve shifts between blue and green, and between blue and red spectrum, are similar. In both cases more events representing changes of the B/G ratio are elicited than R/G ratio, meaning that if there is a blue color spectrum involved in color transitions, ON2/OFF2 events are dominating. This indicates that the camera is capable of detecting transitions between adjacent primary color spectra, e.g., R $\leftrightarrow$ G and B $\leftrightarrow$ G, rather than R $\leftrightarrow$ B directly. Three snapshots with different time-stamps illustrating the live color transitions of the corresponding tests are shown in Fig. 14. In order to discriminate between red and blue spectra, we decoded ON_1 and OFF_1 events as a transitions between adjacent spectra. In other words, based on how many events have been accumulated, ON_1 events are decoded as a color transitions from red through green and finally to blue, and inversely OFF_1, events are decoded as a color transitions from blue through green to red. Finally, events ON_2 and OFF_2 were decoded, as initially assumed in Table I, as a shift between red and green colors. Fig. 16(a) illustrates the decoding process of the events into live color transitions. Every time that an event is received, the color associated to each pixel is updated and stored. Combining this information with the incoming events, the color transitions between primary colors are detected and displayed. Fig. 16(b) displays how events are received within a possible scenario of transient color transitions. It should be noted that for this design, there is no circuit implementation which can directly compare transitions between B/R spectra. The proposed approach, based on analyzing the resulting events, does not provide direct discrimination between B/R spectra, but it provides a possibility to track changes between adjacent spectral regions.

In another experiment, we moved paper sheets with printed blue-green and red-green discontinuities in front of the vision sensor following the direction of the arrows plotted in Fig. 15. We measured the responses to $blue \rightarrow green \rightarrow blue$ and $green \rightarrow red \rightarrow green$ color transitions, as shown in Fig. 15(a) and (b) respectively. Surface slopes in Fig. 15 indicate how fast the color edges were moved through the visual field of the camera. It can be estimated that the entire displacement took approximately 0.5 s. Pixels activity was limited by the refractory time to limit the number of events 1-2 events per edge with such strong color transitions.

2) Uniformity of Response: In order to quantify the uniformity of the response, a gradual $blue \rightarrow green \rightarrow blue$ transition was swept in front of the entire visual field of the sensor. The test was repeated 30 times for 4 different thresholds between ± 50 mV and ± 150 mV. All ON_1 and OFF_1 events were counted and used to calculate the distribution of the

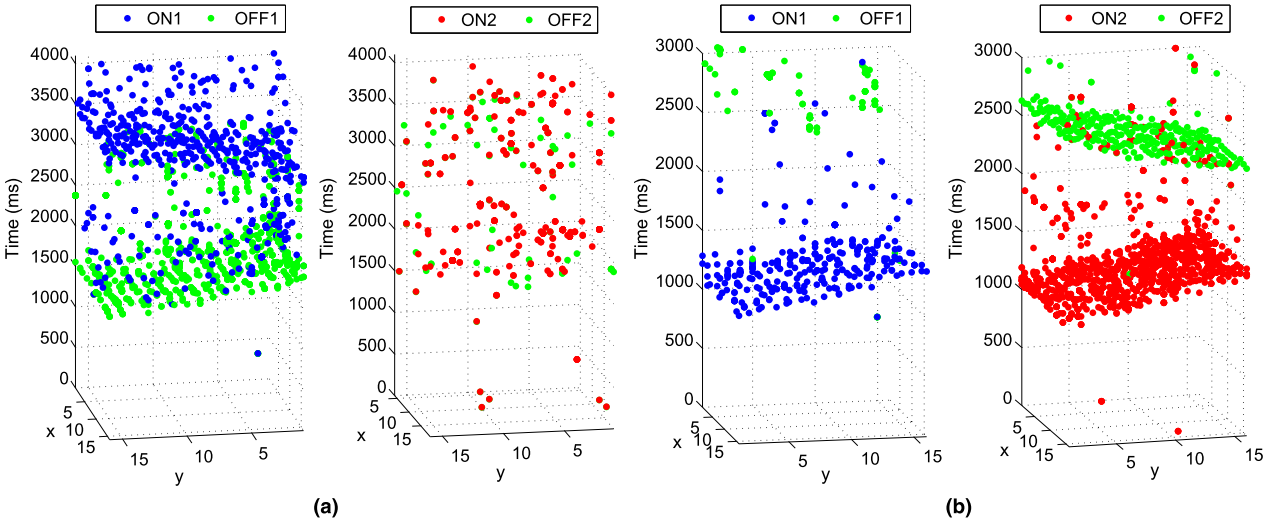

Fig. 15. Space-time plots showing pixel responses to (a) color transition $blue \rightarrow green \rightarrow blue$ and (b) color transition $green \rightarrow red \rightarrow green$. Color edges were printed on a white paper and shifted in front of the camera.

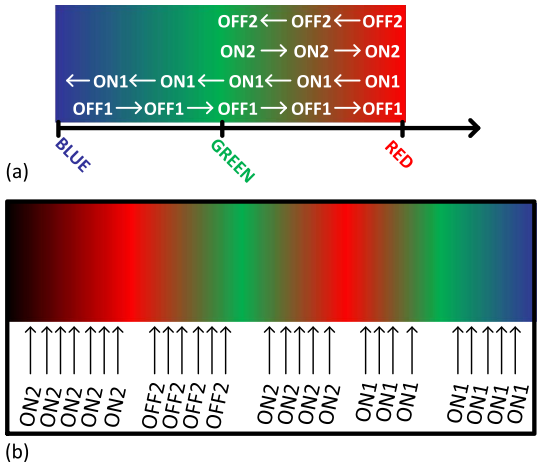

Fig. 16. (a) Illustration how the events from the pixels are decoded into live color transitions. (b) Possible scenario of color transitions. Every time that ON_1 events are received the pixel color shifts to shorter wavelengths.

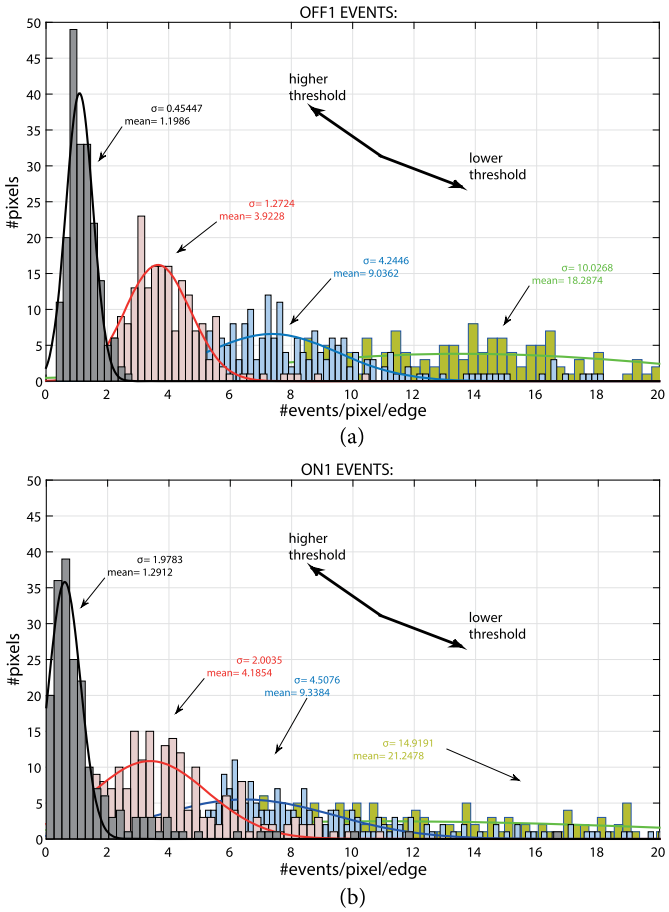

Fig. 17. Vision sensor test of the uniformity of the response. Histograms show the distribution of OFF_1 (a) and ON_1 (b) events per pass of a $blue \rightarrow green \rightarrow blue$ gradual transition for 30 repetitions in front of the visual field of the sensor. For the highest threshold we observed an average of 1.3 ON_1 and 1.2 OFF_1 events per the transition and for the lowest: 21.2 ON_1 and 18.2 OFF_1 events. The thresholds V_{ON_X} and V_{OFF_X} were set between $\pm$50 mV and $\pm$150 mV.

events per pass of a single color transition and corresponding fitted gaussian distributions, shown in Fig. 17. For the highest threshold we observed an average of 1.3 ON_1 and 1.2 OFF_1 events per the transition and for the lowest: 21.2 ON_1 and 18.2 OFF_1 events. Similarly as reported in [16] we can observe that the width of the distributions is inversely proportional to the thresholds, indicating that for small settings of thresholds, the comparators mismatch becomes dominating.

3) Dynamic Range: We tested the sensor intra-scene dynamic range by monitoring the camera response to the movement of the partly shaded rotating colorful disc of Fig. 18(a). We used yellow color instead of green in order to provoke larger variations of B/G ratio. As we explained previously in Section III-B, the top and the middle photodiodes have similar spectral sensitivity, the ratio B/G exhibits weaker dependence on color spectra shifts than the R/G ratio. Yellow-blue shifts in the spectrum are easier to distinguish because yellow color spectrum contains primary colors with longer wavelengths towards red. The disc was exposed to the light of illuminance of $60klux$. A neutral density filter of 2 decades attenuation was placed in front of the sensor covering partly the visual field of the camera

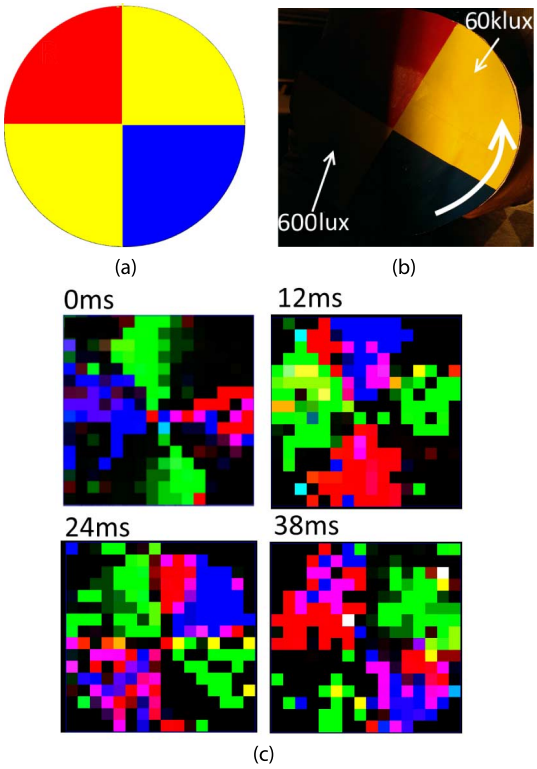

Fig. 18. Test of vision sensor intra-scene dynamic range. (a) A rotating disc painted red-yellow-blue-yellow was placed in front of the camera. (b) Half of the disc was exposed to lower illumination. The darker part was exposed to the light of irradiance of $600lux$, the rest of the disc was exposed to a source irradiance of $60klux$. (c) Several snapshots taken at different timestamps. Disk rotation frequency was 20 rps.

to create an illumination step. We show four different snapshots at different timestamps. We can recognize in the images four edges: one red, one blue and two green. The top green edge at the time of 0 ms indicates a shift from blue to green spectrum and the bottom green edge indicates a shift from red to green spectrum. The blue edge is tailing because the photoreceptor bandwidth is proportional to photocurrent, [20]. This experiment proves that the vision sensor has an intra-scene dynamic range of 40 dB.

The same experimental setup with a rotating colorful disc was used to test the camera dynamic range, but this time we provided uniform light conditions across the visual filed of the camera. The camera was able to discriminate colors for the illumination conditions ranging from $120lux$ up to $100klux$, thus the camera has a dynamic range of 58 dB

4) Temporal Noise: A static uniform white scene was set in front of the vision sensor and all possible sources of unwanted noise, as flickering light bulbs, computer displays, were turned off. For such uniform and noiseless scene conditions we recorded undesired spurious ON_* and OFF_* events within time of 50 s and then we used these results to compute the average event rate. Fig. 19 shows the pixels average event rate and their standard deviation as a function of chip illuminance. Error bars in Fig. 19 top show the maximum and minimum pixel values. Some pixels have an ideal behavior and did not fire. This undesired pixels activity is a result of noise sources in the circuit and it increases inversely proportionally to the light intensity

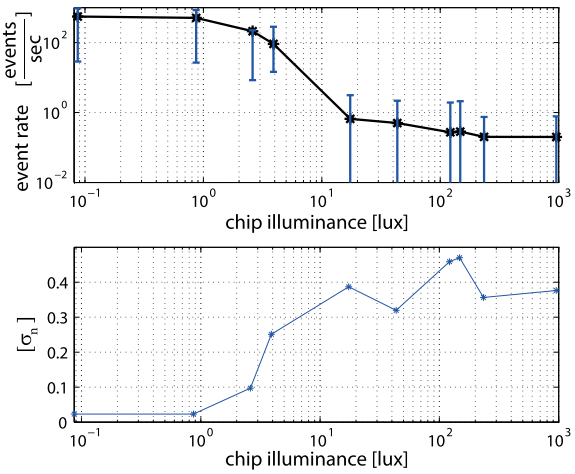

Fig. 19. Pixels temporal noise characterization. We measured the average output event rate for different uniform illumination levels (top). Error bars show the minimum and maximum values. On bottom, we display the normalized standard deviation σ_n for each measurement.

because the power spectral density noise spectrum at the output of differencing amplifier V_{diff*} is, according Berner *et al.* [6]

$$S_o(f) \approx \frac{8A^2U_T^2q}{I_{ph}} \cdot \frac{1}{1+\left(\frac{f}{f_0}\right)^2}. \quad (12)$$

Where A is the gain of the differencing amplifier, I_{ph} is the input photocurrent, and f_0 is the 3 dB cutoff frequency of the differencing amplifier. For illumination conditions below 0.1lux this noise provokes many undesired events which dominate, so the contrast recognition becomes not possible any more, what stablished the lowest value of illumination where the sensor can operate. For higher illumination values, we did not experience any limitation in the sensor operation.

E. Power Consumption

The chip power consumption (excluding pads, and analog and digital buffers of the test pixel) varies between 9–19 mA, depending on bias settings and the event rate. The power consumption could be reduced in further designs by resizing the differencing amplifier transistors of Fig. 3. The differencing amplifiers are implemented as common-source amplifiers with a quiescent current flowing through transistors M_{19}, M_{20}, and M_{23}, M_{24}. This quiescent current is dominant source of power consumption of the pixel and the entire matrix. We managed to limit the quiescent current, and hence decrease the power consumption, by lowering a default bias voltage M_{diff}. Since lowering of the bias voltage would cause V_{diff*} to hit the rail, another solution to limit the power consumption of the sensor is to decrease the conductances of transistors $M_{19}, M_{20}, M_{23}, M_{24}$.

F. Benchmarking and Comparison to the State-of-the-Art

Table IV compares the features and performance of our work with previously reported contributions with pixels having stacked photodiodes to achieve spectral sensitivity. We have classified the sensors according to their functionality, i.e., color intensity detection or color temporal contrast detection. Graaf *et*

TABLE IV
STATE-OF-THE-ART COMPARISON

Work	Graaf 1997 [19]	Graaf 1998 [9]	Olsson 2008 [5]	Berner 2011 [6]	Juanle 2013 [7]	This work
Functionality	PDM Synchronous Pixel (BIFET process)	Synchronous Pixel with in-Pixel A/D Conversion	PDM Color Asynchronous Event Pixel	Dynamic Color Vision Sensor Pixel	PDM/TFS Color Asynchronous Event Sensor	Dynamic Color Vision Sensor
Number of Spectral Regions	Dichromatic	Dichromatic	Dichromatic	Dichromatic	Trichromatic	Trichromatic
Resolution	1 pixel (2 stacked photodiodes)	1 pixel (2 stacked photodiodes)	1 pixel (2 stacked photodiodes)	1 pixel (2 stacked photodiodes)	24×24 (3 stacked photodiodes)	16×16 (3 stacked photodiodes)
Pixel Size and Fill Factor	$400\mu m \times 400\mu m$, ND	Photodiode: $800\mu m \times 600\mu m$, ND	$1188\mu^2$, 8.74%	$29\mu m \times 29\mu m$, 17%	$31\mu m \times 31\mu m$, 28%	$82\mu m \times 82\mu m$, 27%
Dynamic Range	>60dB	80dB	ND	>80dB	>60dB	58dB (40dB intra-scene)
Bandwidth or Output Frequency	20-80kHz	0.2-20kHz	0-35eps	2kHz	0.1-6Meps	2.7kHz

al. proposed a synchronous pixel with two stacked photodiodes in 1997 implemented in BIFET technology [19]. Later on, an improved version in CMOS technology was presented by the same authors, [9]. It was a single synchronous sensor with one pixel and A/D conversion. After these pioneering contributions, Olsson *et al.* proposed a concept of bio-inspired event-based vision pixel capable of differentiating two spectral regions, [5]. It was an octopus pixel. In 2011, Berner *et al.* presented a color dynamic vision pixel to detect temporal transitions between two spectral regions [6]. It was the first bio-inspired pixel capable of doing some in-pixel color processing. Afterwards, the authors initiate a research line based on incorporating stacked diodes with three p/n junctions to discriminate three spectral regions within the visible spectrum and render tri-color images closer to the human perception. The first AER color pixel array was an octopus retina capable of rendering RGB intensity images with PDM (Pulse Density Modulation) or TFS (Time-to-first-spike) readouts [7]. Based on this work and the remarkable contribution of Berner *et al.* [6], we decided to adapt the pixel circuitry to detect transient transitions between primary colors. With this new work we also give light to solve technical questions like the pixel array testing and how to interpret and reconstruct the temporal contrast information provided by three different stacked photodiodes. We have programmed a Java interface to process the incoming events and display real-time images that represent transient color transitions. In theory, any event-based processing already implemented for monochromatic DVSs could be extended to be used with our system. To do so, once a color transition is detected, the same processing conducted with a monochromatic DVS should be implemented. Note that our system responds only to shifts in the spectrum, not to the light intensity changes. Hence, it would be possible to distinguish the color of the different regions of one image, but not their intensity. To achieve color quality in the image reconstruction, it would be necessary to have narrowband spectra photodiodes with the accurate control of the depth of the different p/n junctions. Observing the works reported in Table IV, we believe that further AER color vision sensors will incorporate more than a single pixel and operate in several spectral regions.

IV. CONCLUSIONS

We built and tested the first focal plain array of bio-inspired AER pixels that mimic color opponencies among primary colors in the retina. Its pixels are capable of detecting fast transient color changes between adjacent primary colors (up to 2.7 kHz). We proposed a post-processing method to decode events into color transitions between nonadjacent color spectra ($R \leftrightarrow B$) and implemented an interface displaying these events as real-time color changes. Detailed experimental results from a single test pixel and from a pixel array are reported. Since the vision sensor abandons a global integration time and each pixel communicates asynchronously whenever it detects temporal color contrast, the post processing load on a CPU, based on color codes or colored object outlines, is relaxed. This vision sensor has good potential for an automotive robotics applications where high speed temporal color contrast recognition, especially of fast moving objects in different lighting conditions, is demanded. Pixel design was quite conservative because the photodiodes' spectral sensitivity was unknown beforehand. In future work, pixels size could be better optimized in terms of area. We believe that color change detectors could coexist with other vision sensors in the same chip to model part of the visual processing of the human retina.

REFERENCES

[1] T. Young, "Bakerian lecture: Experiments and calculations relative to physical optics," *Philos. Trans. Roy. Soc.*, vol. 94, pp. 1–16, 1804.
[2] J. E. Dowling, *The Retina: An Approachable Part of the Brain*. Cambridge, MA, USA: Belknap Press, Harvard Univ, Press, 2012.
[3] K. Fukushima, Y. Yamaguchi, M. Yasuda, and S. Nagata, "An electronic model of the retina," *Proc. IEEE*, vol. 58, no. 12, Dec. 1970.
[4] M. Mahowald, *An Analog VLSI System for Stereoscopic Vision*. Norwell, MA, USA: Kluwer, 1994.
[5] J. M. A. Olsson and P. Hafliger, "Two color asynchronous event photo pixel," in *Proc. ISCAS*, 2008, pp. 169–172.

[6] R. Berner and T. Delbruck, "Event-based pixel sensitive to changes of color and brightness," *IEEE Trans. Circuits Syst. I, Reg. Papers*, vol. 58, no. 7, pp. 1581–1590, 2011.
[7] J. A. Leñero-Bardallo, D. Bryn, and P. Häfliger, "Bio-inspired asynchronous pixel event tricolor vision sensor," *IEEE Trans. Biomed. Circuits Syst.*, vol. 8, no. 3, pp. 345–357, Jun. 2014.
[8] Foveon [Online]. Available: http://www.foveon.com
[9] G. de Graaf and R. Wolffenbuttel, "Smart optical sensor systems in cmos for measuring light intensity and colour," *Sens. Actuators*, pp. 115–119, 1998.
[10] J. Tiffin and H. S. Kuhn, "Color discrimination in indurstry," *Archives Ophthal.*, vol. 28, no. 5, pp. 851–859, Nov. 1942.
[11] Ł. Farian, J. A. Leñero-Bardallo, and P. Häfliger, "A bio-inspired aer temporal tri-color differentiator," in *Proc. IEEE Biomedical Circuits and Systems Conf.*, Lausanne, Switzerland, Oct. 2014, pp. 524–527.
[12] Ł. Farian, J. A. Leñero-Bardallo, and P. Häfliger, "Live demonstration: A bio-inspired aer temporal tri-color differentiator," in *Proc. IEEE Biomedical Circuits and Systems Conf.*, Lausanne, Switzerland, Oct. 2014, p. 171.
[13] P. Häfliger, "A Spike Based Learning Rule and its Implementation in Analog Hardware" Ph.D. dissertation, ETH Zürich, Zürich, Switzerland, 2000 [Online]. Available: http://www.ifi.uio.no/~hafliger
[14] K. A. Boahen, "Point-to-point connectivity between neuromorphic chips using address events," *IEEE Trans. Circuits Syst. II, Analog Digit. Signal Process.*, vol. 47, no. 5, pp. 416–434, 2000.
[15] J. A. Leñero-Bardallo and P. Häfliger, "A dual-operation-mode bio-inspired pixel," *IEEE Trans. Circuits Syst. II, Exp. Briefs*, vol. 61, no. 11, pp. 855–859, Nov. 2014.
[16] P. Lichtsteiner, C. Posch, and T. Delbruck, "A 128 $\times$ 128 120 dB 15 μs latency asynchronous temporal contrast vision sensor," *IEEE J. Solid-State Circuits*, vol. 43, no. 2, pp. 566–576, Feb. 2008.
[17] R. Berner, T. Delbruck, A. Civit-Balcells, and A. Linares-Barranco, "A 5 Meps $100 USB 2.0 address-event monitor-sequencer interface," in *Proc. ISCAS*, New Orleans, LA, USA, 2007, pp. 2451–2454.
[18] jAER Open Source Project [Online]. Available: http://sourceforge.net/projects/jaer/.
[19] G. de Graaf, F. Riedijk, and R. Wolffenbuttel, "Color sensor system with a frequency output and an ISS or I2C bus interface," *Sens. Actuators*, pp. 441–445, 1997.
[20] T. Delbruck and C. Mead, "Adaptive photoreceptor with wide dynamic range," in *Proc. IEEE Int. Symp. Circuits and Systems*, May 1994, vol. 4, pp. 339–342.

Łukasz Farian (M'14) received the B.S. degree in automation and robotics from Nicolaus Copernicus University, Torun, Poland, and the M.Sc. degree in nanoelectronics and robotics from the University of Oslo, Oslo, Norway, in 2012 and 2014, respectively.

In 2013, he worked as a Summer Analog Designer Intern at OmniVision Technologies, Oslo, Norway. In 2015, he completed the Space Studies Program at the International Space University at Ohio University, Athens, OH, USA. Currently, he is working toward the Ph.D. degree in nanoelectronics at the University of Oslo, with research focus on integrated circuits for space probes. His research interests include neuromorphic electronics and attitude determination systems for space probes.

Juan Antonio Leñero-Bardallo received the M.Sc. degree in telecommunications engineering and the Ph.D. degree in microelectronics from the University of Seville, Seville, Spain, in 2005 and 2010, respectively.

From January 2006 to January 2010, he worked toward the Ph.D. degree sponsored by a national grant. For two months in 2008, he was a Visiting Scholar at the University of Oslo, Oslo, Norway. From September 2010 to March 2010, he worked as a Postdoctoral Associate at Yale University, New Haven, CT, USA. From March 2010 to August 2013, he was a Postdoctoral Associate at the University of Oslo. Since August 2013, he has been a Postdoctoral Associate at the University of Seville. His main research interests include Address Event Representation vision systems, frame-based vision sensors, smart sensors, wireless vision sensor networks, signal processing, and very large scale integration emulators of biological systems.

Dr. Leñero-Bardallo has been a member of the IEEE Sensory Systems Committee since 2012.

Philipp Häfliger (M'03–SM'10) received the M.Sc. degree in computer science (with astronomy as a second subject) from the Swiss Federal Institute of Technology (ETH), Zürich, Switzerland, and the Ph.D. degree from the Institute of Neuroinformatics at ETH in 1995 and 2000, respectively.

He then moved for a postdoctoral position to the nanoelectronics group at the Institute of Informatics at the University of Oslo, Oslo, Norway, where he has now advanced to Associate Professor. In Oslo, his research focus shifted gradually from neuromorphic (inspired by the nervous system) electronics towards ultra-low-power ASIC design for biomedical devices, in particular wireless microimplants.

Dr. Häfliger has been Chairman of the IEEE Circuits and Systems (CAS) Society's Biomedical and Life Science CAS (BioCAS) Technical Committee (2010–2012), and has served and still serves in various functions for the IEEE ISCAS and IEEE BioCAS conferences. He is an Associate Editor for the IEEE TRANSACTIONS ON BIOMEDICAL CIRCUITS AND SYSTEMS.

Paper II:

Ł. Farian, P. Häfliger, J.A. Leñero-Bardallo
Miniaturized Sun Sensor with In-Pixel Processing for Attitude Determination of Micro Space Probes
International Conference on Event-based Control, Communication, and Signal Processing, 2015

Miniaturized Sun Sensor with In-Pixel Processing for Attitude Determination of Micro Space Probes

Łukasz Farian, Philipp Häfliger, Juan A. Leñero-Bardallo
Nanoelectronics group, Department of Informatics, University of Oslo, Norway

E-mail: lukaszf@ifi.uio.no

***Abstract*—This work presents a novel concept for a miniaturized two-axis asynchronous Sun sensor which will be a part of a sounding rocket- and micro-probe Attitude Determination System. The sensor is composed of only two lines of bio-inspired pixels performing asynchronous in-pixel parallel processing, and two optical slits aligned above the chip. The Sun location is determined with much higher temporal resolution than synchronous sensors could achieve. Furthermore, the sensor output data directly indicates the Sun's position, without the need for any further processing (except initial calibration procedure). Also the power consumption is expected to be small in comparison to traditional Sun sensors, thanks to abandoning the need for a clock. This approach occupies much less area than previously reported Sun sensors. Hence, the remaining chip area can be used to realise a system-on-chip integrating other sensor interfaces, and processing- and communication units. This allows a high degree of integration and miniaturization which is essential for the planned micro-probe application. The simulations proved the Sun sensor to have temporal resolution of 1ms, standby power consumption of only a few pico-Watts and achieved a resolution of $\approx 0.5^{\circ}$.**

I. Introduction

The Sun is the most attractive celestial body for navigation, because it is the brightest object in our solar system and when observed from the Earth orbit it has small enough radius to be modelled as a point source [1]. Hence, Sun sensors are widely used in various systems, e.g. for space applications, such as satellites, sounding rockets, and space probes, as well as terrestrial applications involving renewable energies, tracking the Sun to improve the photovoltaic plants efficiency. In space applications Sun sensors are part of the Attitude Determination and Control System (ADCS) to determine the orientation of space instruments. Sun sensors provide a measurement of the Sun vector in two or more axes in the instrument's coordinates. Most of the Sun sensors share similar operating principle of using patterned masks, such as slits, pinholes or multi-aperture arrays, over a light sensing focal plane. The detector, located under the mask, senses the projected pattern and based on some geometrical properties of this pattern it determines the Sun vector. The Sun sensors can be divided into two groups: digital and analog. With digital Sun sensors, photo-detection is realized by a line [2] or array [3], [4] of pixels. Each pixel in the array accumulates a given amount of photo-charge proportional to the incident light intensity, and this accumulated charge is sampled and digitized with a fixed sampling rate. For each array readout, digital Sun sensors produce raw data from the entire focal plane, and additional post processing with algorithms [5] extracting the peak-illumination patterns has to be performed. The performance of digital Sun sensors strongly depends on the processing workload. This is not efficient in terms of power consumption and the data bandwidth, especially for space applications. Also the temporal resolution of such sensors is limited by the pixels' fixed time intervals for reading out of the accumulated charges. On the other hand, analog Sun sensors [6] [7] use only a few big photodiodes and the Sun vector is obtained from the ratios of the currents generated by these photodiodes. Hence, these sensors are not limited by a global integration time, produce less data and consume less power. However, analog Sun sensors are not robust against spurious light. The photodiodes translate all the reflectances, light from other bright celestial bodies, and stray light into photocurrents with no possibility of spatial selection and exclusion of distractors, unlike digital Sun sensors. Another approach to realize a Sun sensor is to abandon slits or pinholes and to employ full optic lenses to track the entire Sun's disk as in [8]. The authors in [8] achieve high accuracy, but the sensor uses an entire CCD camera and requires sophisticated geometric calibration and complicated feature extraction algorithms to obtain the Sun vector.

II. System Concept and Design

In this paper we propose a Sun sensor that takes advantage of both analog and digital Sun sensors. Namely, it takes advantage of spatial selectivity of vectors of pixels, but it is not limited by a global integration time and frame-delay, it consumes less power and the processing of the data is performed already inside the pixels, with no the need for post-processing to extract the Sun coordinates. The proposed Sun sensor takes its inspiration from neurons that compete through common inhibition. To the best of our knowledge this Sun sensor is the first one which takes its inspiration from biological systems. This asynchronous Sun sensor is designed specifically for micro-satellites and space probes, where the payload size is severely restricted. Thanks to implementing two 1-D pixel vectors instead of a 2D array in a standard CMOS process, the remaining chip area can be used for other sensor-interfaces, analog to digital converters, and communication- and processing circuits for these space probes. The high temporal resolution and fast response is also crucial for space probes and sounding rockets applications, because usually they have high spin rates, quick update rates, and good temporal accuracy of their attitude is thus essential.
The Sun sensor consists only of two one-dimensional pixel arrays organized in an L-shape along two chip borders and two optical slits above, also organized in an L-shape. As illustrated in Fig. 1, the slits are not aligned with the pixel array, but they are rotated 180° and moved such that the corner of the

L-slit is located exactly above the center of the chip. Fig. 1 shows a case for a collimated light beam perpendicular to the surface of the Sun sensor. In this case the Sun projects an L-shape pattern and the two intersection points with the pixel arrays are in their centre. For non-orthonormal orientations the intersection points will shift from the arrays centres and the distance from the centre will indicate the Sun's deviation from the orthonormal position. As shown in Fig. 1 the projected L-shape pattern intersects with the pixels vectors in two places, so only few pixels are illuminated simultaneously, and only these pixels carry relevant information about the Sun orientation. The pixels arrays express a 'winner-takes-all' (WTA) behaviour, so they surpress any but the strongest light source. Hence only the winning pixel (or a configurable specified number of winning pixels) which accumulated the greatest amount of photo-charge will convey its coordinate in the array off-chip on an asynchronous bus.

A. *Circuit design*

Fig. 2 displays the main electronic blocks of the system. It consists of two one-dimensional pixel lines and the Address Event Representation (AER) communication periphery [9]. Each pixel integrates the incident light intensity, and when the integrated charge exceeds a voltage threshold it spikes and sends out a request with its own unique address to the AER periphery. Next to the pixel array there is another block sending communication requests to the AER periphery called *Counter & Timeout*. This block is assigned an unique address and it communicates with the AER arbitration system like the other pixels. However, this block does not sense light, but resets all pixels after a specific number of pixels have spiked. Counting is realized by monitoring how many acknowledge signals the sensor receives on *BUS_REQ_X* and *BUS_REQ_Y*. Additionally, the *Counter & Timeout* block resets all pixels periodically, with the frequency adjustable by an input node *timeout*.

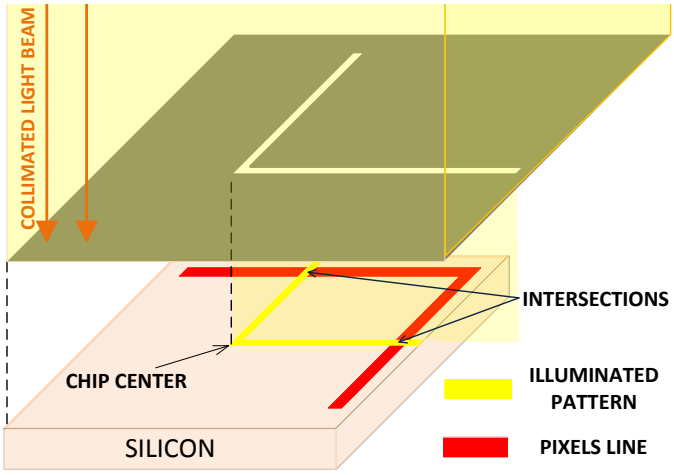

Fig. 1: Concept of placement L-shape slit over the pixels line.

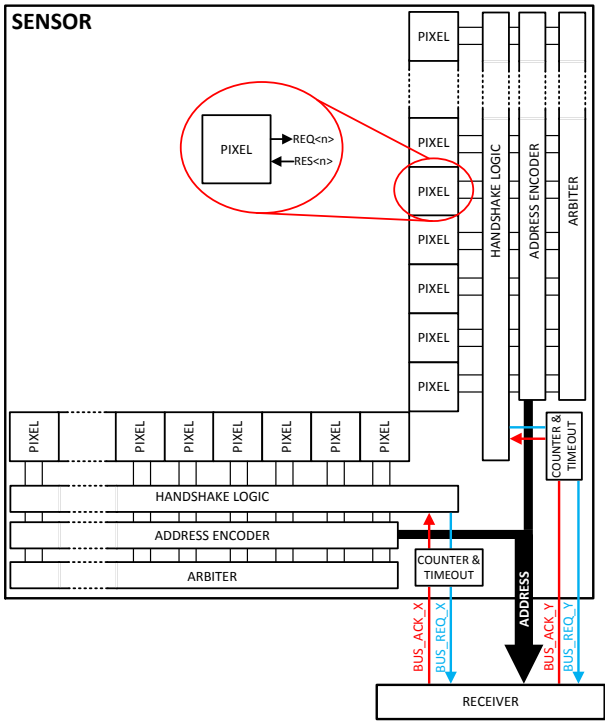

Fig. 2: Block level view of the Sun sensor and pixel core schematics. It consists of two one-dimensional pixel lines and the AER communication periphery.

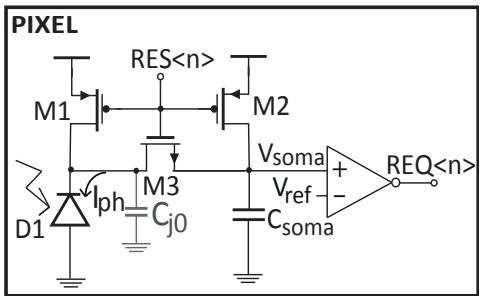

Fig. 3: Pixel core schematics.

B. *Pixel Design*

Fig. 3 shows the schematics of the pixel circuitry. The principle of operation of the pixel is similar to an Integrate-and-Fire (I&F) neuron described by Carver Mead in [10], with the difference, that it is not self-resetting, and the refractory period is not controllable. The input photocurrent I_{ph} is discharging the capacitor C_{soma} until the threshold V_{ref} of the comparator is reached, which triggers the request pulse REQ. Low signal RES from the AER arbitration system turns on transistors M1 and M2 and turns off transistor M3 in order to re-charge the capacitors C_{soma} and reset the pixel. The transistor M3 is used to ensure that the reset time does not depend on the photodiode current. In other words, if transistor M3 is not implemented more time would be required to reset the pixel which is illuminated by a strong light. The behavior of the I&F

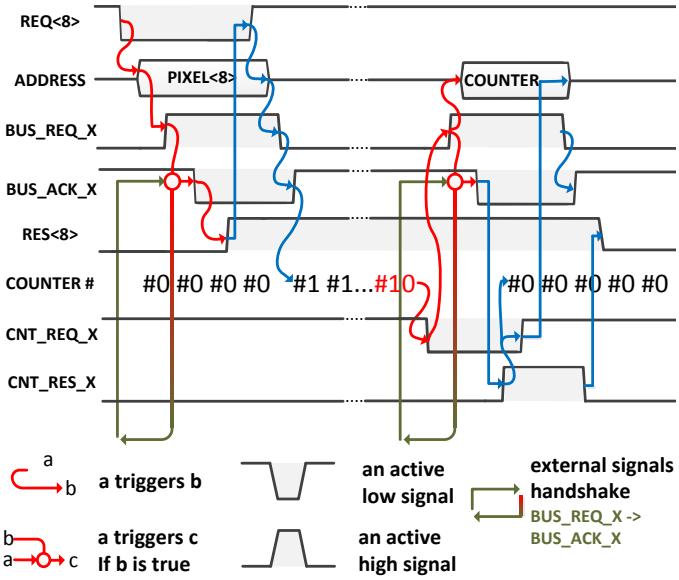

Fig. 4: Asynchronous sequence of a communication cycle triggered by pixel REQ<8> event. COUNTER# is a counter stored register value. Global reset is illustrated after 10 events.

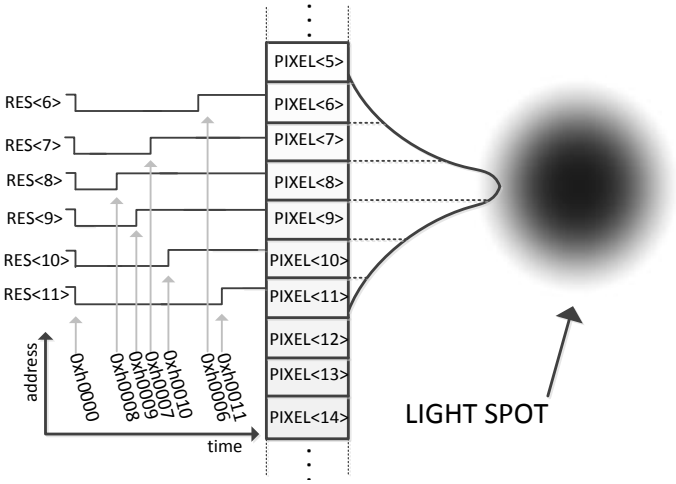

Fig. 5: Time-to-First-Spike principle of operation. The vector of pixels is illuminated by a beam with the corresponding Gaussian intensity profile. First, global reset is indicated by address 0xh0000, then pixels spike in decreasing order of their illumination, such that pixels which are illuminated by a strongest light spike first, in this case the PIXEL<8> spikes first.

neuron is based on the translation of the input photocurrent into spike latency T, such that the pixel illuminated by a strongest light spikes first after the array wide reset:

$$T = \frac{(V_{DD} - V_{ref}) \cdot C_{tot}}{I_{ph}} \quad (1)$$

Voltage $V_{DD} - V_{ref}$ is the voltage drop required for the pixel to spike. The total capacitance seen by the photodiode is $C_{tot} = C_{j0} + C_{soma}$, where C_{j0} is the junction capacitance of the photodiode.

C. Arbitration System

Pixels use Address Event Representation (AER) protocol to send out spikes when they integrate enough photo-charge. Requests are arbitrated using the arbitration system proposed by Häfliger in his PhD dissertation [9] and implemented in some prior vision sensors [11]–[13]. The arbitration system can handle event rates up to 10Meps and is fast enough to arbitrate event rates from a two one-dimensional array of the proposed Sun sensor. It is made up by some logic to handle the AER communication, address encoders, and arbiters. For details refer to [9]. The timing of the different AER signals exchanged between pixels and AER periphery is shown in Fig. 4. As the pixel address is successfully read out, the pixel that has elicited this request is reset and the counter increases its stored register value *COUNTER#* by one. The pixels are being kept in reset and the global reset signal is provided from the *Counter & Timeout* block. In Fig. 4 the global reset is generated after ten spikes.

D. Time-to-First-Spike operation

We use a Time-to-First-Spike (TFS) mode [14] to obtain a WTA selection. The TFS principle of operation is illustrated in Fig. 5. As it was described in the Section II-C, each pixel is allowed to spike at most one single event because the pixels which have spiked are being kept in reset. The first pixels which spike are the winners carrying the most relevant information about the location of the strongest illumination on the array. The resulting output of the Sun sensor will provide a stream of coordinates of the *winning* pixels in decreasing order of their illumination, as illustrated in Fig. 5. Since only a certain number of the strongest winners are allowed to spike before the global reset signal is provided, this operation can be considered as a customizable multiple winners-take-all circuit. Additionally, time delays between consecutive pixels spikes carry information about the strength of the photocurrent according to Eq. 1. The reason for making the system configurable to allow multiple winners is to have the flexibility to analyse the observed scene in more detail to deal with strong distractors or cases when the Sun is outside the field of view. For example with strong distractors the Sun can still be identified by its Gaussian intensity profile and the sensor response to the Sun will look like the function shown in Fig. 5. Single pixel spurious readouts can thus easily be distinguished and rejected, which consequently improves the Sun sensor accuracy.

E. A Micro-Package Optics Integration

Fig. 6 shows in details a micro-package optics onto which the chip will be flip-chip bonded along the chip edges. As described in Section II, the slits are rotated 180° and moved in relation to the pixels such that the corner of the L-slit is located exactly above the center of the chip. Note, that the L-shape optical slit above the chip extends beyond the borders of the chip. With such configuration we obtain a symmetrical field of view for both axes and with proper sizing of the micro-package we avoid the case when the input beam entirely overlaps along

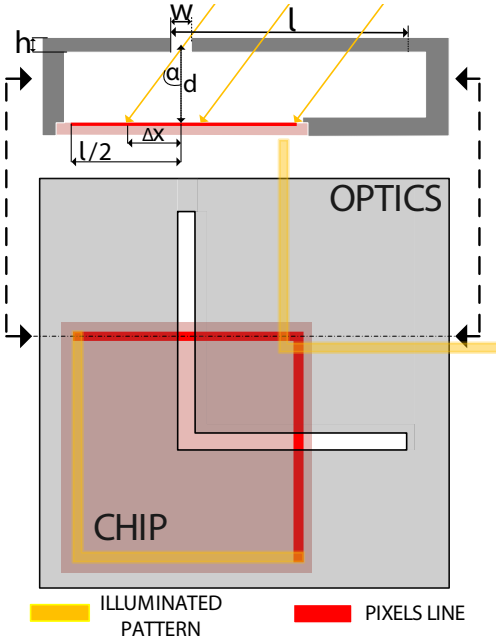

Fig. 6: Vertical cross-section (top figure) and horizontal view (bottom figure) of the Sun sensor structure. Two extreme positions of the illuminated pattern are shown.

one pixel array, and ensures that there are always at most 2 intersection points between beam and the pixels array.
For any non-orthonormal orientation the Sun will project an L-shape pattern shifted from the centre of the pixel vectors and the distance from the centre of these pixel vectors will indicate the Sun's deviation from the orthonormal position. The relation between this distance Δx and the Sun's deviation angle α from the orthonormal position is given as:

$$\alpha = arctan\left(\frac{\Delta x}{d}\right) \tag{2}$$

Based on Equation 2 the maximum Sun angle detectable by the sensor can be derived:

$$\alpha_{max} = min\left[arctan\left(\frac{l}{2 \cdot d}\right), arctan\left(\frac{w}{h}\right)\right] \tag{3}$$

Two extreme positions of illuminated patterns shown in Fig. 6 can be derived from the Eq. 3. The two equations above show that there are two trade-offs, the first between a field-of-view (FOV=$\pm\alpha_{max}$) and the sensor sensitivity determined between the distance d and the pixels vector length l, and the trade-off between FOV and the sensor resolution determined between the slit width w and the micro-package thickness h. The resolution of the Sun sensor is given as: $R = \frac{FOV}{\#pix}$, where $\#pix$ is a number of pixels in one array. Fig. 7 shows how the pixels will be organized in a 2D array. Thanks to a rectangular shape of the pixels layout in the AMS 0.35μm opto-process with a photodiode size of $5\mu m$ x $5\mu m$, the distance of $8\mu m$ between centers of consecutive photodiodes will be achieved. This will enable us to place 250 pixels in line on our silicon die with a useable area of $2mm$ x $2mm$. According to preliminary discussions with a producer

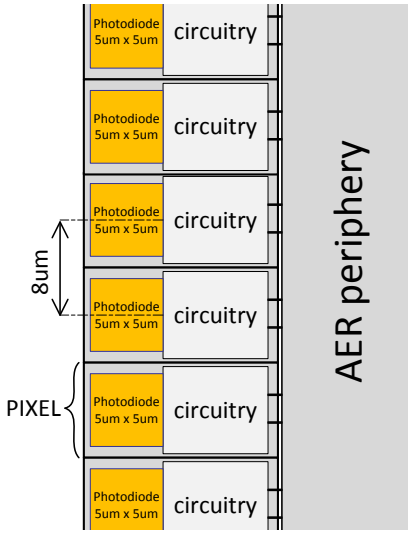

Fig. 7: Structure of the 1-D vector of pixels layout.

of LTCC micro-carriers, we assume the sizes of the micro-package optics and the chip to be: l=2000μm, d=580μm, h=90μm and w=160μm. For these assumptions the Sun sensor field of view will be $|\alpha| \leq 60°$, and the expected Sun sensor resolution in one axis will be $R = \frac{120°}{250} = 0.48°$.

F. Calibration and Data Processing

The calibration process will be necessary to measure and compensate the misalignment between the optics position and the pixels matrices. During the calibration process the Sun sensor will be illuminated by a othonormal light beam and the position of the pixels for such stimuli will be read, similarly as is illustrated in Fig. 1. These new pixels positions for the orthonormal Sun light will be used further for offset subtraction off-chip. This calibration process will be carried out only once after the Sun sensor is produced.
Further, the sensor will provide output data in form of stream of coordinates and the counter stamp indicating the Sun's position according to the relationship from Eq. 2. Since the slit width from Fig. 6 is bigger than the pixel size, it is likely that for the orthonormal light beam, more than one pixel will be illuminated by a maximum plateau equal near solar constant irradiance. As a result, several pixels may spike with similar timing before the Gaussian drop-off becomes valid. This possible limitation can be overcome by the described multiple winners-take-all approach and some additional off-chip processing of the output data to determine the center of the plateau, which is unambiguous to the Sun angle. This possible behavior will be verified in the actual silicon implementation integrated with the optics.

III. Simulation Results

A. Single Pixel Operation

The solar constant irradiance expresses the mean solar electromagnetic radiation per unit area, and is equal to $1360 W/m^2$. The solar constant includes all wavelengths of solar electromagnetic radiation, but the photodiode spectral response

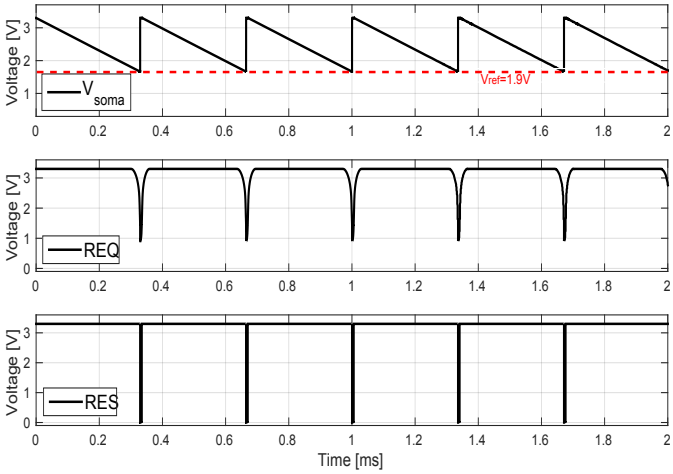

Fig. 8: Simulated transient response of pixel schematics of Fig. 2 to a constant light illumination of irradiance equal to solar constant ($1014W/m^2$).

range is only between $400nm$ and $1100nm$. Within the band of $400nm$ and $1100nm$ the solar electromagnetic radiation reduces to $SC_{band} = 1014W/m^2$ and, hence this value can be assumed to be the maximum radiation to which the winning pixels will be exposed. Fig. 8 shows the pixel response from Fig. 2 to a constant light illumination of irradiance equal to SC_{band}. A photodiode model, provided by the foundry, was used to model the photocurrent as a function of the incident light irradiance. The comparator was realised by a standard differential pair with a threshold $V_{ref} = 1.9V$. The pixel output, REQ was connected back to the reset terminal RES with a few time-delay circuits in between, such that the pixel operated as a self-reset I&F neuron. A MOS capacitor C_{soma} was used with a capacitance of $1.815pF$. The first plot in Fig. 8 shows the voltage V_{soma} on the capacitor being gradually discharged. When the threshold V_{ref} of the comparator is reached the active low request pulse REQ is generated, and the pixel is reset such that the capacitor C_{soma} is re-charged and the cycle repeats. The radiant flux per single pixel R_{peak} for an orthonormal Sun position was calculated using the solar constant SC_{band} and the assumed photodiode size area of $5\mu m$ $\times$ $5\mu m$:

$$R_{peak} = SC_{band} \cdot A = 1014\frac{W}{m^2} \cdot 5 \cdot 5um^2 = 25.2\frac{nW}{pixel} \quad (4)$$

According to Eq. 4 the single pixel of size $5um$ x $5um$ is exposed to a radiant flux of 25.2nW corresponding to a photo current of $8.6nA$ according to simulation. According to Eq. 1 the expected time delay of the pixel to spike for such a stimulus is:

$$T_{max} = \frac{(3.3V - 1.9V) \cdot 1.815pF}{8.6nA} \approx 295us \quad (5)$$

The self-resetting simulation had a slightly longer firing period of $330\mu s$, because of the pulse width and the reset delay.

B. Array TFS response

Fig. 9 shows the simulation results of an array of 25 pixels exposed to a light beam with a Gaussian irradiance profile

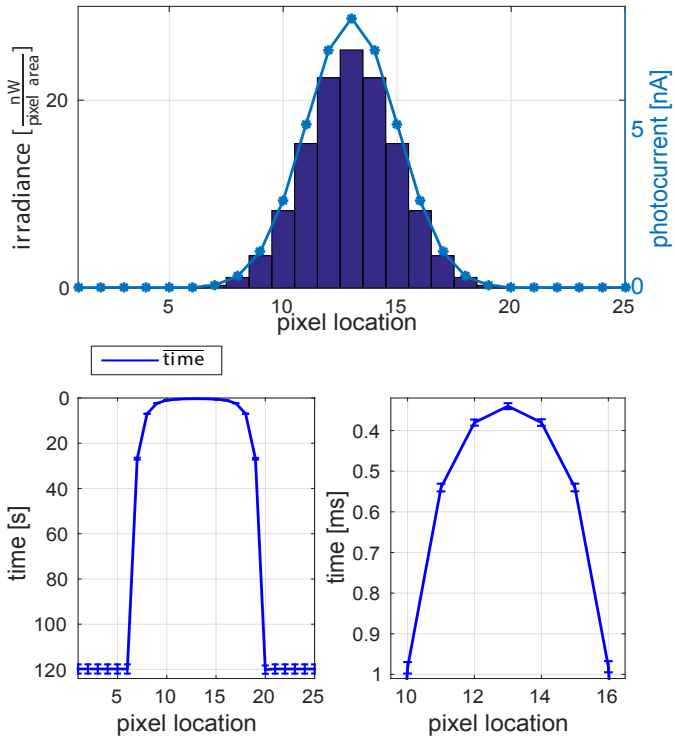

Fig. 9: Profile of the light beam used to stimulate the pixels vector and the corresponding photocurrent generated by the photodiodes (top plot), and pixels average time delays to their first spike (bottom plots) with error bars expressing a range $\overline{time} \pm \sigma$. The average $\overline{time}$ and the standard deviation σ were obtained from 100 Monte Carlo iterations.

with the irradiance peak R_{peak} obtained from Eq. 4. The light beam irradiance profile distribution and the corresponding photocurrents generated by the photodiodes are illustrated by a top bar chart and blue plot respectively. The bottom plots show the pixels average time delays to their first spikes and the error bars express their corresponding standard deviation σ spread around the average $\overline{time}$. The right bottom plot in Fig. 9 shows a closer look on time delays of the 7 *fastest* pixels. Time delays to the pixels first spikes are in increasing order of the their illumination, such that the pixel number 13 is the winner with the average time delay of $334\mu s$, and pixels number 12 and 14 are the consecutive winners which spiked $50\mu s$ later. Since the AER arbitration system [9], which is used to arbitrate the events from the pixel array, can handle event rates up to 10Meps, it is fast enough to resolve the winners from the simulated array.

The same array of 25 pixels was connected to the AER periphery and again exposed to the same light beam of the irradiance peak R_{peak}. Fig. 10 shows the BUS_ACK, CNT_RES and reset signals for 8 *winning* pixels. The pixels were reset after their addresses had been read out successfully in the same order as in Fig. 9. After 8 requests the global reset signal CNT_RES was generated from the *Counter* block and the winners determination procedure restarted. The arbitration system determined 8 winning pixels within time of 1 ms when exposed to the solar constant radiation. Hence the temporal

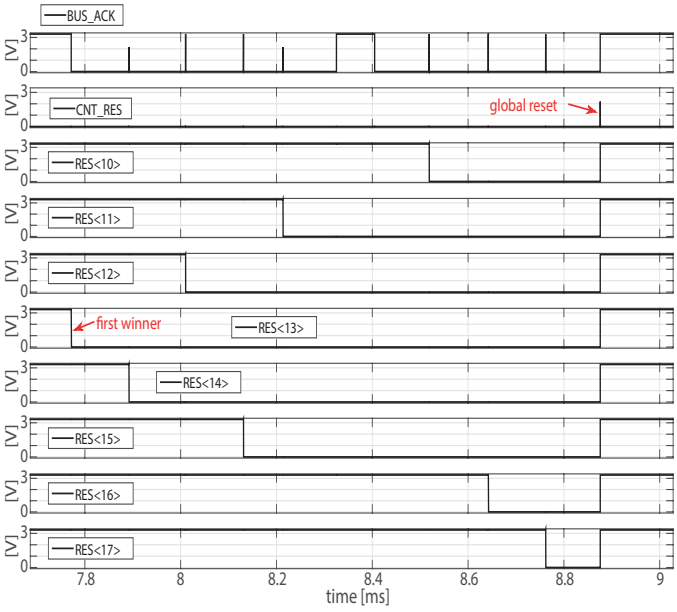

Fig. 10: Communication signals between the pixels array and the AER periphery.

resolution of this proposed Sun sensor is expected to be around 1ms.

C. Power Consumption

Table I summarizes the power consumption of the Sun sensor consisting of 256 pixels. The Table distinguishes the power consumption of the system with no activity of the pixels (standby mode) and with the pixels being active. The entire

TABLE I: Sun sensor estimated power consumption

Power Consumption	Pixel array	AER Periph.	Total
Standby Mode	$7.4pW$	$752nW$	$\approx 7.5pW$
Activity @$5keps$	$540nW$	$4.3mW$	$\approx 4.3mW$

power consumption of the Sun sensor is 7.5pW when the pixels generate no events and 4.3mW when the sensor generates 5 thousand events per second (5keps). The power consumption of the Sun sensor is dominated by the arbitration periphery. As per pixel the dominant power is consumed by the differential pair comparator.

IV. Conclusions

A new concept of a miniaturised two-axis asynchronous Sun sensor was presented. The sensor is comprised of only two 1-D arrays of pixels which perform parallel processing and express a 'winner-takes-all' (WTA) behaviour and optical slits aligned above the chip. We provided simulation results characterizing the Sun sensor performance. The Sun sensor is expected to have temporal resolution of 1ms, what is much higher than what a traditional synchronous sensors could achieve. Also, simulations prove that the sensor is expected to consume only few pico-Watts in standby mode and achieve the resolution of $\approx 0.5^{\circ}$. The estimated layout occupation is much smaller than for the traditional Sun sensors, hence it allows to use the remaining chip area to realise a system-on-chip integrating other sensor interfaces, processing- and communication units necessary for space applications.
The results of this novel concept have been obtained by schematic simulations. Currently, the Sun sensor layout is being designed in the AMS $0.35\mu m$ OPTO CMOS process, and the described micro-package optics is being negotiated with potential producers. Testing of the actual silicon implementation together with the integrated optics will enable to verify the assumptions of the Gaussian irradiance profile of the illuminated pattern, and test the actual response of the pixel array.

V. Acknowledgments

The proposed Sun sensor is planned to be employed in the Sounding Rocket Attitude Determination system and in micro space probes as part of the 4DSpace research initiative at the University of Oslo, Norway. A first launch that might include this Sun sensor is planned within the ICI sounding rockets series in late 2016 (ICI-5).

References

[1] J. R. Wertz, *Spacecraft Attitude Determination and Control*. Kluwer: Ed. Norwell, 1995.

[2] A. Ali and F. Tanveer, "Low-cost design and development of 2-axis digital sun sensor," in *Journal of Space Technology*, vol. I, VI 2011.

[3] C. Liebe and S. Mobasser, "Mems based sun sensor," in *Aerospace Conference, IEEE Proceedings.*, vol. 3, 2001, pp. 3/1565–3/1572.

[4] N. Xie and A. Theuwissen, "A miniaturized micro-digital sun sensor by means of low-power low-noise cmos imager," *Sensors Journal, IEEE*, vol. 14, no. 1, pp. 96–103, Jan 2014.

[5] J. Enright and Godard, "Advanced sun-sensor processing and design for super-resolution performance," in *Aerospace Conference IEEE*, 2006.

[6] F. Delgado, J. Quero, J. Garcia, C. Tarrida, P. Ortega, and S. Bermejo, "Accurate and wide-field-of-view mems-based sun sensor for industrial applications," *Industrial Electronics, IEEE Transactions on*, vol. 59, no. 12, pp. 4871–4880, Dec 2012.

[7] P. Ortega, G. López-Rodríguez, J. Ricart, M. Domínguez, L. Castañer, J. Quero, C. Tarrida, J. García, M. Reina, A. Gras, and M. Angulo, "A miniaturized two axis sun sensor for attitude control of nano-satellites," *Sensors Journal, IEEE*, vol. 10, no. 10, pp. 1623–1632, Oct 2010.

[8] A. Trebi-Ollennu, T. Huntsberger, Y. Cheng, E. Baumgartner, B. Kennedy, and P. Schenker, "Design and analysis of a sun sensor for planetary rover absolute heading detection," *Robotics and Automation, IEEE Transactions*, vol. 17, no. 6, pp. 939–947, XII 2001.

[9] P. Häfliger, "A spike based learning rule and its implementation in analog hardware," Ph.D. dissertation, ETH Zürich, Switzerland, 2000, http://www.ifi.uio.no/~hafliger.

[10] C. M.A. Mead, *Analog VLSI and Neural Systems*. Boston, MA, USA: Addison-Wesley Longman Publishing Co., Inc., 1989.

[11] J. A. Lenero-Bardallo, D. Bryn, and P. Hafliger, "Bio-inspired asynchronous pixel event tricolor vision sensor," *Biomedical Circuits and Systems, IEEE Transactions on*, vol. 8, no. 3, pp. 345–357, June 2014.

[12] J. A. Leñero-Bardallo and P. Häfliger, "A dual-operation-mode bio-inspired pixel," *Circuits and Systems II: Express Briefs, IEEE Transactions on*, vol. 61, no. 11, pp. 855–859, Nov 2014.

[13] Ł. Farian, J. A. Leñero-Bardallo, and P. Häfliger, "A bio-inspired aer temporal tri-color differentiator," *IEEE Biomedical Circuits and Systems Conference (BioCAS), Lausanne, Switzerland*, pp. 524–527, October 2014.

[14] J. Abrahamsen, P. Hafliger, and T. Lande, "A time domain winner-take-all network of integrate-and-fire neurons," in *Circuits and Systems, 2004. ISCAS '04. Proceedings of the 2004 International Symposium on*, vol. 5, May 2004, pp. V–361–V–364 Vol.5.

Paper III:

Ł. Farian, J.A. Leñero-Bardallo, P. Häfliger
A Time-to-First-n-Spikes and Time-out Read-out Extension to the AER Arbitration System
Second International Conference on Event-based Control, Communication, and Signal Processing, 2016

A Time-to-First-n-Spikes and Time-out Read-out Extension to the AER Arbitration System

Łukasz Farian[1], Juan A. Leñero-Bardallo[2], Philipp Häfliger[1]
[1] Nanoelectronics Group, Department of Informatics, University of Oslo, Norway
[2] Instituto de Microelectrónica de Sevilla, IMSE-CNM, CSIC and Universidad de Sevilla

E-mail: lukaszf@ifi.uio.no

***Abstract*—This paper describes extensions of the asynchronous Address Event Representation (AER) arbitration mechanism for VLSI neural networks to obtain a Time-to-First-n-Spikes (TFnS) read-out operation in addition to the standard free running read-out. The global reset of neurons can be programmed to occur after the first n spikes or after a given time-out to the first occurrence of either of these two conditions. This solution does not require any modifications inside the array of the artificial neurons, but uses only a few additional blocks in the periphery. Like the AER communication, the additional blocks also operate asynchronously, they are fully integrated with the AER communication periphery, and they do not affect the system's scalability. The extensions of the AER arbitration system are described, and supporting simulations are provided.**

I. Introduction

The Address Event Representation (AER) protocol emulates a point-to-point communication between layers of neurons. Originally AER was proposed in 1991 by Mead's Lab at California Institute of Technology [1], [2]. The AER arbitrates spikes from artificial neurons and multiplexes their x- and y-coordinates on a digital bus as a stream of digital addresses. A great variety of bio-inspired vision sensors use AER as a communication protocol, such as [3], [4], [5], to name but a few. These sensors realize artificial neuronal networks and mimic biological neural functions to process image information in a much more energy-efficient and faster way than standard digital signal processing algorithms.

One of the most relevant biological function of neural networks is a mutual inhibition; a form of direct competition between neurons. This can be regarded as a form of winner-take-all behavior where only the most excited neurons in neural network convey vital information. An example of mutual inhibition can be found inside the visual system. Thorpe [6] proposed that human selective attention use shunt inhibition performing a competing mechanism to recognize human face with a very short response latency. Human selective attention is based on saliency maps, where the selected stimuli in neuronal network is prioritized and processed first, and less important ones are inhibited, and processed later [17].

Many different implementations were proposed to mimic mutual inhibition in artificial networks, typically by using different types of winner-take-all (WTA) circuits. The first CMOS integrated circuit that realized the winner-take-all function to mimic mutual inhibition was published by Lazzaro et al [7]. The authors presented examples of fully analog

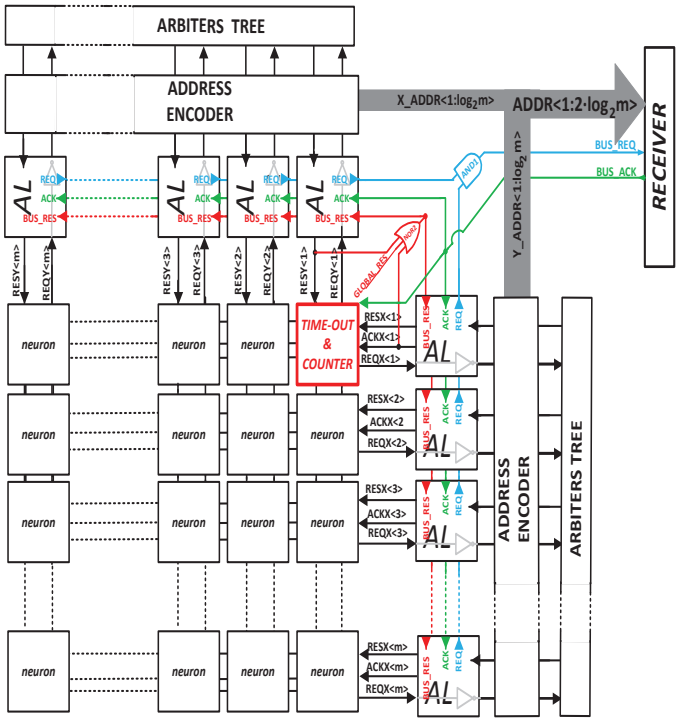

Fig. 1: A block level view of a $m \times m$ neurons array and the AER communication periphery with TFnS and time-out. Proposed additional blocks are marked in red color. *Timer&Counter* block takes the place of one neuron inside the array with address $ADDR < 1 : 2 \cdot log_2 m > 1$ and it is arbitrated like other neurons. External request and acknowledge signals pathways are marked in blue and green respectively.

compact CMOS integrated circuits that realized the winner-take-all function. The Winner-Take-All in asynchronous (AER) system can be implemented as a Time-to-First-Spike (TFS) mechanism. TFS performs a synchronous global reset of the entire array, and then registers the delay between that reset and the time of the first spike for each neuron. There are many examples of vision sensors using Time-to-First-Spike mechanism to process images [8], [9], [10], to name but a few. For instance, Massari et al. [8] built a Time-to-First-Spike

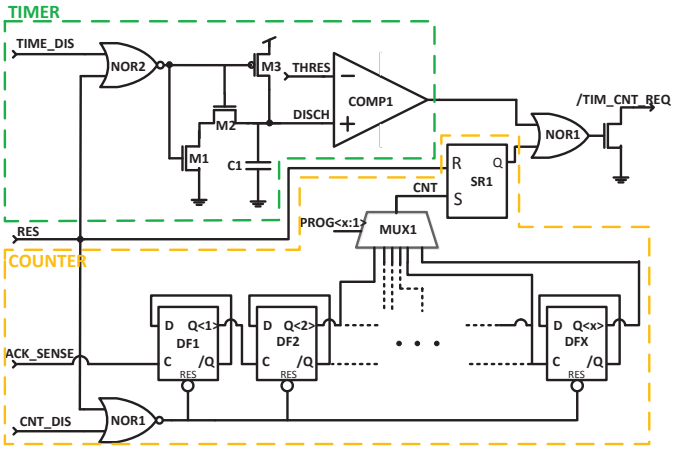

Fig. 2: Schematic of *Timer&Counter* block.

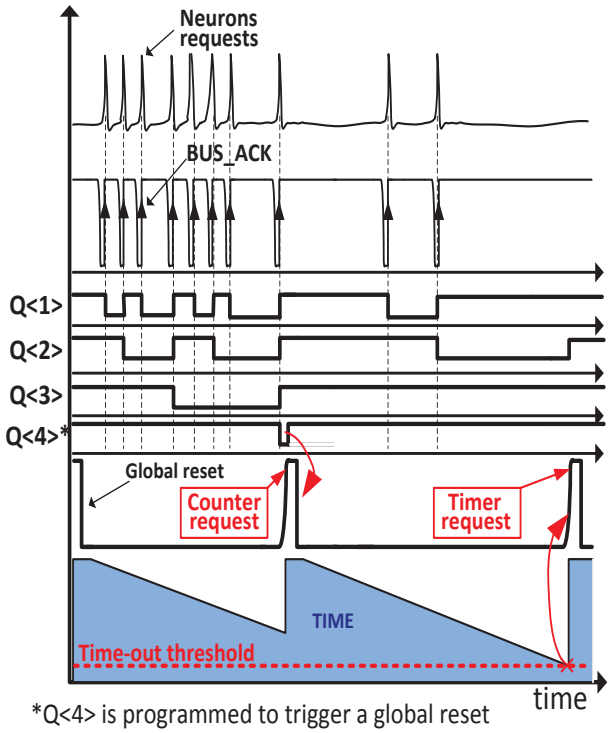

Fig. 3: A time diagram illustrates dependencies between BUS_ACK, *Counter* and *Timer*. The *Timer&Counter* counts number of transitions of BUS_ACK. *Timer&Counter* is rising edge triggered.

camera which detects the most illuminated pixel and transmits its address. Another sensor [9] used a Time-to-First-Spike mechanism to reconstruct time delays of the single spikes from pixels into a light illuminance. TFS operation in [8], [9] and [10] was achieved by adding additional logic inside each pixel, which is not efficient in terms of silicon area.

In this paper we explain how to modify the AER peripheral circuitry to obtain extended TFS function without adding any logic to the array of the artificial neurons, only using a few additional blocks outside the neural network. For some applications, it is desirable to be able to adjust number of winners and the time limit when winners should be resolved. For instance, in a previous work [11], we described a concept of an asynchronous Sun sensor, which uses a WTA selection to indicate a relative position of Sun. Adjustable number of winners and a timer allows pixels organized in 1-D pixel vectors to adapt to the different lighting conditions, what helped to find a correct position of the Sun, and reject spurious readouts. For more details refer to [11]. In this paper, we will describe in details modifications of the original AER communication framework to obtain a Time-to-First-n-Spikes (TFnS) read-out and a Time-to-First-n-Spikes with time-out read-out. The number of winners is adjustable, and the timeout is controlled by an analog input. In our approach WTA selection is implemented asynchronously, and the extension is an integral part of the AER logic.

This article is organized as follows: Section II describes modifications of the original AER arbitration system, and how these modifications can be integrated with the AER framework to obtain above mentioned functionalities. Section III provides the system simulation results in AMS $0.35\mu m$ CMOS process. Finally, Section IV draws some conclusions and possible applications.

II. System Concept and Design

Fig. 1 shows a $m \times m$ neurons array and the new blocks to extend the AER functionality to provide TFnS and time-out modes. We used a version of the arbitration system proposed by Häfliger [12], however other arbitration systems can be extended as well [13]. A typical AER system consists of *Neurons*, *Arbiter Logic (AL)*, *Arbiters Cells* and *Address Encoders*. *Neurons* are the electronic circuits which incorporate some functional properties of biological neurons [14]. Each neuron has its unique address in a two-dimensional plane. *Arbiter Logics* (AL) circuitry works as a mediator between the neurons, the arbiter-cells and the external receiver. AL passes the request signals from neurons to *Arbiters Cells*. *Arbiters Cells* are stacked to build up an *Arbiters Tree* structure to perform arbitration between neurons and grant exclusive acknowledge signals to them. The *Neurons* which are acknowledged send their addresses through *Address Encoders*.

A. AER Logic Extensions

We will now focus on the modifications, highlighted in red in Fig. 1, which we propose to obtain TFnS and/or time-out read-outs.

1) ***Timer&Counter****:* This block is located in the top right corner of the neurons array in Fig. 1 with coordinates (1,1). It is arbitrated like other neurons. The schematic of *Timer&Counter* is shown in Fig. 2. It performs different tasks than standard neurons. Fig. 3 shows an operation of Timer&Counter. It illustrates the dependencies between BUS_ACK, frequency dividers outputs (*Counter*) and the voltage at capacitor C1 (*Timer*). The operation starts with a global reset signal BUS_RES, highlighted by a red line in Fig. 1. BUS_RES signal enters all Arbiter Logics and forces all neurons to reset. The global reset occurrence is flagged by the address of the *Timer&Counter* $ADDR < 1 : 2 \cdot log_2 m >= (1, 1)$. The cycle

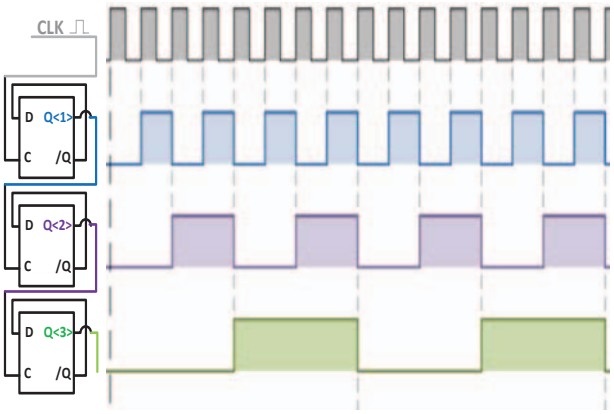

Fig. 4: Series of three D-type flip-flops working as a frequency divider. Each flip-flop divides the frequency of a square-wave CLK pulse by a factor of 2.

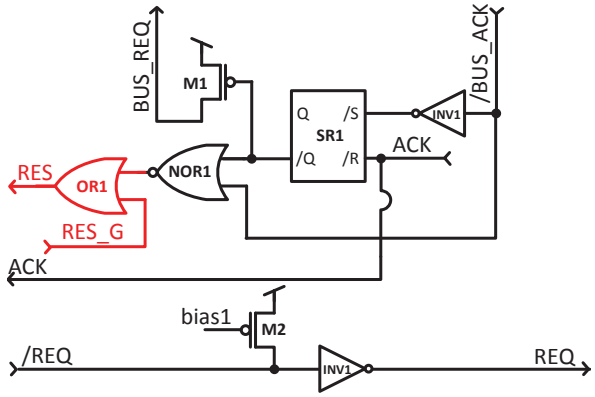

Fig. 5: The arbiter logic circuit *AL* is the mediator between the neurons, the arbiter-cell-tree and the receiver. Compared to the original design [12], an additional OR1 gate is used to initiate the global reset for TFnS mode.

of TFnS begins when the global reset is released and neurons are allowed to send requests. This is illustrated in top plot in Fig. 3. The two bottom plots illustrate the *Counter* register and the *Timer* countdown. Every pulse of a BUS_ACK signal indicates one neuron spike. The rising transition of BUS_ACK increments the counter register. After eight spikes, the counter reaches its threshold and it initiates a global reset, so the next cycle of TFnS can start. During the next cycle in Fig. 3 the global reset is triggered by a timer, because only two neurons spiked.

A detailed structure of *Timer&Counter* is shown in Fig. 2. The *Counter* part consists of the series of D-type flip-flops DF1-DFX working as a frequency divider counter. When the external acknowledge BUS_ACK signal toggles, the rising edge of this signal increases the flip-flop counter register. This is illustrated in Fig.4. Since each flip-flop divides the frequency of the input square-wave by a factor of 2, this counter allows to detect powers of two (2^x) transitions. The outputs of these flip-flops are multiplexed by a mixer MUX1, and one output

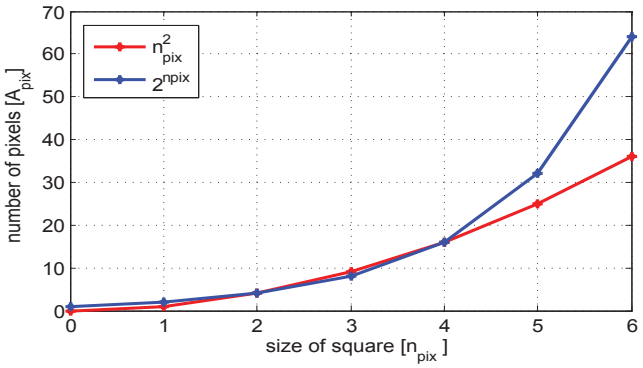

Fig. 6: For a small number of pixels we can approximate: $2^{npix} \approx n_{pix}^2$.

can be chosen by a binary word PROG<x:1>, so the number of winning pixels can be programmed.

The *Timer* circuit consists of a stretched length transistor M1 from Fig. 2 and capacitor C1. Transistor M1 discharges the capacitor C1 until the threshold of the comparator COMP1 is reached, as illustrated in bottom Fig. 3 The time which takes to discharge the capacitor C1 is the time-out. The time-out is controlled by an analog input voltage node *THRESH*, and can be set between range of microseconds and seconds. Transistors M2 and M3 recharge the capacitor C1 to restart the time countdown.

The *Counter* and *Timer* outputs are connected to the nor gate NOR1 in Fig.2. Hence, either *Counter* or *Timer* initiates a request (TIM_CNT_REQ) and further a global reset, after a specific number of winners or a specific time interval.

*2) **Additional logic**:* there are two additional logic gates added to the AER arbitration system. There is one additional nor gate NOR2, marked in red in top right corner in Fig. 1. It distributes a global reset signal BUS_RES. Another additional OR1 gate is placed inside the arbiter logic circuits *AL* (Fig.5) and it receives an input from BUS_RES to initialize a global reset of the entire array.

B. Powers of Two as a Number of Winners

Typically, neurons activities in a two-dimensional neuronal networks follow a Gaussian spatial distribution centered around the neuron with the highest activity. Two-dimensional Gaussian distribution is given as:

$$f = A \cdot exp(-(\frac{(x-x_o)^2}{2\sigma_x^2} + \frac{(y-y_0)^2}{2\sigma_y^2})) \qquad (1)$$

where σ_x and σ_y are their standard deviations, A is the amplitude coefficient, x_o, y_o are the coordinates of the peak. If we assume that both standard deviations are equal $\sigma_x = \sigma_y$, the region with the most excited neurons is defined by a circle with the center (x_o, y_o). The area of the circle is a quadratic function of its radius. Hence programming the number of winners given as powers of two is equivalent to define the area where the most active neurons can spike. Fig. 6 shows that area described by both functions are similar: $n_{pix}^2 \approx 2^{pix}$ for $n_{pix} < 6$. Fig. 7 illustrates that the area with the most excited neurons is defined as a circle with center at the coordinate (12,12). Two

TABLE I: Interface signals controlling the AER read-out modes.

TIME_DIS	CNT_DIS	GLOB_RES	MODE
0	0	0	TFnS + time-out
1	0	0	TFnS
0	1	0	time-out
1	1	0	normal mode
X	X	1	neurons in reset

horizontal planes with area of 2^4 and 2^6 show the distribution of the most active neurons, where the darkest shade of grey indicates most active ones.

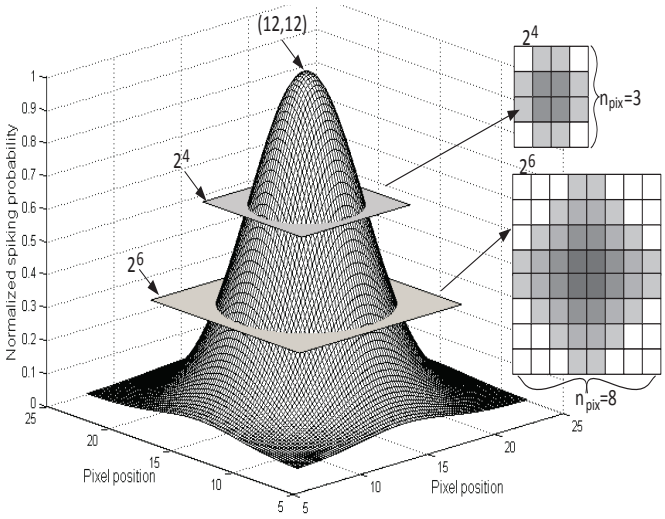

Fig. 7: Two-dimensional Gaussian distribution shown as a 3D plot. Horizontal planes show neurons addresses, the third dimension shows a normalized spiking frequency.

C. Operation Modes

Table I shows interface signals and summarizes all available modes the AER system can work. There are four modes available: TFnS, TFnS+time-out, time-out, and continuous mode. In the continuous mode, all the additional functionalities are turned off, and the AER read-out the neurons spikes in standard continuous way [15]. Array of neurons can be forced to reset by GLOB_RES.

D. Other AER variants

We used a version of the arbitration system proposed by Häfliger [12], however the modifications we describe in this work can extend other arbitration systems as well [13]. Boahen's [13] arbitration system use ACK signals to reset neurons. In order to use our proposed arbitration system with Boahen's variant, the OR gate from Fig. 5 should be connected to the ACK signal instead.

III. Simulation Results

The modified AER system was simulated in the AMS $0.35\mu m$ CMOS process. Fig. 8 shows the test array of 4×4

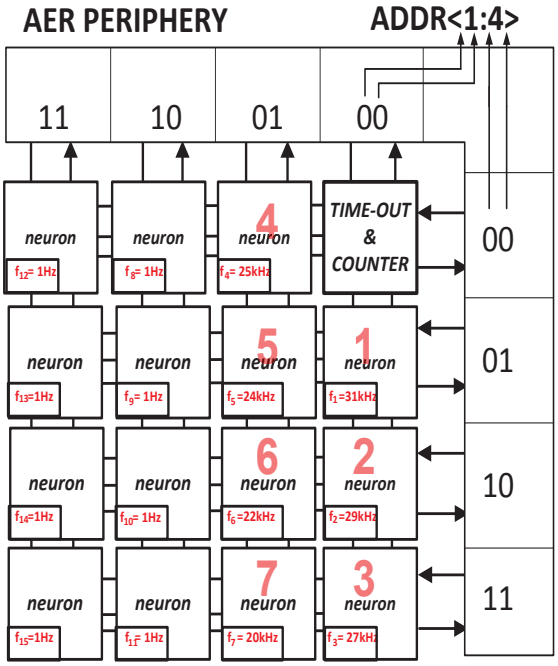

Fig. 8: A test array of 4×4 neurons, integrated wth the AER communication periphery. Neurons spiking frequencies are provided, numbers indicate the spiking order.

neurons integrated wth the AER communication periphery. Neurons were modeled as $I\&F$ structures [16]. I&F neuron receives stimulus at its input (equivalent to a biological dendrite), it integrates it at the soma, and it generates spikes with a frequency proportional to the stimulus. The spiking frequencies of each neuron is marked in the test array in Fig. 8.

First, the AER was configured to read the neurons in TFnS mode with a limit of 8 winners. Fig. 9 shows resulting asynchronous sequence of handshake signals between neurons, the AER periphery and receiver. The membrane potentials of nine most excited neurons are shown in top plot in Fig. 9 as Membrane<1:9> . When the integrated voltage at the neuron's membrane reaches a threshold, the neuron fires. The REQ signal initiates a propagation of handshake signals indicated by red arrows: if the neuron request is acknowledged by the arbiter cell tree, it is granted an access to the bus, and the external request is sent off-chip by BUS_REQ. At the same time, the winning neuron puts out its address on the output bus address ADDR<1:4>, and if it is acknowledged, the neuron is reset. The neurons addresses are encoded as ADDR<1:4>=$xxyy$, where xx and yy are the x- and y-plane addresses respectively. Seven consecutive most active neurons spike in order starting from the most active one, and the handshake repeats 7 times. Q<1> to Q<4> show the current state of the *Counter*, as it was illustrated in Fig.4. The *Counter* is rising edge triggered, such that every rising edge of BUS_ACK increments it. Fig. 10 shows a closer look at the same signals from Fig. 9 when the global reset is triggered by *Timer&Counter* block. Q<4> was programmed to trigger a global reset. When the signal Q<4> toggles down it initiates a global reset of all neurons, and the flip-flops inside the *Counter* (Q<1> to Q<4>). Then, next cycle of TFnS starts. The bus addresses ADDR<1:4>

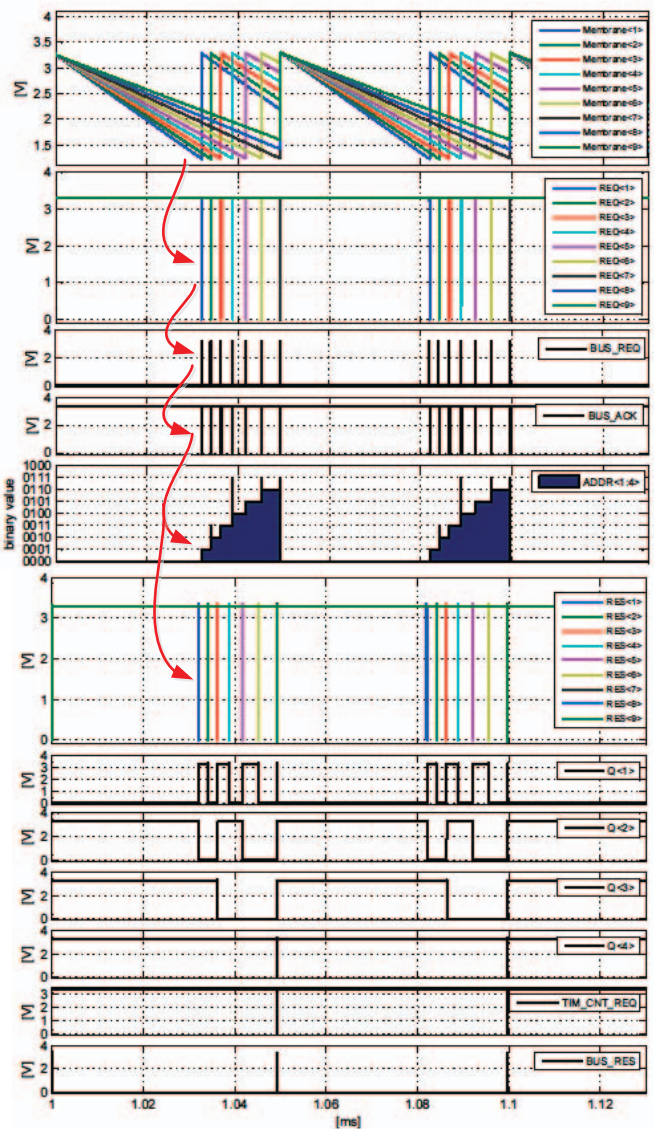

Fig. 9: Asynchronous sequence of handshake signals between neurons, AER periphery and receiver for a TFnS mode. From top: membrane potentials of first 9 I&F neurons, their corresponding request signals REQ<x>, external signals BUS_REQ and BUS_ACK, address ADDR<1:4> at the digital bus, neurons' reset signals RES<x>, 4 counters states Q<1> to Q<4>, *Timer&Counter* request and global reset BUS_RES.

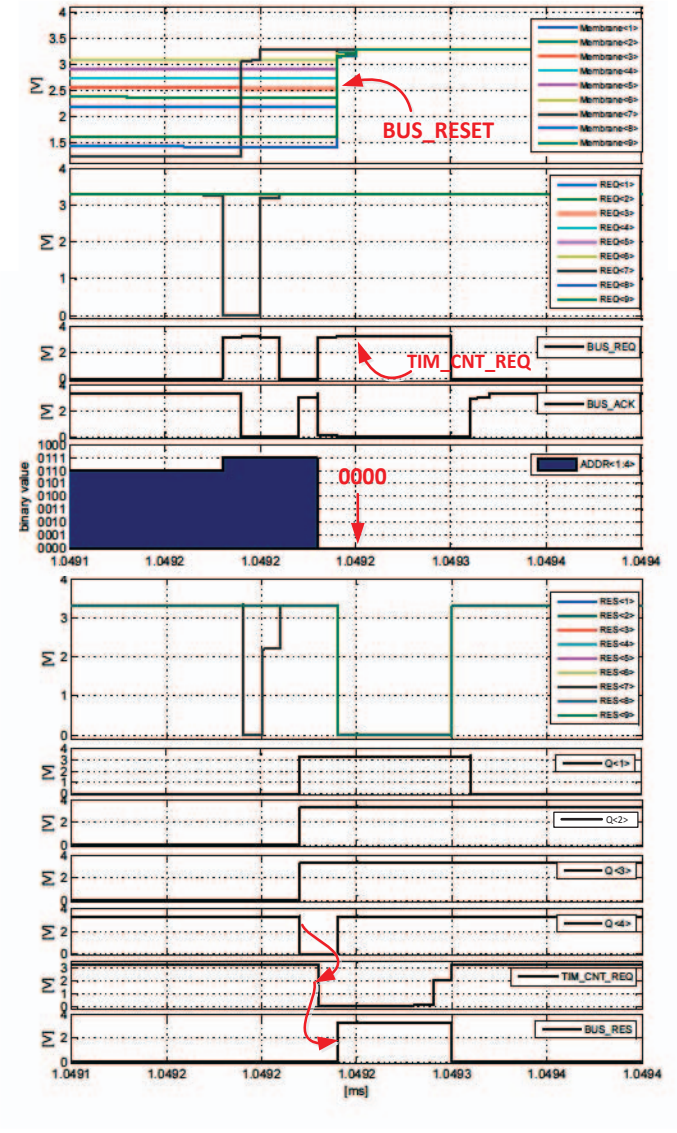

Fig. 10: A closer look at the signals from Fig. 9.

provide a stream of coordinates of the seven winning neurons in decreasing order of their spiking frequencies. The address '0000' indicates the occurrence of a global reset.

Fig. 11 shows an asynchronous sequence of handshake signals for the AER logic configured to read the neurons in time-out mode. The *Counter* was disabled, and the *Timer* was enabled with a time-out programmed to $40\mu s$. Voltage $DISCH$ shows a discharge rate of the *Timer* by a constant current from transistor M1 from Fig. 2. After $40\mu s$ the voltage at the node $DISCH$ reaches a comparator threshold *THRES*, what initiates a global reset BUS_RES of all neurons and the *Timer*.

Only three neurons fired, before a time-out from the *Timer* initiated a global reset of the array, and the next cycle of time-out started. The bus addresses ADDR<1:4> provided a stream of coordinates of the three most excited neurons which spiked within programmed time interval. The occurrence of the periodical time-out reset BUS_RES was flagged by the address '0000'.

IV. Conclusions

We have proposed simple blocks with a low area requirements to be added to extend a free running, individual pixel reset AER arbitration system into a global reset, time-to-first-n-spikes AER arbitration. The global reset can be programmed to occur after the first n spikes or after a given time-out to the first occurrence of either of these two conditions. This solution is practical for processing saliency maps or for implementing soft WTA, e.g. when emulating human selective attention or

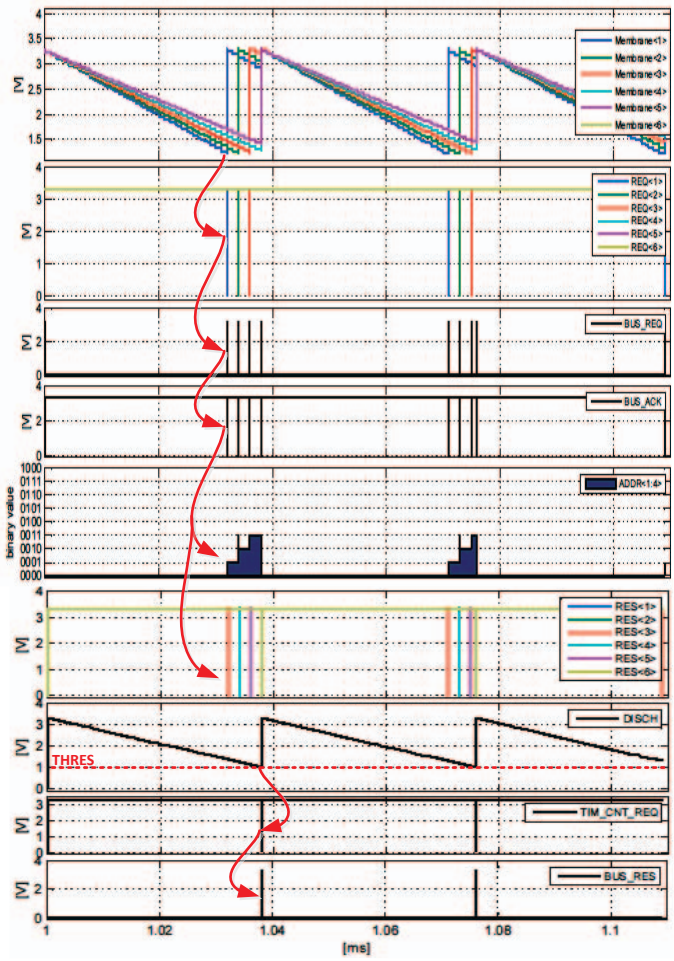

Fig. 11: Asynchronous sequence of handshake signals between neurons, AER periphery and receiver with time-out mode. From top to bottom: membrane potentials of first 6 I&F neurons, their corresponding request signals REQ<x>, external signals BUS_REQ and BUS_ACK, address ADDR<1:4> at the digital bus, neurons' reset signals RES<x>, state of the *Timer*, *Timer&Counter* request and global reset BUS_RES.

in image processing proposed by Thorpe. Furthermore, the proposed extensions can be turned off to allow continuous operation without limiting the number of winners. The proposed additional timers and counters operate asynchronously, which makes the extensions scalable and fully integrated with the asynchronous AER arbitration system. Simulation results in the AMS $0.35\mu m$ CMOS process were provided.

REFERENCES

[1] M. Silvilotti, "Wiring considerations in analog vlsi systems with application to field-programmable networks," Ph.D. dissertation, Cal. Inst. of Tech., Pasadena, California, 1991.

[2] M. A. Mahowald, "VLSI analogs of neuronal visual processing: a synthesis of form and function," *Computation and Neural Systems, Caltech, Pasadena, California*, pp. 27–44, 1992.

[3] J. A. Leñero-Bardallo and P. Häfliger, "A dual operation mode bio-inspired vision sensor," in *Biomedical Circuits and Systems Conference (BioCAS), 2013 IEEE*, Oct 2013, pp. 310–313.

[4] J. Leñero Bardallo, D. Bryn, and P. Häfliger, "Bio-inspired asynchronous pixel event tricolor vision sensor," *Biomedical Circuits and Systems, IEEE Transactions on*, vol. PP, no. 99, pp. 1–1, 2013.

[5] Ł. Farian, J. A. Leñero-Bardallo, and P. Häfliger, "A bio-inspired aer temporal tri-color differentiator pixel array," *IEEE Transactions on Biomedical Circuits and Systems*, vol. 9, no. 5, pp. 686–698, Oct 2015.

[6] S. Thorpe, D. Fize, and C. Marlot, "Speed of processing in the human visual system." *Nature*, vol. 381, p. 520, 1996.

[7] J. Lazzaro, S. Ryckebusch, M. Mahowald, and C. Mead, "Winner-take-all networks of o(n) complexity," vol. 1, 1988.

[8] N. Massari, S. A. Jawed, and M. Gottardi, "A collision-free time-to-first spike camera architecture based on a winner-take-all network," in *Circuit Theory and Design, 2007. ECCTD 2007. 18th European Conference on*, Aug 2007, pp. 950–953.

[9] X. Qi, X. Guo, and J. G. Harris, "A time-to-first spike cmos imager," in *Circuits and Systems, 2004. ISCAS '04. Proceedings of the 2004 International Symposium on*, vol. 4, May 2004, pp. IV–824–7 Vol.4.

[10] J. A. Leñero-Bardallo, T.Serrano-Gotarredona, and B. Linares-Barranco, "A five-decade dynamic-range ambient-light-independent calibrated signed-spatial-contrast aer retina with 0.1-ms latency and optional time-to-first-spike mode," *Circuits and Systems I: Regular Papers, IEEE Transactions on*, vol. 57, no. 10, pp. 2632–2643, Oct 2010.

[11] Ł. Farian, P. Häfliger, and J. A. Leñero-Bardallo, "Miniaturized sun sensor with in-pixel processing for attitude determination of micro space probes," in *Event-based Control, Communication, and Signal Processing (EBCCSP), 2015 International Conference on*, June 2015, pp. 1–6.

[12] P. Häfliger, "A spike based learning rule and its implementation in analog hardware," Ph.D. dissertation, ETH Zürich,Switzerland, Sunderlan, 2000.

[13] K. A. Boahen, "Point-to-point connectivity between neuromorphic chips using address events," *IEEE Trans. Circuits Syst. II*, vol. 47, no. 5, pp. 416–434, 2000.

[14] D. P. M. Northmore and J. G. Elias, "Evolving synaptic connections for a silicon neuromorph," in *Evolutionary Computation, 1994. IEEE World Congress on Computational Intelligence., Proceedings of the First IEEE Conference on*, Jun 1994, pp. 753–758 vol.2.

[15] J. A. Leñero-Bardallo, D. Bryn, and P. Häfliger, "Bio-inspired asynchronous pixel event tricolor vision sensor," *Biomedical Circuits and Systems, IEEE Transactions on*, vol. 8, no. 3, pp. 345–357, June 2014.

[16] E. Culurciello, R. Etienne-Cummings, and K. Boahen, "A biomorphic digital image sensor," *Solid-State Circuits, IEEE Journal of*, vol. 38, no. 2, pp. 281–294, Feb 2003.

[17] D. Sonnleithner and G. Indiveri, "A neuromorphic saliency-map based active vision system," in *Information Sciences and Systems (CISS), 2011 45th Annual Conference on*, March 2011, pp. 1–6.

Paper IV:

J.A. Leñero-Bardallo, J.M. Guerrero-Rodríguez, Ł. Farian, R. Carmona-Galán, Á. Rodríguez-Vázquez
A sun sensor implemented with an asynchronous luminance vision sensor
IEEE European Solid State Circuits Conference, 2017

A sun sensor implemented with an asynchronous luminance vision sensor

J. A. Leñero-Bardallo
and J. M. Guerrero-Rodríguez
Escuela Superior Ingeniería
Universidad de Cádiz
Avda. Universidad de Cádiz 10
Puerto Real 11519, Spain
Emails: {juanantonio.lenero,
,josem.guerrero}@uca.es

L. Farian
Nanoelectronics Group
Department of Informatics
University of Oslo
Blindern 1072
Oslo, Norway
Email: lukaszf@ifi.uio.no

R. Carmona-Galán and
Á. Rodríguez-Vázquez
IMSE-CNM,
CSIC-Universidad de Sevilla
Av/ Américo Vespucio s/n,
41092, Seville, Spain
Emails: {rcarmona,
angel}@imse-cnm.csic.es

***Abstract*—A sun sensor implemented with a spiking pixel matrix is reported. It is the very first one based on an asynchronous event-based pixel array. A paradigm associated to classic digital sun sensors is solved with this approach. Only pixels illuminated by the sun light are readout. Hence, the output data flow is quite reduced. The computational load to resolve the sun position is quite low, comparing to prior sensors. Sensor's latency is in the order of milliseconds. The advantages over implementations with APS pixels are more reduced data flow, less latency, and higher dynamic range.**

Keywords: Sun sensors, AER, Attitude determination, Event-based vision sensors, Space probes.

I. Introduction

Sun sensors are devices on demand to determine the sun position. They have multiple applications. For instance, solar power plants need to know precisely it to adjust accordingly the position of solar cells or heliostats. Sounding rockets and spacecrafts use the sun position to navigate. In this case, fast operation and low power consumption are mandatory. There are two main kinds of sun sensors: analog and digital. Analog sun sensors [1], [2] usually use two different photoactive regions to sense two different photocurrent values. The ratio between them, depends on the sun inclination. They have fast operation and low output data flow. Unfortunately, they are sensitive to mismatch and distractors. Digital sun sensors [3], [4] are built with an image sensor with APS pixels. The entire pixel matrix is readout. Then, the output data is processed to compute the sun position. Digital sun sensors overcome some of the limitations of analog ones, but still they have inherent drawbacks. Although there is a very low number of illuminated and meaningful pixels, the entire pixel matrix has to be readout and processed. This limits the operation speed and increases the computational time. Also, the choice of the integration time complicates the sensor operation. The dynamic range is usually limited to 60-70dB. To amend some of the aforementioned limitations, some authors have presented approaches based on the determination of a Region of Interest (ROI) whith the illuminated pixels, that are readout and processed. However, to determine the ROI requires to readout pixels that are dark and not meaningful. In this article, a new approach based on an asynchronous event-based pixel vision sensor is presented. Only illuminated pixels can send information out of the sensor. There is no need of choosing an integration time to operate. Reading out only one single pixel output, it is possible to resolve the sun position. Furthermore, sensor's dynamic range is higher than in conventional digital sensors with APS pixels.

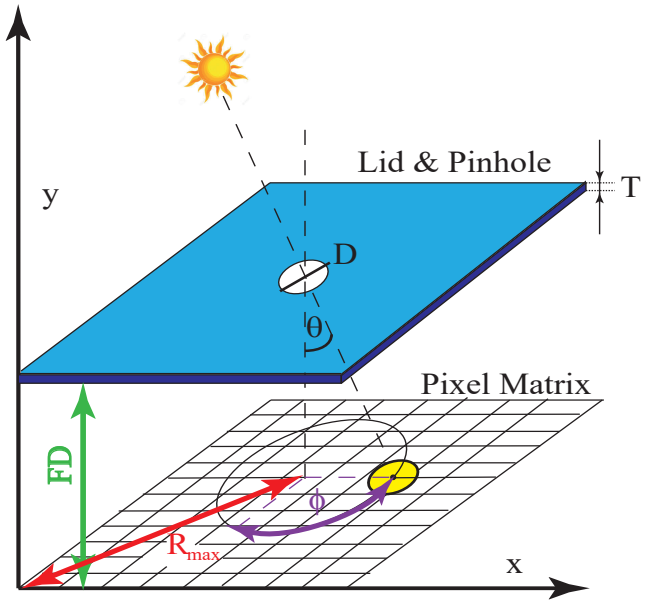

Fig. 1. System implementation sketch. There is a pixel array covered by an opaque lid with a pinhole in its center. Only a reduced number of pixels are illuminated through the pinhole by the sun light projection. Depending on the sun inclination with the sensor's vertical axis, different pixels will be illuminated.

II. System Implementation

Fig. 1 depicts how the optics is arranged. The chip is covered with an opaque lid with a pinhole lens [3], [4]. The sun light illuminates different groups of pixels, depending on the sun position. It is possible to express the latitude, θ, and

978-1-5090-5025-3/17/$31.00 ©2017 IEEE

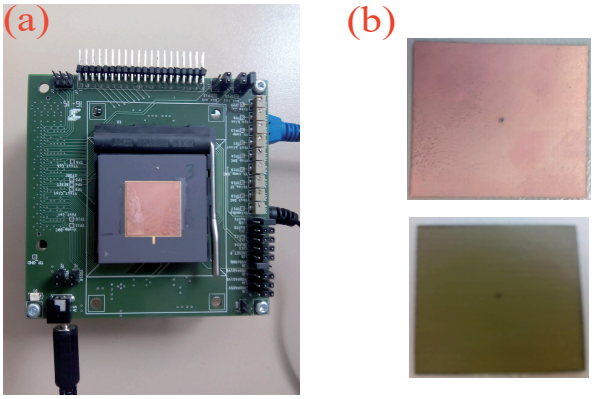

Fig. 2. (a) Sensor's front view. Dimensions are 9.5cm×9.5cm. (b) Detail of the lid with a pinhole. The side that faces the sun is metallic to reflect the sun radiation. The side that is directly over the chip is anti-reflective. Lid dimensions are: Thickness: T=100µm, Width=Length=20mm, Pinhole radius=50µm, Focal Distance: FD=0.6mm.

the azimuth, ϕ, as a function of the illuminated pixels centroid, (x, y), and the design parameters shown in Fig. 1:

$$\theta = arctan\left(\frac{\sqrt{W\cdot(x-x_c)^2 + L\cdot(y-y_c)^2}}{FD}\right) \quad (1)$$

$$\phi = arctan\left(\frac{L\cdot(y-y_c)}{W\cdot(x-x_c)}\right) \quad (2)$$

Where (x_c, y_c) is the centroid of the ROI (center of the illuminated region) when $\theta = 0°$. W=25µm and L=25µm are the pixel width and length, respectively. FD=0.6mm is the focal distance, i.e. the distance between the pixel array and the lid.

Fig. 2.(a) displays the system implementation and its optics. The chip is covered with a lid (Fig. 2.(b)) with a radius of 50µm. The lid is anti-reflective on the side that is facing the sensor and reflective on the other side.

For the implementation of this solar sensor, we chose an asynchronous HDR image sensor already reported elsewhere [5], [6]. The sensor has high dynamic range and several operation modes. It was specially intended to operate under high illumination conditions, being specially suitable for the design of a sun sensor that can be exposed to direct sunlight. Its pixels can be configured to pulse with a frequency proportional to the local illumination. Fig. 3 depicts the pixel schematics when it is configured to perform a light to frequency conversion. There is a block that generate pulses with a frequency proportional to illumination. These pulses activate a sequence of asynchronous communication signals to transmit off-chip the coordinates of the pixel that has fired every time that this occurs.

The light-to-frequency conversion block is an astable oscillator. Its operation period is approximately given by:

$$f_{osc} \approx \frac{I_{ph}}{C_{ph}\cdot(V_{DD}-V_{bot})} = \frac{I_{ph}}{C_{ph}\cdot\Delta V} \quad (3)$$

The event rate can be controlled by adjusting the bias voltage V_{bot}. Pixel transistors have thick gate oxide to allow higher values of ΔV and reduce the event flow in conditions of very illumination. Power supply was set to 5V.

III. Experimental Results

We programmed on the jAER interface [7] a real time algorithm to compute the illuminated pixels centroid and determine the sun position according Equations 1 and 2. Fig. 4 shows the illuminated pixels with the sensor operating.

To calculate the centroid, we apply this simple algorithm periodically:

1) We wait until a certain number of events, $N_{events} \geq 1$, are received. In the meantime, the coordinates of the pixels that fire (x_i, y_j) are stored on a memory.
2) Once the event number is equal to N_{events}, we compute the centroid coordinates.

$$x = \frac{1}{N_{events}}\cdot\sum_{i=1}^{N_{events}} x_i,\ y = \frac{1}{N_{events}}\cdot\sum_{j=1}^{N_{events}} y_j \quad (4)$$

3) Once the centroid, (x, y) is known, the sun position is determined according to Equations 1 and 2.
4) The event counter is reset, $N_{events} = 0$, and the computation is finished. To calculate the sun position again, go to step #1.

To evaluate the sensor performance, we moved quickly in front of the sensor a light beam modelling the sunlight. The y-coordinate was almost constant while the x-coordinate was changing during the experiment. In Fig. 5, we have plotted the sensor transient response. In Fig. 5.(a) we show the recorded events over time. In Fig. 5.(b), there are the computed angles (θ, ϕ) for each computed centroid value at time stamps of 5ms. Results are consistent with Equations 1 and 2.

Time-to-first-spike (TFS) operation [8], [9] is possible. To implement it, the centroid position is computed after receiving a programmable number of events, N_{events}. Then, the sensor is reset and kept idle, enabling the signal $\overline{RES}$ in Fig. 3, until the sun position needs to be determined again. In Fig. 6, we display the sensor performance in TFS mode for different number of events. We observe that is possible to determine the sun position, with an acceptable error, after receiving one single event. Results are improved if the number of events is increased. With $N_{events} = 100$, angles (θ, ϕ) computation error is lower than 0.5°.

The event rate is proportional to illumination and the comparators voltage threshold, ΔV, in Equation 3. In Fig. 7 the measured event rates for different values of the pixel illuminance, with ΔV =0.5V, are plotted. There is a trade-off between speed and output data flow. The user can trade off between these parameters depending on illumination levels. The measured pixel event sensitivity is $S = 0.0762 events/\Delta V \cdot lux$, with $\Delta V = V_{DD} - V_{bot}$. Under typical application scenarios with direct sunlight, the system employs a few milliseconds to compute the sun position.

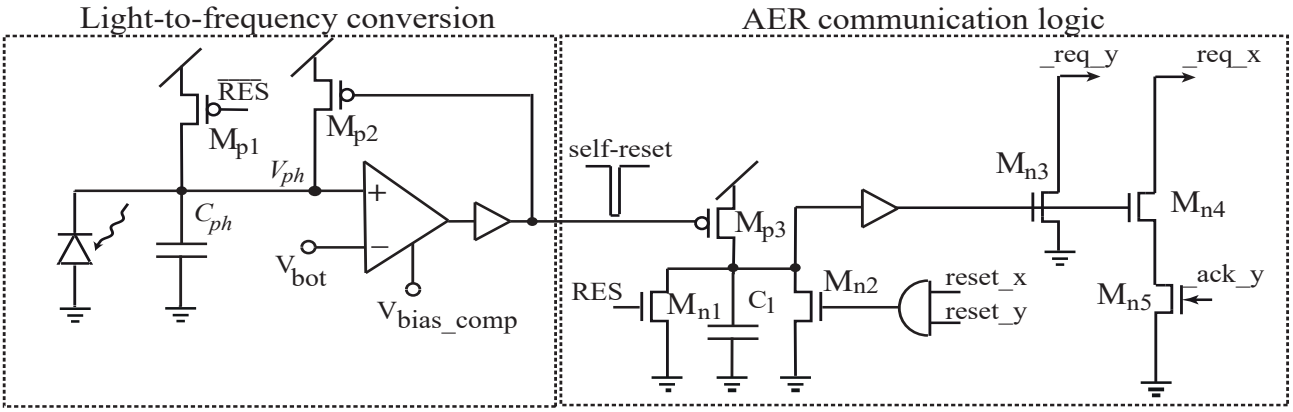

Fig. 3. Pixel schematics. There is circuitry to perform a light to frequency conversion and logic to handle the asynchronous AER communication. Transistor sizes are (W/L, µm/µm): M_{p1}=1/1. M_{p2}=3/1. M_{p3}=0.5/1. M_{n1}=0.5/0.7. M_{n2}=0.7/0.7. M_{n3}=1/0.7. M_{n4}=M_{n5}=0.5/0.7. C_{int} = C_1 =40fF, C_{ph} =5fF. Bias voltages: V_{bot} =1V, V_{bias_comp} =4.3V.

TABLE I
SYSTEM FEATURES AN STATE-OF-THE-ART COMPARISON.

Work	**This Work**	Ning et al. [3]	Galileo ESA [4]	Ortega et al. [1]
Type	Event Based Luminance Sensor	APS Digital Sensor	APS Digital Sensor	Analog Sun Sensor
Technology	AMS 0.18µm HV	0.18µm 1P4M	UMC 0.18µm	ND
Number of Pixels	128×96	368×368	512×512	2 pairs of photodiodes
Pixel Pitch	25µm× 25µm	6.5µm×6.5µm	11µm×11µm	NA
FOV	**146°**	94°	128°	120°
Power Consumption	52mW	42.73mW	520mW	ND
Latency	**<5ms@1klux**	10frames/s	10frames/s	NA
Dynamic Range	**>100dB**	52dB	ND	NA
Resolution	0.03°	0.004°	<0.005°	ND
Accuracy	0.0132°(θ), 0.05°(ϕ)	0.01°	0.024°	0.15°
Amount of data	**1-100 Events**	945pixels	1 frame + ROI	4 analog voltages to be readout

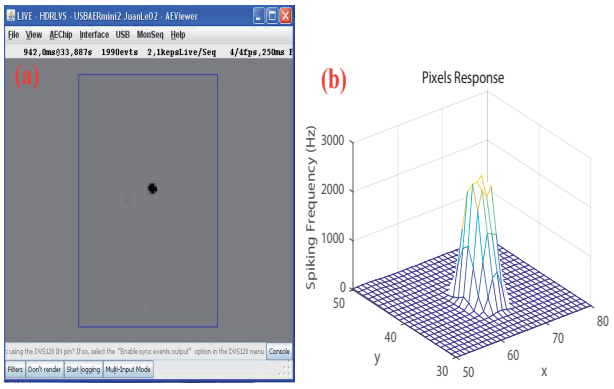

Fig. 4. (a) jAER interface [7] to debug and display the sensor information. The black speckle corresponds to the illuminated region with the sensor operating. (b) Measured spiking frequencies around the illuminated region of interest (ROI).

Table I compares the sensor features against the art. The amount of data required to compute the sun position is lower than in prior devices based on APS pixels. With only one event, it is possible to achieve competitive results in terms of resolution and accuracy. Latency is much lower. The dynamic range is also higher than the obtained with APS image sensors. The resolution and the accuracy could be improved in further designs by implementing a dedicated pixel for a solar sensor and by refining the optics.

IV. CONCLUSIONS

A new sun sensor concept has been presented. It is the very first one that employs a asynchronous pixel matrix whose pixels only send information when they are illuminated. This new approach solves a paradigm traditionally associated to digital sun sensors: pixels that are dark have to be readout. As a result, the output data flow is much more reduced and the operation is faster. The sun position can be resolved with a latency of milliseconds by reading out a reduced number of pixels. In TFS mode, with only the information coming from one single pixel, the sun position can be determined.

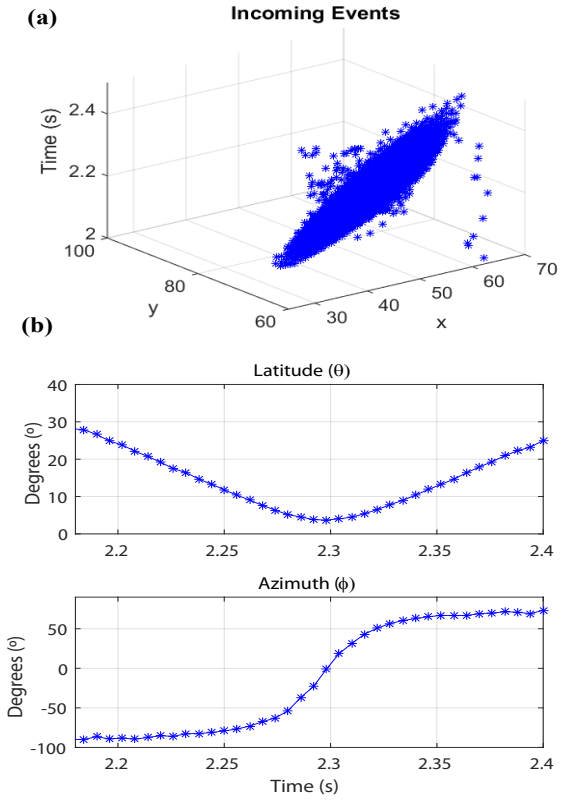

Fig. 5. Sensor's measured transient response. A light beam facing the sensor was rotated to emulate the sun movement. (a) Raster plot: Recorded events versus time. (b) Computed angles (θ, ϕ) at time stamps of 5ms indicating the light source position.

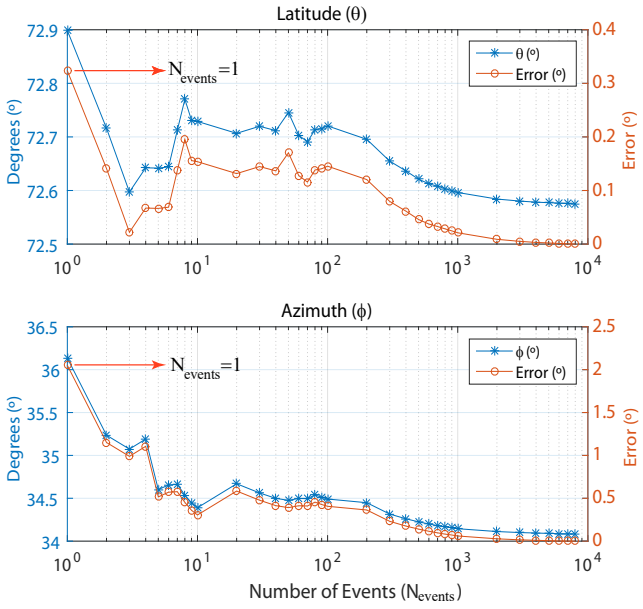

Fig. 6. TFS operation. After reseting the sensor, a certain number of events is received and the sun position is computed. We plot the computed angles (θ, ϕ) and the measurement error for different number of incoming events. With only one event, it is possible to gauge the sun position keeping the error low.

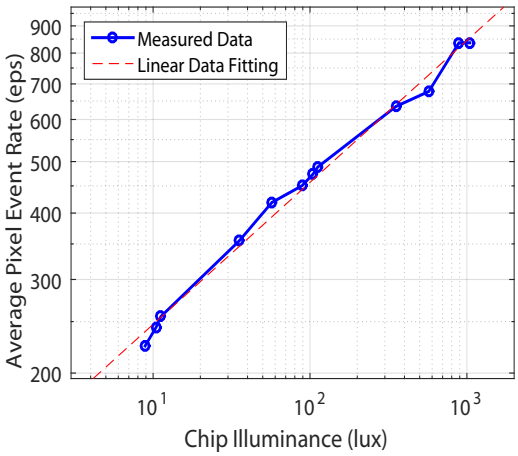

Fig. 7. Blue Trace: measured event rate versus illumination for different chip illuminance values with $\Delta V = V_{DD} - V_{bot}$ =0.5V. Red trace: linear data fitting.

V. Acknowledgements

This work was supported in part by the University of Cádiz under Grant PR2016-072; in part by the Spanish Ministry of Economy and Competitiveness under Grant TEC2015-66878-C3-1-R, Co-Funded by ERDF-FEDER; in part by Junta de Andalucía CEICE under Grant TIC 2012-2338 (SMARTCIS-3D); and in part by ONR under Grant N000141410355 (HCELLVIS).

References

[1] P. Ortega, G. Lopez-Rodriguez, J. Ricart, M. Dominguez, L. M. Castaner, J. M. Quero, C. L. Tarrida, J. Garcia, M. Reina, A. Gras, and M. Angulo, "A miniaturized two axis sun sensor for attitude control of nano-satellites," *IEEE Sensors Journal*, vol. 10, no. 10, pp. 1623–1632, Oct 2010.

[2] A. Ali and F. Tanveer, "Low-cost design and development of 2-axis digital sun sensor," *Journal of Space Technology*, vol. 1, no. 1, pp. 1–5, Junel 2011.

[3] N. Xie and A. J. P. Theuwissen, "A miniaturized micro-digital sun sensor by means of low-power low-noise CMOS imager," *IEEE Sensors Journal*, vol. 14, no. 1, pp. 96–103, Jan 2014.

[4] F. Boldrini, E. Monnini, D. Procopio, B. Alison, W. Ogiers, M. Innocent, A. Pritchard, and S. Airey, "Attitude sensors on a chip: Feasibility study and breadboarding activities," in *Proc. 32nd Annu. AAS Guid. Control Conf.*, February 2009, p. 11971216.

[5] J. A. Leñero-Bardallo, R. Carmona-Galán, and A. Rodríguez-Vázquez, "A wide linear dynamic range image sensor based on asynchronous selfreset and tagging of saturation events," *IEEE Journal of Solid-State Circuits*, vol. 1, no. 1, pp. 1–13, April 2017.

[6] ——, "A high dynamic range linear vision sensor with event asynchronous and frame-based synchronous operation," in *Electronic Imaging, Image Sensors and Imaging Systems 2016*, February 2016, p. 17.

[7] "jAER open source project," http://sourceforge.net/projects/jaer/.

[8] M. Barbaro, P. Y. Burgi, A. Mortara, P. Nussbaum, and F. Heitger, "A 100×100 pixel silicon retina for gradient extraction with steering filter capabilities and temporal output coding," *IEEE Journal of Solid-State Circuits*, vol. 37, no. 2, pp. 160–172, Feb 2002.

[9] J. A. Leñero-Bardallo, R. Carmona-Galán, and A. Rodríguez-Vázquez., "A bio-inspired vision sensor with dual operation and readout modes," *Sensors Journal, IEEE*, vol. 16, no. 2, pp. 1–14, January 2016.

Paper V:

J.A. Leñero-Bardallo, Ł. Farian, J.M. Guerrero-Rodríguez, R. Carmona-Galán, Á. Rodríguez-Vázquez
Sun Sensor Based on a Luminance Spiking Pixel Array
IEEE Sensors Journal, 2017

Sun Sensor Based on a Luminance Spiking Pixel Array

Juan Antonio Leñero-Bardallo, *Member, IEEE*, Lukasz Farian, *Student Member, IEEE*, José-Maria Guerrero-Rodríguez, Ricardo Carmona-Galán, *Senior Member, IEEE*, and Ángel Rodríguez-Vázquez, *Fellow, IEEE*

***Abstract*— We present a novel sun sensor concept. It is the very first sun sensor built with an address event representation spiking pixel matrix. Its pixels spike with a frequency proportional to illumination. It offers remarkable advantages over conventional digital sun sensors based on active pixel sensor (APS) pixels. Its output data flow is quite reduced. It is possible to resolve the sun position just receiving one single event operating in time-to-first-spike mode. It operates with a latency in the order of milliseconds. It has higher dynamic range than APS image sensors (higher than 100 dB). A custom algorithm to compute the centroid of the illuminated pixels is presented. Experimental results are provided.**

***Index Terms*— Sun sensors, AER, attitude determination, event-based vision sensors, space probes.**

I. Introduction

SUN sensors are devices used to determine the sun position. There are multiple applications for them. For instance, solar power plants need to measure the sun position precisely to control the solar cells or the heliostats positions, maximizing energy production. If we speak about navigation systems, the sun is the most prominent celestial body in the solar system. Hence, it is considered as a reference to determine the spacecrafts and sounding rockets attitude.

Depending on the application, sun sensors features can differ. Power plants need devices that are precise and reliable, but they do not require fast operation. However, when gauging space probes attitude in the outer space, fast operation, low power consumption, and reduced output flow are mandatory. There are two main families of sun sensors that are chosen depending on the application scenario: analog and digital.

Analog sensors, [1], [2] are usually designed using two different photoactive regions with dedicated optics. Depending on the sun inclination, the ratio between two different photocurrents gives the sun inclination. The drawback of such kind of sensors is that they are sensitive to scene distractors and noise. If there are different light sources within the visual scene, the measurements results will be affected. Their advantages are fast operation and simplicity. Digital sun sensors, [3], [4], usually employ a frame-based vision sensor with Active Pixel Sensors (APS) pixels and dedicated optics. The whole pixel array is readout. Thereafter, the sun position is determined within the visual scene. These sensors are more reliable because the entire visual scene can be processed to determine the sun position. Hence, distractors and noise impact can be amended. The counterpart is that there is a large amount of black pixels that are not meaningful to determine the sun position. Hence, such sensors require time to readout an entire pixel array, store their outputs on a memory, and finally process the data to determine the sun position. To avoid such a limitation, some research work has been developed. Some authors [3], [4] propose to determine the sun position in two steps: acquisition and tracking. In the first step, the entire pixel matrix or a group of pixels is readout to determine a Region of Interest (ROI) with the illuminated pixels. In the second step, pixels within the ROI are readout to compute the sun position. This approach alleviates the limitation of APS sensors. The drawback is that more dedicated circuitry, pixel control signals, and algorithms are required. Also the amount of pixels to be readout are higher than the ones placed on the ROI.

Event based vision sensors [5]–[8] have pixels that are readout asynchronously. They send events whenever they have information to transmit. Therefore, an entire pixel array does not have to be readout to render one image. As a result, they provide a reduced output data flow and fast operation. Among the event based sensors, the luminance sensors, also known as octopus retinas [9]–[11], are sensors whose pixels send events with a frequency proportional to illumination. Hence, their nature is especially suitable for the design of efficient sun sensors, overcoming some of the limitations of the previous reported ones, i.e. data redundancy and processing time. Only illuminated pixels within the ROI will send information out of chip. The idea of exploiting Address Event Representation (AER) sensors to design sun sensors was already advanced by Farian et al. in a conference paper [12]. The architecture of a sun sensor with two asynchronous pixel rows with a L-shape and dedicated optics was presented. Simulation results were also provided.

In this article, we propose a sun sensor based on an AER luminance sensor. Pinhole optics are mounted on top of the sensor. Pinhole lenses are very robust and compact.

Manuscript received July 26, 2017; accepted August 28, 2017. Date of publication September 6, 2017; date of current version September 25, 2017. This work was supported in part by the University of Cádiz under Grant PR2016-072, in part by the Spanish Ministry of Economy and Competitiveness under Grant TEC2015-66878-C3-1-R, Co-Funded by ERDF-FEDER, in part by Junta de Andalucía CEICE under Grant TIC 2012-2338 (SMARTCIS-3D), and in part by ONR under Grant N000141410355 (HCELLVIS). The associate editor coordinating the review of this paper and approving it for publication was Prof. Kazuaki Sawada. *(Corresponding author: Juan Antonio Leñero-Bardallo.)*

J. A. Leñero-Bardallo and J.-M. Guerrero-Rodríguez are with the University of Cádiz, 11519 Cádiz, Spain (e-mail: juanantonio.lenero@uca.es; josem.guerrero@uca.es).

L. Farian is with the University of Oslo, N-0316 Oslo, Norway (e-mail: lukaszf@student.matnat.uio.no).

R. Carmona-Galán, and Á. Rodríguez-Vázquez are with the Institute of Microelectronics of Seville (IMSE-CNM), CSIC-Universidad de Sevilla, 41092 Sevilla, Spain (e-mail: rcarmona@imse-cnm.csic.es; angel@imse-cnm.csic.es).

Digital Object Identifier 10.1109/JSEN.2017.2749414

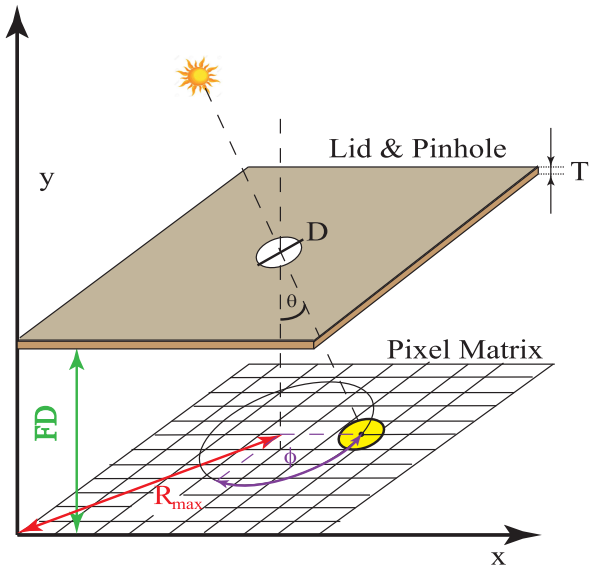

Fig. 1. System implementation. There is a pixel array covered by an opaque lid with a pinhole in its center. Only a reduced number of pixels are illuminated through the pinhole by the sun light projection. Depending on the sun inclination with the sensor's vertical axis, different pixels will be illuminated.

The sun disk is projected over a reduced number of pixels. Thus, that will be the only pixels that will be readout, avoiding to readout a entire pixel matrix. Furthermore, pixels operate asynchronously at high speed (in the order of milliseconds), offering good resolution and high dynamic range operation. The new sensor merges some of the advantages of prior analog and digital sensors and overcomes some of their limitations, i.e. data redundancy, low operation speed, and reduced dynamic range. Experimental results are provided.

II. System Description

The system implementation is based on a pixel array covered by an opaque lid with a pinhole (see Fig. 1), similar to the one devised by Xie and Theuwissen [3] or the European Spatial Agency [4]. Only a reduced number of pixels will be illuminated by the sunlight projection. The rest of pixels will be relatively dark and will send relatively few data. Depending on the sun position, the light spot will be placed at different locations within the pixel array. The centroid of the illuminated pixels, (x, y), will be used to compute the sun position (θ, ϕ) that is determined by the sun latitude, θ, and the azimuth, ϕ. The sun's latitude is given by:

$$\theta = arctan\left(\frac{\sqrt{W \cdot (x - x_c)^2 + L \cdot (y - y_c)^2}}{FD}\right) \quad (1)$$

Where (x_c, y_c) is the centroid of the ROI when $\theta = 0°$. W and L are the pixel width and length, respectively. FD is the focal distance, i.e. the distance between the pixel array and the lid. The azimuth, ϕ, is given by:

$$\phi = arctan\left(\frac{L \cdot (y - y_c)}{W \cdot (x - x_c)}\right) \quad (2)$$

The distance between the array and the lid (FD) is the focal distance. Based on these parameters values, and knowing the number of pixels and their dimensions (width and length) it is possible to determine the expected sensor Field of View (FOV). Let us denote as R_{max} the maximum distance from the center of the array to one of its corners. Taking into account the pixel array dimensions, we can determine R_{max}:

$$R_{max} = \frac{1}{2} \cdot \sqrt{(W \cdot M)^2 + (L \cdot N)^2} \quad (3)$$

M is the number of pixel rows. N is the number of pixel columns. Hence, the maximum sunlight angle of incidence is:

$$\theta_{max} = arctan\left(\frac{R_{max}}{FD}\right) \quad (4)$$

And the FOV will be:

$$FOV = 2 \cdot \theta_{max} = 2 \cdot arctan\left(\frac{R_{max}}{FD}\right) \quad (5)$$

Examining the Equations 4 and 5, we can conclude that we can increase the FOV by minimizing the focal distance from the pinhole to the sensor (FD), and we can improve the sensor resolution by decreasing the pixel dimensions ($W \times L$). As it will be discussed in Section V-C, the sensor resolution will depend on the number of pixels. For this reason, the sensor pixel array resolution cannot be arbitrarily low. In the HDR image sensor chosen to build the sun sensor [13], [14], pixel dimensions are W=L=25μm. The number of rows is M=128, and the number of columns is N=96. To maximize the FOV, we manufactured the lid to place it as close as possible to the sensor, achieving a focal distance of FD=0.6mm. Substituting these parameters in Equations 3, 4 and 5, we obtain an FOV=146°.

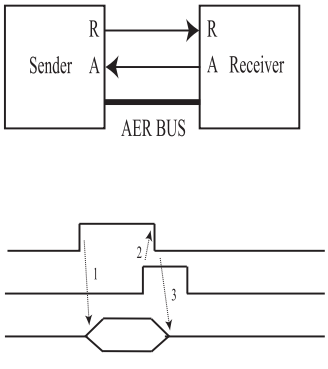

Fig. 2. Signals involved in the AER point to point communication protocol between different chips.

III. Image Sensor With Asynchronous Operation

We designed the sun sensor with a vision sensor with pixels that send their information asynchronously using the AER communication protocol [15]. In Fig. 2, the communication signals exchanged between two devices that use the AER protocol to communicate are depicted. In this particular case, the image sensor will be the sender and an FPGA will be the receiver. Every time that one pixel fires asynchronously, the sensor requests access to a shared AER bus. To do so, the *REQ* signal is activated and the pixel's coordinates are sent through the bus. The receiver, that is an FPGA,

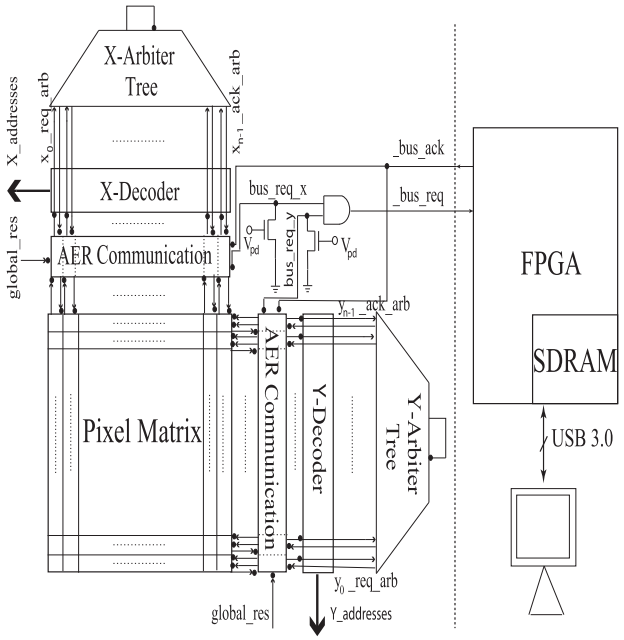

Fig. 3. System block diagram. We display the main sensor blocks. An external Opal Kelly XC7K160T board with an FPGA is attached to the sensor for interfacing. The FPGA can send data to a PC for debugging and monitoring.

will store the address of the pixel that has fired and will send back the *ACK* signal to indicate that has received the address. Thereafter, the sender will release the *REQ* signal and the pixel address from the bus.

In Fig. 3, there is a block diagram of the asynchronous image sensor. In the center, there is a pixel matrix. On the periphery, there is the asynchronous logic to handle the AER communication between the pixels and the receiver (an FPGA). In case there is bus congestion, i.e. several pixels trying to send information simultaneously, such pixels will wait until they have access granted to the bus to send their addresses off-chip. There is some arbiters to avoid colisions between pixels that fire simultaneously [15], [16]. Such blocks receive petitions from the rows or the columns that correspond to the pixel that has fired. Only one this petition will get access to the shared bus. Thus, only one pixel will be allow to transmitt its address to the FPGA. The arbitration process is conducted in two stepts. First, the row petitions are arbitrated. Then the column petitions are arbitrated. At the end, only one row and one column will get access to the shared bus.

In Fig. 4, there is a block diagram showing the connectivity between the external arbitration logic, the arbiters and the pixels row/colunms. In between, the AER logic and the arbitration tree, there is a multiplexer to encode the X/Y coordinates of the pixels that have transmitted an event off-chip. A more detailed description of the asynchronous blocks implementation and their performance can be found elsewhere [15].

The arbitration logic used with this sensor was proposed by Häfliger [17] and used in prior implementations of spiking vision sensors. It can handle events rates of 10Meps for pixels of different columns/rows and event rates of 2Meps for pixels of the same row/column [10], [11]. As it will be discussed

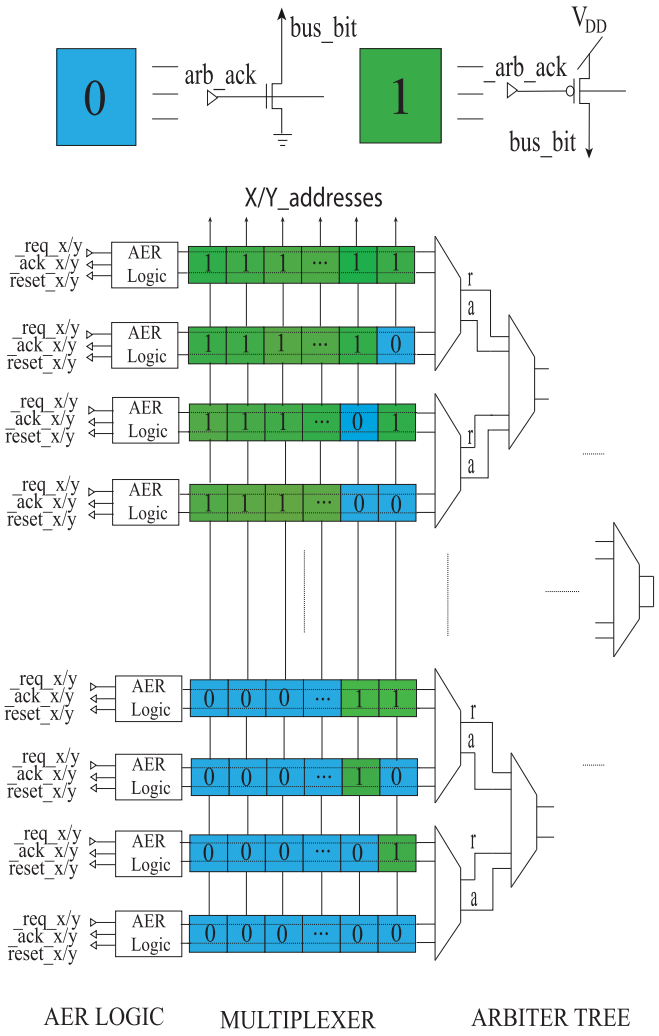

Fig. 4. Detail of the asynchronous communication logic and its connectivity with the pixel matrix rows and colunms. The arbiters blocks are arranged to create an arbitration tree where only one request input signal can be acknowledged.

in Section V, this arbitration speed assures the sun sensor operation because the expected event rates are much lower than the maximum event rates tolerated by the arbitration system. Therefore, the errors introduced by the delays of the AER logic can be neglected in this application.

IV. Pixel Design

In this particular implementation, we employ an AER sensor, [13], [14], whose pixels generate events with a frequency proportional to illumination, as it is depicted in Fig. 5. Sensors built with these kind of pixels are also known as 'octopus' retinas [9]–[11]. There are multiple possible topologies for the pixel design. This particular sensor is intended for High Dynamic Range (HDR) operation. It has different operation modes. In the sun sensor implementation, we just use light to frequency conversion. Fig. 6 shows the pixel circuitry involved in the light to frequency conversion. Pixel operation is initiated with a global reset ($\overline{RES}$). After that, pixel capacitors are discharged with a speed proportional to the local illumination.

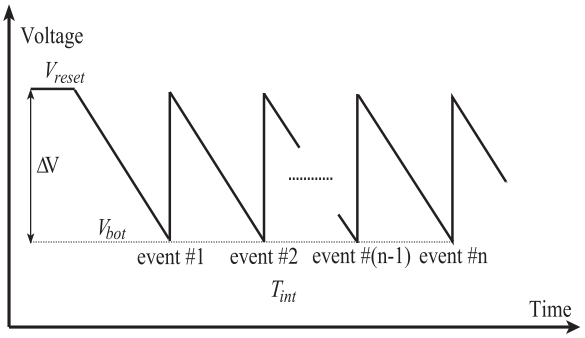

Fig. 5. Pixel transient voltages at the integration capacitance. Every time that voltage level V_{bot} is reached, an event is sent out off chip.

Whenever a pixel voltage reaches the level V_{bot}, the comparator fires and reset the pixel capacitor. Then, the pixel starts over integrating charge again. In the meantime, an analog memory stores on C_1 a value indicating that the pixel has fired and an event needs to be sent out. On the right of Fig. 6, we have highlighted the AER communication logic [17] that handles the communication to transmit off chip an event with the (x,y) coordinates of the pixel that has fired. The digital inputs/outputs are shared between pixels rows (y) and pixel columns (x). Its connection with the AER periphery is depicted in Fig. 4. In Fig. 7, there is a time line of the digital signals involved in the asynchronous communication when one pixel needs to transmitt its address. There are two arbitration processes. First, the pixel rows are arbitered. Then, the columns are arbitared. Once, the pixel gets granted access to the AER bus, its address is sent towards the FPGA using the communication protocol described previously in Fig. 2.

The oscillation period shown in Fig. 5 can be computed as a function of the circuit parameters in Fig. 6. The light-to-frequency conversion block is an astable oscillator. Therefore, its value is approximately given by:

$$f_{osc} \approx \frac{I_{ph}}{C_{ph} \cdot (V_{DD} - V_{bot})} = \frac{I_{ph}}{C_{ph} \cdot \Delta V} \tag{6}$$

It depends on the pixel maximum voltage variation $\Delta V = V_{DD} - V_{bot}$, the pixel integration capacitance C_{ph}, and the photocurrent, I_{ph}. We target for the sun sensor implementation a pixel firing frequency in the order of KHz. Hence, ΔV can be adjusted for this purpose. Since a sun sensor can be exposed to high illumination levels, the integration capacitance values C_{ph} and ΔV should be high enough to assure that. The proposed sensor is suitable for high illumination operation. Transistors with thicker gate oxide are selected for the pixel design. The value of the power supply can be set up to $V_{DD} = 5$V. With standard technology transistors the power supply voltage is 1.8V. Hence, the the maximum value of ΔV to adjust the pixels spikingin rates would be lower with these transistors. Since the sensor could be exposed to direct sunlight in some situations, we opted for having as much flexibility as possible to adjust the event rates for a given illumination.

In Fig. 8, the pixels comparators design is shown. We implemented two-stage comparators. They have low current consumption: 110nA with the nominal biasing $V_{bias_comp} = 4.3$V. The amount of time required by the comparator to reset the voltage at capacitor C_1 in Fig. 6 is $T_{reset} = 400$ns, with $\Delta V = 4$V. The higest pixel oscillation frequency measured when pixels are directly exposed to very bright light was $f_{osc_{max}} = 55$keps, [13]. Hence, the error introduced by the comparator delay is expected to be lower than $T_{reset}/T_{osc_{max}} \approx 2.2\%$.

TABLE I
SPIKING LUMINANCE AER SENSOR FEATURES

Technology	AMS 0.18μm HV
Power Supply	1.8V/5V
Chip Dimensions	4120μm× 3315μm
Pixel Size	25μm × 25μm
Number of Pixels	96×128
Fill Factor	10%
Dynamic Range	>100dB
Event sensitivity to light	0.0762events/$\Delta V \cdot lux$
Power Consumption	52mW, 100keps
Sense Node Capacitance	45fF
FPN (event output)	2.6%
Max. event rate	2Meps (same row), 10Meps (different rows)

Fig. 3 displays a sensor block diagram. The different circuit modules involved in the pixel event-based operation are shown. There is a pixel matrix core and peripheral asynchronous circuitry to manage the AER communication [17]. An external Opal Kelly XC7K160T board is attached to the sensor through a Mezzanine connector for interfacing. The board has a Kintex 7 FPGA that performs several operations: it handles the AER protocol communication signals depicted in Fig. 2, stores the incoming events on a memory, and send/receives data from a PC for system debugging and real time data representation with the standard jAER interface [18].

V. EXPERIMENTAL RESULTS

A. Experimental Setup

The main features of the spiking vision sensor chosen to design the sun sensor are summarized on Table I. Fig. 9 displays a picture of the sensor that is allocated over a PGA144 socket. A lid with a thickness of T=100μm is placed over the chip at a distance of FD=0.6mm. In Fig. 10, we display de lid. It is anti-reflective on one side and reflective on the other one. The reflective side was placed externally to reflect the incident sunlight. The anti-reflective side was placed directly over the chip. It was manufactured using a laser PCB printing machine. For the test, we assembled several prototypes with different radius ranging from 50μm to 100μm to compare their performance. The lid does not need a perfect alignment to operate. Any offset in the measurements will be systematic and known. To start operating, we just need to determine the coordinates (x_c, y_c) of the pixel that is illuminated when there is a light beam aligned to the sensor transversal axis ($\theta = 0°$). Hence, this an advantage for the test over systems with more complex optics that require a precise alignment before operating [12]. To debug and test the sensor,

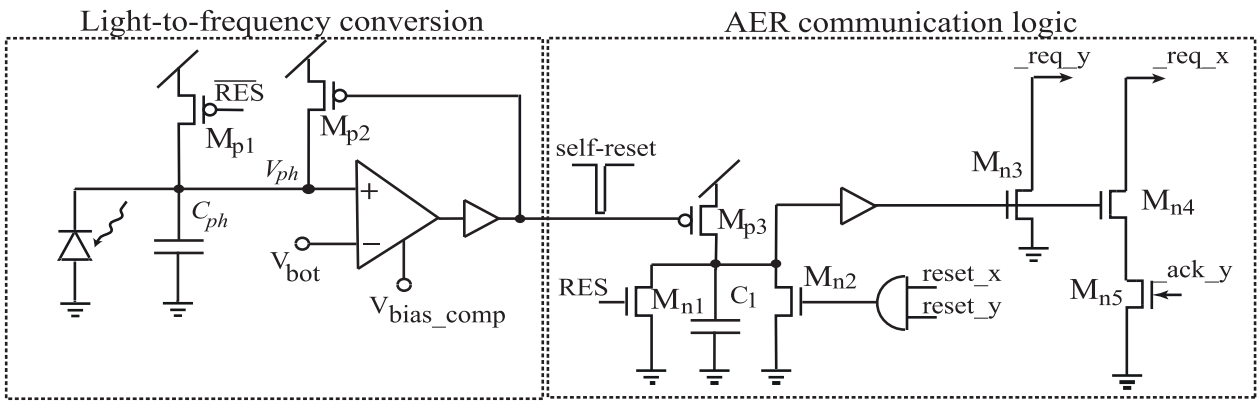

Fig. 6. Pixel schematics. There is circuitry to perform a light to frequency conversion and logic to handle the asynchronous AER communication. Transistor sizes are (W/L, μm/μm): $M_{p1} = 1/1$. $M_{p2} = 3/1$. $M_{p3} = 0.5/1$. $M_{n1} = 0.5/0.7$. $M_{n2} = 0.7/0.7$. $M_{n3} = 1/0.7$. $M_{n4} = M_{n5} = 0.5/0.7$. $C_{int} = C_1 = 40$fF, $C_{ph} = 5$fF. Bias voltages: $V_{bot} = 1$V, $V_{bias_comp} = 4.3$V.

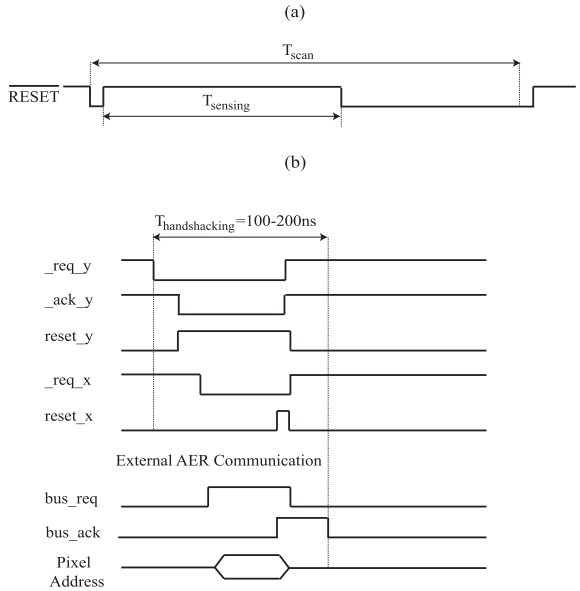

Fig. 7. Time line of the signals involved in the pixel operation. Sensing starts after a global reset. When a certain number of events is received, the pixel is reset again and the sun position is computed. The pixel is kept in a steady state until a new measurement is taken. The time interval between consecutive measurements is denoted as T_{scan}. (a) Pixel control signals time-line. (b) Event communication time line (during T_{int}).

the jAER interface [18] was adapted to display the information coming from our sensor, as it is depicted in Fig. 11.

B. Sun Position Detection Algorithm

One of the advantages of this sensor over the previous reported digital ones [3], [4] is the reduced output data flow and the fast operation. Only illuminated pixels will send data off-chip. Computing their spiking frequency, it will be possible to gauge their illumination precisely. Typically, when the sensor is exposed to sunlight, a group of pixels spike with a frequency distribution as the depicted in Fig. 12. Pixels in the center of the illuminated region will spike with a higher frequency than pixel in the border. Typical pixels firing frequencies in outdoors environments are higher

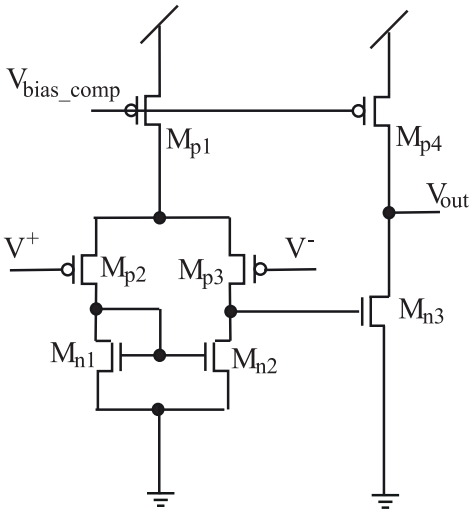

Fig. 8. Schematics of the pixel comparators. Transistor sizes are (W/L, μm/μm): $M_{p1} = M_{p4} = 1/2$, $M_{p2} = M_{p3} = 2/0.7$, $M_{n1} = M_{n2} = 2.8/0.7$, $M_{n3} = 6/0.7$. We set $V_{bias} = 4.3$V. $V_{DD} = 5$V. Its power consumption is approximately 110nA.

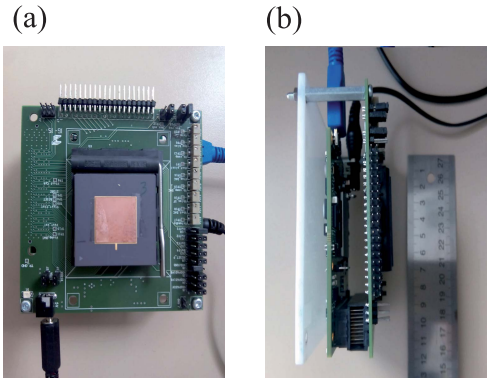

Fig. 9. Sensor photograph. (a) Front view. (b) Lateral view. Detail of the interconnectivity between the sensor and the Opal Kelly XC7K160T board.

than 1keps. This assures a sensor response time in the order of milliseconds. The arbitration logic can cope with events rates up to 10Meps [11], [17]. Hence, it is not a bottle-neck for this application where only a reduced number of illuminated pixels send events off-chip. The amount of time

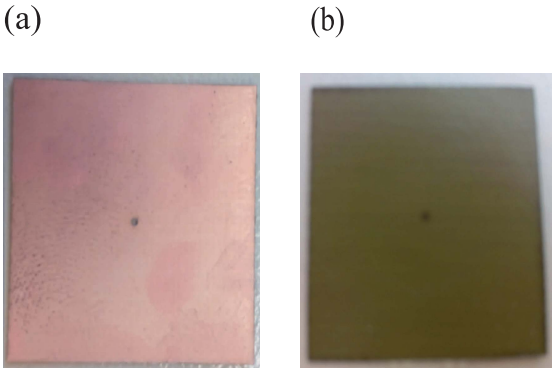

Fig. 10. Lid with a pinhole manufactured to implement the sun sensor. The side that faces the sun (a) is metallic to reflect the sun radiation. The side that is directly over the chip (b) is anti-reflective. Lid dimensions are: Thickness: T=100μm, Width=Length=20mm, Pinhole radius=50μm.

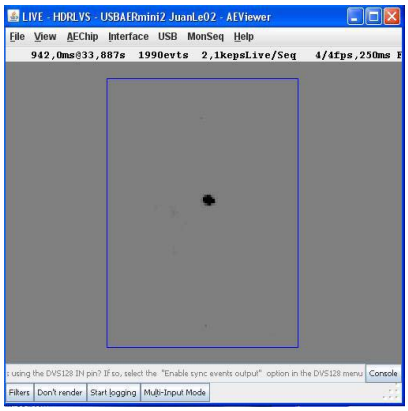

Fig. 11. jAER interface [18] to debug and display the sensor information. The black speckle correspond to the illuminated region when the sensor is operating.

to send one event off-chip (handshacking cycle) lasts about 0.1μs-0.5μs [10], [11]. Therefore, asynchronous communication delays are neglectible in comparison to pixels time response.

In Fig. 12, measured pixel illumination values are shown. Illumination levels range between [0, 2500]. That means that the sensor has to be able to measure an intra-scene dynamic range of $DR = 20 \cdot log_{10}(2500) \approx 70dB$ to capture all the illumination levels of this particular visual scene.

To compute the angles in Equations 1 and 2, the centroid of the illuminated pixels has to be determined. To do so, we apply this simple algorithm:

1) We wait until a certain number of events, $N_{events} \geq 1$, are received. In the meantime, the coordinates of the pixels that fire (x_i, y_j) are stored on a memory.
2) Once the event number is equal to N_{events}, we compute the centroid coordinates.

$$x = \frac{1}{N_{events}} \cdot \sum_{i=1}^{N_{events}} x_i \tag{7}$$

$$y = \frac{1}{N_{events}} \cdot \sum_{j=1}^{N_{events}} y_j \tag{8}$$

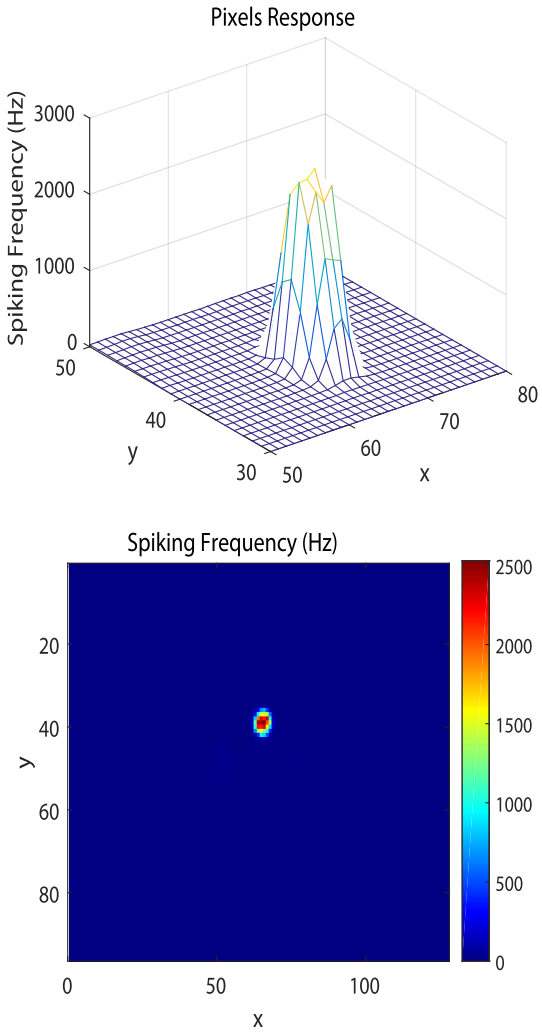

Fig. 12. Typical event response when the sensor is exposed to sunlight. A group of pixels are the one one that send events off-chip. There is a peak of activity in the center of the illuminated region.

3) Once the centroid, (x, y) is known, the sun position is determined according to Equations 1 and 2.
4) The event counter is reset, $N_{events} = 0$, and the computation is finished. To calculate the sun position again, go to step #1.

The proposed algorithm is simple and efficient. It was tested programming it on the jAER interface [18]. It can easily be implemented on an FPGA or a microcontroller. The sun position is not determined until a certain number of events is received. Hence, the amount of data used to determine the sun position is always the same. If no data is received, the sun position will not be computed. The pixels reset signal ($\overline{RES}$ in Fig. 6) can be used as a timer, i.e. if after a certain time interval (T_{scan} in Fig. 7), the number of events received is lower than N_{events}, the counter will be reset and the sun position will not be determined. The user can keep all the pixels reset and release them to compute the sun position. This will allow to save power.

Fig. 13 displays the temporal response of the sensor. We rotated a fast light within the FOV of the sensor.

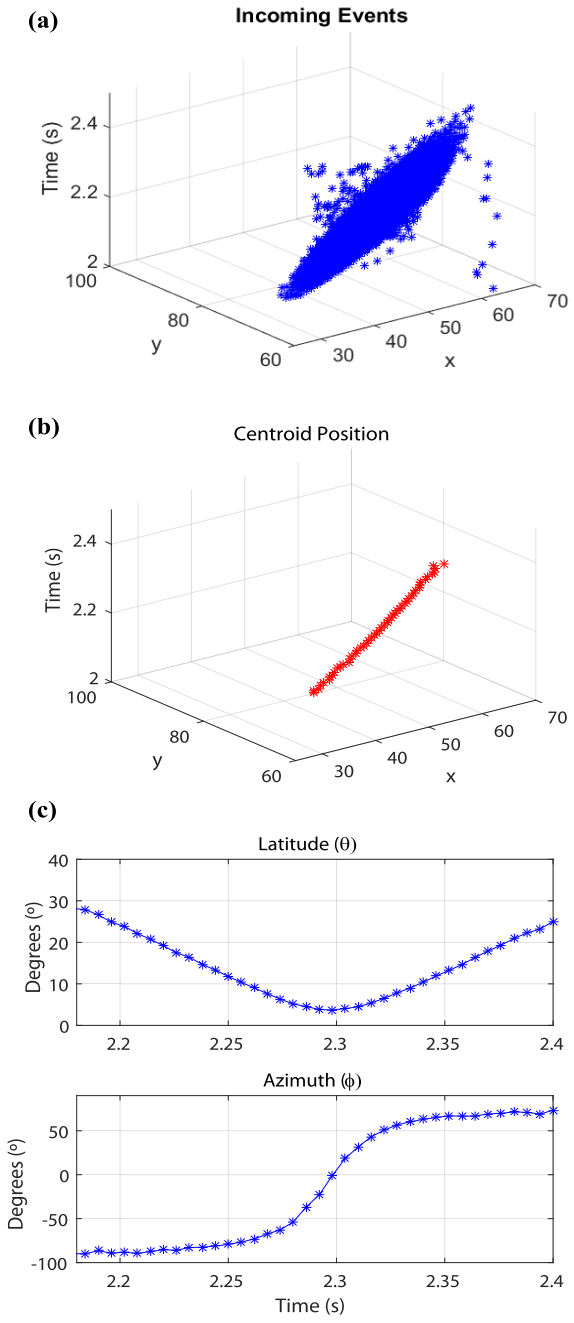

Fig. 13. Sensor transient response. A light beam facing the sensor was rotated to emulate the sun movement. (a) Raster plot: Recorded events versus time. (b) Computed centroids at timestamps of $T_{stamp} = 5$ms. (c) Computed angles (θ, ϕ) that indicate the light source position.

We recorded data and we computed the centroid at different time stamps with the algorithm previously described. The time stamps between algorithm executions were $T_{stamp} = 5$ms. On top, (Fig. 13.(a)), we have plotted a raster plot with the events generated by the different pixels over time. Initially, the sensor was not illuminated. Therefore, there was not event activity. Once, pixels start firing a considerable number of events, their centroids are calculated at time intervals equal to $T_{stamp} = 5$ms with the latest events that were received. Fig. 13.(b) shows the computed centroids coordinates over time. Fig. 13.(c) displays the computed angles that determine the sun position, according Equations 1 and 2, at every time stamp. The latitude, θ, depends on the ratio between the centroid distance to the center of the pixel array and the focal distance. Initially, the distance has its maximum value. Then, the light beam centroid moves towards the the pixel array center and θ is close to zero. When the light centroid passes the center of the pixel array, the distance to it grows, and θ increases too. Finally, when the light beam is out of the field of view of the sensor, events are not generated. The azimuth, ϕ, was swept within a large region. As it can be seen in Fig. 13.(b), the y-coordinate was almost constant while the x-coordinate was changing during the experiment. Thus, the azimuth describes a $arctan\,(x)$ function, as it is expected according Equation 2.

C. Resolution

The algorithm efficiency depends on the number of events available to compute the pixel spiking frequencies. There is a temporal variation of the pixel spiking frequencies (jitter) that depends on the circuit noise. The higher the number of events it is, the more precise the computation it is. In the analysis, let us assume that the number of events per pixel to compute is high enough to ignore the angles computation error due to the number of events. The precision of the algorithm computing the centroid will depend on the lid radius. The higher it is the number of illuminated pixels, the higher it is the algorithm precision. Let us denote the size of the illuminated windows as $N_{window} \times N_{window}$. Therefore, calculating the centroid, the spatial resolution of the algorithm is $1/\left(N_{window} \times N_{window}\right)$. Taking into account the sensor FOV, the number of pixels per row, M=128, and the algorithm spatial resolution, we can determine the sensor resolution:

$$R = \frac{FOV}{M \cdot N_{window} \cdot N_{window}} \tag{9}$$

The number of illuminated pixels depends on radius of the lid pinhole. The lower the radius is, the lower the image bluring is. In our case, image bluring can be beneficial to achieve subpixel resolution. In the measurements of Fig. 12, $N_{window} = 6$. Hence, if the FOV=146°, the expected sensor resolution is R=0.03°. By increasing the radius of the lid it is possible to improve the centroid algorithm determination performance. However, events rates will be higher and the computation time too. Thus, there is a trade-off between these parameters. In this implementation, we reward the fast operation and the reduced data flow.

D. Accuracy

In order to determine the sensor accuracy, we devised the test bench shown in Fig. 14. A 1266-03-000 Gated Cameo laser emitting at 650nm was illuminating the pinhole. Its light intensity was modulated with a power supply, keeping the total sensor event rate generated by the illuminated pixels constant and below 10keps (kilo events per second). Angles were computed 100 times at regular time intervals of 1 second. The standard deviation of the measurements,

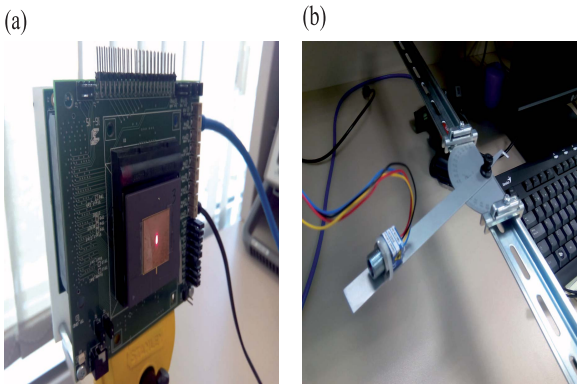

Fig. 14. Experimental setup to measure the sensor's accuracy. A laser (b) was aligned with the center of the sensor's pinhole (a). Its intensity was modulated with a power supply to generate a controlled event rate by the illuminated pixels. Measurements were repeated 100 times at regular time intervals of 1 second to determine the sensor accuracy.

was $\sigma_\theta = 0.0044°$ for the latitude (θ) and $\sigma_\phi = 0.0169°$ for the azimuth (ϕ). Hence, the sensor accuracy for the latitude is $3\sigma_\theta = 0.0132°$ and for the azimuth is $3\sigma_\phi = 0.0507°$. Looking at Equations 1 and 2, it can be appreciated that azimuth angle is more sensitive to errors in the centroid computation than the latitude computation. Latitude depends on the distance to the sensor transversal axis, while the azimuth angle depends on the ratio between the centroid coordinates.

E. TFS Operation

Time-to-first-spike (TFS) operation [10], [19]–[21] is very efficient in terms of data processing when determining the sun position. In this operation mode, pixels are activated after releasing the $\overline{RES}$ signal in Fig. 6, that resets all the pixels of the sensor. Thereafter, events will arrive in order. The highest illuminated pixel will spike first and so on. The centroid position is always close to the position of the highest illuminated pixel. Hence, only receiving one single event, it is possible to gauge the sun position. By increasing the number of events, the measurement error will be reduced at the expense of receiving more data and increasing the computational time. Thus, the operator can trade off the measurement precision for data throughout. Fig. 15 illustrates the performance of the TFS operation. After reseting the sensor pixels, we recorded events during a time interval. We have plotted the computed angles and the error for different number of events (N_{events}). We can notice that angles converge to a final value when the number of events is increased. The error was computed as the difference between the computed angle for each value of N_{events} and the angle computed when $N_{events} = 10,000$. With one single event, the measurement errors are 0.3° and 2° for the latitude and the azimuth respectively. If we increase the number of events to 10, errors are reduced to 0.155° and 0.3° respectively. After receiving 1000 events, the results are not improved significantly by increasing the number of events in the centroid computation. In such case the errors were 0.02° and 0.06° for the latitude and the azimuth respectively.

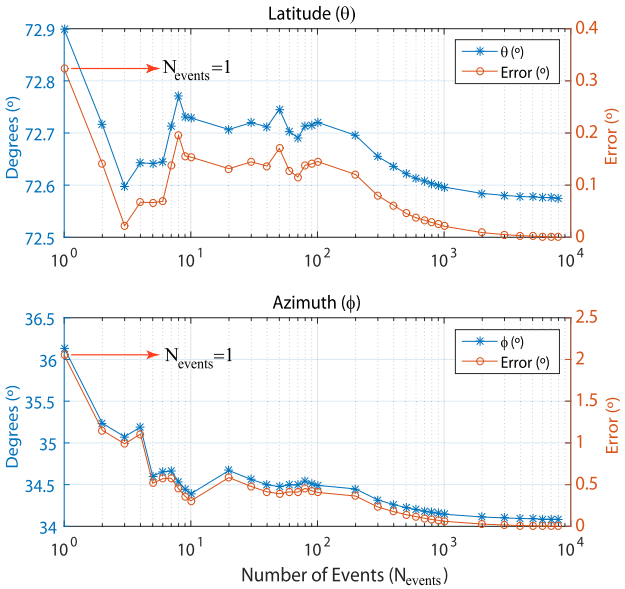

Fig. 15. TFS operation. After reseting the sensor, a certain number of events is received, the sun position (θ, ϕ) is computed. We plot the computed angles and the measurement error for different number of incoming events. With only one event, it is possible to gauge the sun position keeping the error low.

F. Pixels Response Time

According to Equation 6, pixels spiking frequencies are proportional illumination. Pixels time response is inversely proportional to the pixels firing rates. Sun sensors can operate under very intense sun radiation. For this reason, it is desirable to have same control over the event rate in such conditions. The image sensor was devised to operate under very high illumination conditions [13], [14]. The sensitivity to illumination can be adjusted by tuning the voltage V_{bot} in Fig. 6. Frequency response versus illumination was measured. Pixel event sensitivity is $S = 0.0762 events/\Delta V \cdot lux$, with $\Delta V = V_{DD} - V_{bot}$. Pixel transistors have thicker gate oxide and the parameter ΔV can reach values up to 5V. In situations of intense illumination, the number of events can be reduced by setting ΔV close to the value of $V_{DD} = 5$V. With transistors without thick gate oxide, the power supply voltage is limited to 1.8V in the AMS 180nm HV technology. The pixel integration capacitance (C_1 in Fig. 6) also influences the spiking frequencies. To optimize the pixel fill factor, it should be as low as possible. However, the lower the capacitor it is, the higher the mismatch introduce by it on the pixel firing frequency. The AER arbitration logic can tolerate pixel array event rates of 10Meps [17]. That is not a limitation in this application because only a small region of the sensor is illuminated. We did not reach that limit in any operation scenarios.

G. Fixed Pattern Noise

Pixel Fixed Pattern Noise (FPN) in provoked by the offset of the oscillator comparator depicted in Fig. 8, the inter-pxiel variations of the capacitance value C_1 in Fig. 6, and the variations of the reset voltage amplitude. Among this sources of mismatch, the variations of the comparators' voltage threshold is the dominant one [10]. According to the missmatch models

TABLE II
STATE-OF-THE-ART COMPARISON

Work	**This Work**	Ning et al. [3]	Galileo ESA [4]	Ortega et al. [1]
Type	Event Based Luminance Sensor	APS Digital Sensor	APS Digital Sensor	Analog Sun Sensor
Operation Principle	TFS	Frame-based	Frame-based	Photocurrent Ratio
Technology	AMS 0.18µm HV	0.18µm 1P4M	UMC 0.18µm	ND
Power Supply	3.3/5V	3.3/1.8V	3.3/1.8V	ND
Chip Dimensions	4120µm× 3315µm	5mm×5mm	11mm×11mm	6.8mm×13.8mm
Number of Pixels	128×96	368×368	512×512	2 pairs of photodiodes
Pixel Pitch	25µm× 25µm	6.5µm×6.5µm	11µm×11µm	NA
FOV	146°	94°	128°	120°
Power Consumption	52mW	42.73mW	520mW	ND
Latency	<5ms@1klux or lower	10frames/s	10frames/s	NA
Dynamic Range	>100dB	52dB	ND	NA
Resolution	0.03°	0.004°	<0.005°	ND
Accuracy	0.0132°(θ), 0.05°(ϕ)	0.01°	0.024°	0.15°
Amount of data	1-100 Events	368 pixels (acquisition mode) +25×25pixels (tracking mode)=945pixels	1 frame (acquisition mode) + ROI (tracking mode)	4 analog voltages to be readout

provided by the foundry, in our case, matching between capacitors is much better than between transistors. The last source of mismatch can be reduced with a thoughtful design of the pixel reset transistor (M_{p_1} in Fig. 6). On the one hand, the aspect ratio should be as high as possible to minimize the pixel self-reset time. On the other hand, the transistor length should be high enough to minimize the mismatch impact.

To compute the fixed pattern noise, we illuminated all the pixel array with a white Lambertian source with uniform and constant light. We recorded events during 5 seconds and we computed the variations between the pixels spiking frequencies, according to this formula:

$$FPN = \frac{\sum_{i=1}^{N_{pixels}} \sqrt{f_i - \overline{f}}}{N_{pixels} \cdot \overline{f}} = \frac{\sigma_f}{\overline{f}} \tag{10}$$

Where $N_{pixels} = N \cdot M$ is the number of pixels, f_i is the oscillation frequency of the pixel i, and $\overline{f}$ is the average pixel array spiking frequency. The measured FPN was 2.6% for this sensor, with $\Delta V = 4$V. Acording to the typical illuminations values measured in Fig. 12, spiking frequencies variations due to the FPN are not a limitation to guage the pixels illumination values within the illuminated ROI and compute its centroid.

H. Power Consumption

Chip power consumption comes mainly from the pixel comparators shown in Fig. 6. Additionally there is a dynamic power consumption that depends on the event rate. Fig. 16 displays the chip current consumption for different event rates. To measure it, we illuminated the whole pixel array with different illumination values and we measured the event rates. Since we are using a pinhole lens and only a few pixels are illuminated simultaneously, the global event rates are far away of the maximum event rate that the arbitration system can cope. In practical operation scenarios, we never exceeded event rates of 100keps. In such situations, the total system power consumption is 52mW. In further designs, power consumption could be reduced by switching off the comparators during the TFS operation idle intervals.

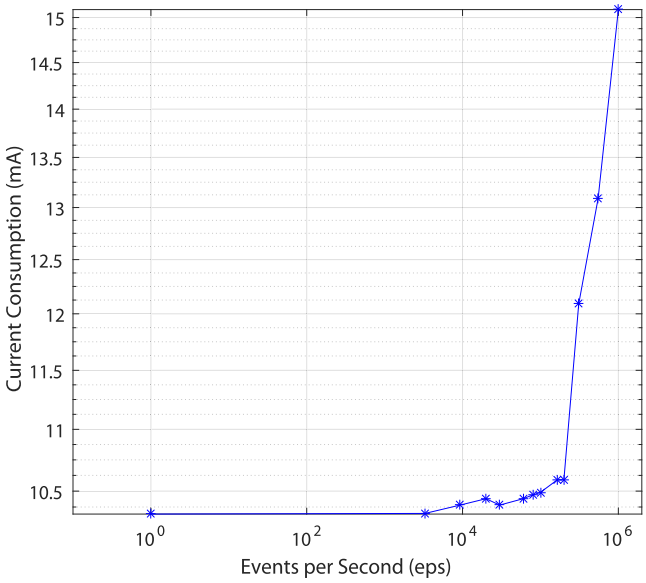

Fig. 16. Sensor current consumption versus event rate.

VI. BENCHMARCKING AND DISCUSSION

AER luminance sensors find a natural application scenario on the design of sun sensors. They have inherent advantages over APS image sensors when the region of interest is composed by a few pixels and the rest of the pixels are not meaningful (dark). To readout the entire pixel matrix is inefficient in terms of speed and data processing. We have demonstrated that, with a reduced number of events, it is possible to resolve the sun position. Operating in TFS mode,

with one single event, it is possible to gauge the sun position with an acceptable precision. In terms of speed, the proposed sensor can operate with latency responses in the order of milliseconds or lower. Regarding sensitivity and accuracy the reported results are alike the reported by previous authors. These parameters could be improved in further designs by reducing the pixel pitch. That is feasible because the proposed pixel [13], [14] has extra functionalities that are not mandatory for the design of a sun sensor.

Table II compares the current sensor against the art. Contrasting the performance in terms of speed and data flow against the digital sensors [3], [4], the performance is better. Such sensors propose to readout the image in two steps (acquisition and tracking) to avoid reading out the entire pixel matrix several times. Still the amount of data required to detect the sun position is much higher. Moreover, Xie and Theuwissen [3] require dedicated WTA (Winner-Take-it-All) circuitry to implement the acquisition mode. In both sensors, the pixel control signals and the readout algorithms are more complex. Comparing to analog sensors, [1], the performance of the proposed sensor is better in terms of accuracy and resolution. The possibility of computing the azimuth angle is missed with analog sensors. Regarding dynamic range, the AER pixel chosen for this implementation outperforms classic APS sensors. Thus, as we have demonstrated, it is possible to compute the centroid with information of pixels that are not overexposed.

All in all, the new sun sensor operates in a simpler and faster way than the previous reported digital sensors, that require elaborate design and readout procedures to avoid reading redundant black pixels. Our design performance could be improved in the future, by reducing the pixel pitch with a dedicated pixel, designed for this specific application. Since the events rates that we have measured in outdoors environments are far away of the maximum event rates that the arbitration system can tolerate, the pixel pitch could be reduced by using transistors without thicker gate oxide, operating with lower power supply voltages of $V_{DD} = 1.8$V.

VII. Conclusion

A new sun sensor designed with a spiking luminance sensor has been described. The sensor solves one paradigm associated to digital sun sensors: data coming from non illuminated pixels are readout and processed. Thus, the new approach is more efficient in terms of speed and output data flow. Furthermore, the sensor has higher dynamic range than APS sensors, leading to a more precise computation of the illuminated pixel centroids. As a further work, system performance can be improved in terms of accuracy and resolution by designing a dedicated pixel for sun sensors.

References

[1] P. Ortega *et al.*, "A miniaturized two axis sun sensor for attitude control of nano-satellites," *IEEE Sensors J.*, vol. 10, no. 10, pp. 1623–1632, Oct. 2010.

[2] A. Ali and F. Tanveer, "Low-cost design and development of 2-axis digital sun sensor," *J. Space Technol.*, vol. 1, no. 1, pp. 1–5, Jun. 2011.

[3] N. Xie and A. J. P. Theuwissen, "A miniaturized micro-digital sun sensor by means of low-power low-noise CMOS imager," *IEEE Sensors J.*, vol. 14, no. 1, pp. 96–103, Jan. 2014.

[4] F. Boldrini *et al.*, "Attitude sensors on a chip: Feasibility study and breadboarding activities," in *Proc. 32nd Annu. AAS Guid. Control Conf.*, Feb. 2009, pp. 1197–1216.

[5] C. Brandli, R. Berner, M. Yang, S.-C. Liu, and T. Delbruck, "A 240×180 130 dB 3 Vs latency global shutter spatio-temporal vision sensor," *IEEE J. Solid-State Circuits*, vol. 49, no. 10, pp. 2333–2341, Oct. 2014.

[6] J. A. Le nero-Bardallo, T. Serrano-Gotarredona, and B. Linares-Barranco, "A five-decade dynamic-range ambient-light-independent calibrated signed-spatial-contrast AER retina with 0.1 ms latency and optional time-to-first-spike mode," *IEEE Trans. Circuits Syst. I, Reg. Papers*, vol. 57, no. 10, pp. 2632–2643, Oct. 2010.

[7] C. Posch, D. Matolin, and R. Wohlgenannt, "A QVGA 143 dB dynamic range asynchronous address-event PWM dynamic image sensor with lossless pixel-level video compression," *IEEE J. Solid State Circuits*, vol. 46, no. 1, pp. 259–275, Jan. 2010.

[8] J. A. Le nero-Bardallo, T. Serrano-Gotarredona, and B. Linares-Barranco, "An asynchronous event-based temporal contrast vision sensor with 3.6 μs response time," *IEEE J. Solid-State Circuits*, vol. 46, no. 6, pp. 1443–1455, Jun. 2011.

[9] E. Culurciello, R. Etienne-Cummings, and K. A. Boahen, "A biomorphic digital image sensor," *IEEE J. Solid-State Circuits*, vol. 38, no. 2, pp. 281–294, Feb. 2003.

[10] J. A. Leñero-Bardallo, R. Carmona-Galán, and Á. Rodríguez-Vázquez, "A bio-inspired vision sensor with dual operation and readout modes," *IEEE Sensors J.*, vol. 16, no. 2, pp. 1–14, Jan. 2016.

[11] J. A. Leñero-Bardallo, D. Bryn, and P. Häfliger, "Bio-inspired asynchronous pixel event tricolor vision sensor," *IEEE Trans. Biomed. Circuits Syst.*, vol. 8, no. 3, pp. 345–357, Jun. 2014.

[12] L. Farian, P. Häfliger, and J. A. Leñero-Bardallo, "Miniaturized sun sensor with in-pixel processing for attitude determination of micro space probes," in *Proc. Int. Conf. Event-Based Control, Commun., Signal Process. (EBCCSP)*, Jun. 2015, pp. 1–6.

[13] J. A. Leñero-Bardallo, R. Carmona-Galán, and Á. Rodríguez-Vázquez, "A wide linear dynamic range image sensor based on asynchronous self-reset and tagging of saturation events," *IEEE J. Solid-State Circuits*, vol. 1, no. 1, pp. 1–13, Apr. 2017.

[14] J. A. Leñero-Bardallo, R. Carmona-Galán, and Á. Rodríguez-Vázquez, "A high dynamic range linear vision sensor with event asynchronous and frame-based synchronous operation," in *Proc. Electron. Imag., Image Sens. Imag. Syst.*, Feb. 2016, pp. 1–7.

[15] K. A. Boahen, "Point-to-point connectivity between neuromorphic chips using address events," *IEEE Trans. Circuits Syst. II, Analog Digit. Signal Process.*, vol. 47, no. 5, pp. 416–434, May 2000.

[16] J. A. Leñero-Bardallo, F. Pérez-Peña, R. Carmona-Galán, and Á. Rodríguez-Vázquez, "Pipeline AER arbitration with event aging," in *Proc. IEEE Int. Symp. Circuits Syst. (ISCAS)*, Baltimore, MD, USA, Mar. 2017, pp. 1–4.

[17] P. Häfliger, "A spike based learning rule and its implementation in analog hardware," Ph.D. dissertation, Inst. Neuroinform., ETH Zurich, Zürich, Switzerland, 2000. [Online]. Available: http://www.ifi.uio.no/~hafliger

[18] *jAER Open Source Project*. Accesed: Jan. 2017. [Online]. Available: http://sourceforge.net/projects/jaer/

[19] P.-F. Ruedi *et al.*, "A 128 × 128 pixel 120 dB dynamic-range vision-sensor chip for image contrast and orientation extraction," *IEEE J. Solid-State Circuits*, vol. 38, no. 12, pp. 2325–2333, Dec. 2003.

[20] M. Barbaro, P. Y. Burgi, A. Mortara, P. Nussbaum, and F. Heitger, "A 100×100 pixel silicon retina for gradient extraction with steering filter capabilities and temporal output coding," *IEEE J. Solid-State Circuits*, vol. 37, no. 2, pp. 160–172, Feb. 2002.

[21] C. Shoushun and A. Bermak, "Arbitrated time-to-first spike CMOS image sensor with on-chip histogram equalization," *IEEE Trans. Very Large Scale Integr. (VLSI) Syst.*, vol. 15, no. 3, pp. 346–357, Mar. 2007.

Juan Antonio Leñero-Bardallo (M'17) received the M.Sc. degree in telecommunications engineering and the Ph.D. degree in microelectronics from the University of Seville, Seville, Spain, in 2005 and 2010, respectively. From 2006 to 2010, he worked towards the Ph.D. degree sponsored by a national grant.

After the completion of the Ph.D. degree, he served in several academic institutions and the semiconductor industry. From March 2010 to September 2010, he was a Post-Doctoral Associate at Yale University, New Haven, CT, USA. From 2010 to 2013, he was a Post-Doctoral Associate at the University of Oslo. From 2013 to 2016, he was a Post-Doctoral Associate at the University of Seville, Spain. From March 2016 to September 2016, he was a Senior Engineer at Chronocam Inc.

Since September 2016, he has been an Assistant Teacher with the University of Cádiz, Spain, where he teaches and conducts research. He coordinates a course in electronics for the bachelor's degree of industrial engineering.

His main research interests include address event representation vision systems, frame-based vision sensors, smart sensors, wireless vision sensor networks, signal processing, and very large scale integration emulators of biological systems. Dr Leñero-Bardallo has been a member of the IEEE Sensory Systems Committee since 2012.

Lukasz Farian received the B.S. degree in automation and robotics from the Nicolaus Copernicus University, Torun, Poland, in 2012, and the M.Sc. degree in nanoelectronics and robotics from the University of Oslo, Norway, in 2014.

He is currently pursuing the Ph.D. degree in nanoelectronics with the University of Oslo with research focused on integrated circuits for space probes. In 2013, he was a Summer Analog Designer Intern with OmniVision Technologies, Oslo. In 2015, he completed a Space Studies Program from the International Space University, OH, USA. He is currently with Nordic Semiconductor Company. His research interests include neuromorphic electronics and attitude determination systems for space probes.

José-Maria Guerrero-Rodríguez received the B.Sc. degree in electronic engineering from the University of Cádiz, Spain, in 1987, the B.Sc. degree in physics, specialized in electronics, from UNED University, Madrid, Spain, in 1999, and the Ph.D. degree in industrial electronics from the University of Cádiz in 2009. He was with several electronic sector companies (telecommunications and hard disk drive manufacturing) as a Test-Engineer or R&D Engineer. He joined the Department of Systems Engineering and Electronics, Engineering School, University of Cádiz, as a Professor of Electronics in 1997. His research is focused on electronic instrumentation and sensors devices and AI techniques application on Intelligent Instrumentation. Also, he is working on other interest areas as analog design and embedded systems programming.

Ricardo Carmona-Galán (SM'16) received the degree in electronic physics and the Ph.D. degree in microelectronics from the University of Seville, Spain, in 2002. He was a Research Assistant with the EECS Department, University of California at Berkeley, Berkeley, and was an Assistant Professor with the School of Engineering, University of Seville. Since 2005, he has been a Tenured Scientist with the Institute of Microelectronics of Seville (CSIC-University of Seville). He has designed several vision chips implementing different focal plane operators for early vision processing. He also held a post-doctoral position with the University of Notre Dame, IN, where he worked on interfaces for CMOS compatible nanostructures for multispectral light sensing. His main research include the VLSI implementation of concurrent sensor/processor arrays for real-time image processing and vision. His current interest lie in the design of low-power smart image sensors, single-photon detection and ToF estimation, and 3-D integrated circuits for autonomous vision systems.

He has co-authored more than 140 journal and conference papers and a book on low-power vision sensors for vision-enabled sensor networks. He has co-invented several patents. He has collaborated with start-up companies in Seville (Anafocus) and Berkeley (Eutecus). He is member of the IEEE Circuits and Systems and Solid-State Circuits Societies, the IEEE Sensor Council and the ACM. He received the Certificate of Teaching Excellence from the University of Seville. He has been the Secretary-Elect of the IEEE CASS Technical Committee on Sensory Systems since May 2017. He has been Associate Editor of IEEE TCAS-I and is an Associate Editor of the *Journal on Real-Time Image Processing* (Springer).

Ángel Rodríguez-Vázquez (F'99) received the bachelor's degree and the Ph.D. degree in physics-electronics from the Universidad de Sevilla, in 1976 and 1982, respectively. After different research stays with the University of California at Berkeley, Berkeley, and Texas A&M University, he became a Full Professor of Electronics with the University of Sevilla in 1995. He co-founded the Instituto de Microlectrónica de Sevilla, a joint undertaken of the Consejo Superior de Investigaciones Científicas and the University of Sevilla and started a Resaerch Laboratory on Analog and Mixed-Signal Circuits for Sensors and Communications. In 2001, he was the Main Promotor and Co-Founder of the start-up company AnaFocus Ltd., and served as the CEO, on leave from University of Sevilla, until 2009, when the company reached maturity as a worldwide provider of smart CMOS imagers and vision systems-on-chip. He is currently a R&D Senior Technologiste with 2v Ltd.

He has authored 11 books, 36 additional book chapters, and some 500 articles in peer-review specialized publications. He has presented invited plenary lectures at different international conferences. His research is on the design of analog and mixed-signal front-ends for sensing and communication, including smart imagers, vision chips, implantable neural recorders/stimulators and biomedical circuits and with emphasis on system integration. His research work has received some 8,028 citations. He has an h-index of 46 and an i10-index of 163. He received a number of awards for his research, including the IEEE Guillemin-Cauer Best Paper Award, two Wiley's IJCTA Best Paper Awards, two IEEE ECCTD Best Paper Awards, one IEEE-ISCAS Best Paper Award, one SPIE-IST Electronic Imaging Best Paper Award, the IEEE ISCAS Best Demo-Paper Award, and the IEEE ICECS Best Demo-Paper Award. He received several national and international awards from the Universidad de Sevilla, including the IEEE Rogelio Segovia Torres Award in 1981.

He has always been looking for the balance between long-term research and innovative industrial developments. He was the Main Promotor and a Co-Founder of AnaFocus Ltd., and he participated in the foundation of the Hungarian start-up company AnaLogic Ltd. He has eight patents filed, some of which are licensed to companies. AnaFocus was founded on the basis of his patents on vision chip architectures.

Dr. Rodríguez-Vázquez has served as an Editor, an Associate Editor, and the Guest Editor of the IEEE and non-IEEE journals, is on the committee of several international journals and conferences, and has chaired several international IEEE and SPIE conferences. He served as VP Region 8 of the IEEE Circuits 1087 and Systems Society from 2009 to 2012, and as the Chair of the IEEE CASS Fellow Evaluation Committee in 2010, 2012, 2013, 2014, and 2015.

Paper VI:

Ł. Farian, P. Häfliger, J.A. Leñero-Bardallo
A Miniaturized Two-Axis Ultra Low Latency and Low-Power Sun Sensor for Attitude Determination of Micro Space Probes
IEEE Transactions on Circuits and Systems I: Regular Papers, 2017

A Miniaturized Two-Axis Ultra Low Latency and Low-Power Sun Sensor for Attitude Determination of Micro Space Probes

Łukasz Farian, *Member, IEEE*, Philipp Häfliger, *Senior Member, IEEE*, and Juan A. Leñero-Bardallo, *Member, IEEE*

***Abstract*— This paper describes design, fabrication process, and comprehensive experimental results of a first prototype two-axis miniaturized spiking sun sensor. The sun sensor is a fusion of analog and digital sensor types, such that it takes advantage of spatial selectivity of digital sensors, and is not limited by the global frame rate as in analog sun sensors. It is composed of spiking pixels, and uses a novel Time-to-First-n-Spikes with time-out readout mode to reduce bandwidth consumption and post-processing computation. A thin glass lid with a metal deposited pattern serves as a mask projecting a light pattern onto the sensor. The sun sensor is able to extract a profile of the incident light in the form of time-stamped events. Its latency depends on light intensity, and for medium radiance conditions is equal to 88 μs. The sun sensor consumes 6.3 μW in normal operation, and has a precision of 0.98°, and a field of view of 144°. The high temporal resolution, low power consumption, and small QFN64 package make this sun sensor suitable for space probe and sounding rocket applications, where low temporal latency and payload size are essential. This sun sensor is designed to be employed in the sounding rocket attitude determination system as part of the 4DSpace research initiative to study ionospheric plasma disturbances.**

***Index Terms*— Sun sensor, AER, attitude determination, even-based vision sensor, space probes, angle measurement, cover glass, field-of-view (FOV).**

I. Introduction

SUN sensors hold a key role in many different systems, either in space or terrestrial applications. In space, sun sensors are used in satellites, sounding rockets, or space probes as a part of the Attitude Determination System (ADCS) to determine the orientation of space instruments. Sun sensors, together with magnetometers and gyroscopes provide detailed information about the instrument attitude. The information about the attitude is critical for the safety of a spacecraft, as it helps to maintain its stabilized orientation, or prevent high spin rates. As the carrying capacity of spacecrafts and sounding rockets is limited, sun sensors must meet design constraints of size, restricted power budget and mass. As for terrestrial applications, sun sensors help track the location of the sun in the sky to adjust the orientation of the photo-voltaic devices and improve their efficiency. The sun is a very useful celestial body to use as a reference, because it is the brightest object in our solar system. When it is observed from earth, the sun has a small enough radius to be modeled as a point source [1]. Sun sensors provide orientation with reference to the sun typically in two axes in the instrument's coordinates: azimuth and elevation. Reference [2]–[5] use patterned masks, such as slits, pinholes or multi-aperture arrays to project the pattern on the photosensitive sensors located underneath. Based on the location or some geometrical properties of this pattern, these sensors determines the sun vector.

Sun sensors can be divided into two groups: digital and analog. Digital sensors sense the light by small photosensitive pixels organized in a line [5] or array [2], [3]. Pixels absorb photons and release electrons through the photoelectric effect. These electrons are accumulated over a specific length of the exposure time as an electrical charge in a PN junction, which is then transferred and digitized. For each array readout, digital sun sensors generate raw data from the entire focal plane with a fixed frame rate. In order to extract information about the sun vector, additional post-processing is required to implement geometric algorithms [6]. These algorithms are complex and use special techniques [7] to accurately estimate the peak-illumination pattern. Since the sun vector is typically recalculated for each frame readout to maintain high accuracy, this approach is not efficient in terms of power consumption and data bandwidth. Additionally, the frame rate of the readout limits the temporal resolution of the sensor.

Analog sensors are comprised of only a few much bigger photodiodes [4], [8] and simpler patterned masks. Analog sun sensors obtain the sun vector from the ratios of the photocurrents from only a few photodiodes as an analog value. Because of their analog operation, they are not limited by the global frame rate, they produce less data, and consume less power. On the other hand, analog sun sensor are not robust to spurious readouts from light distortions or reflections. In other words, analog sun sensor always translate all reflections, light from

Manuscript received May 6, 2017; revised July 29, 2017 and September 26, 2017; accepted October 12, 2017. Date of publication November 2, 2017; date of current version April 2, 2018. J. A. Leñero-Bardallo was supported in part by the University of Cádiz under Grant PR2016-072, in part by Junta de Andalucía CEICE (SMARTCIS-3D) under Grant TIC 2012-2338, and in part by ONR (HCELLVIS) under Grant N000141410355. This paper was recommended by Associate Editor Z. Tan. *(Corresponding author: Łukasz Farian.)*

Ł. Farian and P. Häfliger are with the Nanoelectronics Group, Department of Informatics, University of Oslo, 1072 Blindern, Norway (e-mail: lukaszf@ifi.uio.no; hafliger@ifi.uio.no).

J. A. Leñero-Bardallo is with the Superior College of Engineering, University of Cádiz, Avda, Universidad de Cádiz, Campus Universitario de Puerto Real, 11519 Cádiz, Spain (e-mail: juanantonio.lenero@uca.es).

Color versions of one or more of the figures in this paper are available online at http://ieeexplore.ieee.org.

Digital Object Identifier 10.1109/TCSI.2017.2763990

other bright celestial bodies, and stray light into photocurrents with no possibility of spatial selection or exclusion of these distractors, unlike digital sun sensors.

This paper presents a new spiking sun sensor which is a fusion of analog and digital sensor types, such that it takes advantage of spatial selectivity of digital sensors, and is not limited by the global frame rate as in analog sun sensors. The presented sensor consumes less power that any reported sun sensor, and is integrated inside a very small QFN64 package with micro-optics on top. Its small size and low power consumption make this sun sensor suitable to be employed as a part of ADCS systems for any type of space craft.

As a first target application the developed sun sensor is planned to be integrated in a sounding rocket used for studying ionospheric plasma disturbances. The spin-rate of the rocket during its flight can reach 300 rpm. Therefore, high temporal resolution and very low readout latency response was identified as a design priority.

Basic concept and simulations of this sun sensor have been shown in EBCCSP 2015 [9]. In this paper we provide comprehensive experimental results of the developed sensor, we analyze its performance and compare it to existing state-of-the-art solutions.

This article is organized as follows: Section II introduces the sun sensor concept, and describes its basic structure. Section III provides the design details of the electronic part and integration of the sensor optics. Section IV describes the experimental setup used to evaluate the performance of the sun sensor. Calibration procedure and detailed experimental results for a single pixel and the entire sun sensor are provided. Section V combines the results from the previous section and compares the features and performance of this work with other developed sun sensors. Finally, Section VI draws some conclusions and suggests further system improvements.

II. System Concept

Fig. 1 shows the sun sensor structure: it consists of the chip which is wire bonded inside the QFN64 package, and a thin glass lid with a metal deposited pattern covering this package. The chip comprises two one-dimensional pixel lines organized in an L-shape, and the glass lid located above contains also L-shape slit rotated 180° with respect to the arrays. The principal operation of the sun sensor is to detect two intersection points of illuminated sunlight pattern (yellow color in Fig. 1) and photosensitive pixels lines (red color). As illustrated in Fig. 1, the intersection points' distance Δx from the pixel lines centers indicates the sun's deviation from the orthonormal position. The relation between the distance Δx and the sun deviation angle α from the orthonormal position is expressed by a geometrical dependency, which is discussed in Section III-B.

Note that the L-shape optical slit above the chip extends beyond the borders of the chip. With such a configuration we obtain a symmetrical field of view for both axes and with proper sizing of the micro-package we avoid the case when the input beam entirely overlaps along one pixel array, and

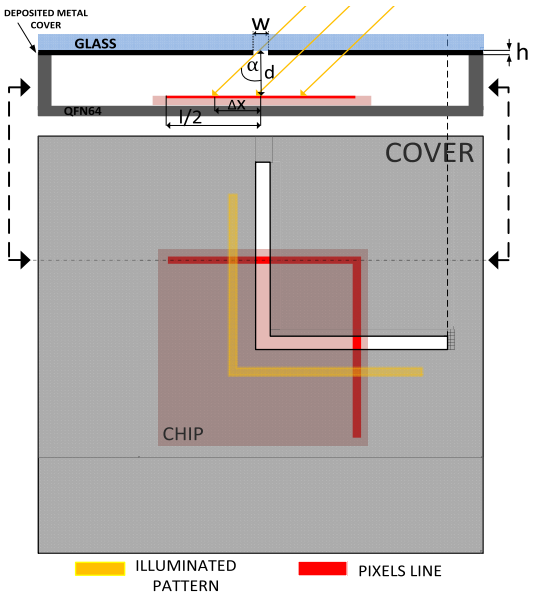

Fig. 1. Vertical cross-section and horizontal view of the sun sensor structure, $d = 356\ \mu$m, $h = 100$ nm, $W = 50\mu$m, $l = 2256\mu$m.

ensures that there are always at most two intersection points between beam and the pixel array.

For any non-orthonormal orientation, the sun projects an L-shape pattern shifted from the center of the pixel vectors and the distance from the center of these pixel vectors indicates the sun's deviation from the orthonormal position. Since the distance d between the chip and the lid has a constant value, the sun angle α can be calculated from this trigonometric function of Δx. The intersection points are sensed by spiking pixels, which are the base components of activity-driven, event based vision sensors. This type of vision sensors conveys compressed image information in the form of time-encoded events [10], [11] instead of conventional frames.

III. System Design

Fig. 2 shows the system block diagram for the electronic part of the sun sensor. It consists of two one-dimensional spiking pixel lines organized in L-shape manner, the Address Event Representation (AER) communication peripherals [12] with *Timer&Counter* blocks [13], and the arbiter.

A. Pixel Design

Each pixels line contains 192 spiking pixels. The principle of operation of the pixel is similar to an Integrate-and-Fire (I&F) neuron described by Carver Mead in [14], with the difference that it is not self-resetting, and that the refractory period is not controllable. The pixel translates the input photocurrent I_{ph} into spike latency T, such that the pixel spiking frequency f_{spike} is proportional to the incident light illumination:

$$f_{spike} = \frac{1}{T} \approx \frac{I_{ph}}{(V_{DD} - V_{ref}) \cdot C_{tot}} \quad (1)$$

Voltage $V_{DD} - V_{ref}$ is the voltage drop required for the pixel to spike. The total capacitance seen by the photodiode is $C_{tot} = C_{j0} + C_1 = 1fF + 529fF = 530fF$, where C_{j0} is the junction capacitance of the photodiode D1, and C_1 is the capacitance of a MOS capacitor ($11\mu m \times 10.75\mu m$). The input photocurrent I_{ph}, proportional to the incident light, discharges the capacitor C_{tot} until the threshold V_{ref} of the comparator is reached. When the voltage threshold is exceeded, the pixel sends out a request *REQ<n>* following with the unique pixel address to the AER peripherals [12]. Low signal *RES<n>* from the AER arbitration system recharges the capacitor C_1 through transistors M2, and resets the pixel. The transistor M1 disconnects the photodiode D1 from the reset transistor M2 to ensure that the pixel reset time does not depend on the photodiode current I_{ph}. If transistor M1 was not implemented, more time would be required to reset the pixels which are strongly illuminated, compared to those less illuminated. The AER arbitration system can properly arbitrate events which occur at least 100 *ns* after each other. If only a junction capacitance C_{j0} was seen on node V_1, the pixels response latency would easily drop below 100 *ns* for light of a moderate irradiance. Therefore, an additional capacitor $C_1 = 529\ fF$ was integrated in the pixel in order to increase its spike latency up to 100 μs for expected sun irradiance. More detailed description of the pixel operation can be found in a previous work reported by the same authors [9].

B. Time-to-First-Spike and Time-Out Operation

The pixel array is controlled by the AER arbitration system with a Time-to-First-n-Spikes (TFnS) with time-out readout mode described in [13]. TFnS is a communication framework extension of the Address Event Representation (AER) communication protocol [12] which enables arbitration and readout of a programmable number of pixels within a programmable time-out limit. The basic principle of TFnS framework is to perform a global reset of all pixels inside one array after the first n pixels have spiked or after a given time-out. As shown in Fig. 1, the L-shape sunlight pattern illuminates only a small portion of the pixels line. TFnS prioritizes the readout of these most illuminated pixels, and suppresses the rest. The *Counter & Timeout* block shown in Fig. 2, is the extension circuitry for implementing TFnS readout mode. The *Counter & Timeout* block is assigned an unique address, and it communicates with the AER arbitration system like the other pixels. It monitors how many acknowledge signals the sensor receives on *BUS_REQ_X* and *BUS_REQ_Y* and resets all pixels periodically or after a specific number of pixels has spiked. More detailed description of the dependencies of asynchronous signals between pixels, *Counter & Timeout* block and external interface is given in [13].

Since both horizontal and vertical pixels lines work independently, their 8-bit address buses and handshake signals (BUS_REQ and BUS_ACK) must be first arbitrated and multiplexed by the arbiter, before they are sent off-chip. The arbiter provides a 9-bit off-chip address bus which contains 8-bit encoded location of the spiking pixels and one additional bit indicating whether the horizontal or vertical array address is multiplexed at the given time.

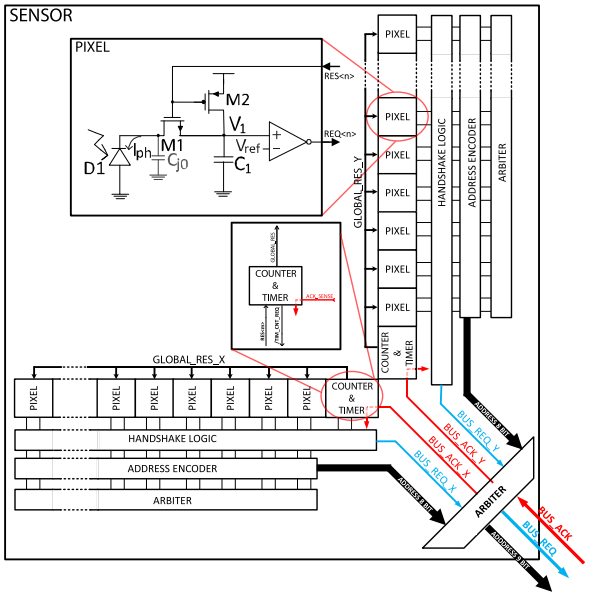

Fig. 2. Block level view of the sun sensor core electronics. It consists of two one-dimensional pixel lines organized in L-shape manner and the AER communication peripherals. C_1 is a MOS capacitor (11μm $\times$ 10.75μm). Size of D1: 5μm $\times$ 5μm. Total capacitance: $C_{j0} + C_1 = 530fF$.

TABLE I
DIMENSIONS USED TO CALCULATE THE SENSOR FOV

W	d	l	h	PIX_{pitch}
$50\,\mu$m	$356\,\mu$m	$2256\,\mu$m	100 nm	$11.75\,\mu$m

C. Optics Integration

The thin glass lid with a metal deposited pattern serves as a mask projecting a light pattern onto the sensor. The mask was manufactured by depositing a $100nm$ thick light reflecting nickel chromium metal film on a $600\mu m$ thick microscope glass. The glass with the deposited pattern was diced into a 9×9 mm square which fits the QFN64 package. The lid parameters are provided in Table I.

Fig. 3 top shows a microphotograph of the QFN64 package with wire-bonded chip inside, and Fig. 3 bottom shows a complete sun sensor with L-shape mask attached on the top of the package. The deposited metal was flipped down towards the QFN64 package to avoid light penetration through the gap between the mask and the package from the sides.

Fig. 4 shows how a sun vector is determined with respect to the sun sensor coordinate system. The corner of the L-shape slit serves as the origin of the sensor coordinate system. Angles θ and ϕ are projected on the XZ and YZ planes. For $\theta = \phi = 0°$ the sun is located perpendicular to the sun sensor. Based on geometrical dependencies from Fig. 1 the azimuthal

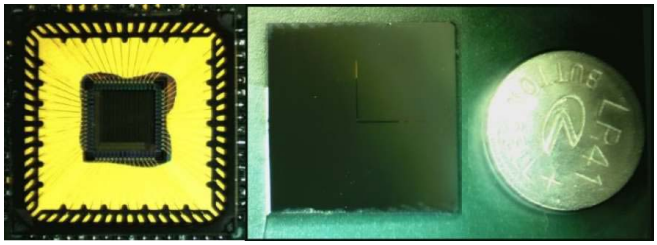

Fig. 3. QFN64 package with wire-bonded chip (left), and complete sun sensor implementation with L-shape mask attached on top (right). Size: 9.5 × 9.5 × 1 *mm*. A standard LR41 watch battery is shown for comparison.

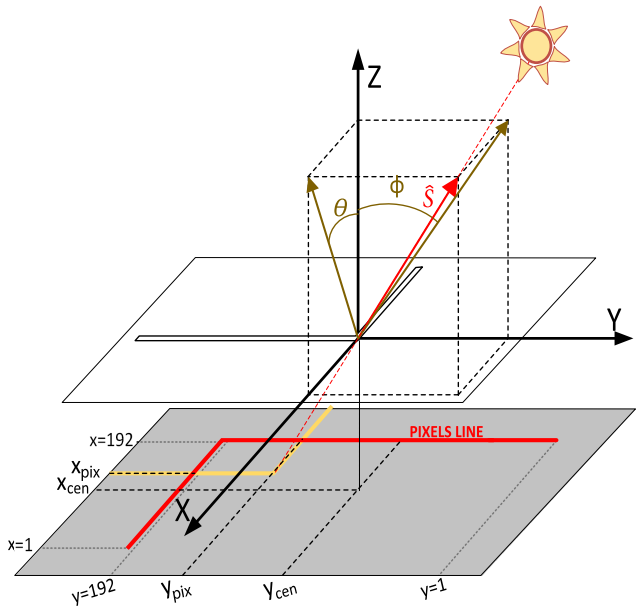

Fig. 4. Sun vector in sun sensor's coordinate system.

angle θ is given as:

$$\theta = \arctan\left(\frac{\Delta x}{d}\right) = \arctan\left(\frac{(x_{pix} - x_{cen}) \cdot PIX_{pitch}}{d}\right) \quad (2)$$

where Δx is the distance from the center of the pixel vector, x_{cen} is the pixels line location equivalent to the orthonormal orientation of the sun, and PIX_{pitch} is the pixel pitch. Both x_{cen} and x_{pix} are expressed as pixels addresses inside the pixels vector, and they can take values between 1 and 192. Similarly, the polar angle ϕ is given as:

$$\phi = \arctan\left(\frac{\Delta y}{d}\right) = \arctan\left(\frac{(y_{pix} - y_{cen}) \cdot PIX_{pitch}}{d}\right) \quad (3)$$

The unit vector $\hat{S}$ which points towards the sun with respect to the sun sensor's coordinate system is given as:

$$\hat{S} = \frac{[cot(90° - \theta) \quad cot(90° - \phi) \quad 1]^T}{\sqrt{S_s^T S_s}} \quad (4)$$

S_s is a non-normalized sun vector:

$$S_s = \begin{bmatrix} X_s \\ Y_s \\ Z_s \end{bmatrix} = \begin{bmatrix} cot(90° - \theta) \\ cot(90° - \phi) \\ 1 \end{bmatrix} \quad (5)$$

The maximum sun angle detectable by the sensor is the extreme position of illuminated pattern shown in Fig. 1 and can be derived as:

$$\theta_{max} = \phi_{max} = min\left[arctan\left(\frac{l}{2 \cdot d}\right), arctan\left(\frac{W}{h}\right)\right] \approx arctan\left(\frac{l}{2d}\right) \quad (6)$$

From Fig. 1, l is the length of the pixel array, d is the distance between the pixel array and the metal mask, W is the width of the slit, and h is the thickness of the metal mask. Field-of-view is limited either by the pixel array length or the slit dimensions. Since the slit width is much wider than the metal thickness, the second term in Eq. 6 can be ignored. Considering the parameters shown in Table I, the sun sensor azimuthal and polar field-of-view is: $FOV_\phi = FOV_\theta = 2 \cdot \theta_{max} = 2 \cdot \phi_{max} = 144°$.

IV. Experimental Results

An integrated circuit with core electronics was fabricated in the AMS 0.35μm CMOS image sensor process. This is an optimized standard process to obtain better responsivity of the photodiodes due to an extra anti-reflective coating (ARC). The AER data from the sun sensor was logged by the USBAERmini2 board [15] and this data was then sent through a USB port to a PC. A custom Java interface [16] was adapted to show real time pixels spikes and also reconstructed angle.

Fig. 5 shows a chip microphotograph (top) and the layout of 4 pixels (bottom). The AER communication peripherals are located under the pixels vector. Only the outer bottom and outer left areas of the chip are occupied by the sensor (8% of the chip area) and the remaining chip area is available for other SoC interfaces.

A. Experimental Setup

Fig. 6 shows a photograph of the experimental setup used for characterization of the sun sensor. The PCB with the sun sensor was attached to the pan-tilt unit PTU-D300 to rotate the sensor in pitch and yaw with respect to a light source. A sun sensor sent out data to a computer through a USBAERmini2 [16] PCB. To characterize the sun sensor accuracy, a halogen work light was placed 5 meters away from the sun sensor to imitate a real sun, e.g. a light source at infinite distance.

The readout latency was characterized for a direct sunlight. Since the measurements were carried out in Norway in winter season, the solar radiation receipt was a fraction of the total solar irradiance. Aside from the readout latency, testing the sun sensor at a fraction of the total solar irradiance (either due to high latitude or use of halogen lamp) did not affect the accuracy of the reported measurements, except for the readout latency which is expected to be better for total solar irradiance exposure.

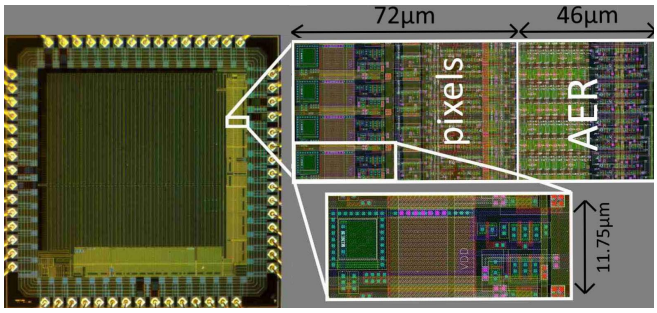

Fig. 5. Microphotograph of the chip (top), layout of 4 pixels (bottom). Chip dimensions: 2.5 mm × 2.5 mm, pixel pitch: 11.75 μm, pixel length: 72 μm

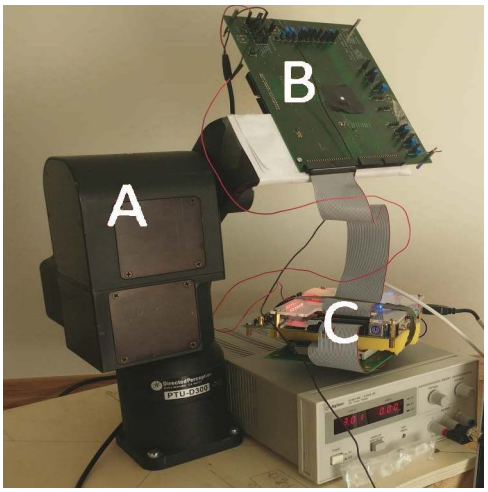

Fig. 6. Experimental setup to characterize sun sensor accuracy, A - Pan-tilt Unit, B - PCB with sun sensor, C - USBAERmini2 PCB reading data.

Example video illustrating operation of the sun sensor attached to the PTU is provided in [17].

A model with rotation matrices was developed to transform pan and tilt of the PTU to pitch and yaw of the sun sensor with respect to the halogen lamp source.

The graphical user interface is shown in Fig. 7. The interface displays locations of pixels spikes in time, and provides current azimuthal and polar angles in real time.

B. Alignment and Calibration

Any misalignment between the L-shape pattern mask and the pixel vectors degrades the sun sensor accuracy. There are two main sources of misalignment: fabrication accuracy of the L-shape pattern and die attach accuracy. The L-shape pattern mask was fabricated with high accuracy and resolution of $\pm 100nm$, and the die was attached inside the package with an accuracy of $\pm 250\mu m$. Taking into account that the pixel pitch is $PIX_{pitch} = 11.75\mu m$, the worst case misalignment between the L-shape mask and the pixel vectors is 21 pixels. In the next step, the sun sensor was exposed to the orthonormal light ray, and the glass lid position was accurately adjusted until pixels addresses for both the azimuth and elevation were identical. As illustrated in Fig. 8, if the intersection points between both pixel vectors and the incident orthonormal light ray pattern are the same, the pattern mask and the pixel vectors are aligned. The alignment accuracy of this calibration method is equal to $\pm\frac{1}{2}PIX_{pitch}$.

The sun sensor orientation was swept in azimuthal plane from $-90°$ to $+90°$, while the polar angle was constant and equal to $0°$ with respect to the halogen lamp. Recorded

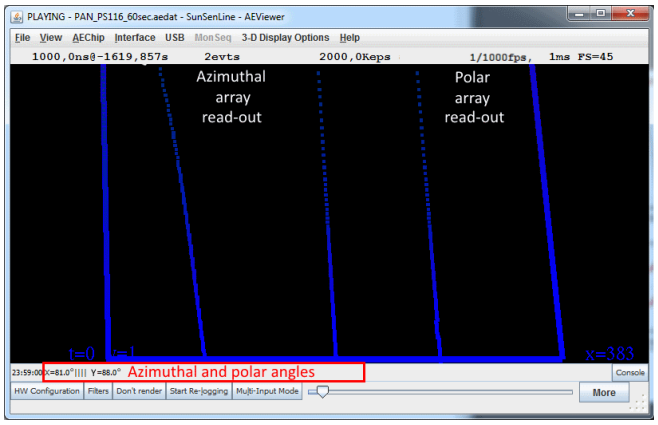

Fig. 7. jAER interface adapted to readout azimuthal and polar angles. Locations of active pixels are represented along time scale (y-axis).

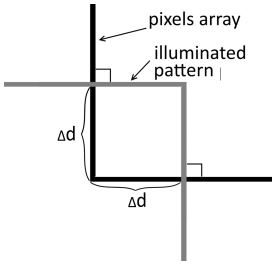

Fig. 8. The same intersection points (Δd) between the pixel vectors and the incident orthonormal light ray pattern ensure alignment between pattern mask and the pixel vectors.

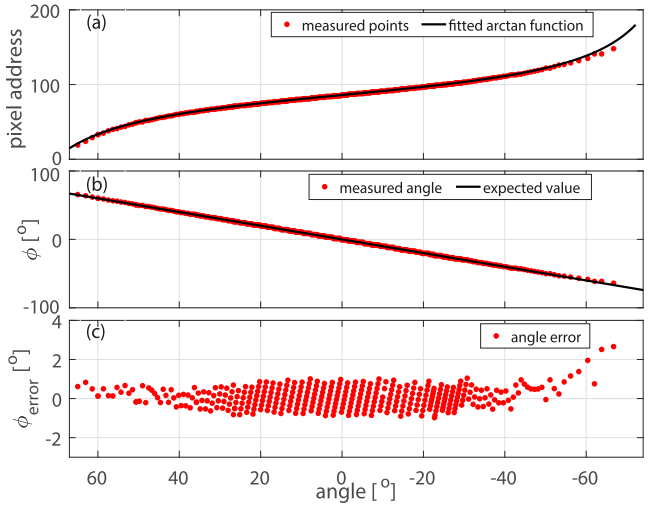

Fig. 9. Measured azimuthal pixel addresses, for the sun sensor orientation swept from $-90°$ to $+90°$, and fitted *arctan* function (a), corresponding angles after using a fitting function compared with expected angles values (b), error between measured and expected angle (c).

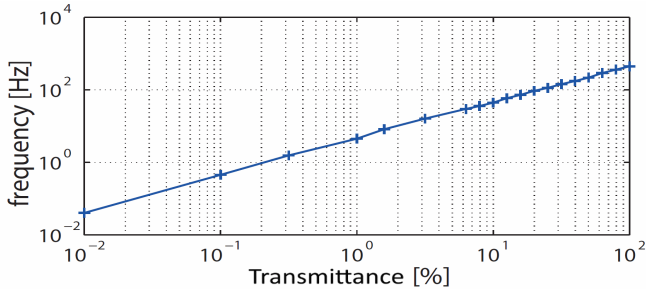

Fig. 10. Pixel spiking frequency versus light intensity. Reference light irradiance for transmittance of 100% is 2W/m^2.

pixel addresses for azimuthal plane are shown in Fig. 9(a), where x-axis represents sensor rotation in degrees, and y-axis represents recorded pixel addresses. Function from Eq. 7 was fitted to the recorded data, and two coefficients: x_{cen} and d were obtained by curve best fitting.

$$\theta = \arctan\left(\frac{(x_{pix} - x_{cen}) \cdot PIX_{pitch}}{d}\right) \tag{7}$$

The pixel pitch is equal to $PIX_{pitch} = 11.75\mu m$. The overlapping black line in Fig. 9(a) shows the fitted function with extracted coefficients: $d = 356\mu m$, and $x_{cen} = 86$. Fig. 9(b) shows measured angle ϕ with use of the fitted function, and Fig. 9(c) shows error between measured and expected angles. For angles ϕ between $\pm 60°$, the error is equal to the quantization error, and is related to the sensor resolution. Maximal error is located at negative endpoint of the sensor field-of-view, and is equal to 2.65°.

The error between measured and expected angles in Fig. 9(c) shows a clear sawtooth pattern which is caused by the quantization error. Due to uneven steps between the consecutive output angle values the sensor resolution varies across its field-of-view. The sun sensor quantization error $\Delta\theta$ is given as:

$$\Delta\theta = \frac{\partial\theta}{\partial x_{pix}} = \frac{d \cdot PIX_{pitch}}{d^2 + PIX_{pitch}^2 (x_{pix} - x_{cen})^2} \tag{8}$$

The quantization error varies across the sensor FOV between $0.22° - 1.89°$, and it reaches its maximum $\Delta\theta = PIX_{pitch}/d = 1.89°$ for perpendicular light.

C. Sensor Performance

In Subsection IV-C experimental results are reported. Subsections IV-C1 and IV-C2 help the reader understand how the pixel and the AER arbitration system operate in the TFnS mode. Single pixel principal operation and the handshake signals exchanged between the AER arbitration system and the pixel are presented. These two experiments were performed without the mask installed. Subsection IV-C3 shows how the pixel readout would look like without TFnS and time-out readout modes implemented. The remaining tests reported in this subsection (IV-C4-IV-C8) present performance of a complete system with the mask installed and aligned with the detector. Subsection IV-C4 illustrates advantages of using time-out readout mode. In Subsections IV-C5 and IV-C6 sensor latency response and accuracy are reported. Subsection IV-C7 shows how the sun sensor can extract the profile of the incident light. Finally, power consumption of the system is reported in Subsection IV-C8.

1) Pixel Sensitivity to Light: To illustrate the relation between pixels spiking frequency and the incident light intensity, neutral density filters of transmittance from 100% down to 0.01% were placed between the sensor and the coherent light source. Pixels were configured as free running, in order not to constrain their spiking frequency with TFnS nor time-out readout mode. In free running mode, TFnS and time-out readouts are disabled and the sun sensor works as a standard event-based sensor, e.g. pulse frequency modulator (PFM). Fig. 10 shows the pixel spiking frequency f_{spike}, which is linearly proportional to the light intensity according to Eq. 1. Based on Fig. 10, the dynamic range (DR) of the sensor is at least $20 \cdot log_{10}(10\,000) = 80dB$. The linearity of the spiking frequency within the measured range of light intensity is measured by coefficient of determination, and is equal to $R^2 = 99.94\%$.

2) TFnF Operation: A single pixel operation, for TFnS disabled and enabled is shown in Fig. 11(a-b) and Fig. 11(c-d) respectively. For this experiment, the pixel array was illuminated by uniform white light. The pixel input voltage of the comparator V_1 and handshake signals between the pixel and the AER peripherals $REQ< 1 >$ and $RES< 1 >$ are shown in Fig. 11. When the TFnS mode is disabled, a typical Integrate-and-Fire ($I\&F$) neuron operation (i.e. pulse frequency modulation (PFM)) is observed, e.g. whenever voltage V_1 exceeds the threshold V_{ref} the pixel spikes and generates a request $REQ < 1 >$. The input photocurrent from photodiode D1 discharges the capacitor C_1 until the threshold V_{ref} is of the comparator is reached. This triggers the request pulse $REQ < 1 >$, and in return, the AER arbitration system pulls down RES$< 1 >$ to reset the pixel. Fig. 11b) shows a closer look at a single handshake cycle.

When TFnS mode is enabled, the pixel does not operate as a typical I&F neuron. As shown in Fig. 11c) and d), when the request pulse REQ<1> is triggered, the AER arbitration system pulls down and keeps RES<1> low until the AER arbitration system counts overall 15 pixels spikes, before the next cycle can start.

3) Free-Running Mode: This experiment illustrates how the pixel readout would look like if the TFnS and time-out readout modes were not implemented, i.e. PFM. Fig. 12 shows measured response of the azimuthal array for the sun sensor operating in free-running mode, and for a static near-perpendicular light source. The closer to the $\theta = 0°$ position, the higher the PFM. Fig. 13 shows the same data, but as spiking frequency obtained by averaging pixels spikes over 1 sec. The highest spiking frequency is observed for an angle $-1.83°$ and is equal to 3.3 kHz. Mean value and standard deviation of the distribution is equal to $\bar{\theta} = -1.66°$ and $\theta_\sigma = 25.1°$, respectively. Two horizontal lines without data are places where the communication between the sun sensor and the receiver was corrupted by buffer overrun inside USBAERmini2. Since in free-running mode all pixels were allowed to spike with no time-out constraints, nor with a

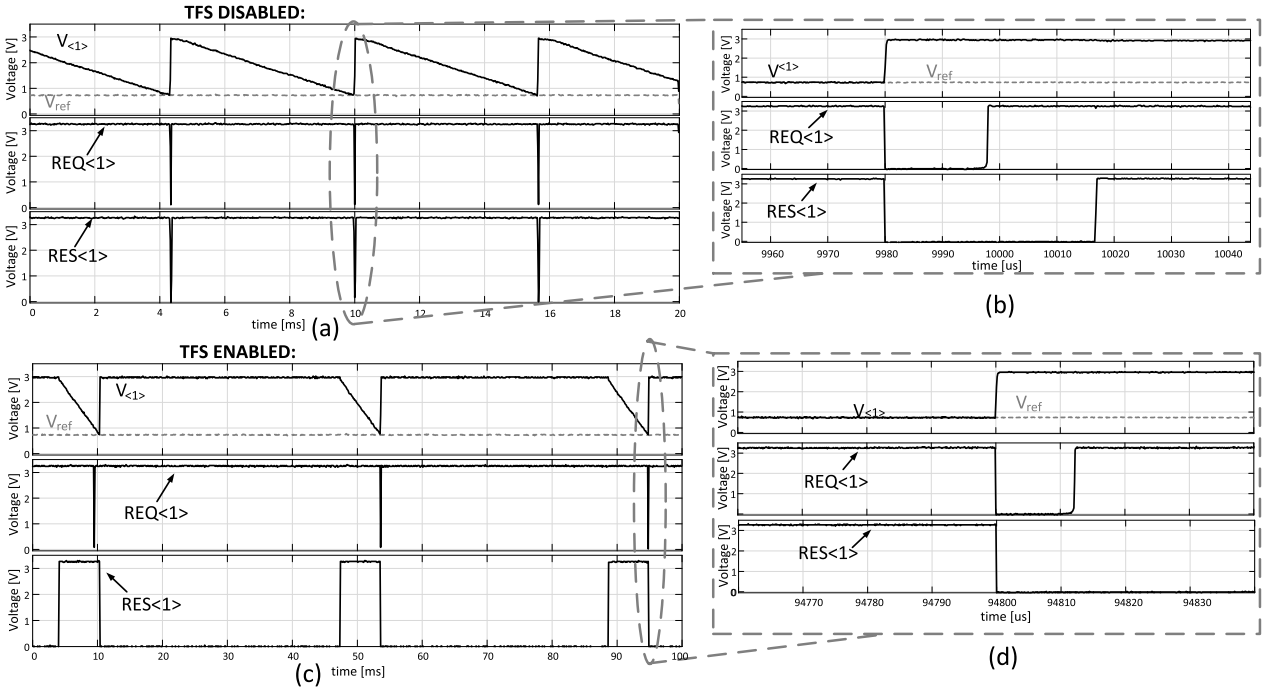

Fig. 11. Measured single pixel response and handshake signals to a radiant flux of 64 W/m^2 for the TFS mode disabled ((a),(b)), and TFS mode enabled (c),d)). V_1 is the input voltage of the comparator, the grey dashed line shows the value of the threshold voltage V_{ref} set to $0.7V$, REQ<1> and RES<1> are the handshake signals between the pixel and the AER peripherals.

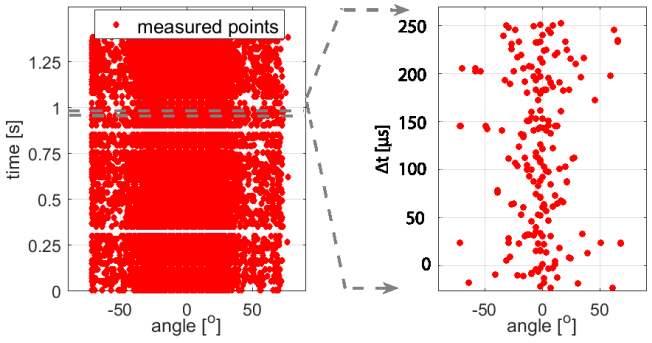

Fig. 12. Sun sensor operating in free-running mode.

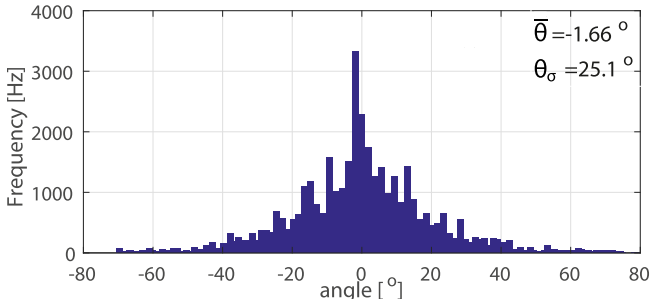

Fig. 13. Frequency of readout versus angle for free-running mode, $\mu = -1.66°$, $\sigma = 25.1°$.

limit of winners, an instantaneous spiking frequency of the entire array exceeded the maximum data rate of the receiver (10 *Meps*).

4) Time-Out Mode: Fig. 14 illustrates the readout of the array for the same light conditions as in the previous test, but the sun sensor configured in time-out readout mode. The time-out slot was set to $18ms$. Fig. 14(a) shows a global reset flag (address all zeros) and Fig. 14(b) and (c) show azimuthal angle readout for two different timescales. All pixels corresponding to angles θ between $-66°$ and $68°$ spiked within the given time-out slot. The readouts encoded in time differences follow the intensity profile of a Gaussian beam, with a maximum plateau located at an angle of $-1.89°$, and a symmetrical drop-off observed on both sides of the plateau.

Results in Fig. 14 show the advantage of time-out readout mode over free-running readout mode in terms of data bandwidth. The sensor generated approximately 1000 times less data in time-out mode to obtain the same information about the profile of the incident light as in free-running mode. A time-out mode together with TFnS mode is also useful to discard spurious readouts when the Sun is not within the sun sensor field of view. If the time-out is set properly, spurious readouts due to reflections from the Moon and the Earth can be avoided. As a result, if the sun sensor is not exposed to the direct sunlight, it will not transfer any data, except the reset flag, with address all zeros, indicating that time-out occurred.

The output current of the photodiode decreases to the cosine of the sunlights angle of incidence [18]. At the maximum viewing angle, the output current will be equal to 31.2% of the expected maximum solar energy which is delivered for orthonormal light. Albedo of the Earth and the Moon is equal to 30% [19] and 13.6% [20] respectively. In order to avoid

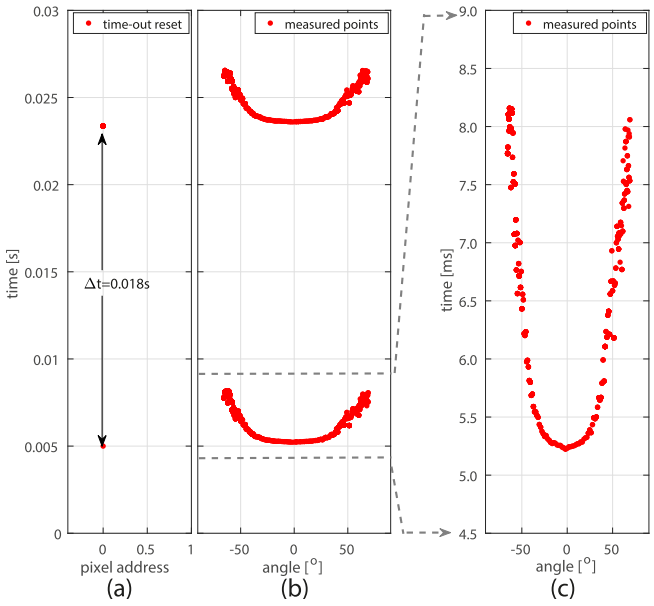

Fig. 14. Illustration of time-out readout mode for an azimuthal angle, with a near-perpendicular light and static sun sensor. The time-out slot was set to $18ms$. Figure (a) shows a global reset flag, (b) and (c) - show the readout of azimuthal angle in two different timescales.

spurious readouts due to Earth and Moon albedo, the time-out threshold should be set marginally below the calculated 31.2% of the expected maximum solar energy. This approach ensures that the time-out is long enough for the most outer pixels corresponding to the sensor maximum viewing angle to spike, but also the time-out is short enough to discard potential spurious readouts due to Earth and Moon albedo. A small reduction of the FOV can be considered in further designs in case higher margin proves to be necessary after performing tests in-flight.

5) Latency: The sun sensor, with TFnS and time-out readout modes enabled, was rotated in the polar plane with a rotational speed of 300 rpm, which is the maximum expected rotational speed of a sounding rocket during a flight. The sun sensor was exposed to direct sunlight of irradiance 240 W/m^2. The measured polar angle for a 5 rps experiment is shown in Fig. 15(a). Fig. 15(b) shows a latency between two consecutive sensor readouts. Fig. 15(c) and (d) show a closer look at angle and readout latency around 0°. The latency is equivalent to the spiking frequency of the sun sensor. For a moderate irradiance of 240 W/m^2 the speed of the sun sensor is $11.3keps$. The dominating contributor to the readout delay is the discharge of the capacitor C_1 by the photocurrent, until the threshold V_{ref} is reached. This delay is proportional to the illumination, and it explains the curved shape of the readout latency in Fig. 15(b). The latency reaches its minimum of $88\mu s$ for orthonormal light (0°), and it increases as the incident light angle decreases. Therefore, the sun sensor speed depends on the angle of the incident light. The other contributors to the readout delay are the handshake cycle between the array and the USBAERmini2 receiver, and the global reset phase. They are usually much shorter than the first contributor, and equal to $15\mu s$. The measured latency follows a periodic pattern, which is an effect of the TFnS mode. During each readout cycle the TFnS framework prioritizes only one most illuminated pixel, and suppresses the rest. The effect of TFnS is that the peaks of the time delay indicate when the illuminated light pattern perfectly overlaps with the winning pixel, and the maximum solar energy is delivered to this pixel. When the illuminated pattern continues shifting towards the neighboring pixel, time to discharge of the capacitor C_1 by the photocurrent increases. After the minimum of the time delay is reached, the neighboring pixel receives more energy, and it becomes the next winner.

6) Accuracy and FOV: Fig. 16 shows the sun sensor accuracy within its FOV. For this experiment, a sun sensor was attached to the PTU to sweep its orientation with respect to a halogen lamp placed 5 meters away from the sun sensor. The lamp provided an irradiance of 2.4 W/m^2 to the surface of the sun sensor. More than 200 points of different combinations of polar ϕ and azimuthal θ angles were measured. Fig. 16(a) and Fig. 16(b) illustrate the sun sensor accuracy test, where x- and y-axis are predicted angles, and z-axis is the measured angle. A green plane serves as predicted angles reference. Fig. 16(c) and Fig. 16(d) show a spread of the angles θ and ϕ around the predicted value. RMS error is $\theta_{err_{RMS}} = 1.6°$ for azimuthal angle and $\phi_{err_{RMS}} = 2.7°$ for polar angle. Fig. 16(e) and Fig. 16(f) shows the error distribution. The smallest error is observed when either polar or azimuthal angle is close to 0°. The maximum errors are observed when both polar or azimuthal angles are close to their limits of the FOV: $\theta_{err_{max}} = 5.7°$ and $\phi_{err_{max}} = 3.9°$, located in corners of FOV. If angles within a reduced circular field-of-view are considered (80% of entire FOV), the maximum errors are $\theta_{err_{max}} = 4.2°$ and $\phi_{err_{max}} = 4.1°$, and RMS errors are: $\theta_{err_{RMS}} = 0.98°$ and $\phi_{err_{RMS}} = 0.42°$.

The quantization error related to the sensor resolution contributes between $0.22° - 1.88°$ depending on the incident light angle.

The pixels vectors and the mask intersect with accuracy of $\frac{1}{2}PIX_{pitch}$ after calibration, described in Section IV-B. The $\frac{1}{2}PIX_{pitch}$ misalignment causes tilt error between the mask and the pixels vectors, which contributes up to $\pm PIX_{pitch}$ error at the limit of FOV due to an angle modulation. Hence, the misalignment between the mask and the pixel vectors contributes in total $\pm\frac{3}{2}PIX_{pitch}$, which corresponds to $\pm 2.83°$ error.

The temporal quantization error does not impact the sensor accuracy because the sensor temporal resolution is very low (below $100\mu s$).

The accuracy of the instruments used for calibration and the accuracy of a developed model transforming pan and tilt of the PTU to the actual pitch and yaw of the sun sensor were not considered when calculating the sun sensor accuracy.

Based on results from Fig. 16, field-of-view (FOV) of the sun sensor is $+71.8°; -70.2°$. The FOV is non-symmetrical because the intersection between the pixel vectors and the incident light ray pattern in Section IV-B was shifted 10 pixels from the ideal intersection point $x_{ideal} = 192/2 = 96$.

To measure the precision of the sun sensor, a laser beam was pointed to a slit, such that few pixels inside the array were illuminated. Angles θ and ϕ were measured 5000 times. The

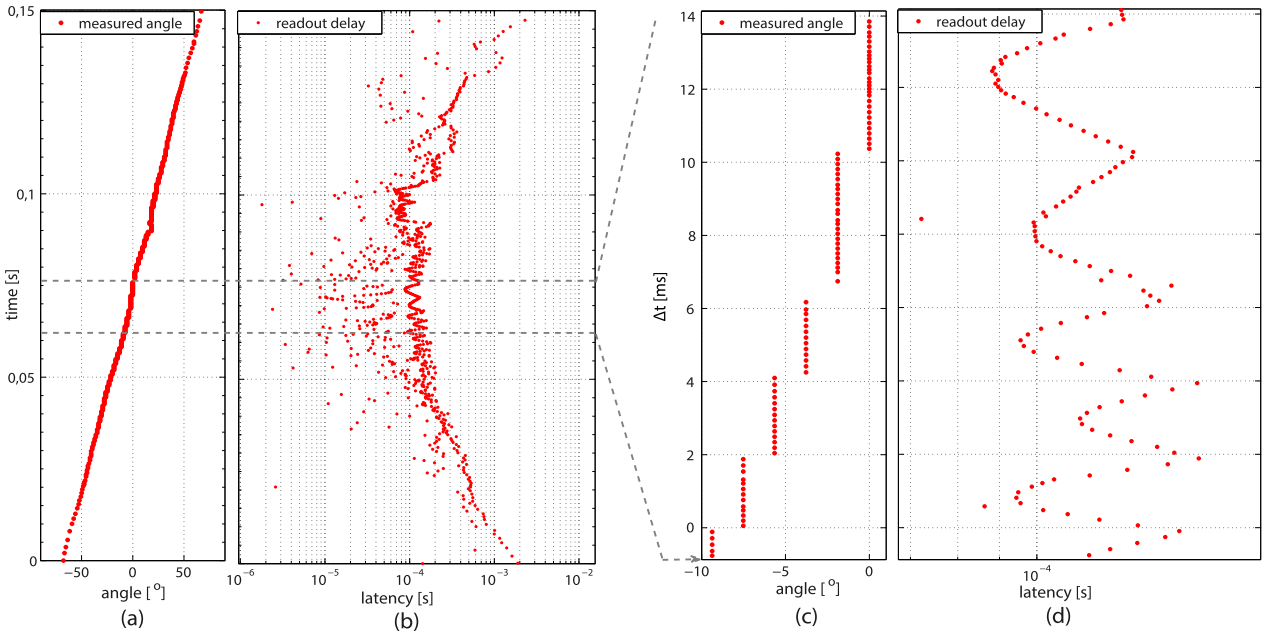

Fig. 15. Recorded polar angle (a) for the sun sensor rotating with angular speed of 300 rpm, and latency between two consecutive readouts (b). Figures (c) and (d) show closer look for an angle around 0°. The surface of the sun sensor was exposed to a radiant flux of 240 W/m^2.

sun sensor precision expressed in terms of standard deviation is $0.104°(3\sigma_\theta)$ for azimuthal angle , and $0.061°(3\sigma_\phi)$ for polar angle.

7) Light Profile Extraction: TFnS mode with multiple winners makes it possible to extract the profile of the incident light in the form of time stamped events. Top plot in Fig. 17 illustrates recorded light profile by sun sensor operating in TFnS timeout-out mode with a limit of 15 winners. Bottom plots in Fig. 17 zoom in on angles close to endpoint values and 0°. A profile of the incident beam changes depending on the actual angle of the light. The beam that passes through the slit and hits the photoactive array of pixels becomes collimated, but also contains diverging rays. These diverging rays spread as the ray propagates, and cause the light beam to disperse with distance. As a result, a sharp cusp characterizes a profile of orthonormal light in bottom center in Fig. 17, while profiles for endpoint angles are more flat (bottom left and right figures). If there are two cusps, it means that there is a reflection. Multiple winners TFnS mode can be enabled for a moment to sample the wider field of view, and assess if the sun is within the sensor FOV.

8) Power Consumption: Table II summarizes power consumption of the sun sensor. We report the power consumption of the system in reset mode, and with the pixels being active. The first case was achieved by forcing all pixels being reset by the global reset signal, and in the second case the sun sensor operated in normal conditions, exposed to direct sunlight of irradiance 240 W/m^2.

When the sun sensor is in reset mode, the main contributor to the power power consumption is the differential pair comparator located inside each pixel. The entire power consumption of the sun sensor operating in TFnS mode is $1.9\mu A$ for a single winner, and it increases to $2.1\mu A$ for 15 winners. Power consumption of the sun sensor operating in free-running mode (TFnS disabled) is highest because in this mode all pixels are allowed to spike with no timeout constraints, nor with a limit to the number of winners. Hence, the power consumption is dominated by the arbitration peripherals which arbitrate the incoming requests from free-running pixels.

TABLE II
SUN SENSOR POWER CONSUMPTION

Mode	Pixels Activity [eps]	Current Consumption @3 V
Reset Mode	no activity	1.43 μA
TFnS 1 winner	8 k	1.9 μA
TFnS 15 winners	42 k	2.1 μA
TFnS disabled	58 k	5.0 μA

V. BENCHMARKING AND COMPARISON TO THE STATE-OF-THE-ART

Table III compares the features and performance of our work with other sun sensors. We have classified the sun sensors according to type and operation principle. The sun sensor described by Ortega *et al.* [4] is an analog sun sensor, integrating four silicon photodiodes and small PCB with auxiliary electronics inside aluminum box. The angle is extracted continuously by comparing photodiodes currents. The two other sensors are digital. The sun sensor described by Xie and Theuwissen [3] uses a CMOS active pixel sensor (APS) as a sensing element and a pinhole as a mask. A sensor proposed by Liebe *et al.* [21] is also an APS detector, and it implements a mask with hundreds of small pinholes.

Our sensor is much smaller and lighter than any other reported sun sensor. Thanks to implementing auxiliary electronics in silicon and using QFN64 package, our sensor volume is 120 times smaller and much lighter than [4]. Also, in terms of used silicon area, our sun sensor is much smaller. Due to use of only two single vectors of pixels, we reduced the area of used silicon, such that only 8% of the chip

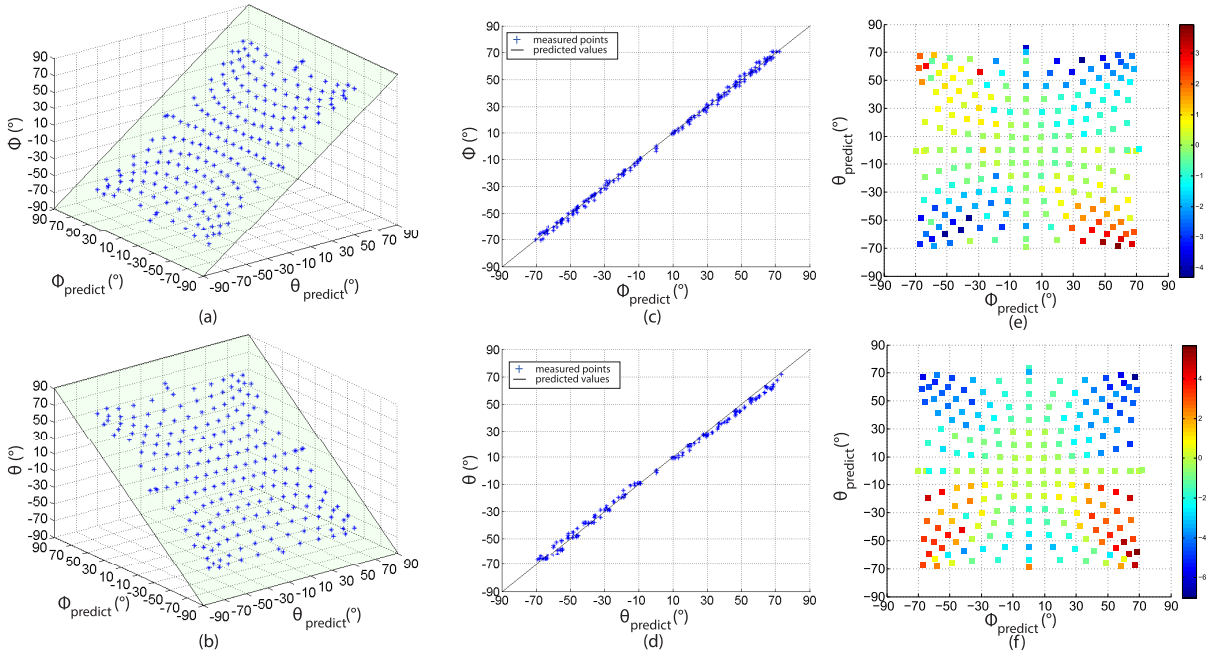

Fig. 16. Measured azimuthal (a) and polar (b) angles, x- and y-axis is predicted angle, and z-axis is measured angle. The green plane serves as predicted angle reference. Figure (c) and (d) show a spread of the measured angles θ and ϕ around the predicted value from xz-axis and yz-axis perspective, and (e) and (f) illustrate distribution of angle error as a color map.

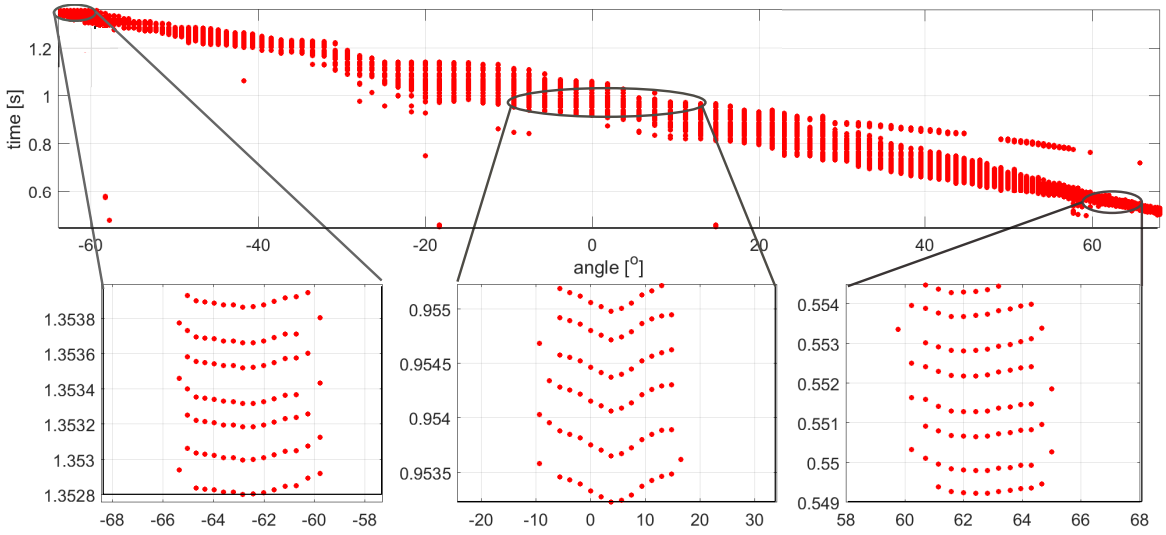

Fig. 17. Recorded polar angle for TFnS time-out mode with 15 winners (top). Three bottom plots show closer look for endpoint angles and an orthonormal angle. The sun sensor surface was exposed to direct sunlight of irradiance 240 W/m^2.

area is occupied by the implemented sun sensor. Digital sun sensors [21], [3] use entire imager matrix, and require high-performance analog-to-digital converters, and extra digital processing circuits for complex centroid algorithms.

For the measurements, we used a USBAERmini2 board to communicate asynchronously with the sun sensor. However, it is not necessary to use the dedicated board for normal operation of the sun sensor. Instead, a simple state machine with few logic cells can be used to acknowledge incoming requests and readout the sensor output. Therefore, it is not included in the estimate of the sun sensor volume and weight.

Due to on-chip TFnS with time-out processing, our sun sensor requires less data to determine the sun position compared to digital sensors. Digital sensors [3], [21] perform readout in two stages (acquisition and tracking) to avoid reading out the entire pixel matrix several times. Even with this optimization, the amount of data required to detect the sun position is much higher, and much more computing power is needed to calculate the angle based on this data. Sun sensors proposed by Liebe *et al.* [21] and Xie and Theuwissen [3] require processor intensive algorithms to extract angles. To obtain the sun angle, these sensors require many steps: readout all pixels' analog values, compare all pixels' values with thresholds, detect the brightest point, and calculate the centroid position. Due to implementation of TFnS and time-out readout framework, most of the processing in our sensor is performed on-chip and the sun sensor generates compressed information about the angle in the form of time-encoded events. If the sun sensor is

TABLE III
STATE-OF-THE-ART COMPARISON

	Ortega et al. [4]	Xie et al. [3]	Liebe et al. [21]	**This work**
Type	Analog Sun Sensor	APS Digital Sensor	APS Digital Sensor	**Event Based Sensor**
Operation Principle	Photodiodes Ratio	Frame-based	Frame-based	**TFnS**
Technology	ND	$0.18\,\mu$m 1P4M	$0.5\,\mu$m CMOS	**AMS 0.35 μm opto (C350)**
Power Supply	ND	$3.3/1.8\,$V	ND	**3 V**
Packaged sensor size	$(3 \times 3 \times 1.2)\ cm^3$ (including auxiliary electronics)	ND	$4.2\,\mathrm{cm}^3$ (including complete APS chip)	$\mathbf{(9.5 \times 9.5 \times 1)\ mm^2}$ **(including auxiliary electronics in silicon)**
Sensor Weight	24 grams (including auxiliary electronics)	ND	11 grams (including complete APS chip)	**0.3 grams (including auxiliary electronics in silicon)**
Pixel array	4 photodiodes	368×368 pixels	512×512 pixels	$\mathbf{2 \times 192}$ **pixels**
Pixel size	$0.75\,\mathrm{mm} \times 2\,\mathrm{mm}$	$6.5\,\mu\mathrm{m} \times 6.5\,\mu\mathrm{m}$	$12\,\mu\mathrm{m} \times 12\,\mu\mathrm{m}$	$\mathbf{11.75\ \mu m \times 72\ \mu m}$
Silicon die size	$(7.5 \times 8.5)\ mm^2$	$(5 \times 5)\ mm^2$	$(6.1 \times 6.1)\ mm^2$	$\mathbf{(2.5 \times 2.5)\ mm^2}$ **(8% of area used)**
FOV	120^o	$\pm 47^o$	160^o	$\mathbf{144^o}$
Resolution	ND	0.004^o	ND	$\mathbf{0.22^o - 1.88^o}$
Accuracy	0.15^o	ND	$\approx 0.04^o$	$\mathbf{0.98^o}(\theta)$ and $\mathbf{0.42^o}(\phi)$.
Precision	ND	0.01^o	ND	$\mathbf{0.104^o}(\theta)$, $\mathbf{0.061^o}(\phi)$
Latency	ND	10 fps	30 fps	$\mathbf{88\ \mu s}$ **(equivalent to 11.3 kfps)**
Power consumption	ND	42.73 mW	30 mW	$\mathbf{6.3\ \mu W}$
Dynamic Range	ND	52dB	ND	**>80dB**
Amount of data	4 analog voltages	945 pixels	262 kpixels	**1-2 events**

not exposed to direct sunlight, it does not transfer any spurious data, due to the proposed time-out readout framework.

Due to replacing a frame-based readout with an event-based (AER) framework, our sun sensor outperforms any standard APS-based sensor.

A great advantage of the proposed sun sensor over the others, is the small readout latency. Since our sensor is event-based, it is not limited by a fixed frame rate, and its speed excceds 11keps. Such a low latency response makes this sun sensor suitable to determine the attitude of fast spinning objects, such as sounding rockets during flight. On the other hand, the speed of digital frame-based sun sensors [3] and [21] is limited to 10 fps and 30 fps respectively. Analog sun sensors speed is limited by the conversion time of analog-to-digital converters, which is not reported in [4].

Thanks to a new readout framework, and low circuit simplicity, the sun sensor power consumption is kept very low, and is over three decades lower than reported power consumption of other works. Reported power consumption in [3] and [21] is much higher due to use of APS sensor, and in [4] due to use of discrete components to implement auxiliary electronics.

The accuracy of a proposed sun sensor is worse than [4] and [21]. It could be improved if a more elaborated run calibration approach and more complex model were used to calculate angles. For example, the calibration procedure in [4] consisted of a high-accuracy Angular Positioning System instrument to achieve high precision calibration curves and to compensate any misalignment suffered by the sensor in their manufacturing steps.

VI. CONCLUSIONS

A new type of sun sensor based on asynchronous spiking pixels has been described in this paper.

The sun sensor is much smaller and lighter than any other reported sun sensor. A novel Time-to-First-n-Spikes (TFnS) with time-out readout mode lowers the bandwidth consumption and post-processing computation of the sun sensor, and helps to discard spurious readouts when the sun is not within the sun sensor field of view. The high temporal resolution and fast response makes this sun sensor suitable for space probes and sounding rockets applications. Thanks to implementing two 1-D pixel vectors instead of a 2D array in a standard CMOS process, the sun sensor occupies only 8% of the chip area, and the remaining area can be used for other sensor interfaces. With regard to dynamic range, the used AER type of our design outperforms any standard APS-based sensors. The sun sensor is able to extract the profile of the incident light in the form of time-stamped events. The extracted incident light profile can help distinguish between the sun and other distractors, and also to further analyze the incident sun light properties.

The sun sensor accuracy is $\theta_{err_{RMS}} = 0.98°$ for the azimuthal angle, and $\phi_{err_{RMS}} = 0.42°$ for the polar angle. The maximum accuracy errors are $\theta_{err_{max}} = 4.2°$ for the azimuthal angle and $\phi_{err_{max}} = 4.1°$ for the polar angle.

There are three main error contributors to the sensor overall accuracy: the quantization error, the misalignment between the mask and the pixel vectors, and an accuracy of the sensor model. The quantization error related to the sensor resolution contributes between $0.22° - 1.88°$. The misalignment between the L-shape mask and the pixel vectors contributes maximum $\pm 2.83°$. The quantization error can be improved by decreasing the pixel pitch PIX_{pitch}, by increasing the sensor resolution, or by increasing the distance d between the chip and the lid. More precise calibration scheme using multiple pixels readout to extract the incident light profile could be used to improve the alignment between the mask and the pixels vectors.

A simple geometry model for transforming pixel address into angle was sufficient to prove a principle of this new concept. The model can be further improved to include a

refractive coefficient of the glass, and include more than one winner to interpolate the peak of the incident light pattern to calculate the angle. This would improve the accuracy and spatial resolution of the sun sensor.

To summarize, the proposed device is a new type of a miniaturized event-based sun sensor, which uses spiking pixels to measure sun angle in 2-axes. It consumes $6.3\mu W$ in normal operation, which is much less than any state-of-the-art sun sensor. Due to on-chip processing, and compressing the angle information, the sensor produces much less data and is much faster than digital sensors. The small form factor of a QFN64 package and less than 1 gram weight makes this sensor cheap to employ in space crafts and satellites.

ACKNOWLEDGMENTS

The proposed sun sensor is planned to be employed in the Sounding Rocket Attitude Determination System and in micro space probes as part of the 4DSpace [22] research initiative at the University of Oslo, Norway. A first launch that might include this sun sensor is planned within the ICI sounding rockets series in 2018.

REFERENCES

[1] J. R. Wertz, *Spacecraft Attitude Determination and Control*. Norwell, MA, USA: Kluwer, 1995.
[2] C. C. Liebe and S. Mobasser, "MEMS based sun sensor," in *Proc. IEEE Aerosp. Conf.*, vol. 3. Mar. 2001, pp. 3-1565–3-1572.
[3] N. Xie and A. J. P. Theuwissen, "A miniaturized micro-digital sun sensor by means of low-power low-noise CMOS imager," *IEEE Sensors J.*, vol. 14, no. 1, pp. 96–103, Jan. 2014.
[4] P. Ortega *et al.*, "A miniaturized two axis sun sensor for attitude control of nano-satellites," *IEEE Sensors J.*, vol. 10, no. 10, pp. 1623–1632, Oct. 2010.
[5] A. Ali and F. Tanveer, "Low-cost design and development of 2-axis digital sun sensor," *J. Space Technol.*, vol. 1, no. 1, 2011.
[6] J. P. Enright and Godard, "Advanced sun-sensor processing and design for super-resolution performance," in *Proc. IEEE Aerosp. Conf.*, Mar. 2006, p. 14.
[7] Y.-K. Chang, B.-H. Lee, and S.-J. Kang, "High-accuracy image centroiding algorithm for CMOS-based digital sun sensors," in *Proc. IEEE Sensors*, Oct. 2007, pp. 329–336.
[8] F. J. Delgado, J. M. Quero, J. Garcia, C. L. Tarrida, P. R. Ortega, and S. Bermejo, "Accurate and wide-field-of-view MEMS-based sun sensor for industrial applications," *IEEE Trans. Ind. Electron.*, vol. 59, no. 12, pp. 4871–4880, Dec. 2012.
[9] Ł. Farian, P. Häfliger, and J. A. Leñero-Bardallo, "Miniaturized sun sensor with in-pixel processing for attitude determination of micro space probes," in *Proc. Int. Conf. Event-Based Control, Commun., Signal Process. (EBCCSP)*, Jun. 2015, pp. 1–6.
[10] E. Culurciello, R. Etienne-Cummings, and K. A. Boahen, "A biomorphic digital image sensor," *IEEE J. Solid-State Circuits*, vol. 38, no. 2, pp. 281–294, Feb. 2003.
[11] C. Posch, T. Serrano-Gotarredona, B. Linares-Barranco, and T. Delbruck, "Retinomorphic event-based vision sensors: Bioinspired cameras with spiking output," *Proc. IEEE*, vol. 102, no. 10, pp. 1470–1484, Oct. 2014.
[12] P. Häfliger, "A spike based learning rule and its implementation in analog hardware," Ph.D. dissertation, ETH Zürich, Zürich, Switzerland, 2000.
[13] Ł. Farian, J. A. Leñero-Bardallo, and P. Häfliger, "A time-to-first-n-spikes and time-out read-out extension to the AER arbitration system," in *Proc. Int. Conf. Event-Based Control, Commun., Signal Process. (EBCCSP)*, Jun. 2016, pp. 1–6.
[14] C. M. A. Mead, *Analog VLSI and Neural Systems*. Boston, MA, USA: Addison-Wesley, 1989.
[15] R. Berner, T. Delbruck, A. Civit-Balcells, and A. Linares-Barranco, "A 5 Meps $100 USB2.0 address-event monitor-sequencer interface," in *Proc. ISCAS*, New Orleans, LA, USA, May 2007, pp. 2451–2454.
[16] *jAER Open Source Project*. [Online]. Available: http://sourceforge.net/projects/jaer/
[17] Ł. Farian. *Sun Sensor Measurement Setup p.1*. YouTube. Accessed: Oct. 2017. [Online]. Available: https://www.youtube.com/watch?v=zf9UUiSX1tM
[18] J. R. Wertz, *Spacecraft Attitude Determination Control*. Dordrecht, The Netherlands: Reidel, 1978.
[19] M. Bortman, *Environmental Encyclopedia*. London, U.K.: Gale, 2003.
[20] G. Matthews, "Celestial body irradiance determination from an underfilled satellite radiometer: application to albedo and thermal emission measurements of the moon using CERES," *Appl. Opt.*, vol. 47, no. 28, pp. 4981–4993, Sep. 2008.
[21] C. C. Liebe, S. Mobasser, Y. Bae, C. J. Wrigley, J. R. Schroeder, and A. M. Howard, "Micro sun sensor," in *Proc. IEEE Aerosp. Conf.*, vol. 5. Mar. 2002, pp. 5-2263–5-2273.
[22] UiO. *4DSpace—Strategic Research Initiative*. Accessed: Oct. 2017. [Online]. Available: http://www.mn.uio.no/fysikk/english/research/projects/4dspace/

Łukasz Farian received the B.S. degree in automation and robotics from the Nicolaus Copernicus University, Toruń, Poland, in 2012, and the M.Sc. degree in nanoelectronics and robotics from the University of Oslo, Norway, in 2014, where he is currently pursuing the Ph.D. degree in nanoelectronics with research focus on integrated circuits for space probes. In 2013, he was a Summer Analog Designer Intern with OmniVision Technologies, Oslo. In 2015, he completed a Space Studies Program at the International Space University, OH, USA. He is currently with Nordic Semiconductor company. His research interests include neuromorphic electronics and attitude determination systems for space probes.

Philipp Häfliger (SM'10) received the M.Sc. degree in computer science (with astronomy as a minor subject) from the Swiss Federal Institute of Technology (ETH), Zürich, Switzerland, in 1995, and the Ph.D. degree from the Institute of Neuroinformatics, ETH, in 2000. He then held a post-doctoral position at the Nanoelectronics Group, Department of Informatics, University of Oslo, Norway, where he currently a Professor. In Oslo, his research focus shifted gradually from neuromorphic (inspired by the nervous system) electronics toward mixed-signal ASIC design, in particular for biomedical devices, such as wireless microimplants, and more recently for micro-probes for space research. He was the Chairman of the IEEE Circuits and Systems (CAS) Society's Biomedical and the Life Science CAS (BioCAS) Technical Committee from 2010 to 2012. He has served and still serves in various functions for the IEEE ISCAS and the IEEE BioCAS conferences, and as Associate Editor for the IEEE TRANSACTIONS ON BIOCAS.

Juan A. Leñero-Bardallo received the M.Sc. degree in telecommunications engineering and the Ph.D. degree in microelectronics from the University of Seville, Seville, Spain, in 2005 and 2010, respectively. In 2010, he was a Post-Doctoral Associate with Yale University, New Haven, CT, USA. From 2010 to 2013, he was a Post-Doctoral Associate with the University of Oslo, Oslo, Norway. From 2013 to 2016, he was a Post-Doctoral Associate with the University of Seville. In 2016, he was a Senior Engineer with Chronocam Inc. Since 2016, he has been an Assistant Teacher with the University of Cádiz, Cádiz, Spain, where he is currently involved in teaching and conducting research. He also coordinates a course in electronics for the bachelor's degree in industrial engineering. He served in several academic institutions and semiconductor industry. His current research interests include address event representation vision systems, frame-based vision sensors, smart sensors, wireless vision sensor networks, signal processing, and very large scale integration emulators of biological systems. He has been a member of the IEEE Sensory Systems Committee since 2012.

Paper VII:

Ł. Farian, J.A. Leñero-Bardallo, P. Häfliger
Live Demonstration: A Miniaturized Two-Axis Low Latency and Low-Power Sun Sensor for Attitude Determination of Sounding Rockets
IEEE International Symposium on Circuits and Systems, 2018

Live Demonstration: A Miniaturized Two-Axis Low Latency and Low-Power Sun Sensor for Attitude Determination of Sounding Rockets.

Łukasz Farian[1], Juan A. Leñero-Bardallo[2], Philipp Häfliger[1]
[1] Nanoelectronics Group, Department of Informatics, University of Oslo, Norway, lukaszf@ifi.uio.no
[2] Institute of Microelectronics of Seville (IMSE-CNM), CSIC-Universidad de Sevilla, Spain, juanle@imse-cnm.csic.es

***Abstract*—This demo shows a first prototype two-axis miniaturized spiking sun sensor. The device is composed of spiking pixels, and uses a novel Time-to-First-n-Spikes with time-out readout mode to reduce bandwidth consumption and post-processing computation. Due to on-chip processing, and compressing the angle information, the sensor produces much less data and is much faster than digital sensors. Its response latency is 88 μs, and average power consumption is 6.3 μW. An integrated circuit with core electronics was fabricated in the AMS 0.35 μm CMOS image sensor process, and was integrated inside a very small QFN64 package with micro-optics on top.**

I. Demonstration Setup

Fig. 1 shows a demonstration setup. The demonstration system is composed of a PCB with a sun sensor [1], a USBAERmini2 data logger [2], two Nordic Semiconductor nRF52 Bluetooth® low energy development kits, a laptop, a rotating table, and a light source. The sun sensor sends its information about its orientation with respect to the light source via a data logger to the laptop. The laptop has a dedicated Java interface [3] installed to display locations of pixels spikes in time, and provide azimuthal and polar angles in real time. A custom MATLAB script analyzes and provides detailed information about the recorded data. Another sun sensor, powered from battery, is installed on a rotating table and communicates with a data logger via Bluetooth low energy connection.

II. Visitor Experience

The sun sensor comprises a chip with two one-dimensional pixel lines organized in an L-shape, and the thin glass lid with a metal deposited pattern. The principal operation of the sensor is to detect two intersection points of illuminated sunlight pattern and photosensitive pixels lines [1]. The intersection points are sensed by spiking pixels, that fire with a frequency proportional to illumination [4].

A video demonstrating the demo is provided in [5]. Visitors can challenge the sun sensor response speed by moving a light source within its field-of-view. The system will detect a light source and it will display computed azimuthal and polar angles on a laptop screen in real time. Another sun sensor, installed on a rotating table, will communicate wirelessly with a data logger to mimic a real operation during a sounding rocket flight. Few different sensor readout modes will be presented to explain advantages of a TFnS readout mode. A profile of the incident light in the form of time stamped events will be shown to illustrate how the extracted incident light profile can help to distinguish between the sun and other distractors.

Juan A. Leñero-Bardallo was sponsored in part by Grants TEC2015-66878-C3-1-R, Co-Funded by ERDF-FEDER; Junta de Andalucía CEICE TIC 2012-2338 (SMARTCIS-3D), and ONR grant N000141410355 (HCELLVIS).

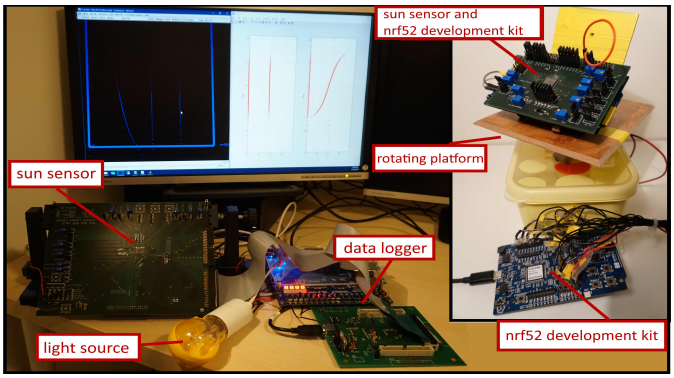

Fig. 1. Experimental setup.

III. Reference Publication

The article of Farian et al. [1] describes design, fabrication process, and comprehensive experimental results. The board used to store and transmit the sensor information to a PC is described in [2].

References

[1] Ł. Farian, P. Häfliger, and J. A. Leñero-Bardallo, "A miniaturized two-axis ultra low latency and low-power sun sensor for attitude determination of micro space probes," *IEEE Transactions on Circuits and Systems I*, vol. PP, no. 99, pp. 1–12, 2017.
[2] R. Berner, T. Delbruck, A. Civit-Balcells, and A. Linares-Barranco, "A 5Meps $100 USB 2.0 address-event monitor-sequencer interface," in *ISCAS 2007, New Orleans*, 2007, pp. 2451–2454.
[3] "jAER open source project," http://sourceforge.net/projects/jaer/.
[4] E. Culurciello, R. Etienne-Cummings, and K. Boahen, "A biomorphic digital image sensor," *Solid-State Circuits, IEEE Journal of*, vol. 38, no. 2, pp. 281–294, Feb 2003.
[5] Ł. Farian. Live demonstration proposal: A miniaturized two-axis low latency and low-power sun sensor. Youtube. [Online]. Available: https://youtu.be/wdfOjKqEiS4

Presentation I:

J.A. Leñero-Bardallo, Ł. Farian, J.M. Guerrero-Rodríguez, R. Carmona-Galán, Á. Rodríguez-Vázquez
On the Design of Sun Sensors with Event-Based Operation.
Workshop on Architecture of Smart Cameras, 2017

On the design of sun sensors with event-based operation

Juan A. Leñero-Bardallo[a], Lukasz Farian[b], José Mª Guerrero-Rodríguez[a], Ricardo Carmona-Galán[c] , Ángel Rodríguez-Vázquez[c]

[a]University of Cádiz, Escuela Superior de Ingeniería, Avda. Universidad 10, Puerto Real (Spain)

[b]University of Oslo, Department of Informatics, Blindern 1072, Oslo (Norway)

[c]Institute of Microelectronics of Seville (CSIC – Universidad de Sevilla), Avda. Américo Vespucio s/n Seville (Spain)

Contact: juanantonio.lenero@uca.es

Abstract.- Sun sensors are devices on demand to determine the sun position. Usually, they provide the sun latitude and inclination referred to its centroid. There are multiple application scenarios for these devices: control of heliostats and solar cells in solar power plants, navigation systems for sounding rockets, ect. The most extended approach to implement sun sensors is to use frame-based image sensors to sense the sun radiation. Its pixels are readout periodically. Thereafter, the sun position is determined after processing all the pixels illumination values. This approach is highly inefficient in terms of speed, data computation and power consumption. The reason is that only a reduced group of pixels is exposed to sunlight. Thus, the rest of pixels are dark and meaningless to resolve the sun position. Furthermore, the entire pixel matrix has to be readout periodically to gauge the sun position.

On the contrary, event-based sensors have pixels that do not have to be scanned periodically. Their pixels do not have to be readout at fixed time intervals because they are autonomous and they send information asynchronously –if they need to do it. Among these sensors, there is a family that performs a light-to-frequency conversion known as octopus retinas. Their pixels spike asynchronously with a frequency proportional to light intensity. Every time that a pixel fires, it sends its coordinates through a shared bus. Such devices solve the paradigm associated to conventional sun sensors: pixels that are dark will not be readout. Therefore, the amount of data to compute the sun position will be much lower. Moreover, the dynamic range is higher and their operation speed is faster.

Two different event-based sun sensors developed by the authors will be presented. The first one is a sensor with a dedicated optics and ad hoc pixel design. The second one is a luminance event-based sensor whose pixels spike with a frequency proportional to the local illumination. It was adapted to operate as a sun sensor by assembling it pinhole optics. Experimental results taken with both sensors will be displayed. Details about the implementation of each one will be provided. The performance of both sensors will be compared against the art. In Figure 1, both sensors are shown. For each one, a sketch depicting how the optics and the pixel arrays are arranged is provided. A photo of each sensor with its optics is also displayed.

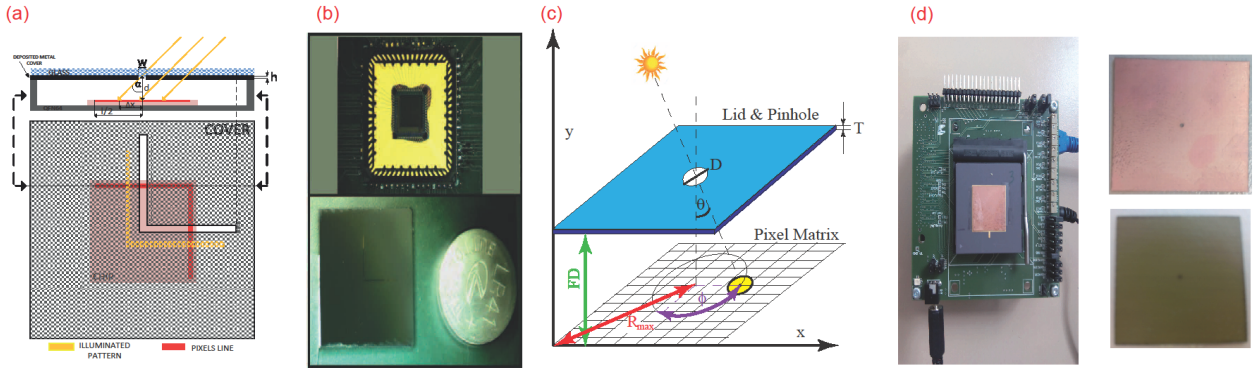

Figure 1: Two different event-based sun sensors implemented by the authors. (a) Sketch of the first sun sensor optics and its pixel array with L-shape. (b) Photograph of the first sun sensor implementation and its optics. (c) Sketch of the second sun sensor optics and its pixel array. (d) Photograph of the second sun sensor implementation and detail of its optics.

Acknowledgements: This work was supported in part by the University of Cádiz under Grant PR2016-072; in part by the Spanish Ministry of Economy and Competitiveness under Grant TEC2015-66878-C3-1-R, Co-Funded by ERDF-FEDER; in part by Junta de Andalucía CEICE under Grant TIC 2012-2338 (SMARTCIS-3D); and in part by ONR under Grant N000141410355 (HCELLVIS).

On the design of sun sensors with event-based operation

Juan A. Leñero-Bardallo[1], Lukasz Farian[2], José M. Guerrero-Rodríguez[1], Ricardo Carmona-Galán[3] and Ángel Rodríguez-Vázquez[3]

{juanantonio.lenero}@uca.es

[1]University of Cádiz
Section of Electrical Engineering
Spain

[2]University of Oslo
Department of Informatics
Oslo, Norway

[3]University of Sevilla
Institute of Microelectronics of Sevilla
Spanish Council of Research
Spain

- *Sun Sensors*
- *Review of the state-of-the-art*
- *Event-based sun sensors*
- *Conclusions*

Sun Sensors

- **Sensors that determine the Sun position (attitude and azimuth) referred to its centroid.**

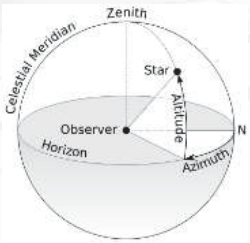

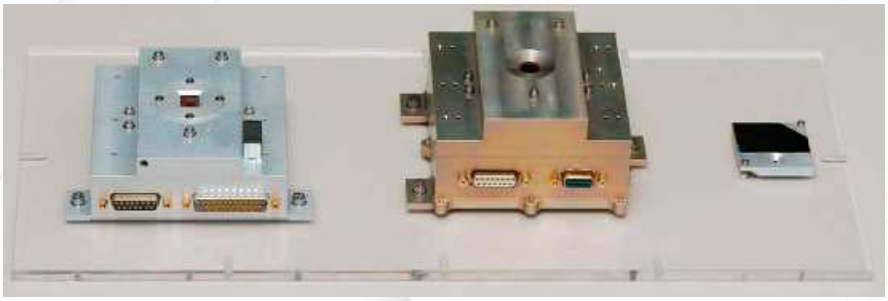

N. Xie and A. J. P. Theuwissen, "*A miniaturized micro-digital sun sensor by means of low-power low-noise CMOS imager*," IEEE Sensors Journal, vol. 14, no. 1, pp. 96–103, Jan 2014.

3

Sun Sensors Applications

- **Control of heliostats position.**
  - Accuracy.
  - Precision.

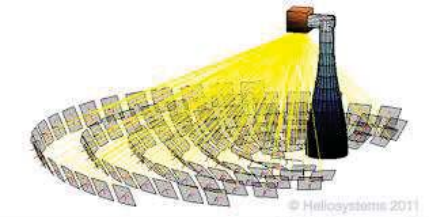

- **Control of solar cells position.**
  - Accuracy.
  - Precision.

- **Navigation systems for spacecrafts and sounding rockets.**
  - Low latency-> Low computational load
  - Accuracy.
  - Precision.

4

- Sun Sensors
- Review of the state-of-the-art
- Event-based sun sensors
- Conclusions

Types of Sun Sensors (I)

Analog sun sensors: the ratio between two photocurrents depend on the sun position.

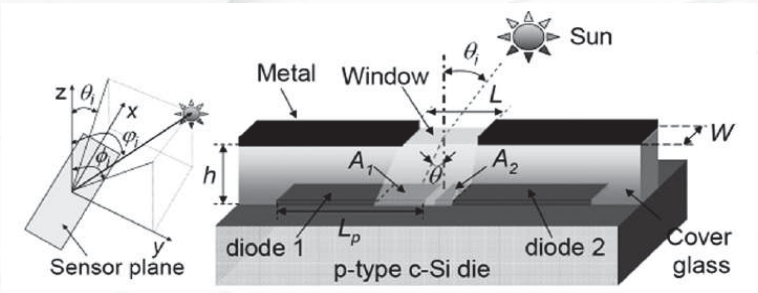

- **Fast operation.**
- **Sensitive to scene light sources.**
- **Prone to missmatch and noise.**

P. Ortega, et al., *"A miniaturized two axis sun sensor for attitude control of nano-satellites,"* IEEE Sensors Journal, vol. 10, no. 10, pp. 1623–1632, Oct 2010.

Types of Sun Sensors (II)

Digital sensors: A entire pixel matrix is readout. The sun position is computed by processing this data. Typically APS pixels and frame-based image sensors are employed.

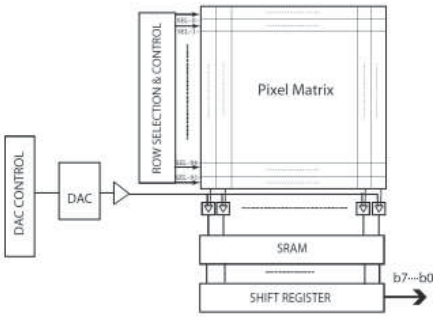

- ✓ **Reliable and robust to perturbations of external light sources.**
- ✓ **Conventional image sensors can be adapted to operate as a sun sensor**
- ✓ **Dark pixels are readout and processed.**

- × **The pixel matrix has to be scanned periodically.**
- × **Power consumption is high.**
- × **The exposition time has to be adapted to the illumination conditions**

Digital Sun Sensors

How to avoid data redundancy?

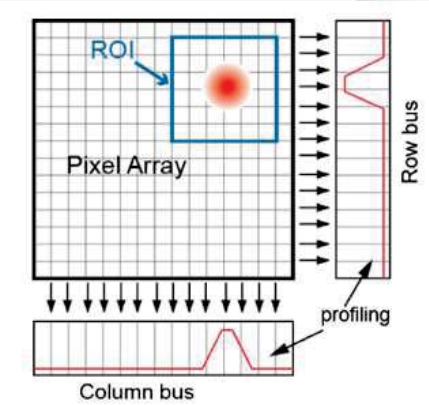

Pixel illumination values are readout in two different steps:

1. **The pixel matrix is readout to determine the ROI.**
2. **All pixels within the ROI are readout and processed to compute the sun position.**

- **Dark pixels are still readout.**
- **The pixel matrix has to be scanned periodically if the ROI changes its position**
- **An integration time has to be set.**
- **Dedicated pixel readout circuitry**

N. Xie and A. J. P. Theuwissen, "*A miniaturized micro-digital sun sensor by means of low-power low-noise CMOS imager*," IEEE Sensors Journal, vol. 14, no. 1, pp. 96–103, Jan 2014.

F. Boldrini et al., *"Attitude sensors on a chip: Feasibility study and breadboarding activities,"* in Proc. 32nd Annu. AAS Guid. Control Conf., February 2009, p. 11971216.

- Sun Sensors
- Review of the state-of-the-art
- Event-based sun sensors
- Conclusions

Event-based Vision Sensors

- Pixels send information asynchronously.
- There is not an integration time.
- Octopus sensors perform a light-to-frequency conversion.
- Dark pixels do not send any information off-chip.
- Fast operation.
- High dynamic range.

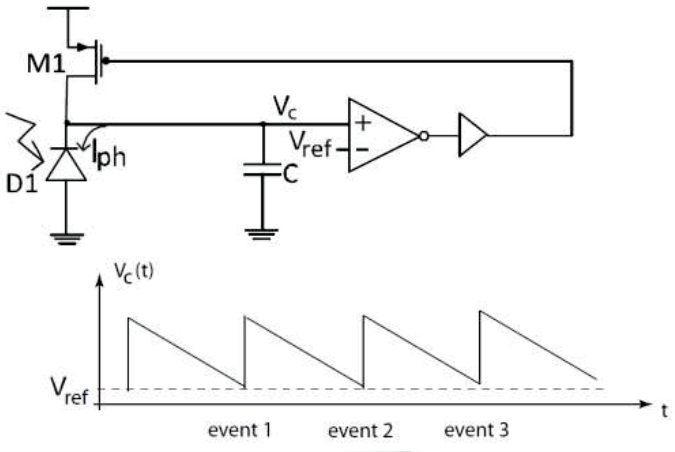

Event-based Vision: Optopus Sensor + Pinhole Optics

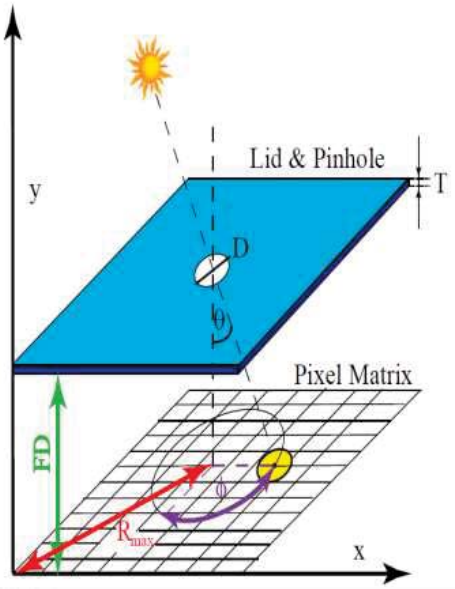

Sensor Implementation

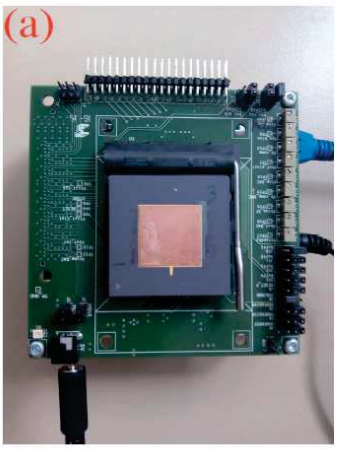

Lid detail

D=100µm, FD=600µm, T=500µm

Event-based Vision: Optopus Sensor + Pinhole Optics

Only illuminated pixels send out information

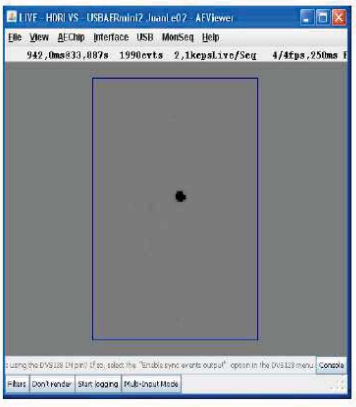

Interface to monitor the sensor activity

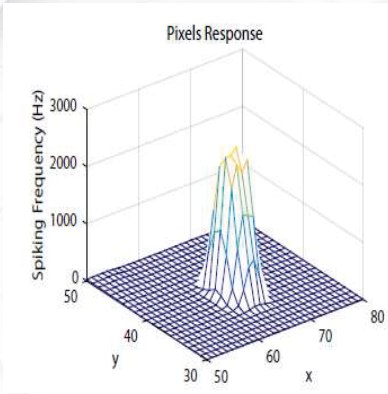

Pixels response

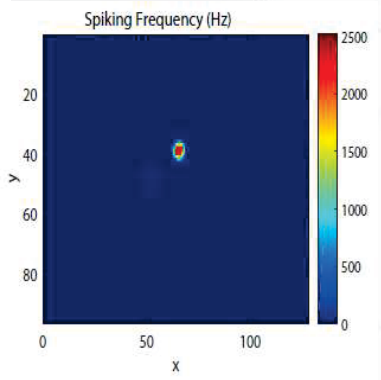

Example: 70dB intra-scene dynamic range

Event-based Vision: Optopus Sensor + Pinhole Optics

Sensor operation and centroid computation

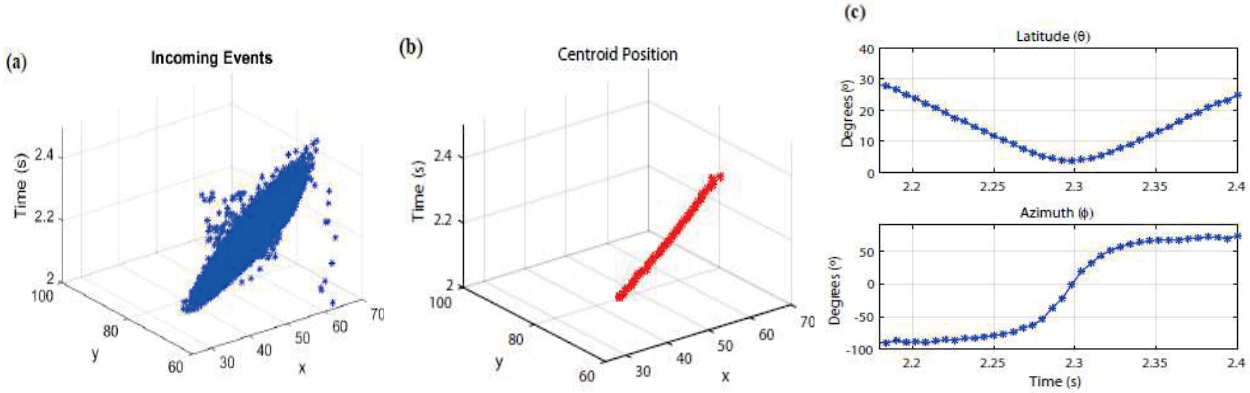

$$\theta = arctan\left(\frac{\sqrt{W\cdot(x-x_c)^2 + L\cdot(y-y_c)^2}}{FD}\right) \qquad \phi = arctan\left(\frac{L\cdot(y-y_c)}{W\cdot(x-x_c)}\right)$$

$$x = \frac{1}{N_{events}}\cdot\sum_{i=1}^{N_{events}} x_i \qquad y = \frac{1}{N_{events}}\cdot\sum_{j=1}^{N_{events}} y_j$$

13

Event-based Vision: Optopus Sensor + Pinhole Optics

Time-to-first-spike Operation

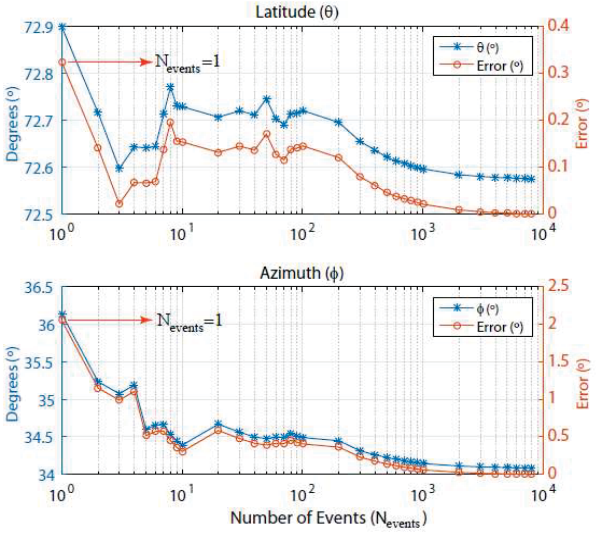

- It is posible to resolve the sun position receiving one event.
- Trade-off between the output data flow and error.

14

Event-based Vision: Optopus Sensor + Pinhole Optics

Sensor's performance against the art

Work	This Work	Ning et al. [3]	Galileo ESA [4]	Ortega et al. [1]
Type	Event Based Luminance Sensor	APS Digital Sensor	APS Digital Sensor	Analog Sun Sensor
Operation Principle	TFS	Frame-based	Frame-based	Photocurrent Ratio
Technology	AMS 0.18µm HV	0.18µm 1P4M	UMC 0.18µm	ND
Power Supply	3.3/5V	3.3/1.8V	3.3/1.8V	ND
Chip Dimensions	4120µm× 3315µm	5mm×5mm	11mm×11mm	6.8mm×13.8mm
Number of Pixels	128×96	368×368	512×512	2 pairs of photodiodes
Pixel Pitch	25µm× 25µm	6.5µm×6.5µm	11µm×11µm	NA
FOV	146°	94°	128°	120°
Power Consumption	52mW	42.73mW	520mW	ND
Latency	<5ms@1klux or lower	10frames/s	10frames/s	NA
Dynamic Range	>100dB	52dB	ND	NA
Resolution	0.03°	0.004°	<0.005°	ND
Accuracy	0.0132°(θ), 0.05°(ϕ)	0.01°	0.024°	0.15°
Amount of data	1-100 Events	368 pixels (acquisition mode) +25×25pixels (tracking mode)=945pixels	1 frame (acquisition mode) + ROI (tracking mode)	4 analog voltages to be readout

15

Event-based Vision: Custom Design

Sensor's lid arrangement

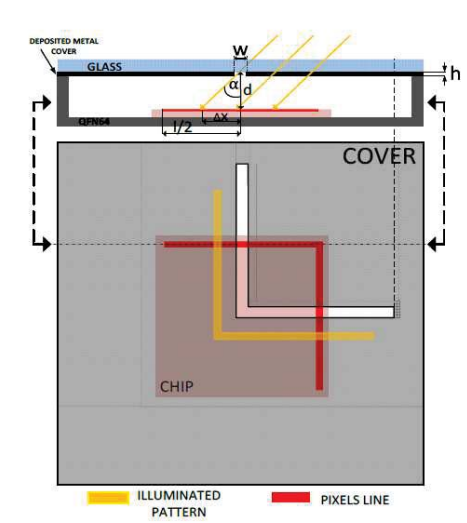

Sensor's block diagram

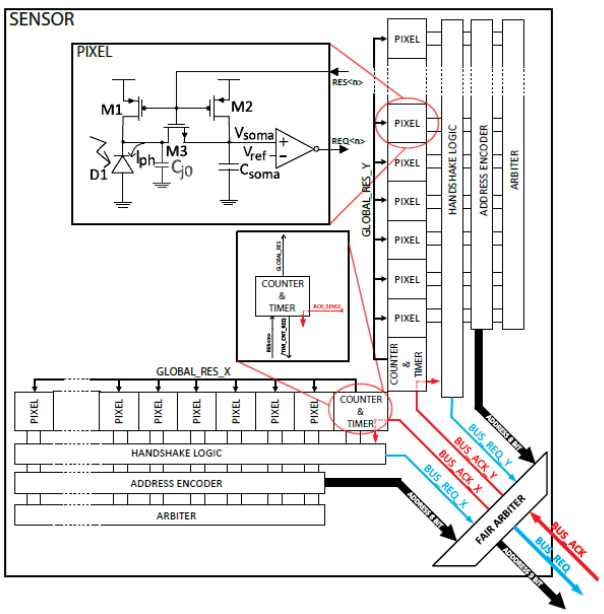

w=50µm, *d*=375µm, *l*=2256µm, *h*=100nm

16

Event-based Vision: Custom Design

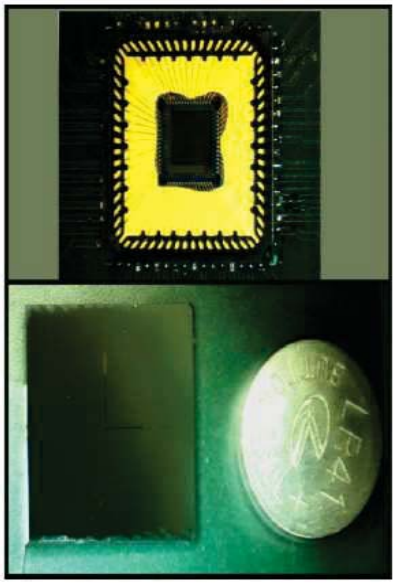

Dimensions: 9.5mmx9.5mmx1mm

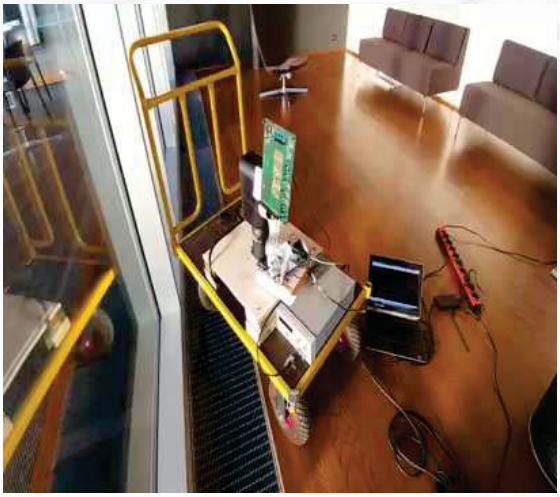

Sensor test with real sunlight

Event-based Vision: Custom Design

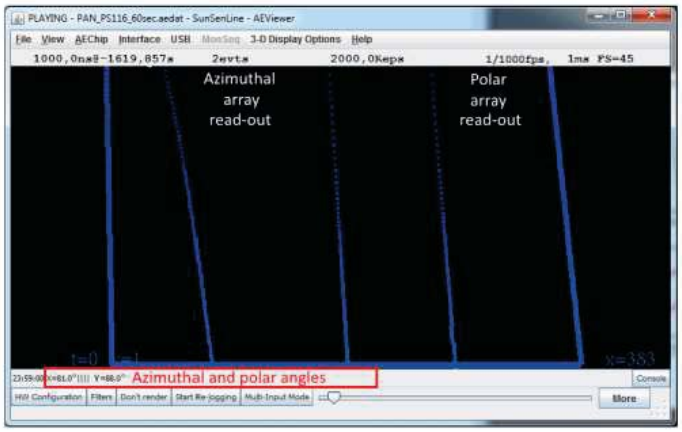

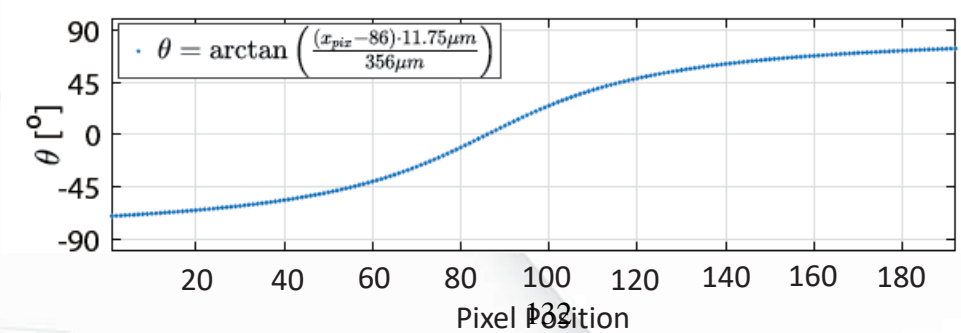

Event-based Vision: Custom Design

Sensor's performance against the art

	Ortega et al. [8]	Xie et al. [4]	Liebe et al. [16]	This work
Type	Analog Sun Sensor	APS Digital Sensor	APS Digital Sensor	Event Based Sensor
Operation Principle	Photodiodes Ratio	Frame-based	Frame-based	TFnS
Technology	ND	$0.18\mu m$ 1P4M	$0.5\mu m$ CMOS	AMS 0.35μm opto (C350)
Power Supply	ND	$3.3/1.8V$	ND	3V
Sensor size	(3 x 3 x 1.2) cm	ND	$4.2cm^3$	(9.5 x 9.5 x 1) mm
Sensor Weight	24 grams	ND	11 grams	0.3 grams
Pixel array	4 photodiodes	368 x 368	512 x 512	2 x 192 pixels
Pixel size	$0.75mmx2mm$	$6.5\mu m$ x $6.5\mu m$	$12\mu m$ x $12\mu m$	9μm x 32μm
Chip size	$6.8mmx13.8mm$	$5mmx5mm$	$6.1mmx6.1mm$	2.5mm x 2.5mm (8% of area used)
FOV	120^o	$\pm 47^o$	160^o	144^o
Resolution	ND	0.004^o	ND	$0.22^o \div 1.88^o$
Accuracy	0.15^o	ND	$\approx 0.04^o$	$0.98^o(\theta)$ and $0.42^o(\phi)$.
Precision	ND	0.01^o	ND	$0.104^o(\theta)$, $0.061^o(\phi)$
Latency	ND	10fps	30fps	88μs (eqiuvalent to 11.3kfps)
Power consumption	ND	$42.73mW$	$30mW$	6.3μW

Event-based Vision: Custom Design

- ✓ **Better resolution.**
- ✓ **Better accuracy**
- ✓ **Less power consumption**

- × Requires precise optic aligment.
- × Design of visión sensor is specific for this application
- × Requires dedicated ah hoc optics design too.

Conclusions

- A new approach to implement sun sensors has been developed.
- Dark pixels do not send any information off-chip.
- Fast operation.
- Higher dynamic range operation.
- There is not an integration time.
- Very compressed data flow on TFS mode.
- Two different event-based sensors have been described and compared.